Computer Simulation and Topological Modeling of Radiation Effects in Zircon

By
Yi Zhang

B. Eng., Engineering Physics, Tsinghua University, P.R. China (2001)
S. M., Nuclear Engineering, Massachusetts Institute of Technology (2003)

Submitted to the Department of Nuclear Science and Engineering
in partial fulfillment of the requirements for the degree of

DOCTOR OF PHILOSOPHY
at the
MASSACHUSETTS INSTITUTE OF TECHNOLOGY

February 2006

Signature of Author _____
Department of Nuclear Science and Engineering
February 1, 2006

Certified by _____
Linn W. Hobbs (thesis supervisor)
Professor of Material Science and Engineering
Professor of Nuclear Science and Engineering

Certified by _____
Sidney Yip (thesis committee member)
Professor of Nuclear Science and Engineering
Professor of Material Science and Engineering

Certified by _____
Nicola Marzari (thesis committee member)
Associate Professor of Materials Science and Engineering

Accepted by _____
Jeffrey A. Coderre
Chairman, Department Committee on Graduate Students

Topological Modeling of Radiation Effects in Zircon

By
Yi Zhang

Submitted to the Department of Nuclear Science and Engineering
on February 1, 2006, in partial fulfillment of the requirements
for the degree of
Doctor of Philosophy

Abstract

The purpose of this study is to understand on atomic level the structural response of zircon ($ZrSiO_4$) to irradiation using molecular dynamics (MD) computer simulations, and to develop topological models that can describe these structural changes.

Topological signatures, encoded using the concepts of primitive-rings and local clusters, were developed and used to differentiate crystalline and non-crystalline atoms in various zircon structures. Since primitive-rings and local clusters are general concepts applicable to all materials, and the algorithms to systematically identify them are well-established, topological signatures based on them are easy to implement and the method of topological signatures is applicable to all structures. The method of topological signatures is better than the Wigner-Seitz cell method, which depends on the original crystalline reference grid that is unusable in heavily damaged structures or regions; it is also better than those methods based only on local structures limited to first coordination shell, since one can decide whether or not to include ring contents of large rings into the topological signatures, effectively controlling the range of the topological signatures.

The early-stage evolution of non-crystalline disorder and the subsequent recrystallization in zircon collision cascade simulations were successfully modeled by using the topological signatures to identify non-crystalline atoms. Simply using the number of displaced atoms was unable to correctly show the initial peak of structural damage followed by the subsequent annealing stage. Using the topological signatures, amorphization within a single collision cascade was observed in zircon. In the radiation-induced amorphous zircon simulated in this study, the method of topological signatures was able to differentiate the amorphous region in the center of the simulation box and the crystalline region surrounding it. A few isolated remnant crystalline islands were identified in the amorphous region. About 5% of atoms in melted and melt-quenched structures were identified as crystalline atoms.

Different amorphous zircon structures were found to be topologically different. Upon amorphization of zircon, the average ring size and the number of atoms in local cluster were found to increase. Larger average ring sizes were found in more pervasively amorphized structures. The radiation-induced amorphous structure was the least pervasively amorphized one, followed by the melt-quenched. The liquid-state amorphous structure was most pervasively amorphized and had the largest average ring size.

Phase-separation of zircon into SiO_2- and ZrO_2-rich local regions was observed when zircon was amorphized in simulations, either thermally or by radiation. It was found in simulations using constant pressure ensembles that the zircon structure underwent abnormally huge volume swelling when it amorphized, which was attributed to the ion charges used in the potential model. Although the ion charges used in the originally chosen potential model were overall balanced, they were not balanced with regard to the phase decomposition products, and thus resulted in strong Coulombic repulsive force within locally SiO_2- and ZrO_2-rich regions when phase separation occurred. After the ion charges were re-balanced (and other potential parameters refitted), the volume expansion was found to be under control. The charge imbalance of SiO_2 units was also found to produce unrealistically large fraction of 3-coordinated Si and shorter Si-O bond length. The issue of charge-balance with regard to phase decomposition products applies to all complex ceramics that decompose into separate phases upon amorphization.

Threshold displacement energies in zircon were systematically determined. Many special directions, such as those directed toward neighboring atoms or open spaces surrounding the PKA, were considered. Cascade detail was extensively examined, including PKA trajectory, cascade extent, time scale, thermal spike, recoil density, distribution of PKA energy among sub-lattices and number of displaced atoms. The crystallographic features of the zircon structure were found to have profound implications for collision cascades. It was found that energetic PKAs were always deflected into the open channel along the z direction. Their displacements along the longitudinal x direction were never greater than about 4 nm in our simulations. The estimation of the cascade extent assuming homogeneous media thus greatly over-predicts the PKA displacement along the longitudinal direction.

The effects of PKA mass on collision cascade were studied by comparing the cascades caused by Zr and U PKAs. The U atoms were simply "super-mass" Zr atoms in this study: U-Zr, U-Si and U-O interactions were the same as Zr-Zr, Zr-Si and Zr-O interactions, respectively. It was found that heavier PKAs produced longer cascades, more structural damage, and higher temperature in thermal spike. U also traveled further along the longitudinal x direction because it was less prone to change of velocity direction. The depleted regions in the core of the cascades surrounded by a densified shell, which were found in simulations by Trachenko *et al.*, were not found in our study.

After extensive tests of recently published zircon potentials, it was found that three out of the five tested potentials yielded poor elastic constants and appear to be unfit for serious simulations. Published simulation results using these potentials should accordingly be viewed cautiously.

Acknowledgements

I'm most grateful to Professor Linn W. Hobbs, who introduced me to the subject and guided me through the entire project. The frequent discussions about thesis progress were especially helpful.

I'd also like to thank Professor Sidney Yip and Professor Nicola Marzari for serving on my thesis committee and for providing helpful comments about my thesis work.

Dr. Xianglong Yuan helped me in the early days with the software tools, topological modeling, and MD simulations in general. Dr. Kevin Chu of MIT Department of Mathematics provided much needed help in trouble-shooting the Beowulf cluster and setting up the compilation and parallel computing environment. Dr. Ramaswami Devanathan of PNNL was very helpful in providing useful discussions about potential fittings and MD simulations. Dr. Kostya Trachenko of the Department of Earth Sciences, University of Cambridge, UK provided useful comments on MD simulations of zircon. Dr. Julian Gale of Curtin University of Technology, Australia, the author of the code GULP, sent me GULP free of charge and answered my questions on how to use it. Dr. Bill Smith of Daresbury Laboratory, UK, the principal author of DL_POLY, provided me the code DL_POLY, as well as answers to my questions. Without your help, this thesis could not have been completed. Thank you all!

But above all, I want to thank my wife, Lin. Without you, my life would be meaningless.

Table of Contents

List of Figures

List of Tables

Chapter 1: Introduction

1.1 Purpose of this study

The purpose of this study is to understand on atomic level the structural response of zircon to irradiation using molecular dynamics (MD) computer simulations, and to develop topological models that can describe these structural changes.

1.2 The reason of investigating zircon

Zircon ($ZrSiO_4$) has been proposed as one of the leading candidate host materials to encapsulate highly radioactive nuclear waste produced from both civilian nuclear energy usage and nuclear weapons programs.

The technology of using UO_2 fuel in light water reactors (LWRs) is very mature. UO_2 has been used as fuel for LWRs since the very beginning of peaceful utilization of nuclear energy. Because UO_2 fuel contains mostly the isotope U-238 (>95% weight percent in a typical LWR fuel) which is converted to plutonium by interacting with neutrons when irradiated in reactors, a large amount of plutonium has been produced during the last few decades. Most of the plutonium produced from this source currently resides in the spent fuel form and is mostly in custody of private power companies. Another major source of plutonium is from military weapons. As the Cold War ended, many nuclear warheads have been disassembled and they must be properly disposed of. The plutonium inventories in the world are shown in Table 1.1.

Table 1.1: Plutonium stockpiles [1]

Country of Origin	Weapon-Grade Plutonium	Commercial-Grade Plutonium
Argentina	0	6 metric tons (t)
Belgium	0	23-31 t
Brazil	0	0.6 t
Britain	7.6 t	98.4 t (~51 t separated)
China	1.7-2.8 t	1.2 t
France	6-7 t	151-205 t (~70 t separated)
Germany	0	75-105 t (~17 t separated)
India	150-250 kg	6 t (<1 t separated)
Israel	300-500 kg	0
Japan	0	119-262 t (~21 t separated)
Kazakhstan	2-3 t	0
North Korea	25-35 kg	0
Pakistan	0	0.5 t (0 separated)
Russia	140-162 t	65 t (~30 t separated)
United States	85 t	257.2 t (14.5 t separated)

(t = metric ton (2,200 pounds); kg = kilogram)

A worldwide concern about the large stockpile of plutonium from either disassembled nuclear warheads or civilian source has existed for many years. Because of its radioactivity, plutonium is hazardous like any other radioactive material. It takes a very long time for plutonium to decay. For example, ^{239}Pu has a half life of 24,000 years, and it decays to ^{235}U, which is another long-lived radioactive material with a half life of 700,000,000 years. Moreover, both ^{239}Pu and ^{235}U are excellent materials for building nuclear weapons. The danger of these materials falling into unscrupulous hands or organizations is apparent.

Nuclear transmutation is one of several proposed ways to reduce the growing amount of plutonium inventory. Nuclear fuels made partly from nuclear waste can be put into existing fast or thermal reactors for this purpose. However, this method is not as straightforward to carry out as it may sound, because nuclear waste has isotopic contents that are much

different from those of traditional nuclear fuels. In addition, reprocessing nuclear fuels is not allowed in many countries.

Central storage is another possible choice. The US Department of Energy's proposal for a central repository in Yucca Mountain, NY passed in Congress in 2002. In a central storage scheme, we must make sure that the radioactive waste is isolated from the environment for at least tens of thousands of years. The standard waste form chosen historically for central storage is borosilicate glass [2, 3]. However, this waste form is not designed on the basis of high chemical and physical durability and relies mainly on geologic isolation to prevent radioactive nuclides from reaching the biosphere. Another waste form, which is the stimulus of this research, is crystalline ceramics [4]. This waste form is durable for millions, even billions, of years, confirmed by the studies of geologically ancient minerals containing trace radioactive elements that occur in nature.

Zircon ($ZrSiO_4$) has been the mostly investigated waste host in the crystalline ceramics category [4-6]. Zircon is an extremely durable mineral with great mechanical strength, thermodynamic stability and slow kinetics for corrosion processes. Zircon occurs in nature with uranium and thorium concentration up to 5000 ppm [6]. Zircon's tendency to concentrate trace elements (lanthanides and actinides) combined with its resistance to chemical and physical degradation makes it a good nuclear waste host candidate.

Although zircon has many other applications, such as its use in geological dating, it is its application in nuclear waste disposal and its role as a model paradigm for other more highly optimized ceramic waste hosts that stimulate this study. In order to fully evaluate the potential of crystalline

ceramics as nuclear waste hosts, it is crucial to understand the effects of irradiation on their structures and especially, perhaps the most potentially deleterious in these effects, radiation-induced amorphization.

1.3 Computer simulation for studying radiation effects

Over the past few decades, different methodologies of computer modeling have advanced along with increasing computational power. *Ab initio* approaches start from first principles and are the most accurate from a theoretical point of view. However, *ab initio* methods are computationally expensive, thus are best used on small systems with typically at most dozens of atoms. This restriction makes them ineffective in studies of radiation-induced collision cascades, which could involve thousands of atoms.

The Monte Carlo method uses a random number generator to assist in generating the next candidate system configuration, and then decides whether or not to advance to this new configuration using criteria based on energies or possibly other properties. Kinetic Monte Carlo approaches can be used in macroscopic simulations of radiation damage evolution.

The binary collision approximation (BCA) has also been used in the early simulation studies because of its simplicity and early lack of computational power. In BCA, the trajectories of energetic particles are represented as series of two-body encounters. BCA models cannot treat simulations of low kinetic energies or the thermal equilibration of damage. Therefore they are generally not quantitative enough for investigating collision cascade details.

Molecular dynamics (MD) simulations provide at present the best means of describing the collision cascade in greatest detail. MD simulations have

been successfully used to study radiation effects in metals and semiconductors. Radiation-induced fatigue in metals and ion-beam processing of semiconductors are some of the applications. MD simulations were used to investigate radiation dynamics in metals in as early as the 1960s [7-9]. MD simulations have also been very useful in studying radiation effects in ceramics, although with less success. The major impediment is the fact that ceramics are much more structurally complex and compositionally diverse. Different ceramics can have very different responses to irradiation, due to differences in structure, atomic bonding, defect configurations, *etc*. Reliable interatomic potentials for ceramics are also much harder to develop. Generally, it is not straightforward to transfer some simulation capabilities and methodologies from less complex systems, such as metals and semiconductors, to ceramics.

Many oxide ceramics are ionic in nature. The ionic oxide system demands handling of long-range interactions, which makes computer simulation of non-equilibrium events computationally expensive. This is especially true for simulations of high energy collision cascades, because we must use a very small time step size initially.

This computational complexity requires usage of simple potential models, so as to enable simulations done in reasonable computing times. All of the potential models appearing in the literature at this time have been limited to simple ones. The five candidate potential models considered in Chapter 3 use only pair potentials. However, to reproduce physical reality in such complex structures using simple potential models is very challenging. Standing controversies in the literature surrounding collision cascade simulation in zircon, for example that between the University of Cambridge group and the PNNL group [Trachenko *et al*, 10 and 11, Corrales *et al*, 12],

is a testimony to the complexity of the task. We will provide more details of this controversy when discussing choice of empirical potentials in Chapter 3.

The most thoroughly studied ceramic is probably silicon carbide, considering the range and combination of experimental, theoretical and computer simulation studies. However, bonding in SiC is predominantly covalent, the composition is only binary, and anti-site disorder is tolerated, making it a poor model for polyatomic, more ionic ceramics. Radiation effects in zircon have also been widely studied recently, due in part to its potential application as a nuclear waste encapsulation host or as a model crystalline ceramic material. Many computer simulations of zircon [10, 13-22] have been performed. Vastly different potentials are used in these MD simulations by various authors, which we will evaluate in Chapter 3.

1.4 Topological modeling

The topology of a network of atoms describes the way the atoms are connected to each other. Topological modeling has been a useful tool in investigating network structures and rigidity constraints [23-27]. Silicon carbide [28], silica [29, 30] and alkali silicates [31, 32] are among the materials to which topological modeling has been successfully applied. It is easy to see the usefulness of topological methods for glass or other amorphous materials, because the convenient organizing paradigms of unit cell and symmetry are not available. However, topological analysis is by no means limited only to these materials. In fact, it is a very general approach, as atom connectivity is ubiquitous among all materials.

In Chapter 7, bond lengths, bond angles and coordination numbers are analyzed for crystalline, melted, melt-quenched and radiation-induced

amorphous zircon. Polymerization of Si coordination polytopes in amorphous zircon is also investigated.

The concept of continuous closed paths in networks of connected atoms – or rings – together with the related concepts of primitive ring, ring statistics and local cluster, are central to topological analysis [33-50]. In partly amorphized structures, such as zircon after displacive irradiation, the long range periodicity of the crystalline structure has mostly lost, while the short range structure is often not sufficiently well defined to describe the remnant structure and separate amorphized regions from crystalline ones. In this case, primitive ring counts and local cluster enumeration excel in providing the requisite medium-range information. The topology around each atom in a crystalline structure is well defined and unique. If the topological relationships among neighboring atoms can be quantified, they can be used to identify remnant crystalline regions in an amorphizing matrix of atoms, as is done in Chapter 7. They may also be used to evaluate the amorphized structures and to distinguish between different amorphous structural possibilities.

References of chapter 1

[1] Bulletin of the Atomic Scientists, September/October 1999.

[2] Glass as a Waste Form and Vitrification Technology: Summary of an International Workshop. National Academy Press, Washington, DC, 1996.

[3] I.W. Donald, B.L. Metcalfe and R.N.J. Taylor. The Immobilization of High Level Radioactive Wastes Using Ceramics and Glasses. J. Mater. Sci. 32, 5851 (1997).

[4] W.J. Weber, R.C. Ewing, C.R.A. Catlow, T. Diaz de la Rubia, L.W. Hobbs, C. Kinoshita, Hj. Matzke, A.T. Motta, M. Nastasi, E.H.K. Salje, E.R.

Vance and S.J. Zinkle. Radiation Effects in Crystalline Ceramics for the Immobilization of High-Level Nuclear Waste and Plutonium. J. Mater. Res. 13, 1434 (1998).

[5] R.C. Ewing, W. Lutze and W.J. Weber. Zircon: A Host-Phase for the Disposal of Weapons Plutonium. J. Mater. Res. 10, 243 (1995).

[6] R.C. Ewing. Nuclear Waste Forms for Actinides. Proc. Natl. Acad. Sci. U.S.A. 96, 3432 (1999).

[7] C. Erginsoy, G.H. Vineyard and A. Englert. Dynamics of Radiation Damage in a Body-Centered Cubic Lattice. Phys. Rev. 133, A595 (1964).

[8] C. Erginsoy, G.H. Vineyard and A. Shimizu. Dynamics of Radiation Damage in a Body-Centered Cubic Lattice. II. Higher Energies. Phys. Rev. 139, A118 (1965).

[9] J.B. Gibson, A.N. Goland, M. Milgram and G.H. Vineyard. Dynamics of Radiation Damage. Phys. Rev. 120, 1229 (1960).

[10] K. Trachenko, M.T. Dove and E.K.H. Salje. Large Swelling and Percolation in Irradiated Zircon. J. Phys.: Condens. Matter 15, L1 (2003).

[11] K. Trachenko, M.T. Dove and E.K.H. Salje. Reply to Comment on "Large Swelling and Percolation in Irradiated Zircon". J. Phys.: Condens. Matter 15, 6457 (2003).

[12] L.R. Corrales, W.J. Weber, A. Chartier, C. Meis and J.-P. Crocombette. Comment on "Large Swelling and Percolation in Irradiated Zircon". J. Phys.: Condens. Matter 15, 6447 (2003).

[13] M.J. Akhtar and S. Waseem. Atomistic Simulation Studies of Zircon. Chem. Phys. 274, 109 (2001).

[14] J.P. Crocombette and D. Ghaleb. Molecular Dynamics Modeling of Irradiation Damage in Pure and Uranium-Doped Zircon. J. Nucl. Mater. 295, 167 (2001).

[15] B. Park, W.J. Weber and L.R. Corrales. Molecular-Dynamics Simulation Study of Threshold Displacements and Defect Formation in Zircon. Phys. Rev. B 64, 174108 (2001).

[16] R.E. Williford, R. Devanathan and W.J. Weber. Computer Simulation

of Displacement Energies for Several Ceramic Materials. Nuclear Instruments and Methods in Physics Research B 141, 94 (1998).

[17] R.E. Williford, W.J. Weber, R. Devanathan and A.N. Cormack. Native Vacancy Migrations in Zircon. J. Nucl. Mater. 273, 164 (1999).

[18] K. Trachenko, M.T. Dove and E.K.H. Salje. Structural Changes in Zircon under Alpha-Decay Irradiation. Phys. Rev. B 65, 180102(R) (2002).

[19] G.-M. Rignanese, X. Gonze and A. Pasquarello. First-Principles Study of Structural, Electronic, Dynamical, and Dielectric Properties of Zircon. Phys. Rev. B 63, 104305 (2001).

[20] K. Trachenko, M.T. Dove and E.K.H. Salje. Atomistic Modelling of Radiation Damage in Zircon. J. Phys.: Condens. Matter 13, 1947 (2001).

[21] R. Devanathan, L.R. Corrales, W.J. Weber, A. Chartier and C. Meis. Molecular Dynamics Simulation of Disordered Zircon. Phys. Rev. B 69, 064115 (2004).

[22] K. Trachenko, M.T. Dove, T. Geisler, I. Todorov and B. Smith. Radiation Damage Effects and Percolation Theory. J. Phys.: Condens. Matter 16, S2623 (2004).

[23] L.W. Hobbs. The Role of Topology and Geometry in the Irradiation-Induced Amorphization of Network Structures. J. Non-Cryst. Solids 182, 27 (1995).

[24] L.W. Hobbs. Network Topology in Aperiodic Networks. J. Non-Cryst. Solids 192&193, 79 (1995).

[25] L.W. Hobbs, A.N. Sreeram, C.E. Jesurum and B.A. Berger. Structural Freedom, Topological Disorder, and the Irradiation-Induced Amorphization of Ceramic Structures. Nucl. Instr. and Meth. B 116, 18-25 (1996).

[26] L.W. Hobbs, C.E. Jesurum and B. Berger. Rigidity Constraints in Amorphization of Multiply-Polytopic Multiply-Connected Ceramic Structures. Mat. Res. Soc. Symp. Proc. 540, 717 (2000).

[27] L.W. Hobbs, C.E. Jesurum and B. Berger. in: Rigidity Theory and Applications, ed. P.M. Duxbury and M.F. Thorpe. Plenum Press, New York, 1999.

[28] X. Yuan and L.W. Hobbs. Modeling Chemical and Topological Disorder in Irradiation-Amorphized Silicon Carbide. Nucl. Instr. and Meth. B 191, 74-82 (2002).

[29] L.W. Hobbs and X. Yuan. Topology and Topological Disorder in Silica. in: Defects in SiO_2 and Related Dielectrics: Science and Technology. ed. G. Pacchioni, L. Skuja and D. Griscom. Kluwer, Dordrecht, Netherlands, 2000.

[30] L.W. Hobbs, C.E. Jesurum and B. Berger. The Topology of Silica Networks. in: Structure and Imperfections in Amorphous and Crystalline Silicon Dioxide. ed. R.A.B. Devine, J.-P. Duraud and E. Dooryhee. John Wiley & Sons, 2000.

[31] X. Yuan and A.N. Cormack. Si–O–Si Bond Angle and Torsion Angle Distribution in Vitreous Silica and Sodium Silicate Glasses. J. Non-Cryst. Solids, 319, 31 (2002).

[32] X. Yuan and A.N. Cormack. Local Structures of MD-Modeled Vitreous Silica and Sodium Silicate Glasses. J. Non-Cryst. Solids 283, 69 (2001).

[33] K. Goetzke and H.-J. Klein. Properties and Efficient Algorithmic Determination of Different Classes of Rings in Finite and Infinite Polyhedral Networks. J. Non-Cryst. Solids 127, 215 (1991).

[34] W. Jin, R.K. Kalia, P. Vashishta and J.P. Rino. Structural Transformation in Densified Silica Glass: A Molecular-Dynamics Study. Phys. Rev. B 50, 118 (1994).

[35] B. Mihailova, N. Zotov, M. Marinov, J. Mikoliv and L. Konstantinov. Vibrational Spectra of Rings in Silicate Glasses. J. Non-Cryst. Solids 168, 265 (1994).

[36] J.P. Rino, I. Ebbsjo, R.K. Kalia, A. Nakano and P. Vashishta. Structure of Rings in Vitreous SiO_2. Phys. Rev. B 47, 3053 (1993).

[37] X. Yuan and A.N. Cormack. Efficient Algorithm for Primitive Ring Statistics in Topological Networks. Comp. Mater. Sci. 24, 343 (2002).

[38] C.S. Marians and L.W. Hobbs. Network Properties of Crystalline Polymorphs of Silica. J. Non-Cryst. Solids 124, 242 (1990).

[39] L. Guttman. Ring Structure of the Crystalline and Amorphous Forms of Silicon Dioxide. J. Non-Cryst. Solids 116, 145 (1990).

[40] R.J. Bell and P. Dean. The Structure of Vitreous Silica: Validity of the Random Network Theory. Philos. Mag. 25, 1381 (1972).

[41] A.C. Wright and J.A.E. Desa. III-V Analogues and Bonding Topology in Vitreous Silica. Phys. Chem. Glasses 19, 140 (1978).

[42] B.P. Feuston and S.H. Garofalini. Empirical Three-Body Potential for Vitreous Silica. J. Chem. Phys. 89, 5818 (1988).

[43] A.N. Cormack and Y. Cao. in: Modeling of Minerals and Silicated Materials. ed. B. Silvi and P. D'Arco. Kluwer, Dordrecht, 1997.

[44] L.W. Hobbs, C.E. Jesurum, V. Pulim and B. Berger. Local Topology of Silica Networks. Philos. Mag. A 78, 679 (1998).

[45] S.V. King. Ring Configurations in a Random Network Model of Vitreous Silica. Nature 213, 1112 (1967).

[46] B. Vessal. Simulation Studies of Silicates and Phosphates. J. Non-Cryst. Solids 177, 103 (1994).

[47] R.G.D. Valle and H.C. Andersen. Molecular Dynamics Simulation of Silica Liquid and Glass. J. Chem. Phys. 97, 2682 (1992).

[48] L.F. Gladden, M. Vignaux, P. Chiaranussati, R.W. Griffiths, S.D. Jackson, J.R. Jones, A.P. Sharratt, F.J. Robertson, G. Webb, P. Chieux and A.C. Hannon. Structural Studies of High Surface Area Silicas. J. Non-Cryst. Solids 139, 47 (1992).

[49] C.S. Marians and L.W. Hobbs. Local Structure of Silica Glasses. J. Non-Cryst. Solids 119, 269 (1990).

[50] L. Guttman and S.M. Rahman. Simulation of the Structure of Amorphous Silicon Dioxide. Phys. Rev. B 37, 2657 (1988).

Chapter 2: Model of zircon structure

2.1 Zircon ($ZrSiO_4$) crystalline structure

We will only briefly review zircon crystalline structure, as it has been described in great detail elsewhere [1-4].

Zircon, $ZrSiO_4$, adopts a body-centered tetragonal crystal structure. The space group zircon belongs to is $I4_1/amd$ (No. 141). The primitive cell of zircon contains two formula units of $ZrSiO_4$, whereas the conventional unit cell contains four formula units. A depiction of the conventional zircon unit cell is shown in next section (Figure 2.2).

Zr atoms in zircon occupy the *4a* Wyckoff sites; Si atoms occupy the *4b* Wyckoff sites; and O atoms occupy the *16h* Wyckoff sites (0, *u*, *v*), with *u* and *v* parameters determined experimentally. We will see in Section 2.2 how to use this information together with experimentally determined *u* and *v* values to generate zircon atom positions.

The principle structural unit of zircon can be described as a chain of alternating edge-sharing SiO_4 tetrahedra and ZrO_8 triangular dodecahedra extending parallel to the *c* axis, with the chains joined along the *a* axis by edge-sharing ZrO_8 triangular dodecahedra. These features are shown to be correctly represented in our zircon structure model developed in next section, as seen in Figures 2.7 and 2.8.

2.2 Model of zircon structure

A general reference that contains crystal structure information for many

materials is Wyckoff's *Crystal Structures*. Zircon structure is found in volume 3 of this reference [5]. The space group of zircon is given as D_{4h}^{19}(I4/amd); cell edge lengths are given as a_0 = 6.6164 Å, c_0 = 6.0150 Å; and the atomic positions of tetragonal $ZrSiO_4$ are given as

Zr: (4a)	000; 0 ½ ¼; ½ 0 ¾; ½ ½ ½
Si: (4b)	0 0 ½; 0 ½ ¾; ½ 0 ¼; ½ ½ 0
O: (16h)	$0\,u\,v$; $0\,\bar{u}\,\bar{v}$; $u\,0\,\bar{v}$; $\bar{u}\,0\,\bar{v}$;
	$0,\ u+½,\ ¼-v$; $0,\ ½-u,\ ¼-v$; $\bar{u},\ ½,\ v+¼$; $u,\ ½,\ v+¼$;
	B.C.

with parameters u = 0.20 and v = 0.34.

The information shown above is all we need to derive atomic positions. However, the parameters in [5] are not the most accurate ones available. The exact year these parameters were determined is not given, other than an explicit mention of "many years ago" relative to the publishing year (1963) of [5]. Zircon structure parameters were also determined experimentally by Robinson, Gibbs and Ribbe [2] in 1971. These parameters are the ones we will use.

With the zircon structure parameters from [2], we can use the *International Tables for X-ray Crystallography* [6] to generate the full set of atom positions. The reason parameters in [5] are mentioned, even though they will not be used, is because [5] provides a valuable check when deriving atom positions. There is a shift of origin between the data in [2] and [5], and the reference we used to generate the full set of atom positions [6] uses the same origin convention as [5]. Before we can use [2] and [6] together, an origin shift of the data found in [2] is performed to adopt the origin convention used in [5]. So, the data in [5] can serve as a useful check to make sure the origin shift is performed correctly.

In reference [2], zircon crystalline structure data are given as

Space group: $I4_1/amd$ (In [5]: I4/amd)
Cell edge lengths: $a = 6.607$ Å (6.6164 in [5]), $c = 5.982$ Å (6.0150 in [5]).
Atom positions:

Zr: (0.0, 0.75, 0.125) (In [5]: (0, 0.5, 0.25))
Si: (0.0, 0.75, 0.625) (In [5]: (0, 0.5, 0.75))
O: $y = 0.0661$, $z = 0.1953$ (In [5]: $u = 0.20$, $v = 0.34$)

Atom position parameters given in [5] are shown in parentheses. For O atom positions, symbols y and z are used in [2] whereas u and v are used in [5], but it's apparent they represent the same parameters.

Comparison of the Zr, Si and O atom positions given in [2] and [5] clearly shows that there is a shift of origin involved. For all the positions, if we add (0, -0.25, 0.125) to the atom position data of [2], we can get the values given in [5]: for Zr, shifting (0.0, 0.75, 0.125) of [2] by [0, -0.25, 0.125] yields the (0, 0.5, 0.25) reported in [5]; where for Si, shifting (0.0, 0.75, 0.625) position of [2] by [0, -0.25, 0.125] yields the (0, 0.5, 0.75) in [5].

The situation is a little more complicated for O. Shifting $y = 0.0661$ and $z = 0.1953$ by -0.25 and 0.125, respectively, yields $y = -0.1839$ and $z = 0.3203$. These are quite different from $u = 0.20$ and $v = 0.34$ reported in [5], unless we reverse the sign of y and use $y = 0.1839$. The remaining differences can be accepted as data differences between different experiments.

But can we legitimately reverse the sign of y (or u)? The answer is yes. Due to symmetry, there is no difference in using y or $-y$ for generating atom positions. The equality of using either y or $-y$ can also be seen quantitatively later when we actually use these parameters to generate oxygen atom

positions. We will see that for every position generated using y, there is a corresponding position generated using $-y$, so it really does not matter whether we used y or $-y$ in the first place.

The reason for this over-elaborated discussion of atomic positions is that the crystallographic structure of $CaTiO_3$ perovskite sent to us by Trachenko *et al.* was wrong, admitted by Trachenko in a private email communication, which made us extra careful in dealing with atomic positions of all complex structures, including zircon.

Page 245 of [6] is devoted to the $I4_1/amd$ space group to which zircon belongs. The essential information from this page is reproduced below.

Coordinates of equivalent positions: (0,0,0; 0.5,0.5,0.5)+
(This means for every location (x, y, z) below, there is a corresponding one at $(x + 0.5, y + 0.5, z + 0.5)$.)

4a: (0, 0, 0) (0, 0.5, 0.25)
4b: (0, 0, 0.5) (0, 0.5, 0.75)
8c: (0, 0.25, 0.125) (0, 0.75, 0.125)
(0.25, 0, 0.875) (0.75, 0, 0.875)
8d: (0, 0.25, 0.625) (0, 0.75, 0.625)
(0.25, 0, 0.375) (0.75, 0, 0.375)
8e: (0, 0, z) (0, 0, -z)
(0, 0.5, 0.25 + z) (0, 0.5, 0.25 – z)
16f: (x, 0.25, 0.125) (-x, 0.25, 0.125)
(x, 0.75, 0.125) (-x, 0.75, 0.125)
(0.25, x, 0.875) (0.25, -x, 0.875)
(0.75, x, 0.875) (0.75, -x, 0.875)
16g: (x, x, 0) (-x, -x, 0)
(x, 0.5 + x, 0.25) (-x, 0.5 – x, 0.25)
(x, -x, 0) (-x, x, 0)
(x, 0.5 – x, 0.25) (-x, 0.5 + x, 0.25)
16h: (0, x, z) (0, -x, z)

$(0, 0.5 + x, 0.25 - z)$ $(0, 0.5 - x, 0.25 - z)$
$(x, 0, -z)$ $(-x, 0, -z)$
$(x, 0.5, 0.25 + z)$ $(-x, 0.5, 0.25 + z)$

32i: (x, y, z) $(-x, -y, z)$
$(x, 0.5 + y, 0.25 - z)$ $(-x, 0.5 - y, 0.25 - z)$
$(-x, y, z)$ $(x, -y, z)$
$(-x, 0.5 + y, 0.25 - z)$ $(x, 0.5 - y, 0.25 - z)$
$(y, x, -z)$ $(-y, -x, -z)$
$(y, 0.5 + x, 0.25 + z)$ $(-y, 0.5 - x, 0.25 + z)$
$(-y, x, -z)$ $(y, -x, -z)$
$(-y, 0.5 + x, 0.25 + z)$ $(y, 0.5 - x, 0.25 + z)$

Generating Zr and Si atom positions at 4a and 4b sites does not need any additional parameters. For O atoms at the 16h site, we need parameters x and z. A simple comparison reveals that the "x" here is equivalent to the "y" used in [2], or the "u" used in [5]; the "z" here is equivalent to the "z" used in [2], or the "v" used in [5]. As can be seen in the coordinates for the 16h sites above, for every coordinate that's generated using x, there is a corresponding one using $-x$. For example, for $(0, 0.5 + x, 0.25 - z)$, there is $(0, 0.5 - x, 0.25 - z)$. This justifies our previous proposition that we can inverse x (y in [2]) without affecting the atom positions generated.

Using $x = 0.1839$ and $z = 0.3203$, we generate coordinates for all the O atoms. During this process, equivalent positions due to crystalline periodicity are used to make sure every coordinate is between 0 (inclusive) and 1 (exclusive), because we do not want atoms to be out of the simulation cell. For example, 1.0 is equivalent to 0.0, -0.3 is equivalent to 0.7, *etc.* The final zircon crystal structure determined using experimental data in [2] is shown below

Cell edge lengths:
$a = 6.607$ Å, $c = 5.982$ Å
(For tetragonal system $a = b$).

Atom positions:
Zr: 4a
Si: 4b
O: 16h with $x = 0.1839$ and $z = 0.3203$

Full atom coordinates:
Zr (0.0, 0.0, 0.0)
Zr (0.5, 0.5, 0.5)
Zr (0.0, 0.5, 0.25)
Zr (0.5, 0.0, 0.75)
Si (0.0, 0.0, 0.5)
Si (0.5, 0.5, 0.0)
Si (0.0, 0.5, 0.75)
Si (0.5, 0.0, 0.25)
O (0.0, 0.8161, 0.3203)
O (0.5, 0.3161, 0.8203)
O (0.0, 0.1839, 0.3203)
O (0.5, 0.6839, 0.8203)
O (0.0, 0.3161, 0.9297)
O (0.5, 0.8161, 0.4297)
O (0.0, 0.6839, 0.9297)
O (0.5, 0.1839, 0.4297)
O (0.8161, 0.0, 0.6797)
O (0.3161, 0.5, 0.1797)
O (0.1839, 0.0, 0.6797)
O (0.6839, 0.5, 0.1797)
O (0.8161, 0.5, 0.5703)
O (0.3161, 0.0, 0.0703)
O (0.1839, 0.5, 0.5703)
O (0.6839, 0.0, 0.0703)

There are 24 atoms in the unit cell (4 $ZrSiO_4$ units). Figure 2.1 shows the zircon unit cell with exactly the 24 atoms whose coordinates have been shown above. There are 4 blue Zr atoms; 4 pink Si atoms; and 16 red O atoms. This figure shows the model ready to be repeated in x, y and z directions to form a supercell, which can then be used in computer simulations. However, Figure 2.1 is not the conventional way to draw unit cell. A conventional unit cell representation usually also includes all the

replicates of the atoms at the unit cell boundary, as shown in Figure 2.2. For example, for Zr at (0, 0, 0), its replicates at (1, 0, 0), (0, 1, 0), (0, 0, 1), (1, 1, 0), (1, 0, 1), (0, 1, 1) and (1, 1, 1) are also included. Figure 2.2 has been rotated from Figure 2.1 for better viewing. Orientations of axis are shown at the lower-left corners of both figures.

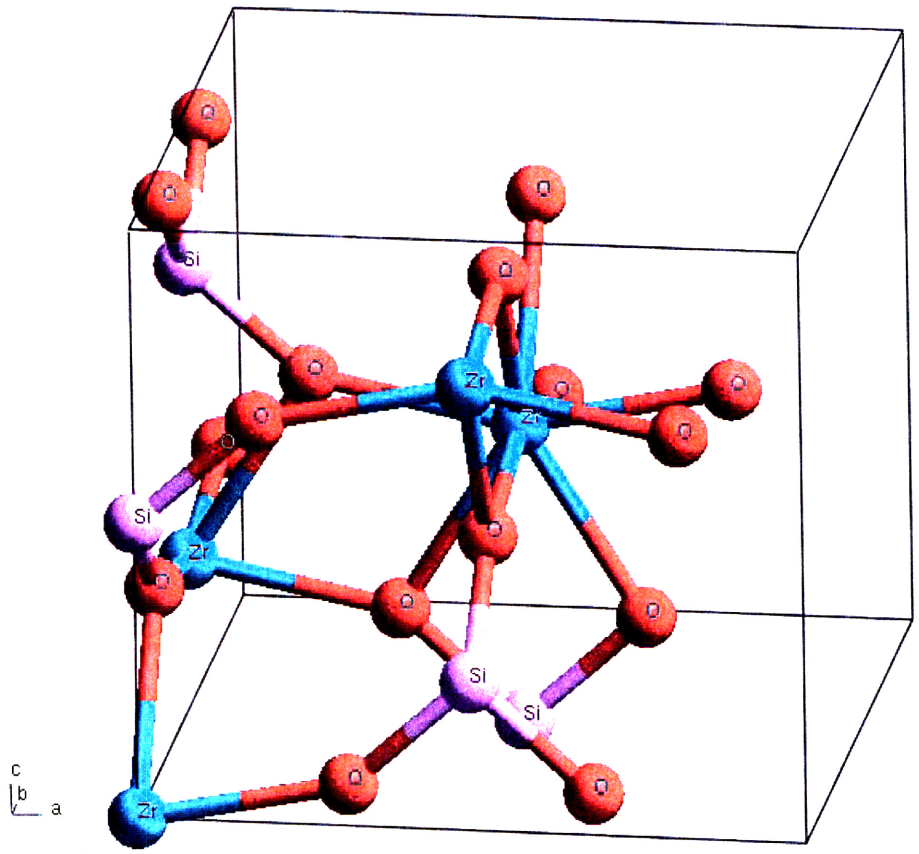

Figure 2.1: Non-conventional zircon unit cell showing the 24 atoms in the unit cell. A conventional unit cell figure would also include replicates of the atoms at the boundary, as shown in Figure 2.2.

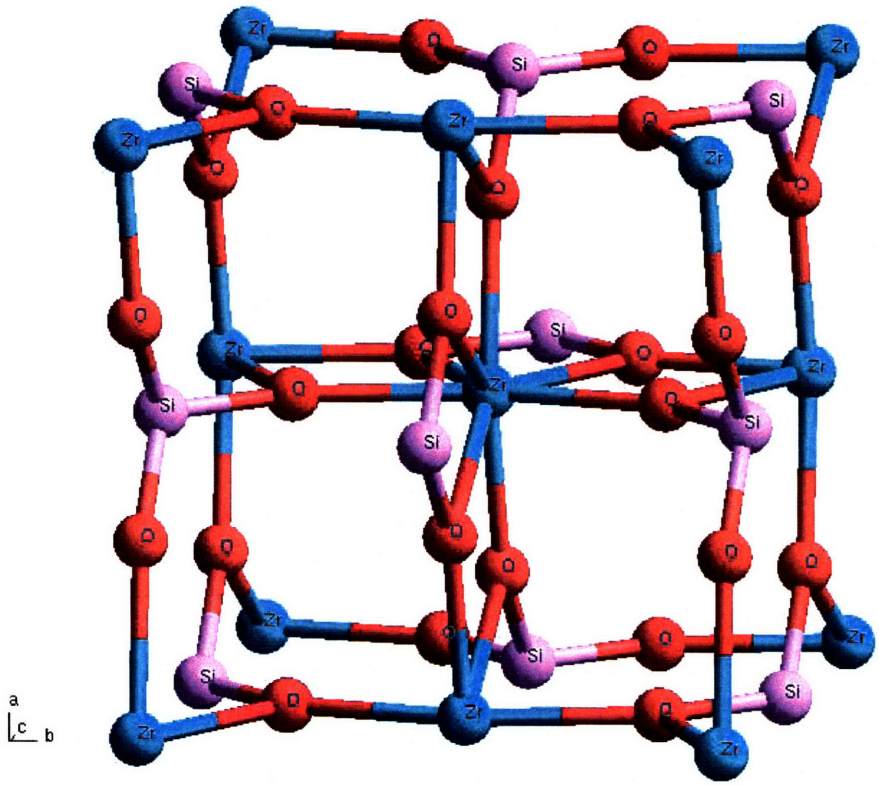

Figure 2.2: Zircon unit cell showing the 24 atoms in the unit cell and all the replicated atoms at the boundary. For example, for Zr at (0, 0, 0), its replicates at (1, 0, 0), (0, 1, 0), (0, 0, 1), (1, 1, 0), (1, 0, 1), (0, 1, 1) and (1, 1, 1) are all included in the figure.

Figure 2.3 shows the unit cell with only stick bonds. This representation is especially helpful for appreciating the overall bond geometry in the zircon structure.

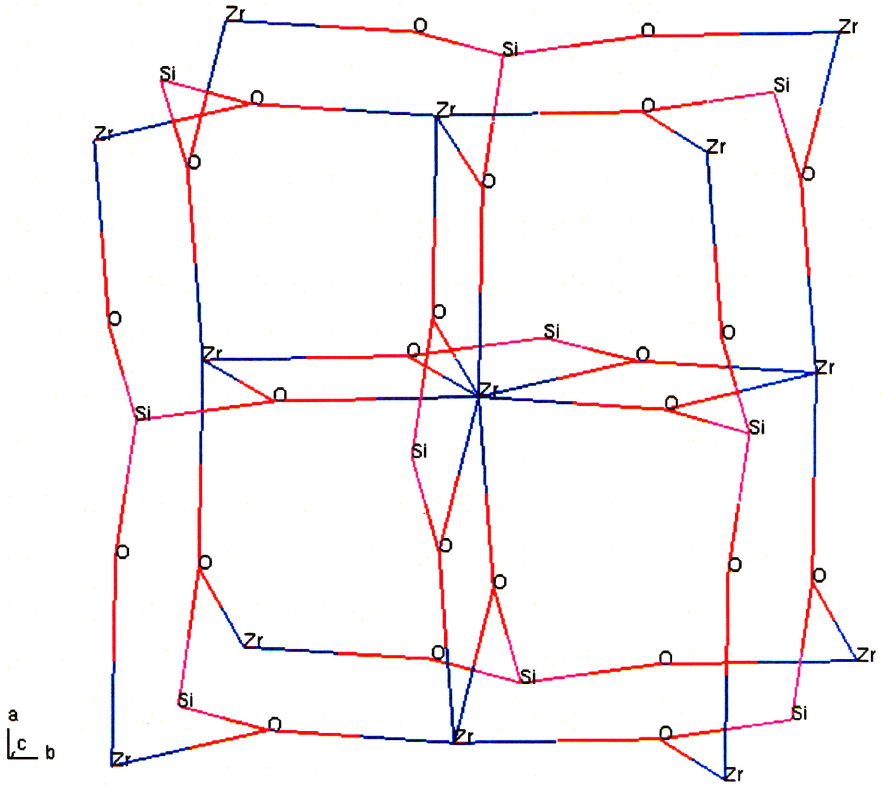

Figure 2.3: Zircon unit cell showing the 24 atoms in the unit cell and all the replicated atoms at the boundary. This is the same structure as Figure 2.2, but with only sticks representing Zr-O and Si-O bonds.

Figure 2.4 shows a close-packed view of the unit cell.

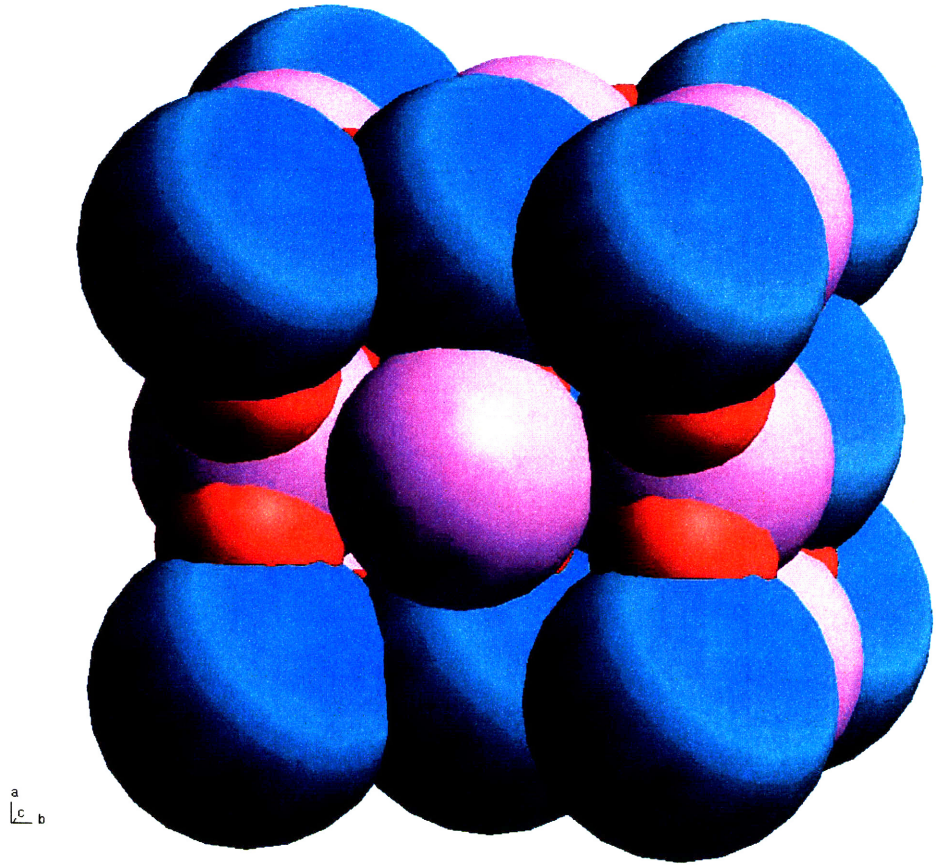

Figure 2.4: (Color) Close-packed representation of zircon unit cell. Zr atoms are blue; Si atoms are pink; and O atoms are red.

Figures 2.5 and 2.6 are representations of the 6×6×6 zircon supercell, viewed from different directions. The structure is viewed from the $[0\bar{1}0]$ direction in Figure 2.5 and from the [001] direction in Figure 2.6.

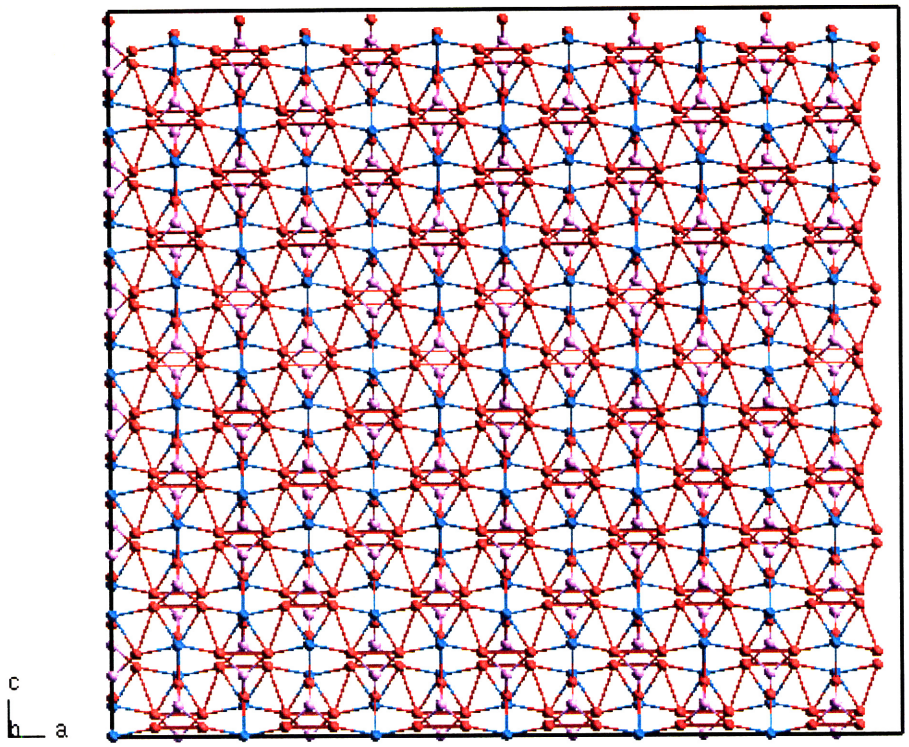

Figure 2.5: (Color) 6×6×6 zircon supercell viewed from the $[0\bar{1}0]$ direction. Zr atoms are blue; Si atoms are pink; and O atoms are red.

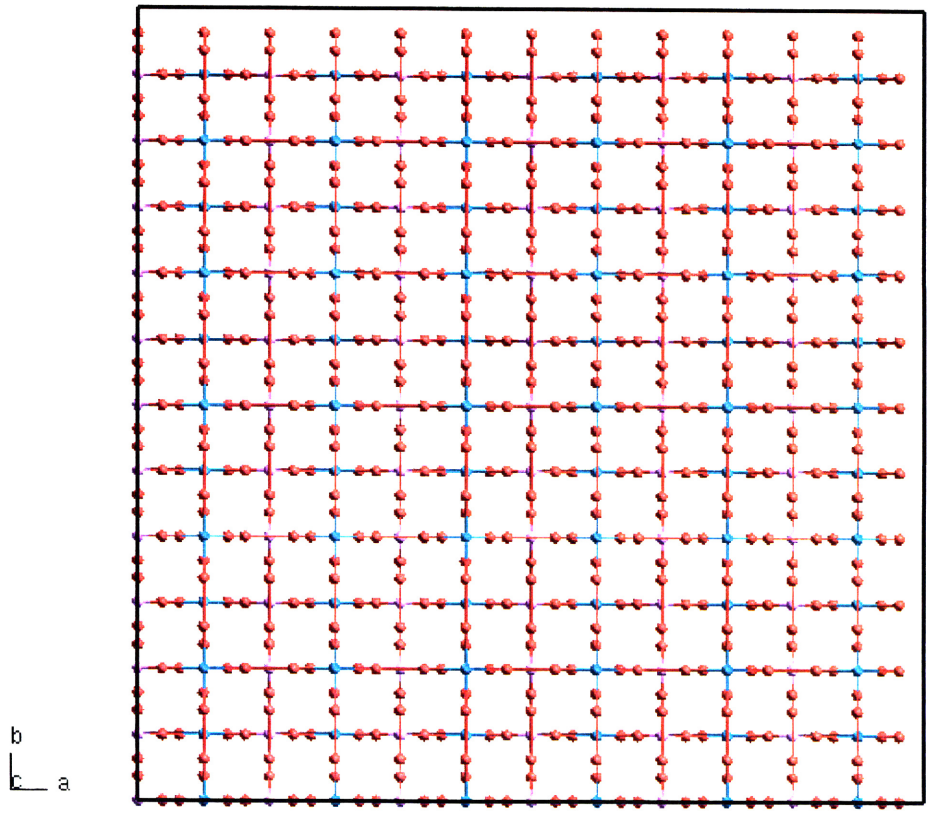

Figure 2.6: (Color) 6×6×6 zircon supercell viewed from the [001] direction. Zr atoms are blue; Si atoms are pink; and O atoms are red. The tetragonal structure and the open channels along the *c* axis are apparent.

In Section 2.1, we mentioned that the principal zircon structural units can be considered as a chain of alternating edge-sharing SiO_4 tetrahedra and ZrO_8 triangular dodecahedra extending parallel to the *c* axis, with the chains joined along the *a* axis by edge-sharing ZrO_8 triangular dodecahedra. We now investigate whether these features are present in our zircon model.

The first check is for the chain of alternating edge-sharing SiO_4 tetrahedra and the ZrO_8 triangular dodecahedra extending parallel to the *c* axis. A 1×1×2 supercell is made for this purpose and is shown in Figure 2.7. The alternating SiO_4 and ZrO_8 structural units are marked in the figure.

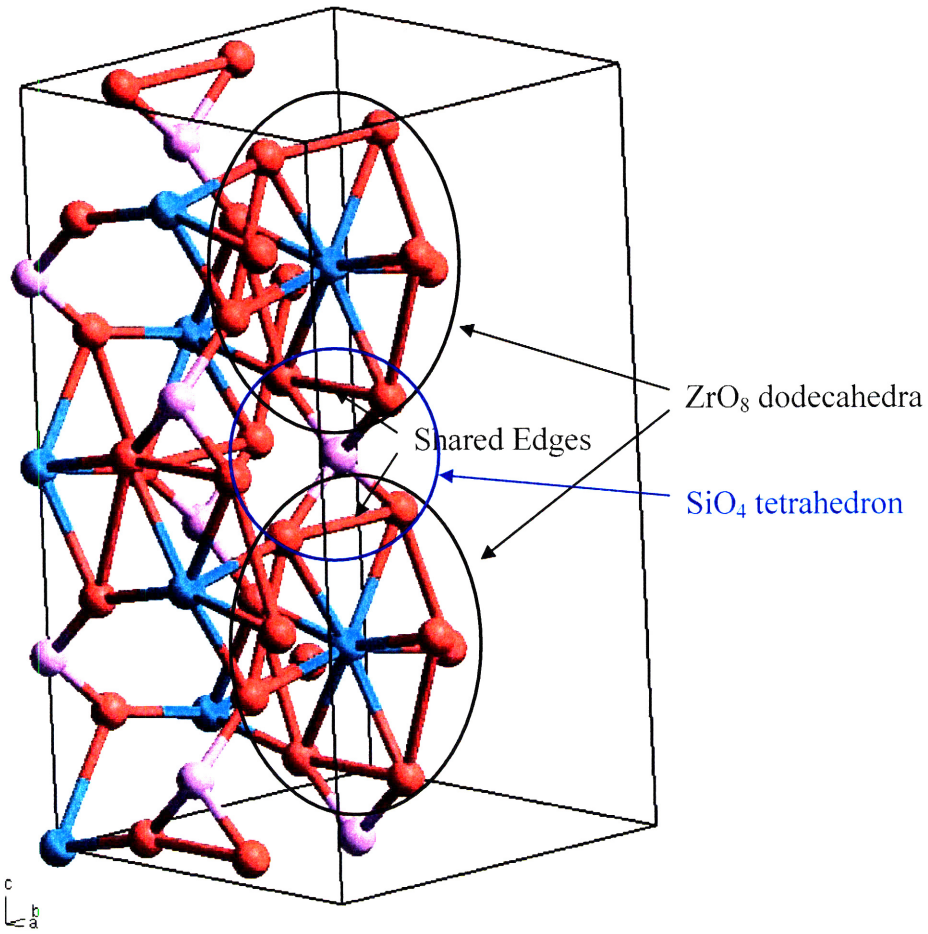

Figure 2.7: (Color) Edge-sharing SiO_4 tetrahedra and ZrO_8 triangular dodecahedra parallel to the *c* axis. Zr atoms are blue; Si atoms are pink; and O atoms are red.

Figure 2.8 shows that the chains shown in Figure 2.7 are joined along the *a* axis by edge-sharing ZrO_8 dodecahedra, as observed in experiments.

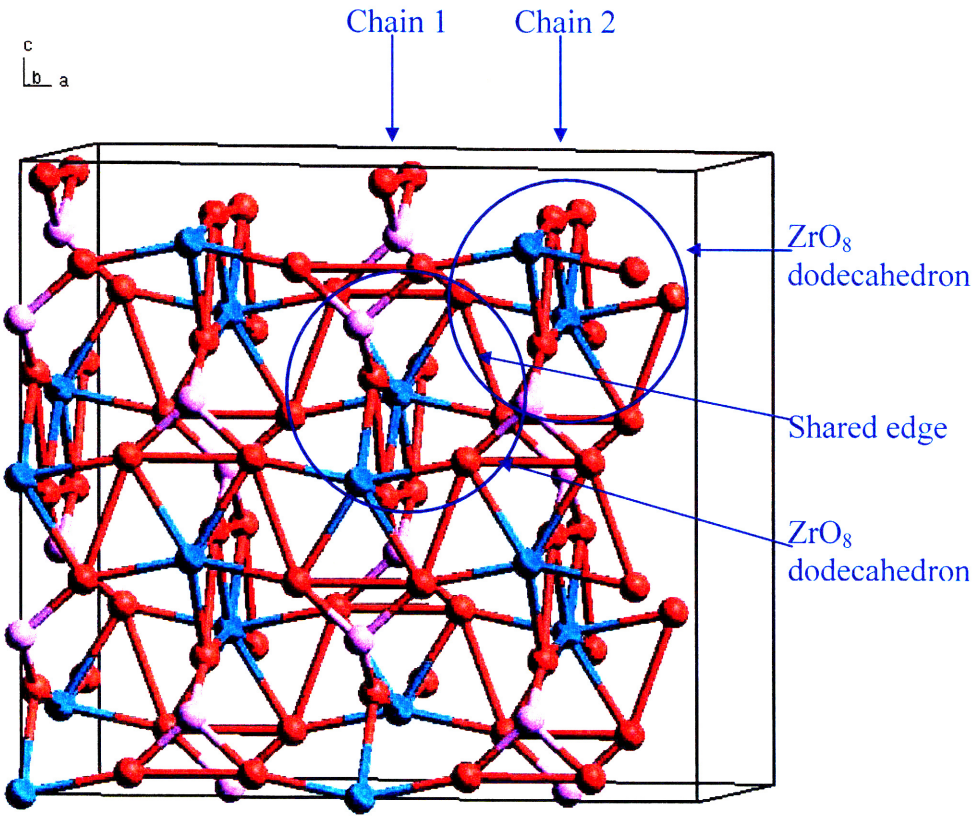

Figure 2.8: (Color) Alternating edge-sharing SiO_4 tetrahedra and ZrO_8 triangular dodecahedra chains are joined along the *a* axis by edge-sharing ZrO_8 triangular dodecahedra. Zr atoms are blue; Si atoms are pink; and O atoms are red.

Thus the essential zircon structural features determined experimentally are correctly represented in our computer model.

The zircon figures shown so far are all atomistic. The macroscopic appearances of zircon gem stone and a mineral specimen collected from the field are respectively shown in Figure 2.9 and Figure 2.10.

Figure 2.9: Polished and facetted zircon gem stone [12].

Figure 2.10: Zircon mineral specimen showing 4-fold (actually 4i) axis [13].

2.3 Comparison of model and experimental zircon structures

The zircon structure model developed in Section 2.2 is compared to the experimental structure in this section. Bond lengths, bond angles, cation-cation distances and coordination numbers (multiplicities) are among the structural features compared.

Bond lengths are determined from the radial distribution function (RDF) and, similarly, bond angles are determined from bond angle distribution function (BADF). The algorithms used for calculating RDF and BADF are described in Sections 2.3.1 and 2.3.2, respectively. Comparison of the results is presented in Section 2.3.3.

2.3.1 Algorithm for RDF calculation

Bond lengths can be determined from the RDF. For a crystalline structure, the RDF plot should consist of well-defined δ-function peaks at 0 K, from which we can easily obtain interatomic distances and thus bond lengths.

The RDF is a well-defined concept and is described in standard solid-state references (see, for example, Kittel [14]). However, the algorithm to calculate it from computer model structures, although not complicated, is not readily obtainable from the literature. As a result, a RDF calculation algorithm is described in detail here. First a few definitions

Concentration of atoms: number of atoms per unit volume
$\rho(r)$: the concentration of atoms at distance r from a given atom
ρ_0: the average concentration of atoms
$\rho(r) = g(r) \cdot \rho_0$

g(r) is the radial distribution function.

We will first calculate $\rho(r)$ and ρ_0. The quotient of the two will be the required RDF, g(r). The algorithm can be broken down into the following steps

1) Define the desired range of r for the RDF. For example, range = 10 Å.
2) Choose a discretization width dr, which defines the resolution in the

RDF. For example, dr = 0.002 Å.

3) Choose the pair of atoms, atom1 and atom2, that defines the partial RDF. For example, to calculate Si-O RDF, choose Si as atom1 and O as atom2. To calculate a total RDF without specification, no atom needs to be chosen at this step.
4) Select an atom1 in the system and count number of atom2 atoms that are within distance (r, r + dr) from atom1. Denote this count as n(r). When calculating distances between atoms, make sure to take periodic boundary conditions into consideration (see, for example, Allen and Tildesley [15] for how to calculate distances under periodic boundary conditions).
5) Because $(4\pi r^2)\, dr\, \rho(r) = n(r)$, we can calculate $\rho(r)$ using $\rho(r) = n(r) / (4\pi r^2\, dr)$.
6) Accumulate n(r) from r = 0 to the range chosen in step 1) to get the total count of atom2 atoms within the chosen range from the chosen reference atom1 atom.
7) The total volume is $4\pi(\text{range}^3)/3$.
8) Divide the total count in 6) by the total volume in 7); this is the average concentration ρ_0.
9) Divide the $\rho(r)$ in step 5) by the ρ_0 in step 8) to obtain the RDF for the reference atom chosen in step 4). Calculate the RDF for all atom1 atoms or for all atoms in the system if no specific atom1 is chosen in step 3). The average of all these respective RDFs is the RDF result sought.

The above algorithm calculates the RDF for a given system configuration. This configuration could be the model zircon crystalline structure we have developed in Section 2.2, or it could be a snapshot of the zircon structure during the course of molecular dynamics simulation. In the latter case, in

order to achieve better statistics and therefore smoother RDF curves, it is often necessary to calculate RDFs at multiple snapshots (at multiple time steps) near the end of the MD simulation and take the average of these RDFs as the final result. For example, some RDFs calculated in Chapter 4 and Chapter 7 are averaged over the final 5.0 ps of simulations.

2.3.2 Algorithm for BADF calculation

The calculation of bond angle distribution function (BADF) is a little more complicated than that of RDF because a triplet of atoms is involved for each bond angle, instead of just a pair in the RDF case. In addition, calculating the bone angle requires the definition of "bond" *a priori*, which in turn mandates specification of a bond-length cutoff value (how close two atoms need to be before they are considered bonded). For Si-O, a substantially covalent bond actually forms, whereas for Zr-O the bonding is predominantly ionic and therefore not pairwise directional; we shall, however, continue to use the term "bond" advisedly for all such attractive interionic pairs which sit in local minima of a larger Coulomb potential.

Bond-length cutoffs can be determined from the RDF plots calculated using the algorithm described in Section 2.3.1. Figure 2.11 shows the Si-O RDF of zircon after performing a molecular dynamic simulation at 5000 K (the structure has already melted at this temperature). We can choose the bond-length cutoff at the first valley of RDF plot, with a value of 2.43 Å in the case of Figure 2.11.

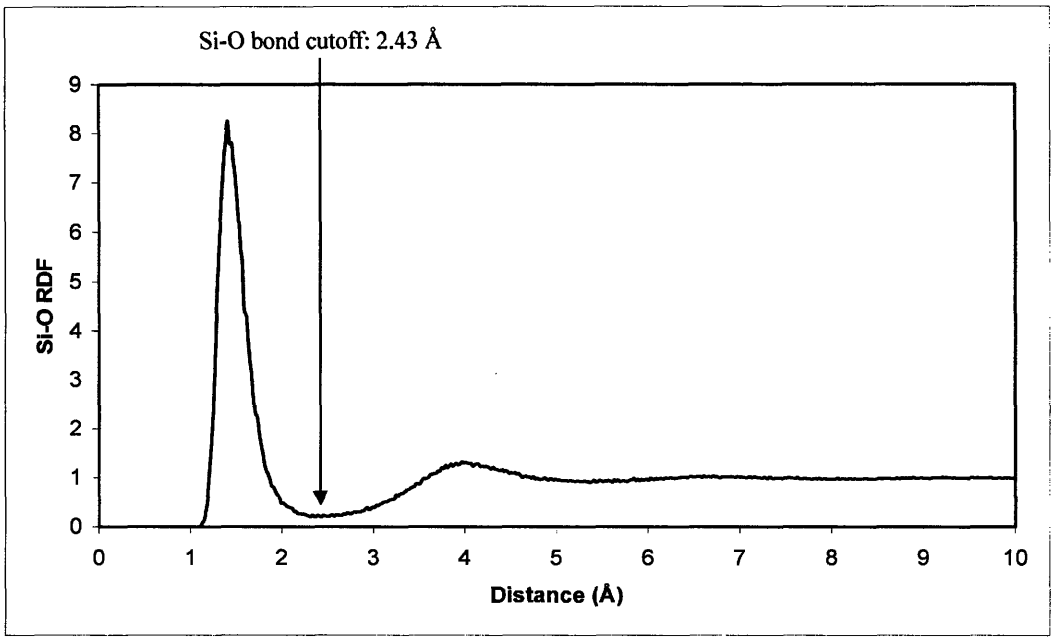

Figure 2.11: Si-O RDF of zircon at 5000 K. Si-O bond-length cutoff can be chosen at the first valley.

RDF peaks are much sharper for crystalline structures. Figure 2.13 in Section 2.3.3 is the Si-O RDF plot of crystalline zircon where the sharp peaks are apparent. In that case, there is no "valley" in the curve, so we cannot use the method used in Figure 2.11. Instead, we can take the average of the locations of first two peaks as the cutoff value (in other words, halfway between the nearest and next-nearest neighbors for the pair of specified atom types). In Figure 2.13, the first and second RDF peaks are at distances of 1.62 Å and 3.33 Å, respectively, so the cutoff value can be chosen as (1.62 + 3.33) / 2 = 2.475 Å. This procedure gives the same results for O-Si and Si-O cutoffs because the sharp peaks in O-Si and Si-O RDF plots appear at the same locations.

These rules for determining bond-length cutoff values may not be the best ones; they are certainly not the only choices made. But they will nonetheless be used throughout this study when bond-length cutoff values need to be

determined, because they are reasonable and fit our needs sufficiently well.

Another difficulty when calculating BADF is to actually calculate the bond angle for a triplet of atoms. Again periodic boundary conditions need to be taken into consideration. Figure 2.12 is a two-dimensional example. In this figure, the rectangle in the center denotes the simulation cell and the other 8 rectangles are image replicates from imposition of periodic boundary conditions. To calculate the bond angle between bond 1-2 and bond 2-3, the angle 1-2-3', not the angle 1-2-3, should be chosen because atom 3' is closest to atom 2 of all the images of atom 3 (including atom 3 itself).

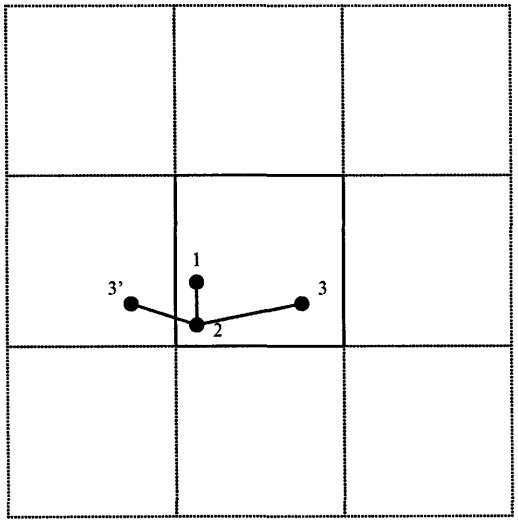

Figure 2.12: Taking periodic boundary condition into consideration when calculating bond angles. The rectangle in the center is the simulation cell. The other 8 rectangles are its replicates from imposition of periodic boundary conditions. The bond angle between bond 1-2 and bond 2-3 is properly the angle 1-2-3', because atom 3' is closest to atom 2 of all the images of atom 3 (including atom 3 itself).

The Law of Cosines can be used to actually calculate the numerical value of the bond angle. Again, we use Figure 2.12 as an example of calculating bond angle 1-2-3' and denote the length of bond 1-2 as a; length of 2-3' as b;

length of 1-3' as c; and the angle we want to calculate (1-2-3') as θ. From the Law of Cosines we have: $c^2 = a^2 + b^2 - 2ab\cos\theta$. Solving this equation will give us get the angle θ we want once we know values of a, b and c, which can be calculated from atom positions.

With the problems of defining bond-length cutoff values and calculating bond angles sorted out, we are ready to present the algorithm for BADF calculation. First are some definitions

Concentration of angle: count of bond angles per unit angle interval.
$\rho(\theta)$: concentration of angle at angle θ.
ρ_0: average concentration of angle.
$\rho(\theta) = g(\theta) \cdot \rho_0$

$g(\theta)$ is the bond angle distribution function.

We will first calculate $\rho(\theta)$ and ρ_0. The quotient of the two will be the required BADF, $g(\theta)$. The algorithm we use can be broken down into the following steps, which are parallel to the RDF calculation algorithm presented in Section 2.3.1. To calculate the bond angle distribution function for atom1-atom2-atom3 bond angles

1) Choose a discretization width $d\theta$, which defines the resolution of the BADF. For example, $d\theta = 0.02°$.
2) Define bond-length cutoff values for bonds atom1-atom2 and atom2-atom3.
3) For each triplet of atom1-atom2-atom3 in the system, compare the lengths atom1-atom2 and atom2-atom3 (taking periodic boundary conditions into consideration) to the cutoff values defined in step 2). If any one of these distances is longer than the corresponding cutoff, no bond angle exists for this triplet of atoms. In this case, progress to

consider the next atom1-atom2-atom3 triplet. Otherwise, calculate the atom1-atom2-atom3 bond angle, again taking periodic boundary conditions into consideration. Iterate through all atom1-atom2-atom3 triplets in the system and count the number of angles in each interval $(\theta, \theta + d\theta)$. Denote this count as $n(\theta)$.

4) Because $d\theta\ \rho(\theta) = n(\theta)$, we can calculate $\rho(\theta)$ using $\rho(\theta) = n(\theta) / d\theta$.
5) Accumulate $n(\theta)$ from $\theta = 0°$ to $\theta = 180°$ to obtain the total count of atom1-atom2-atom3 bond angles from 0° to 180°.
6) Divide the total bond count by 180° to obtain the average concentration of angle ρ_0.
7) Divide the $\rho(\theta)$ in step 4) by the ρ_0 in step 6) to obtain the BADF sought.

The above algorithm calculates the BADF for a given system configuration. This configuration could be the model zircon crystalline structure we have developed in Section 2.2, or it could be a snapshot of the structure during the course of molecular dynamics simulations. In the latter case, in order to achieve better statistics and therefore smoother BADF curves, it is often necessary to calculate BADFs at multiple snapshots (at multiple time steps) near the end of the MD simulation and take the average as the final result. For example, we generally calculate the BADF by averaging over the last 5.0 ps of our MD simulations.

2.3.3 Comparison of model and experimental zircon structures

Using the algorithm given in Section 2.3.1 and the crystalline zircon structure model developed in Section 2.2, we can calculate RDFs for various pair of atoms, from which we can obtain bond lengths.

The first peak of Figure 2.13, the Si-O RDF of crystalline zircon, occurs at a distance of 1.62 Å. So Si-O bond length is 1.62 Å. In the Zr-O RDF (Figure 2.14), the first two peaks are very close to each other. The first peak is located at a distance of 2.13 Å and the second 2.27 Å. They denote two different Zr-O interatomic distances in the ZrO_8 triangular dodecahedron, agreeing with the experimental fact that in zircon ZrO_8 triangular dodecahedral unit four oxygen atoms are closer to the Zr atom in the center than the other four. The bond length difference is (2.27 - 2.13) / 2.27 ~ 6.2%, also in agreement with the experimental value. In Figure 2.17, Zr-Zr interatomic distance (not bond length, because Zr does not form a "bond" to another Zr) is found to be 3.63 Å. Other bond length values and interatomic distances shown in Table 2.1 are determined similarly.

Figure 2.19 shows what could be called total radial distribution function (total RDF). When calculating the partial RDF for a given pair of atoms, we care about atom identities. For example, for Si-O RDF, we count number of oxygen atoms at different distances from a silicon atom. In the total RDF, however, we no longer care about the identity of atoms. Pairs of atoms of any type are counted in calculating RDF.

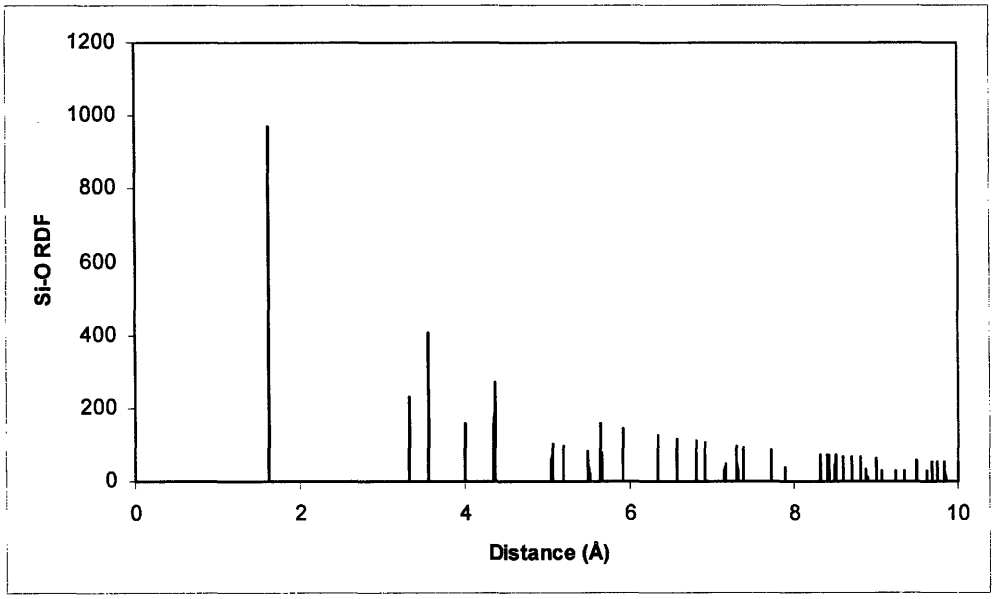

Figure 2.13: Si-O partial RDF of crystalline zircon.

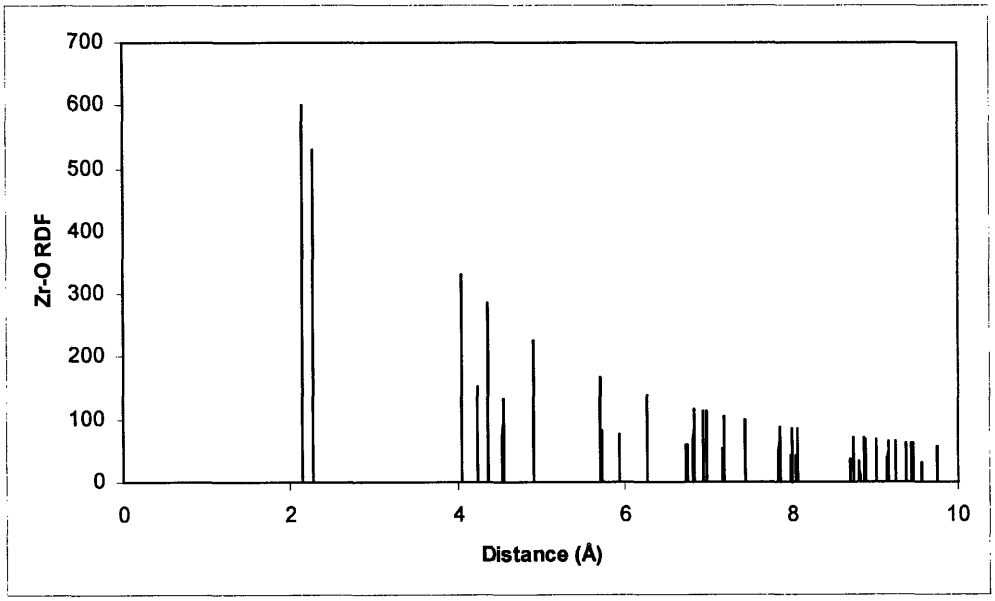

Figure 2.14: Zr-O partial RDF of crystalline zircon.

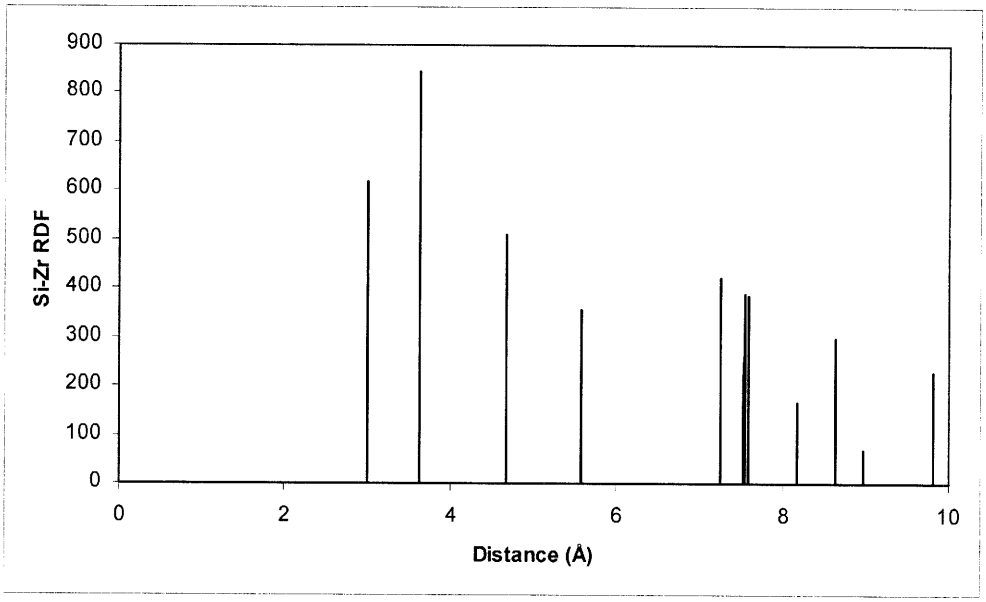

Figure 2.15: Si-Zr partial RDF of crystalline zircon.

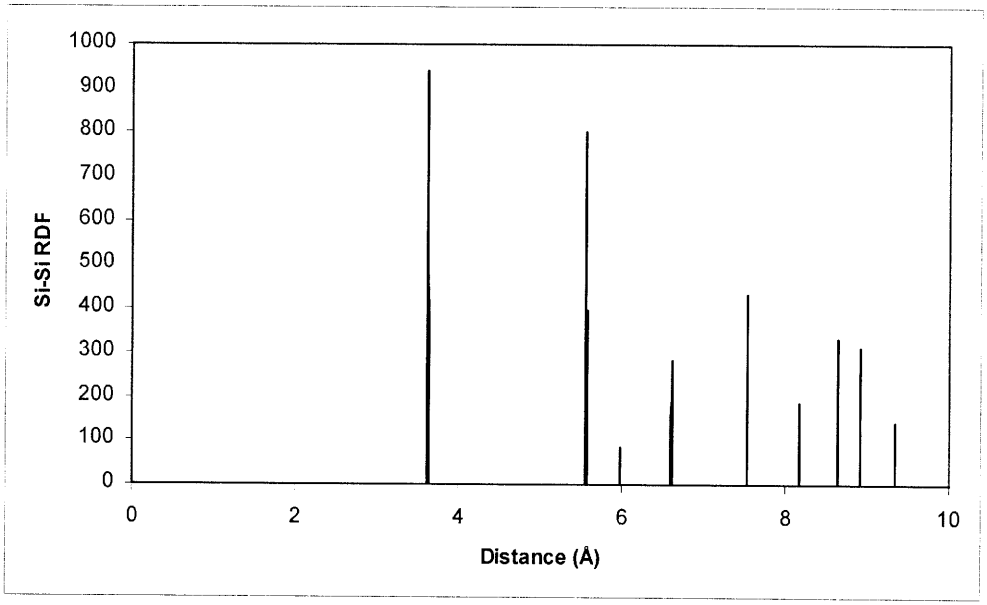

Figure 2.16: Si-Si partial RDF of crystalline zircon.

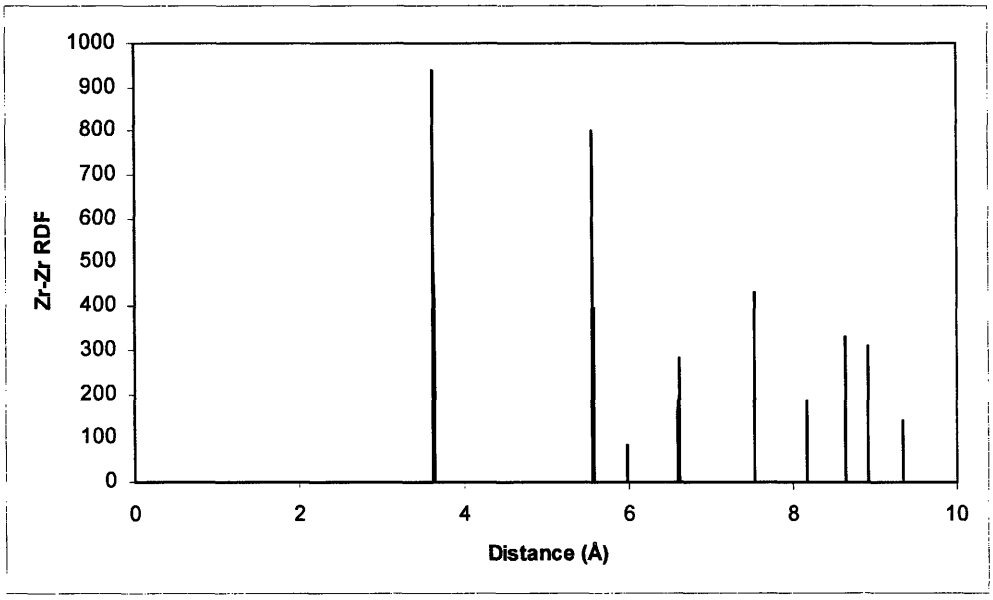

Figure 2.17: Zr-Zr partial RDF of crystalline zircon.

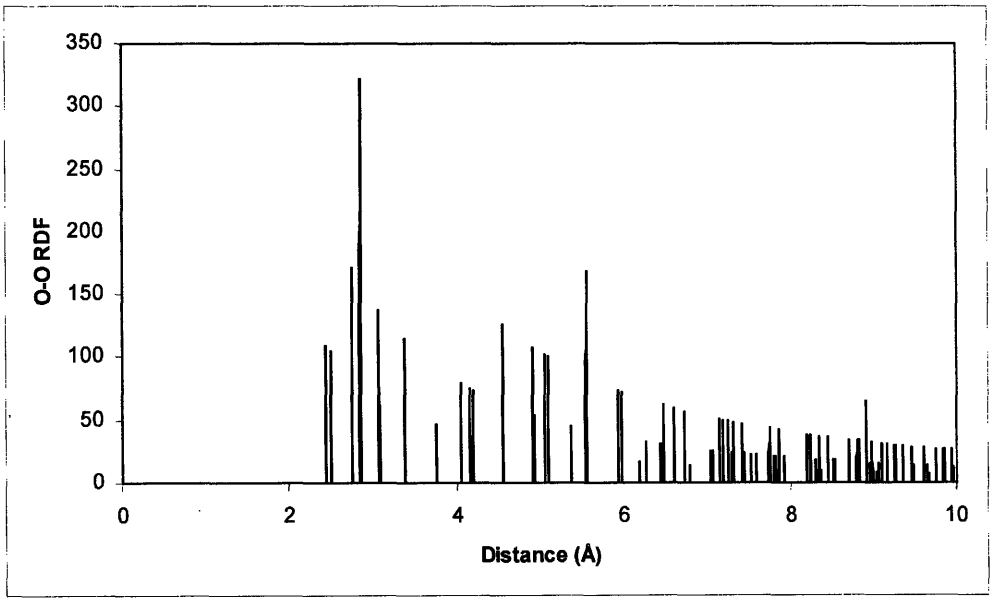

Figure 2.18: O-O partial RDF of crystalline zircon.

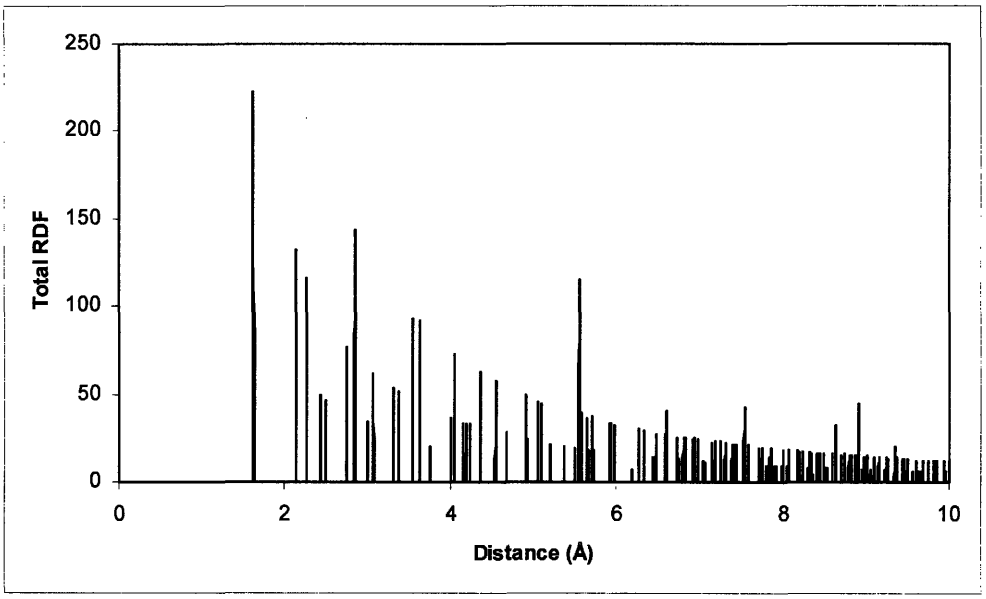

Figure 2.19: Total RDF of crystalline zircon.

Bond angles are calculated analogously: we calculate the BADF and look for peaks in the BADF plots. As described in Section 2.3.2, we first need to define bond length cutoffs before we can calculate bond angles.

The following bond angles are calculated: Zr-O-Zr, Zr-O-Si, O-Si-O and O-Zr-O, so we need bond length cutoff values for Zr-O and Si-O. Bond angle for Si-O-Si can not be calculated in crystalline zircon because there is no bridging oxygen between Si ions. (However, in melted, melt-quenched or radiation-induced amorphous zircon, Si coordination units are polymerized and there are bridging oxygen ions between Si ions. Polymerization of Si coordination units is investigated in Section 7.4.)

The Si-O bond length cutoff value has already been determined in Section 2.3.2 as 2.475 Å. For Zr-O, we refer to Zr-O RDF plot in Figure 2.14. The first three peaks are at 2.13 Å, 2.32 Å and 4.05 Å. As discussed previously, 2.13 Å and 2.32 Å are the distances of shorter and longer Zr-O bonds in

ZrO_8 triangular dodecahedra, so both of them should be considered distances between Zr and the first shell of neighboring O atoms. The second shell is at a distance of 4.05 Å (where the third peak of Zr-O RDF plot occurs). If we again use the average of the distances to the first and second shells of neighbors as the cutoff value, the Zr-O bond-length cutoff value is (2.32 + 4.05) / 2 = 3.185 Å. This is the bond-length cutoff value we will use.

With bond-length cutoff values defined, we are ready to calculate the BADF. O-Si-O, O-Zr-O, Zr-O-Zr and Zr-O-Si bond angle distribution functions are shown in Figures 2.21, 2.22, 2.23 and 2.24, respectively. The sharp peaks in Figure 2.21 occur at angles 96.99° and 116.05°, which are therefore the values of O-Si-O bond angles. These are the values shown in Table 2.1. Other bond angle values shown in the table are determined similarly.

The existence of two kinds of angles (96.99° and 116.05°) means the SiO_4 tetrahedra in zircon are seriously distorted. This is one of the reasons why three-body potentials that keep O-Si-O angle at 109° are not optimal for zircon. To form an O-Si-O bond angle, there are totally six ways to choose two O atoms from the four O atoms surrounding each Si. Two out of the six choices yield a bond-angle value of 97.00°, shown in Figure 2.20. The edge connecting the two O atoms involved in the 97.00° O-Si-O bond angle is shared between SiO_4 and ZrO_8 units. The other four of the six choices yield an O-Si-O bond angle value of 116.04°. The ratio of bond angles (2:4) agrees with what we see in Figure 2.21. The slight differences between bond angles calculated directly from atom positions in SiO_4 unit and from the location of the sharp peaks in BADF of Figure 2.21 (97.00° versus 96.99° and 116.04° versus 116.05°) are artifacts of the resolution chosen when calculating BADF using the algorithm described in Section 2.3.2.

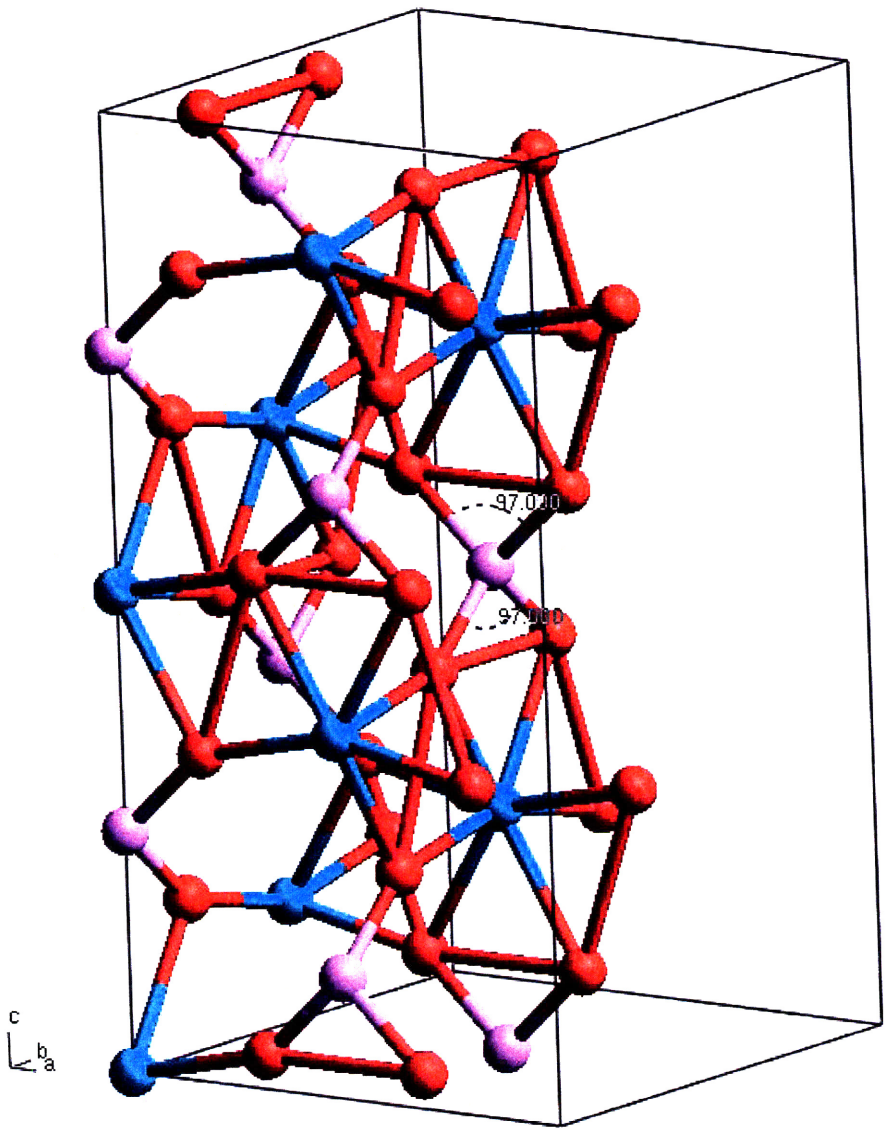

Figure 2.20: Two kinds of O-Si-O bond angles (97.00° and 116.04°) exist in zircon crystalline structure. There are totally six ways to choose two O atoms from the four O atoms surrounding each Si to form an O-Si-O bond angle. Two of them yield bond angle value of 97.00°, shown in the figure. The other four yield 116.04°.

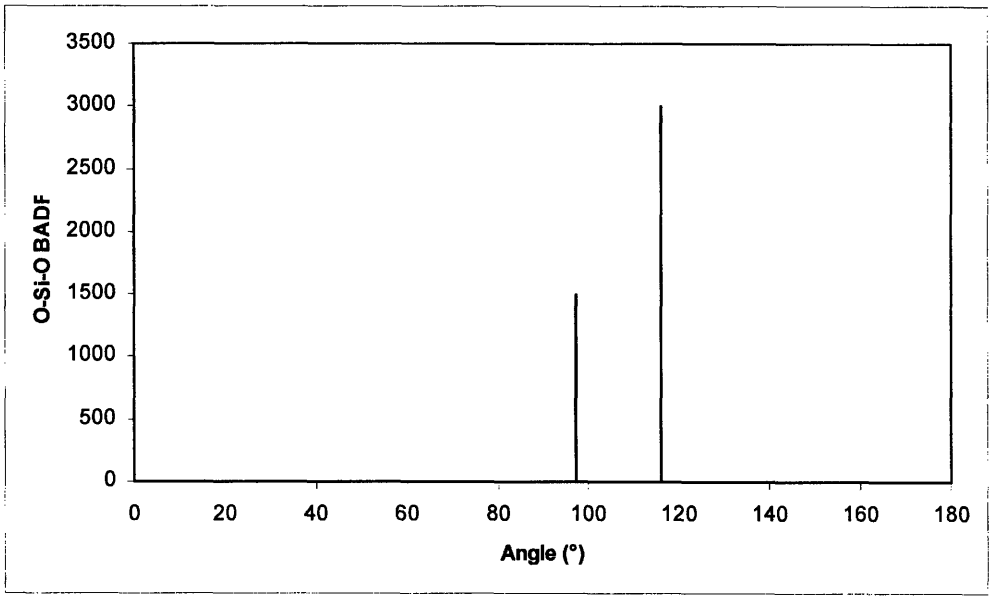

Figure 2.21: O-Si-O BADF of crystalline zircon.

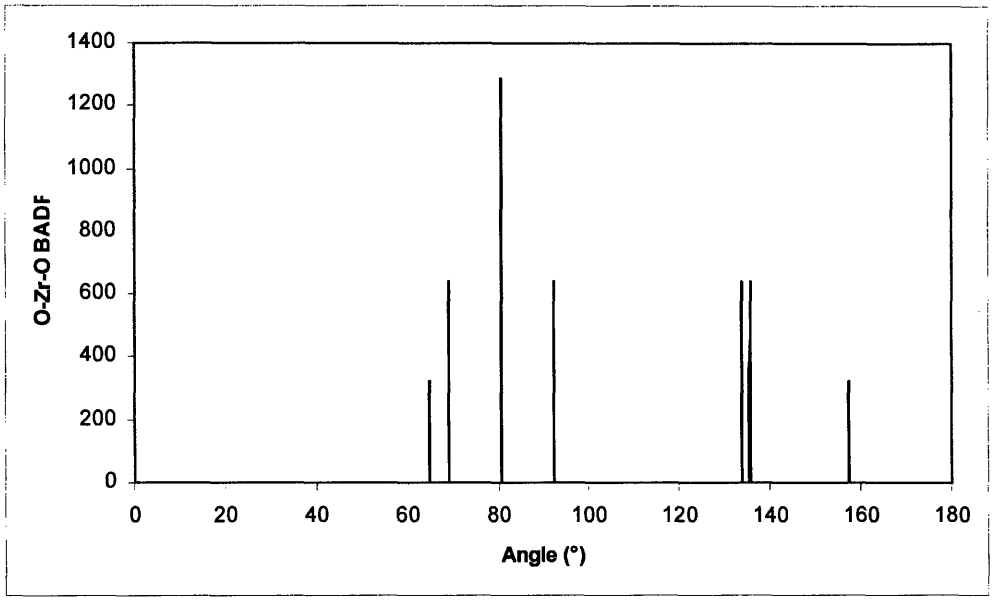

Figure 2.22: O-Zr-O BADF of crystalline zircon.

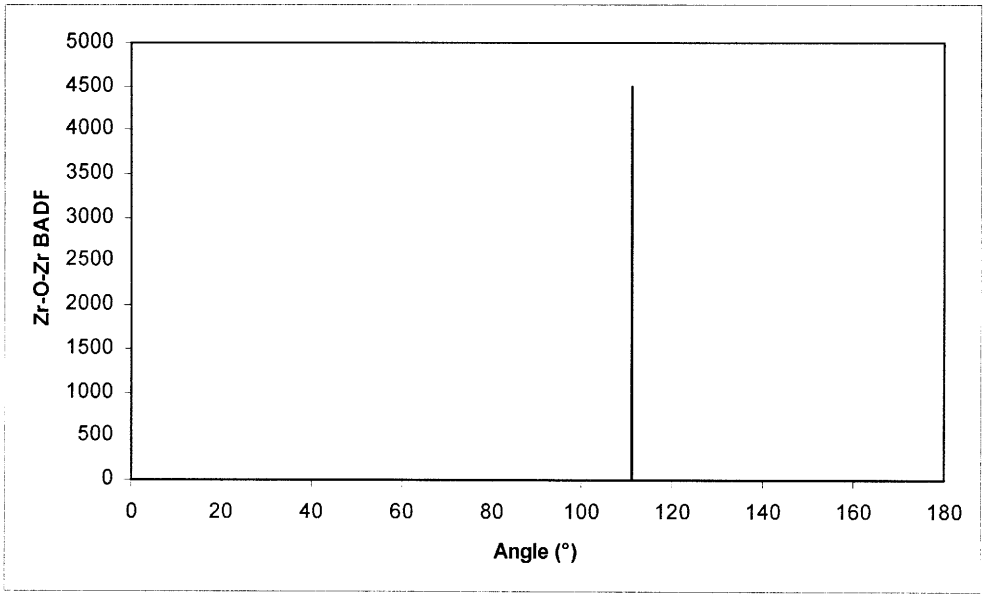

Figure 2.23: Zr-O-Zr BADF of crystalline zircon.

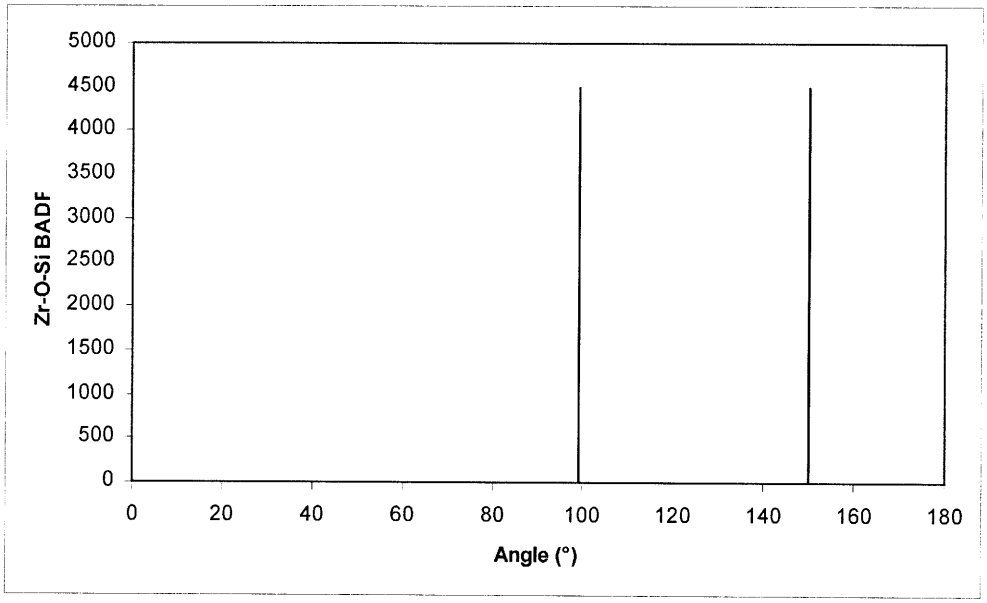

Figure 2.24: Zr-O-Si BADF of crystalline zircon.

Table 2.1: Comparison of model and experimental zircon structures

Experimental structure [2]	Model structure of this study
SiO_4 Tetrahedron:	SiO_4 Tetrahedron:
Si-O: 1.622 A, {4} (multiplicity in {})	Si-O: 1.622 A, {4} (multiplicity in {})
O-O(1): 2.430 A, {2} Angle at Si: 97.0	O-O: 2.430 A, {2} Angle at Si: 96.99
O-O(2): 2.752 A, {4} Angle at Si: 116.06	O-O: 2.752 A, {4} Angle at Si: 116.05
ZrO_8 Triangular Dodecahedron:	ZrO_8 Triangular Dodecahedron:
Zr-O(A): 2.268 A, {4}	Zr-O(A): 2.269 A, {4}
Zr-O(B): 2.131 A, {4}	Zr-O(B): 2.130 A, {4}
O(A)-O(A'): 2.430 A, {2} Angle at Zr: 64.8	O(A)-O(A'): 2.430 A, {2} Angle at Zr: 64.76
O(A)-O(B): 2.842, {8} Angle at Zr: 80.41	O(A)-O(B): 2.842 A, {8}, Angle at Zr: 80.404
O(A)-O(B'): 2.494, {4} Angle at Zr: 69.00	O(A)-O(B'): 2.494 A, {4}, Angle at Zr: 69.005
O(B)-O(B'): 3.071, {4} Angle at Zr 92.23	O(B)-O(B'): 3.071 A, {4}, Angle at Zr: 92.233
Cation-Cation Distances:	Cation-Cation Distances:
Zr-Zr': 3.626 A, Angle at O: 111.02	Zr-Zr': 3.626 A, Angle at O: 110.995
Zr-Si: 2.991 A, Angle at O: 99.17	Zr-Si: 2.991 A, Angle at O: 99.120
Zr'-Si: 3.626 A, Angle at O: 149.81	Zr'-Si: 3.626 A, Angle at O: 149.885

From Table 2.1, we can see that the zircon model structure developed in Section 2.2 reproduces experimental bond lengths, bond angles and coordination numbers (multiplicities in Table 2.1) very well. This shows that the shift of origin and sign reversal of y, used in Section 2.2 when developing the model, does not alter zircon structure in any physically significant way, as expected.

References of chapter 2

[1] A. Beltrin, S. Bohm, A. Flores-Riveros, J.A. Ingualada, G. Monros and J. Andres. Ab Initio Cluster-in-the-Lattice Description of Vanadium-Doped Zircon: Analysis of the Impurity Centers in Vanadium(4+)-Doped Zircon ($ZrSiO_4$). J. Phys. Chem. 97, 2555 (1993).

[2] K. Robinson, G.V. Gibbs and P.H. Ribbe. The Structure of Zircon: A Comparison with Garnet. Am. Mineral. 56, 782 (1971).

[3] Z. Mursic, T. Vogt, H. Boysen and F. Frey. Single-Crystal Neutron Diffraction Study of Metamict Zircon up to 2000 K. J. Appl. Crystallogr. 25, 519 (1992).

[4] Z. Mursic, T. Vogt and F. Fray. High-Temperature Neutron Powder Diffraction Study of $ZrSiO_4$ up to 1900 K. Acta Crystallogr., Sect. B: Struct. Sci. B48, 584 (1992).

[5] R.W.G. Wyckoff. Crystal Structures. Vol. 3. New York, Interscience Publishers, 1971.

[6] International Tables for X-ray Crystallography. Published for the International Union of Crystallography by D. Reidel Pub. Co., 1985.

[7] K. Trachenko, M.T. Dove, T. Geisler, I. Todorov and B. Smith. Radiation Damage Effects and Percolation Theory. J. Phys.: Condens. Matter 16, S2623 (2004).

[8] K. Trachenko, M.T. Dove and E.K.H. Salje. Atomistic Modelling of Radiation Damage in Zircon. J. Phys.: Condens. Matter 13, 1947 (2001).

[9] K. Trachenko, M.T. Dove and E.K.H. Salje. Large Swelling and Percolation in Irradiated Zircon. J. Phys.: Condens. Matter 15, L1 (2003).

[10] K. Trachenko, M.T. Dove and E.K.H. Salje. Structural Changes in Zircon under Alpha-Decay Irradiation. Phys. Rev. B 65, 180102(R) (2002).

[11] K. Trachenko, M.T. Dove and E.K.H. Salje. Reply to Comment on "Large Swelling and Percolation in Irradiated Zircon". J. Phys.: Condens. Matter 15, 6457 (2003).

[12] Zircon gem picture by Rodrigue & Sons, Co. Retrieved in October, 2005 from http://www.awesomegems.com/.

[13] Zircon mineral picture retrieved in October, 2005 from http://hyperphysics.phy-astr.gsu.edu/hbase/minerals/zircon.html.

[14] C. Kittel. Introduction to Solid State Physics, 7th Ed. New York, Wiley, 1996.

[15] M.P. Allen and D.J. Tildesley. Computer Simulation of Liquids. New York, Oxford University Press, 1987.

Chapter 3: Empirical potential for zircon simulation

3.1 General requirements of potential model for cascade simulations

This chapter evaluates zircon potential models available in the literature. The best one among those evaluated is found to reproduce key experimental properties required for collision cascade simulations quite well and is thus used for later simulations.

Empirical potentials are often used in computer modeling of materials. Ideally, we would want all material properties calculated using the empirical potential to match experimental values. However, each potential model, no matter how complex it is, has only a limited number of parameters that can be varied. It is unrealistic to expect to reproduce a potentially infinite number of experimental properties using potentials with limited parameters. However, this doesn't mean that empirical potentials are not useful. Some properties are more important than others in certain applications, so although in general we cannot reproduce every experimental property, in many cases it is sufficient to reproduce just the properties that are important in the relevant context.

For molecular dynamics (MD) simulations, at a minimum the potential model should be able to reproduce the crystalline structure and fundamental equilibrium mechanical properties. For collision cascade simulations, because the system will be brought far from equilibrium by the thermal spike and shock wave created by the collision cascade, the requirements of the potential model are more restrictive. In addition to the properties mentioned above, it is also crucial to reproduce fundamental equilibrium thermodynamic properties and kinetic properties.

There is a tradeoff when selecting a potential model for zircon collision cascade simulations. On one hand, zircon has a complex structure and tends to require complex potentials for accurate modeling; on the other hand, due to the long range electrostatic forces inherent in a partially ionic structure, combined with the small time step size and large simulation cell required for high energy cascade simulations, collision cascade simulation for zircon is computationally expensive and demands simpler potentials.

Investigators in this field generally have favored simpler potentials over more complex ones. Mostly two-body potentials are used. This is a useful simplification so long as the key properties can be reproduced with reasonable accuracy using the potential. However, as can be seen later in this chapter, some of the potentials published in the literature cannot reproduce elastic constants well, while others do not take into account thermal and kinetic properties. It is found that investigators in this field generally have recognized the importance of reproducing the crystalline structure. However, without the ability to reproduce other crucial properties, the potentials are unfit for collision cascade simulations and conclusions drawn from simulations based on these potentials should be viewed cautiously.

Many potential models for collision cascade simulations include a short-range Ziegler-Biersack-Littmark (ZBL, [1]) part. The ZBL potential is a universal screened Coulombic potential that applies very well to a wide range of nuclei in close encounters [1]. Its form will be shown in Section 3.2. It is necessary to include the ZBL potential at short range because most, if not all, empirical potentials are developed and fitted to experimental material properties at or near equilibrium. Their applicability to atoms at

short range is uncertain. Some potential models are known to exhibit unrealistic behavior when the interatomic distance is close to zero. These potentials can be used successfully at or near equilibrium, but for collision cascade study, where particles can get very close to each other, shifting to a well-established potential form such as ZBL at short range is preferred.

The ZBL potential can be incorporated into the complete potential model in many different ways. At equilibrium distance, most potential models already have a short-range part (such as the Born-Mayer form) in addition to a possible long-range part (such as Coulombic interaction). There is much freedom in choosing how a gradual elision is achieved. In some models, the short-range interaction is gradually elided into the ZBL form as the interatomic distance is decreased. In others, the ZBL part is turned on when the distance is shorter than a predefined threshold and turned off when it's not. See Section 3.2 on how the ZBL potential is included in some of the candidate potential models.

The potential chosen is of fundamental importance because every conclusion derived from simulations depends on its accuracy. Potential development has always been difficult for computer simulation studies of complex structures like zircon, and often investigators do not agree on whether a potential is good enough. For example, Trachenko *et al.* [2] developed a theory based on MD simulation results to explain the large swelling of zircon under irradiation. They performed molecular dynamics simulation of the overlap of two radiation events and found that the first event produced a damage region where the core is depleted and the boundary is densified. The damage produced by the second event was found to scatter away from the densified boundary. These results, combined with percolation theory, were used by them to develop a new model for swelling.

However, Corrales *et al.* [3] criticized this study. They claim that the potential used by Trachenko *et al.* reproduced only some of the crystallographic properties at equilibrium and did not adequately describe the atomic scattering physics for zircon. The interatomic potential model used by Trachenko *et al.*, they claim, yielded a significantly more rigid structure, with very high Frenkel defect formation energies and extremely low entropy and specific heat capacity. The potential used also did not include ZBL at short-range. For their part, Trachenko *et al.* refuted their claims in defense of their potential model [4]. Trachenko *et al.* claim that their simulation results were not significantly altered if the ZBL potential was included. At the same time, they also pointed out several weaknesses of the potential model used by Corrales *et al.* They commented that the Corrales *et al.* potential model was inherently unstable in simulations, with a negative value of the elastic constant C_{66}. They also claim that the zircon structure fell apart even when equilibrating at 300 K when the Corrales *et al.* potential was used.

There are still other arguments advanced on both sides of this controversy, which will not be discussed here. The controversy clearly arises because there is no consensus on which criteria, of the many different criteria against which an interatomic potential model for simulations of radiation damage in ceramics can be assessed, are paramount.

In the next section, we will test the empirical potentials used by these two sets of investigators, together with some other potentials published recently in the literature, against the requirements describe at the beginning of this section. It turns out that both their potentials have shortcomings and most of the criticisms on both sides apply. The final empirical potential model chosen for this study is neither of the two potentials involved in this

controversy.

3.2 Candidate potential models

Five potential models have been published in recent literature for use in zircon MD simulations. They are referenced here as potentials 1, 2, 3, 4 and 5 for convenience. Because many of the potential models include or elide into the same ZBL potential at short range, we describe the ZBL potential before providing further details of these candidate potentials.

For nuclei with charges Z_1 and Z_2, the Coulombic potential between the two is

$$V = \frac{Z_1 Z_2 e^2}{4\pi\varepsilon_0 r}, \tag{3.1}$$

where $e = 1.6022 \times 10^{-19}$ C is the elementary charge, $\varepsilon_0 = 8.8542 \times 10^{-12}$ F/m is the vacuum permittivity and r is the distance, in meters, between the two charges.

The ZBL potential is a screened Coulombic potential with the form

$$V = \frac{Z_1 Z_2 e^2}{4\pi\varepsilon_0 r}\Phi, \tag{3.2}$$

The only difference between the ZBL and Coulombic potentials is the addition of a screening function Φ. There have been several proposed forms for Φ in different potential models, but in the ZBL potential Φ is of form

$$\Phi = 0.18175e^{-3.1998x} + 0.50986e^{-0.94229x} + 0.28022e^{-0.4029x} + 0.02817e^{-0.20162x}, \tag{3.3}$$

where $x = \frac{r}{a_I}$, r is the distance between the two particles, $a_I = \frac{0.8854a_0}{Z_1^{0.23} + Z_2^{0.23}}$, and $a_0 = \frac{4\pi\varepsilon_0\hbar^2}{me^2} = 0.5292$ Å is the Bohr radius.

3.2.1 Potential 1 detail

Potential 1 is from Trachenko *et al.* [5] and contains a short range interatomic part and a long range Coulombic part. Table 3.1 shows the forms and parameters of the short range part.

Table 3.1: Short range part of potential 1

Atom Pair	Potential Form	Potential Parameters
Zr-O	$Ae^{-\frac{r}{\rho}} - \frac{C}{r^6}$ (Buckingham)	A = 1477 eV, ρ = 0.317 Å, C = 0
O-O	$Ae^{-\frac{r}{\rho}} - \frac{C}{r^6}$ (Buckingham)	A = 9245 eV, ρ = 0.2617 Å, C = 100 eV Å^6
Si-O	$D(e^{-2\alpha(r-r_0)} - 2e^{\alpha(r-r_0)})$ (Morse)	D = 1.252 eV, α = 2.83 Å^{-1}, r_0 = 1.627 Å

Cutoff values for the short-range potential were not reported. The long-range electrostatic interaction is of the classical Coulombic form (3.1). The only parameters needed for Coulombic interactions are the charges of the ion cores, which are given in Table 3.2 and are seen to represent partial charges.

Table 3.2: Ion core charges of potential 1

Ion Name	Charge
Zr	+3.428
Si	+1.356
O	-1.196

The authors stated that at short distances the pair potentials were fitted to the ZBL potentials, but did not specify how this was done.

3.2.2 Potential 2 detail

Potential 2 is from Trachenko *et al.* [6]. It uses a Buckingham pair-potential form $Ae^{\frac{-r}{\rho}} - \frac{C}{r^6}$ for Si-O, Zr-O and O-O interactions. The parameters are given in Table 3.3.

Table 3.3: Buckingham potential parameters of potential 2

Atom Pair	A (eV)	ρ (Å)	C (eV Å^6)
Si-O	1354.9546	0.3104097	5.33
Zr-O	8000000	0.14	0
O-O	22764	0.149	27.879

Cutoff values for these Buckingham potentials were not reported.

Trachenko *et al.* [2] stated that the Si-O potential parameters used in [6] are taken from simulation of quartz by Sanders, Leslie and Catlow [7], where a three-body potential was also used, with parameters selected to keep the O-Si-O angle in the SiO_4 tetrahedron at approximately 109°. However, as seen in Chapter 2, the SiO_4 tetrahedron in zircon is not exactly a regular tetrahedron. The O-Si-O bond angles have two values: 97° and 116°, not a single value of 109°. The three-body potential used to maintain the O-Si-O angle at 109° is thus not used in zircon simulations.

The long-range electrostatic interaction is of the classical Coulombic form. The ion charges used, given in Table 3.4, are the formal ion charges.

Table 3.4: Ion charges of potential 2

Ion Name	Charge
Zr	+4.0
Si	+4.0
O	-2.0

3.2.3 Potential 3 detail

Potential 3 is from Crocombette and Ghaleb [8]. A two-body potential of the Born-Mayer-Huggins (BMH) type is used for each pair of atoms. BMH potentials have the form

$$\phi_{ij} = b(1+\frac{q_i}{n_i}+\frac{q_j}{n_j})e^{\frac{\sigma_i+\sigma_j-r_{ij}}{\rho_{ij}}} + \frac{1}{4\pi\varepsilon_0}\frac{q_i q_j}{r_{ij}}, \qquad (3.4)$$

where q_i and q_j are charges of the interacting ions i and j; n_i and n_j are the numbers of valence shell electrons (n_i = 8 for all ions in the case of zircon). The values of parameters b, ρ_{ij}, and σ_i are given in Table 3.5.

Table 3.5: BMH potential parameters of potential 3

Parameter		Value
b		0.221 eV
ρ_{ij}	Si-O	0.29 Å
	Zr-O	0.29 Å
	O-O	0.35 Å
σ	Si	1.11 Å
	O	1.42 Å
	Zr	1.31 Å

The charges q_i and q_j for Zr, Si and O are given in Table 3.6.

Table 3.6: Ion charges of potential 3

Ion Name	Charge
Zr	+4.0
Si	+4.0
O	-2.0

The cutoff radius of the exponential term is 6.7 Å.

For interatomic distances smaller than 1 Å, the interaction is represented by the ZBL potential. The two kinds of potentials are connected between 0.9

and 1.0 Å with a fifth-order polynomial to ensure continuity of the potential and of its first two derivatives, but the exact form of this fifth-order polynomial is not given in [8].

3.2.4 Potential 4 detail

Potential 4 is from Devanathan *et al.* [9]. The interactions for Zr-O, Si-O and O-O atom pairs are in the form of Born-Mayer potential given by

$$V = Ae^{\frac{-r}{\rho}}, \tag{3.5}$$

where r is the distance between atoms, A and ρ are potential parameters which are shown in Table 3.7.

Table 3.7: Born-Mayer potential parameters of potential 4

Atom Pair	A (eV)	ρ (Å)
Zr-O	1967.0	0.305004
Si-O	1277.0	0.227225
O-O	1755.0	0.306820

The cutoff value for Born-Mayer potential is 10 Å.

In addition to the Born-Mayer form of potential mentioned above, a Coulombic electrostatic interaction additionally exists between each pair of ions, with the charges of the ions given in Table 3.8.

Table 3.8: Ion charges of potential 4

Ion Name	Charge
Zr	+3.8
Si	+2.0
O	-1.45

At distances much less than the equilibrium interatomic separation, the

Born-Mayer potential (V_{BM}) is joined smoothly to the repulsive ZBL potential (V_{ZBL}) using a Fermi function F(r) to give an effective short-range interaction

$$V(r) = F(r)V_{BM}(r) + (1 - F(r))V_{ZBL}(r), \tag{3.6}$$

The Fermi function F(r) has the form

$$F(r) = \frac{1}{1 + e^{-b_f(r - r_f)}}, \tag{3.7}$$

where b_f and r_f were chosen parameters which are given in Table 3.9.

Table 3.9: Fermi function parameters of potential 4

Atom Pair	b_f (Å^{-1})	r_f (Å)
Zr-Zr	6.0	1.00
Zr-Si	6.0	1.00
Zr-O	6.0	0.87
Si-Si	6.0	1.00
Si-O	6.0	0.62
O-O	6.0	0.30

3.2.5 Potential 5 detail

Potential 5 is from Park, Weber and Corrales [10]. In this potential model, the interaction between ions has a Buckingham form $Ae^{\frac{-r}{\rho}} - \frac{C}{r^6}$, with parameters shown in Table 3.10.

Table 3.10: Buckingham potential parameters of potential 5

Atom Pair	A (eV)	ρ (Å)	C (eV Å^6)
Zr-O	1400.8284	0.3500	10.000
Si-O	1380.9073	0.3205	10.000
O-O	22764.000	0.1490	10.879

A cutoff value for Buckingham potential was not reported. There are also

classical Coulombic interactions between the ions. The charges of the ions, shown in Table 3.11, are the formal charges.

Table 3.11: Ion charges of potential 5

Ion Name	Charge
Zr	+4.0
Si	+4.0
O	-2.0

At very short distances, the ZBL repulsive potential is used. When the distance is greater than 1.0 Å, the ZBL potential is turned off; when distance is less than or equal to 1.0 Å, the ZBL potential is turned on while the Buckingham potential is turned off.

3.3 Evaluation of potentials

In this section, we evaluate the five potential candidates presented in Section 3.2. Version 1.3 of the GULP code [11] is used for this analysis. The General Utility Lattice Program (GULP) is designed to perform a variety of tasks relating to three dimensional solids. Quotes from GULP's manual [12]: "Although it started life as an attempt to produce an input-file-driven program for interatomic potential fitting, it has now expanded to encompass energy minimization, phonon calculations and other useful facilities".

We first ascertain that the zircon crystalline structure can be reproduced with acceptable accuracy, using the various potential candidates in turn. Starting with the zircon model structure deduced from experiment in Chapter 2, GULP was used to perform energy minimization to find the local minimum energy configuration. This configuration should be close to the original crystalline structure for acceptable potentials.

Among other results, the GULP output file gives lattice constants and oxygen position parameters u and v for energy minimization calculations of materials belonging to the space group $I4_1/amd$. From these outputs, the zircon structure can be generated, just as was done in Chapter 2 from experimental data. This structure is then the stable structure under the specific potential used. After having generated the zircon structure, bond lengths and bond angles can be calculated. The algorithm described in Section 2.3.1 can be used to calculate RDF, from which bond length can be determined; the algorithm described in Section 2.3.2 can be used to calculate BADF, from which bond angle can be determined. The calculated results are compared to experimental values in Table 3.12, with percent deviations given in parentheses.

Table 3.12: Comparison of zircon experimental structure with stable structures resulting from use of various candidate potentials in the GULP code

Property	Experimental value [13]	Potential 1	Potential 2	Potential 3	Potential 4	Potential 5
Unit cell volume ($Å^3$)	261.13	260.20 (-0.36%)	259.00 (-0.82%)	189.76 (-27.33%)	265.59 (+1.71%)	261.97 (+0.32%)
Lattice constant a (Å)	6.607	6.641 (+0.52%)	6.475 (-2.00%)	5.756 (-12.88%)	6.602 (-0.08%)	6.343 (-4.00%)
Lattice constant c (Å)	5.982	5.900 (-1.38%)	6.177 (+3.26%)	5.728 (-4.25%)	6.093 (+1.86%)	6.511 (+8.85%)
u	0.8161	0.8151 (-0.13%)	0.8344 (+2.24%)	0.8153 (-0.10%)	0.8157 (-0.04%)	0.8152 (-0.11%)
v	0.3203	0.3320 (+3.66%)	0.3188 (-0.48%)	0.3205 (+0.07)	0.3240 (+1.16%)	0.3255 (+1.63%)
Si-O bond length (Å)	1.62	1.58 (-2.47%)	1.55 (-4.32%)	1.48 (-8.64%)	1.62 (0.00%)	1.63 (+0.62%)
Zr-O bond length (Å)	2.13	2.15 (+0.94%)	2.21 (+3.76%)	1.86 (-12.68%)	2.13 (0.00%)	2.06 (-3.29%)
	2.27	2.31 (+1.76%)	2.24 (-1.32%)	2.12 (-6.61%)	2.32 (+2.20%)	2.42 (+6.61%)
O-Si-O bond angle	97.0	102.2 (+5.36%)	87.5 (-9.79%)	91.9 (-5.26%)	97.2 (+0.21%)	91.8 (-5.36%)
	116.1	113.2 (-2.50%)	121.4 (+4.57%)	118.9 (+2.41%)	115.9 (-0.17%)	119.0 (+2.50%)
O-Zr-O bond angle	64.8	64.2 (-0.93%)	57.2 (-11.73%)	60.2 (-7.10%)	63.3 (-2.31%)	57.9 (-10.65%)
	69.0	70.9 (+2.75%)	72.5 (+5.07%)	72.5 (+5.07%)	70.6 (+2.32%)	74.9 (+8.55%)
	80.4	79.0 (-1.74%)	80.3 (-0.12%)	79.2 (-1.49%)	79.6 (-1.00%)	77.9 (-3.11%)
	92.2	92.9 (+0.76%)	92.1 (-0.11%)	92.7 (+0.54%)	92.6 (+0.43%)	93.3 (+1.19%)
	133.8	135.1 (+0.97%)	130.0 (-2.84%)	132.6 (-0.90%)	133.9 (+0.07%)	132.8 (-0.75%)
	135.5	135.9 (+0.30%)	140.5 (+3.70%)	138.5 (+2.21%)	136.5 (+0.74%)	140.0 (+3.32%)
	157.2	154.0 (-2.04%)	157.8 (+0.38%)	154.9 (-1.46%)	155.6 (-1.02%)	152.4 (-3.05%)
Zr-O-Si bond angle	99.1	96.8 (-2.32%)	107.7 (+8.68%)	104.0 (+4.94%)	99.8 (+0.71%)	105.2 (+6.16%)
	149.9	154.1 (+2.80%)	144.9 (-3.34%)	148.5 (-0.93%)	150.8 (+0.60%)	149.7 (-0.13%)
Zr-O-Zr bond angle	111.0	109.1 (-1.71%)	107.5 (-3.15%)	107.5 (-3.15%)	109.4 (-1.44%)	105.1 (-5.32%)

For potentials where cutoff values are not reported in the original references (potentials 1, 2, 5), a 10 Å cutoff is used. No comparison of calculated Si-O-Si bond angles is made since in crystalline zircon Si-O-Si bond angles do not exist.

Mechanical properties, including bulk modulus and elastic constants, can also be calculated by GULP. Results are shown in Table 3.13.

Table 3.13: Comparison of experimental zircon bulk modulus and elastic constants with those calculated using the candidate potentials

Property	Experimental value [14-19]	Potential 1	Potential 2	Potential 3	Potential 4	Potential 5
Bulk modulus (GPa)	225.0	222.12 (-1.28%)	577.05 (+156.47%)	550.18 (+144.52%)	223.12 (-0.84%)	259.28 (+15.24%)
C_{11} (GPa)	424.0	434.39 (+2.45%)	1148.49 (+170.87%)	1075.07 (+153.55%)	445.36 (+5.04%)	504.76 (+19.05%)
C_{33} (GPa)	490.0	519.03 (+5.92%)	1283.39 (+161.92%)	1114.17 (+127.38%)	479.19 (-2.21%)	522.40 (+6.61%)
C_{44} (GPa)	114.0	106.58 (-6.51%)	139.41 (+22.29%)	229.87 (+101.64%)	84.35 (-26.01%)	119.38 (+4.72%)
C_{66} (GPa)	49.0	31.51 (-35.69%)	-0.33 (-100.67%)	26.70 (-45.51%)	63.87 (+30.35%)	-0.0428 (-100.09%)
C_{12} (GPa)	70.0	47.99 (-31.44%)	109.55 (+56.50%)	191.37 (+173.39%)	64.08 (-8.46%)	72.34 (+3.34%)
C_{13}(GPa)	149.0	146.88 (-1.42%)	385.45 (+158.69%)	333.76 (+124.00%)	133.17 (-10.62%)	171.53 (+15.12%)

From Table 3.13, potential 2 can be eliminated, since the calculated bulk modulus and elastic constants are too far off compared to the experimental values: bulk modulus, C_{11}, C_{33}, C_{66} and C_{13} all exhibit more than 100% differences. C_{66} is even more troublesome: it has a negative value. The structure cannot behave correctly in MD simulations using this potential.

Potential 2 is from reference [6], whose authors indeed used this potential for MD simulations of zircon. The original paper verified the potential only by comparing unit cell parameters, bond lengths and bond angles calculated using the potential to the experimental values (Table 2 in [6]), but didn't mention bulk modulus and elastic constants at all. Given the fact that mechanical properties cannot be reproduced well using this potential, the conclusions made in the paper [6] should be viewed with great caution.

Potential 5 also has the same problem: a negative value of C_{66}. Potential 5 is from reference [10], which used MD simulations to determine threshold

displacements energies and defect formation in zircon. This study did verify the potential by comparing the calculated unit cell parameters and elastic constants to experimental values (Table III in [10]). The values of C_{11}, C_{33}, C_{44}, C_{12} and C_{13} shown in the last column of Table III of [10] agree with the values we calculated in Table 3.13, and are not too off from experimental values. However, mysteriously, Table III of reference [10] did not report a C_{66} value, even though all other elastic constants are reported. We will avoid using potential 5 in this study because of its negative C_{66} value.

Potential 3 can also be eliminated. Although it produces a positive C_{66} value, elastic constants calculated using this potential are too large: +153.6% greater than the experimental value for C_{11}, +127.4% for C_{33}, +101.64% for C_{44}, +173.4% for C_{12} and +124.0% for C_{13}. The structure would be too stiff if this potential was used. Again, let's see why this is happening: did the authors check the potential? Potential 3 is from reference [8], and it turns out that the authors of [8] did not check the potential against elastic constants.

This leaves us with potentials 1 and 4. Both potentials did equally well on the properties compared in Tables 3.12 and 3.13. Thermal properties and the dielectric constant ε calculated using these two potentials are shown in Table 3.14. Again, GULP 1.3 was used for the calculations.

Table 3.14: Thermal properties and dielectric constant calculated using potentials 1 and 4

Property	Experimental value [14-19]	Potential 1	Potential 4
C_p at 300 K ($J\ mol^{-1}\ K^{-1}$)	98.6	93.55 (-5.12%)	102.1 (+3.55%)
Entropy at 300 K ($J\ mol^{-1}\ K^{-1}$)	84.4	76.17 (-9.75%)	84.4 (0.00%)
Dielectric constant ε	8-12	$\varepsilon_{xx} = \varepsilon_{yy} = 3.90$; $\varepsilon_{zz} = 4.40$	$\varepsilon_{xx} = \varepsilon_{yy} = 5.44$; $\varepsilon_{zz} = 12.0$

Some comments are offered here on how the values in Table 3.14 are calculated. Dielectric constants are directly available in the output file of GULP. For entropy, the unit for the experimental value is Joule per Kelvin per mol formula unit, but the output from GULP yields entropy in units of Joule per Kelvin per mol primitive cell. Because each zircon primitive cell contains two $ZrSiO_4$ formula units, we need to divide the entropy value in the GULP output file by 2 before it is compared to the experimental value. For example, the entropy value shown in GULP output file calculated using potential 4 is 168.73 J/(mol K). Dividing this by 2 yields the value 84.4 shown in Table 3.14.

For heat capacity, the result directly available in the GULP output file is the heat capacity at constant volume. To transfer to the heat capacity at constant pressure shown in Table 3.14, we can use the following well-established relationship (see, for example, Atkins [20])

$$C_p = C_v + \frac{\alpha^2 TV}{\kappa_T}, \tag{3.8}$$

where α is expansion coefficient, with an experimental value of 11.80×10^{-6} K^{-1} [21]; T is system temperature and we will use T = 300 K for room temperature; V is the molar volume and can be calculated from density and molecular molar weight. Molar weight M for zircon is

$$M = (91.224 + 28.0855 + 15.9994 \times 4) \times 10^{-3} \text{ (kg/mol)}$$
$$= 183.307 \times 10^{-3} \text{ (kg/mol)}$$

The density of zircon is 4.675×10^3 (kg/m^3) [21], so molar volume V is

$$V = M/\text{Density} = 39.21 \times 10^{-6} \text{ (m}^3\text{/mol)}$$

κ_T is isothermal compressibility and is defined as

$$-1/V\ (dV/dP)T = 1/(\text{isotherm bulk modulus})$$

From [21], experimental value of isothermal bulk modulus is 227.12 GPa, so κ_T is $1 / (227.12 \times 10^9)$.

Collecting the contribution to 3.8, we have

$$C_p = C_v + (11.80 \times 10^{-6})^2 \times 300 \times (39.21 \times 10^{-6}) \times (227.12 \times 10^9)$$
$$= C_v + 0.372$$

Quantities are in units of J/(K mol) in this formula.

For example, in the case of potential 4, C_v calculated by GULP is 203.437 J/(mol K). Dividing this by 2 to transfer from primitive cell to formula unit basis, we have $C_v = 101.719$. So $C_p = 101.719 + 0.372 = 102.1$, which is the value shown in Table 3.14.

From Table 3.14, we see that potential 4 has much better entropy and dielectric constant values, and a slightly better heat capacity value. Potential 4 also has much better entropy values at higher temperatures (Table 3.15 and Figure 3.1 in Section 3.4, although the values for potential 2 are not shown) and better calculated kinetic properties (self-diffusion coefficients and activation energies for self-diffusion calculated in Chapter 4). In

addition, potential 4 has a very clear and detailed analytical description of how the ZBL potential is included at short range, whereas the paper where potential 1 is described [5], while mentioning that the potential was fitted to the ZBL potential at short range, provides no details on how this was achieved. Considering the overall performance, potential 4 is the winner of the five candidate potentials. In next section we discuss this potential further.

3.4 Discussion of the chosen potential

In Section 3.3, we have seen that potential 4 is able to reproduce the zircon crystal structure and the mechanical, thermal and dielectric properties of crystalline zircon with acceptable accuracy. In this section, we look more closely at some other aspects of this potential.

Zircon consists of zirconium, a transition metal; silicon, a group IV element; and oxygen, a group VI element. Although the Si-O interaction is mostly covalent with partial ionic character, it is well established that a potential based on ionic interactions is generally suitable for studying zircon's properties. The formal charges for Zr, Si and O are +4, +4 and -2, respectively, but it might be useful to use partial charges instead of formal charges to account for the anisotropy in the zircon structure. Partial charges also make sense from the point of view that some interactions in zircon, such as that between Si and O, are only partially ionic. The chosen potential indeed uses partial charges, with +3.8 for Zr, +2.0 for Si and -1.45 for O.

The GULP code also has the ability to fit particle charges. In GULP's input file, one can specify ion charges as variable (all other potential parameters fixed) and let GULP fit charges to the crystalline structure and material properties, such as experimental bulk modulus and elastic constants. The

fitting process needs an initial set of ion charges to start with. If formal charges (+4 for Zr, +4 for Si and -2 for O) are used initially, the resulting charges are: Zr: +3.954; Si: +1.948. By overall charge neutrality, the charge of O must be -1.476. These values are close to the ones shown in Table 3.8. The differences are caused by using the experimental zircon crystalline structure instead of the optimized structure under this particular potential model. If we use the optimized structure (column 6 for potential 4 in Table 3.12) with lattice parameters $a = b = 6.602$, $c = 6.093$ and with oxygen position parameters $u = 0.8157$ and $v = 0.3240$, the optimal charges will be Zr: 3.800, Si: 2.000, O: 1.450, exactly the same as those used by the chosen potential. This is probably because the developers of potential 4 used similar process to fit ion charges. The charges are not, however, balanced with respect to potential decomposition products (e.g. SiO_2, ZrO_2) that appear in radiation-disordered or phase-segregated non-crystalline atomic arrangements, and we explore alternative partial charge choices in Section 6.6.

Coughlin and King [15] showed experimental data of entropy increments as temperature is increased from room temperature. We have calculated the same values using the chosen potential, which are compared to experimental data from [15] in Table 3.15. Data in the second column of Table 3.15 is directly copied from [15], which reports entropy increments in unit of cal / (K mol). Data in the third column are the same as those in the second column, but transferred to unit of J / (K mol) using 1 cal = 4.184 Joule. The last column shows entropy increments calculated using the chosen potential.

Table 3.15: Comparison of calculated and experimental entropy increments at different temperatures

Temperature	Experimental S_T-$S_{298.15}$		Calculated (Joule / (K mol))	
(K)	cal / (K mol)	Joule / (K mol)	S_T	S_T-S_{298}
298	N/A	N/A	83.684	0.00
300	N/A	N/A	84.363	0.68
400	7.53	**31.51**	116.033	**32.35**
500	13.86	**57.99**	143.426	**59.74**
600	19.48	**81.50**	167.199	**83.51**
700	24.50	**102.51**	188.045	**104.36**
800	29.01	**121.38**	206.535	**122.85**
900	33.08	**138.41**	223.109	**139.43**
1000	36.77	**153.85**	238.106	**154.42**
1100	40.13	**167.90**	251.787	**168.10**
1200	43.22	**180.83**	264.357	**180.67**
1300	46.08	**192.80**	275.977	**192.29**
1400	48.74	**203.93**	286.778	**203.09**
1500	51.23	**214.35**	296.864	**213.18**
1600	53.58	**224.18**	306.324	**222.64**
1700	55.80	**233.47**	315.228	**231.54**
1800	57.91	**242.30**	323.639	**239.95**

Figure 3.1 shows the comparison between experimental and calculated entropy increments. The agreement between calculated and experimental values is apparent.

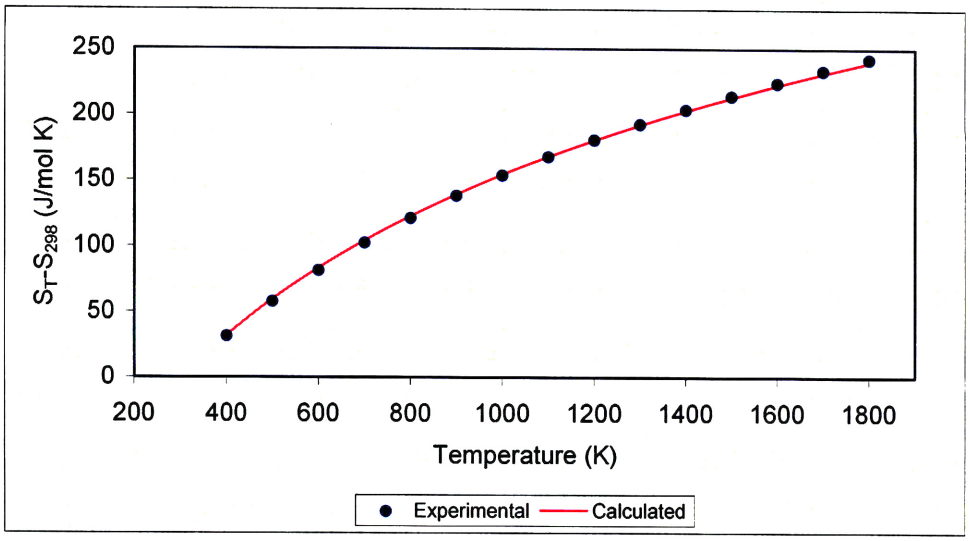

Figure 3.1: Comparison of experimental [15] and calculated entropy increments from room temperature to different temperatures

We saw in Section 3.2 that four out of the five candidate potentials (potentials 1, 3, 4 and 5) have incorporated the ZBL potential at short range, all using different, or unknown, ways. Different potential models can certainly incorporate the ZBL potential in different ways, but there are some basic requirements on the way the ZBL potential should be included. First of all, the equilibrium properties should not be changed. This means that, at distances comparable to or greater than the equilibrium interatomic distance, the ZBL-incorporated potential should be very close to the original non-ZBL-incorporated potential. Another requirement is that, at very short distance, the ZBL potential should be the dominant part, since this is the purpose of introducing it in the first place. In addition, the potential and its derivative should be continuous functions, so that no artificial discontinuities are introduced into the system.

The chosen potential (potential 4) incorporates the ZBL potential using the relationship

$$V(r) = F(r)V_{BM}(r) + (1 - F(r))V_{ZBL}(r), \tag{3.9}$$

where F(r) is the Fermi function ($F(r) = \frac{1}{1+e^{-b_f(r-r_f)}}$). For potential V to be close to V_{BM} at r comparable to equilibrium interatomic distance, and close to V_{ZBL} at small r, we require F(r) to be close to 1 when r is comparable to equilibrium interatomic distance and close to 0 when r is very small. The parameters for the Fermi function used by potential 4 have already been shown in Table 3.9. We explore whether these choices meet the above mentioned requirements.

From Table 3.9, we can see that for Zr-Zr, Zr-Si and Si-Si interactions, the parameters are the same: $b_f = 6.0$ and $r_f = 1.0$. Figure 3.2 is the plot of the Fermi function using these two values:

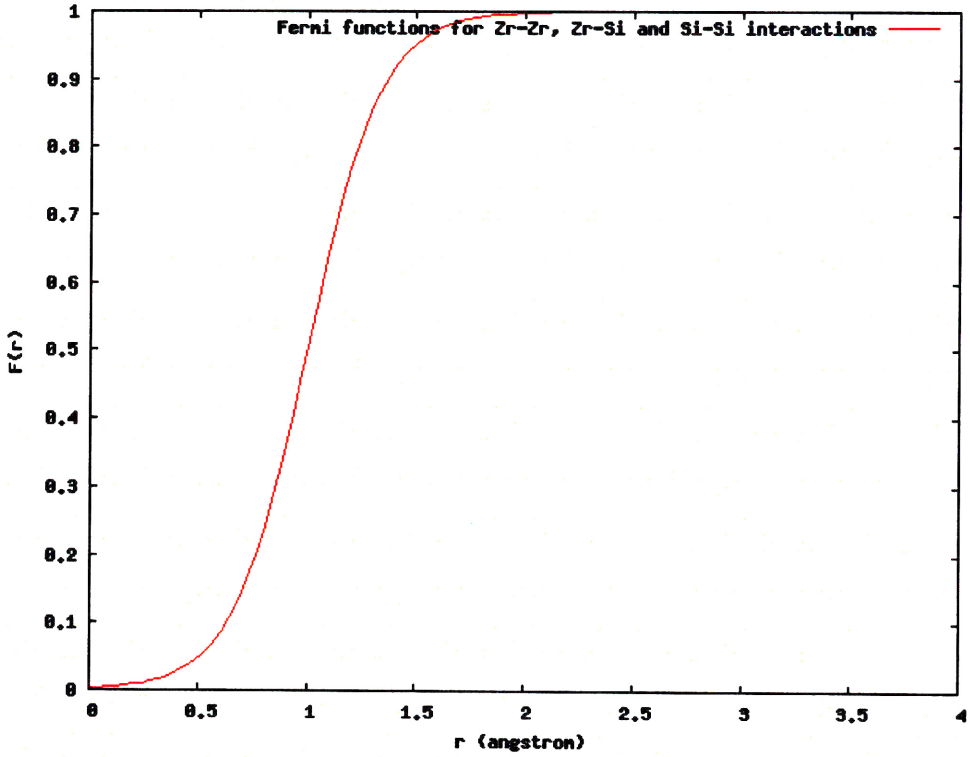

Figure 3.2: Fermi function to incorporate the ZBL potential for Zr-Zr, Zr-Si and Si-Si interactions.

The shortest interatomic distances for Zr-Zr, Zr-Si and Si-Si atom pairs are 3.627 Å, 2.991 Å and 3.627 Å, respectively. We can see in Figure 3.2 that at these distances F(r) is indeed very close to 1. As r goes to 0, F(r) decreases quickly to 0, as required. The other interactions use different b_f and r_f values, but the Fermi functions all behave similarly and meet the requirements.

There is actually much freedom in choosing b_f and r_f values to meet the requirements. In addition, using Fermi function is by no means the best or the customary way to combine equilibrium potential and the ZBL potential together. For example, potential 3 uses a fifth order polynomial function.

Finally, Figure 3.3 shows the potential energies for Zr-O, Si-O and O-O interactions. Figure 3.4 shows the same interactions but excluding long range Coulombic part of the potentials. That is, only the Born-Mayer parts combined with the ZBL potential are included.

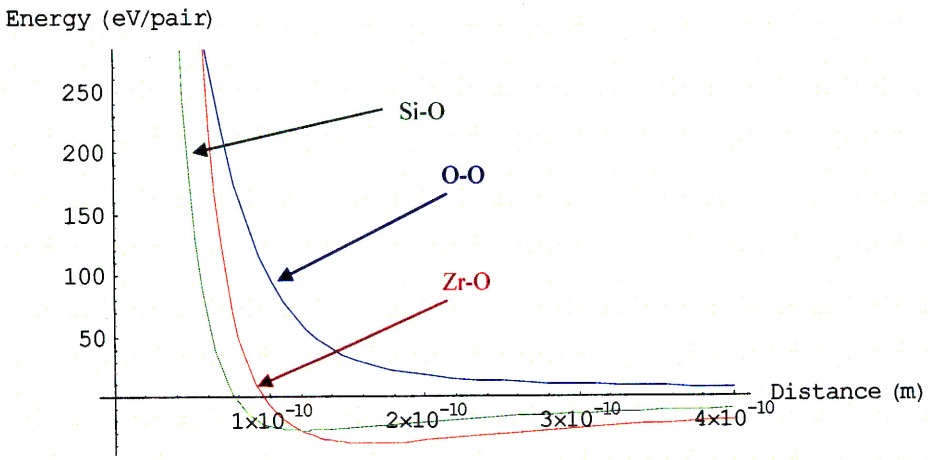

Figure 3.3: Potential energies of Zr-O, Si-O and O-O interactions.

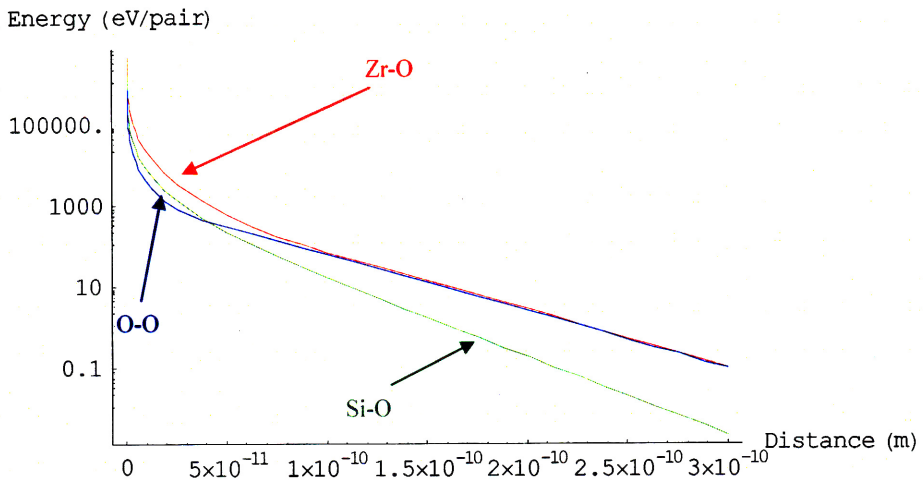

Figure 3.4: Short range potential energies of Zr-O, Si-O and O-O interactions (potentials excluding Coulombic parts).

The potential functions are continuous functions. Although not shown here, the first derivatives of potentials are also continuous.

Thus far the potential looks good on the properties we have checked, but we cannot say we have full confidence in using this potential for collision cascade MD simulations yet. MD simulations are not involved in any of the previous calculations, and we have not tested any kinetic behavior of zircon under this potential. In next chapter, we will first test whether zircon structure can hold at 300 K in MD simulation using the chosen potential. Then we will move on to calculate melting temperature and some kinetic properties, such as self-diffusion coefficients and activation energies for self-diffusion.

References of chapter 3

[1] J.F. Ziegler, J.P. Biersack and U. Littmark. The Stopping and Range of

Ions in Solids (Volume 1 of: The stopping and ranges of ions in matter, edited by J.F. Ziegler.). New York, Pergamon, 1985.

[2] K. Trachenko, M.T. Dove and E.K.H. Salje. Large Swelling and Percolation in Irradiated Zircon. J. Phys.: Condens. Matter 15, L1 (2003).

[3] L.R. Corrales, W.J. Weber, A. Chartier, C. Meis and J.-P. Crocombette. Comment on "Large Swelling and Percolation in Irradiated Zircon". J. Phys.: Condens. Matter 15, 6447 (2003).

[4] K. Trachenko, M.T. Dove and E.K.H. Salje. Reply to Comment on "Large Swelling and Percolation in Irradiated Zircon". J. Phys.: Condens. Matter 15, 6457 (2003).

[5] K. Trachenko, M.T. Dove, T. Geisler, I. Todorov and B. Smith. Radiation Damage Effects and Percolation Theory. J. Phys.: Condens. Matter 16, S2623 (2004).

[6] K. Trachenko, M.T. Dove and E.K.H. Salje. Atomistic Modelling of Radiation Damage in Zircon. J. Phys.: Condens. Matter 13, 1947 (2001).

[7] M.J. Sanders, M. Leslie and C.R.A. Catlow. Interatomic Potentials for SiO_2. J. Chem. Soc., Chem. Commun. 19, 1271 (1984).

[8] J.P. Crocombette and D. Ghaleb. Molecular Dynamics Modeling of Irradiation Damage in Pure and Uranium-Doped Zircon. J. Nucl. Mater. 295, 167 (2001).

[9] R. Devanathan, L.R. Corrales, W.J. Weber, A. Chartier and C. Meis. Molecular Dynamics Simulation of Disordered Zircon. Phys. Rev. B 69, 064115 (2004).

[10] B. Park, W.J. Weber and L.R. Corrales. Molecular-Dynamics Simulation Study of Threshold Displacements and Defect Formation in Zircon. Phys. Rev. B 64, 174108 (2001).

[11] J.D. Gale and A.L. Rohl. The General Utility Lattice Program. Mol. Simul. 29, 291 (2003).

[12] J.D. Gale. General Utility Lattice Program User's Manual.

[13] K. Robinson, G.V. Gibbs and P.H. Ribbe. The Structure of Zircon: A Comparison with Garnet. Am. Mineral. 56, 782 (1971).

[14] H. Ozkan, L. Cartz and J.C. Jamieson. Elastic Constants of Nonmetamict Zirconium Silicate. J. Appl. Phys. 45, 556 (1974).

[15] J.P. Coughlin and E.G. King. High-Temperature Heat Contents of Some Zirconium-Containing Substances. J. Am. Chem. Soc. 72, 2262 (1950).

[16] F. Gervais, B. Piriou and F. Cabannes. Anharmonicity in Silicate Crystals: Temperature Dependence of Au Type Vibrational Modes in $ZrSiO_4$ and $LiAlSi_2O_6$. J. Phys. Chem. Solids 34, 1785 (1973).

[17] R.C. Ewing, W. Lutze and W.J. Weber. Zircon: A Host-phase for the Disposal of Weapons Plutonium. J. Mater. Res. 10, 243 (1995).

[18] A.F. Wells. Structural Inorganic Chemistry. Oxford University Press, Oxford, 1984.

[19] J.A. Speer. Reviews in Mineralogy, vol. 5. Mineralogical Society of America, Chelsea, MI, 1982.

[20] P.W. Atkins. Physical Chemistry, 5th Ed. New York, W.H. Freeman, 1994.

[21] R.S. Carmichael, editor. Handbook of Physical Properties of Rocks, vol. 3. Boca Raton, Fla., CRC Press, 1982.

Chapter 4: Non-cascade MD simulations of zircon

After obtaining zircon crystal structure and choosing an empirical potential, we are ready for MD simulations. The simulations in this chapter do not include any radiation-induced collisions from the introduction of energetic primary knock-on atoms (PKA). PKAs are introduced into the simulations beginning in Chapter 5.

4.1 Simulation setup details

This section discusses the computer hardware, simulation software and the starting zircon structure for simulation. The starting configuration for simulation is not exactly the zircon crystal structure derived from experimental data in Chapter 2; see Section 4.1.3 for details.

4.1.1 Beowulf cluster hardware

For many years, Beowulf clusters have been cost-effective alternatives to expensive supercomputers. Beowulf clusters use only available mass-commodity PCs and components, the main reason Beowulf clusters are much cheaper than large supercomputers. Individual PCs (or nodes, as they are often called in the context of clusters) do their computations in parallel and communicate with each other through a fast network.

The hardware specifications of the Beowulf cluster used for simulations are not particularly important for this study, as the main conclusions do not depend on what computers are used, but they are listed here for completeness. The Beowulf cluster used has 16 dual processor computer nodes (32 processors total) and uses a gigabit Ethernet network for

communications between nodes. Each node has 2 Athlon MP 2000+ (1.67 GHz) processors and 1 GB memory. The network switches used are Netgear 16 port unmanaged Gigabit Ethernet switches; Network adapters used are 3COM Gigabit 1000BaseT NIC.

4.1.2 Cluster and simulation software

The operating system used is Red Hat Enterprise Linux. Cluster management and monitoring tools include Portable Batch System (PBS), a batch queuing and cluster load management system; and Ganglia, a distributed cluster monitoring tool [1]. Compilers used are the GNU compiler collection, Intel Fortran compiler and Intel C/C++ compiler for Linux.

The Message Passing Interface (MPI) is a library specification for message-passing parallel computing, proposed as a standard by a broadly based committee of vendors, implementers and users. MPI is just a standard specification, not an implementation. Various implementations abiding by the standard have been developed by research groups as well as commercial companies. The MPI implementation used in this study is LAM/MPI (Local Area Multicomputer/Message Passing Interface). It was developed and is maintained by the Open Systems Laboratory at Indiana University.

GULP is used for potential fitting and calculations of material properties. A very brief introduction for GULP was already given in Chapter 3. Gnuplot and GDIS are used for plotting and zircon structure visualization. The MD simulation code used is DL_POLY, with extensive modifications for certain types of simulations. The modifications include introducing a heat bath at the boundary of the simulation cell as an energy removal mechanism,

gradually reducing temperature of simulation cell boundary to simulate quenching, using variable time step size for high energy collision cascade simulations, suppressing initial Maxwell-Boltzmann distribution velocity generation, and suppressing velocity rescaling when full control over atom velocities is needed. Custom versions of DL_POLY have been made with various combinations of above mentioned modifications. Sometimes simulations were conducted using the original DL_POLY code, sometimes using the code with some or all of above mentioned modifications, depending on the specific needs.

Further discussions are devoted to DL_POLY, since it is the major MD simulation code used. DL_POLY is a package of subroutines, programs and data files designed to facilitate molecular dynamics simulations of macromolecules, polymers, ionic systems and solutions on a distributed memory parallel computer [2, 3, 4]. It is available in two forms: DL_POLY 2 and DL_POLY 3. These two forms differ primarily in their methods of exploiting parallelism. DL_POLY 2 uses Replicated Data (RD) strategy [5-8] whereas DL_POLY 3 is based on the Domain Decomposition (DD) strategy [5, 6, 9, 10].

DL_POLY 2 works well for molecular simulations of systems consisting of up to order 30,000 atoms, using computer systems of order 100 processors; DL_POLY 3 is best suited to large computer systems with up to 1000 processors and large molecular simulations with in total 10^4 to 10^7 atoms [4].

It should be stressed that although DL_POLY 3 has a higher version number than DL_POLY 2, it serves a totally different scale of problems and computer systems and is not meant to be a replacement for the DL_POLY 2 code.

In fact, there are other reasons why DL_POLY 3 cannot replace DL_POLY 2, at least for now. At the beginning of this study, DL_POLY 3 was evaluated to see whether it was worth migrating over from DL_POLY 2. At that time, 2.14 was the highest version number for DL_POLY 2 and 3.01 for DL_POLY 3. We decided to stay with DL_POLY 2 because DL_POLY 3 was not found to be stable enough for serious simulations at that time. More specifically, the following DL_POLY 3 code bugs were discovered:

- In the DL_POLY 3 user's manual, the documentation for formatted HISTORY file says record (we can think of a record as one line of output data) 2 of data for each time step will output the number of atoms in the simulation cell after outputting the trajectory key and periodic boundary key. However, in reality, the number of atoms is not written. This does not affect the simulation itself, but does cause a problem with personal tools for analyzing the HISTORY file when migrating from DL_POLY 2 to DL_POLY 3.
- The subroutine for writing the unformatted HISTORY file is not available.
- DL_POLY 3.01 produces wrong values of total energy and van der Waals energy in the OUTPUT file. OUTPUT is one of few files that are written by DL_POLY containing important data and results about the MD simulation. A simple and proven model of FCC Au structure was used for testing. DL_POLY 2 outputed a negative total energy, as expected for a stable system. This energy was also close to the total energy value calculated using GULP, so it was likely to be correct. However, the total energy and van der Waals energy values calculated by DL_POLY 3 were positive.

These problems were confirmed by Dr. Bill Smith of Daresbury Laboratory, UK, author of the DL_POLY code. There were probably other problems that weren't encountered during the brief usage of DL_POLY 3. In an email sent out to the DL_POLY mailing list, Dr. Smith said on April 2, 2004 that "Our last message announced the appearance of the domain decomposition version of DL_POLY, which was released as version 3.01. Since then it has

become apparent that, though the basic algorithms were sound, there were enough bugs and conflicts among its features to justify a major overhaul ...".

It was preferable to spend most of the time available analyzing MD simulation results of radiation effects in zircon, not debugging the software and tools to be used, so it was natural to choose DL_POLY 2 as the main MD simulation software. There have been several new releases of DL_POLY 3 since then; the problems mentioned above should have been fixed, although this was not verified.

Another reason to use DL_POLY 2 instead of DL_POLY 3 is that, as mentioned before, DL_POLY 2 is best for computer systems of order 100 processors, whereas DL_POLY 3 is for larger systems with up to 1000 processors [4]. Our Beowulf cluster has only 32 processors (Section 4.1.1), so if DL_POLY 3 were used, probably the overhead of domain decomposition methodology would offset its benefits.

4.1.3 MD simulation method

The starting zircon configuration for MD simulation is not the structure derived from experimental data in Chapter 2. Rather, it is the experimental structure after energy minimization using GULP, since it is the stable one under the chosen potential. This structure is very close to the experimental one, as we have already seen in Table 3.12 (compare column 2, the column for experimental structure, with column 6, the column for the chosen potential).

The short range part of the chosen potential model, with a Born-Mayer form potential combined with the ZBL potential using Fermi functions, is not

directly specifiable in DL_POLY input files. Fortunately, DL_POLY accepts short range potentials in tabular form. As a result, the potential values are tabulated evenly from 0 to 10 Å at 10,000 locations, and this table is used as the short-range potential input.

Periodic boundary conditions were used in all simulations. The supercell size used in this chapter was 6x6x6 (in total 5184 atoms) and the time step used was 1 fs (10^{-15} seconds), unless otherwise specified (larger simulation cells and shorter time step sizes are used in Chapters 5 and 6 for energetic cascade simulations). Most of the time the properties were determined over 10 or 20 ps MD runs. Either constant volume or constant pressure simulations were performed, depending on the specific purposes of the simulations.

4.2 MD Simulation at 300 K and 5000 K

The experimental melting temperature of zircon is in the range of 2000~2600 K. Butterman and Foster [11] reported that $ZrSiO_4$ decomposes into ZrO_2- and SiO_2-rich liquid at about 1960 K, and the two-phase region extends from 1960 to 2675 K. Figure 4.1 shows the SiO_2-ZrO_2 phase diagram [12]. The *y* axis in Figure 4.1 is temperature in units of degrees Celsius. We can see that, at a temperature slightly lower than 1700 °C (1973 K), $ZrSiO_4$ decomposes into ZrO_2 solid solution and SiO_2 liquid; at a temperature just lower than 2400 °C (2673 K), zircon has entirely melted. These values agree well with the 2000~2600 K melting point range cited by Butterman and Foster [11]. Later we will use 2000~2600 K as zircon's experimental melting temperature.

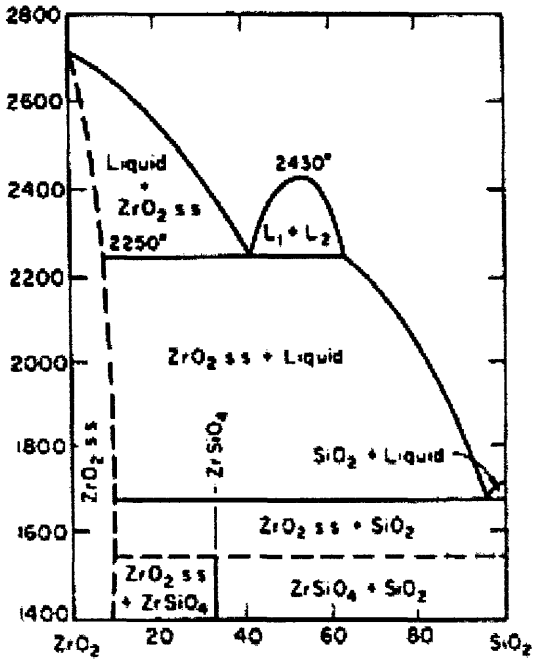

FIG. 362.—System SiO_2–ZrO_2. ss = solid solution.

N. A. Toropov and F. Ya. Galakhov, *Izvest. Akad. Nauk S.S.S.R. Otdel Khim. Nauk*, 1956, 160. See also, C. E. Curtis and H. C. Sowman, *J. Am. Ceram. Soc.*, 36 [6] 198 (1953).

Figure 4.1: SiO_2-ZrO_2 phase diagram [12].

Given this range of melting temperature, at 300 K zircon is of course still a solid. Atoms should be able to vibrate only around their equilibrium sites and the crystalline structure should be preserved. At 5000 K, zircon should have melted and the crystalline structure lost. If the structure developed in Chapter 2 and the potential chosen in Chapter 3 are realistic descriptions of zircon, these facts must be reflected in MD simulations.

To test whether this is the case, 20 ps MD simulations were performed under a constant temperature, constant pressure ensemble at both 300 K and

5000 K. The first 10 ps of simulations were for equilibration, during which time velocities of atoms in the system were rescaled periodically to maintain the system at the desired temperatures. No velocity rescaling was performed for the remaining 10-ps simulations, during which time material properties were determined.

4.2.1 System temperature

MD simulations in this section were performed using a constant temperature ensemble, so temperatures should be kept constant for successful simulations. Time step size used in simulations was 1 fs. During the first 10,000 time steps (10 ps), velocity rescaling was performed every 10 time steps (0.01 ps). Figure 4.2 plots the temperatures against simulation times for both 300 K and 5000 K simulations.

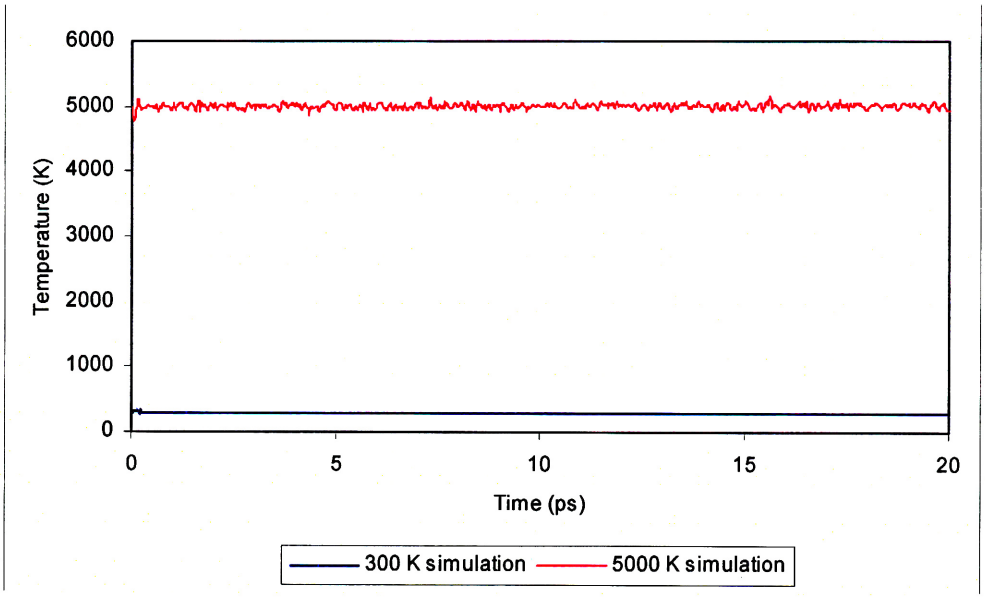

Figure 4.2: System temperatures at different simulation times of 300 and 5000 K NPT zircon simulations.

For both 300 and 5000 K cases, the temperatures are seen to be well under

control. It is useful to check system temperatures because, as will be seen in Section 5.4, abnormal behavior of system temperature is often an indicator of invalid simulation.

4.2.2 Total energy of the system

During the initial 10 ps of simulation, when velocity rescaling was applied periodically, the total energy (kinetic energy + total energy) of the system was not preserved, because the velocity rescaling effectively changes kinetic energy of atoms and thus the total energy. But after velocity rescaling was turned off, the total energy should be preserved. Of course, in reality there won't be absolute conservation, but the perturbation should be small. These features are apparent in Figures 4.3 and 4.4.

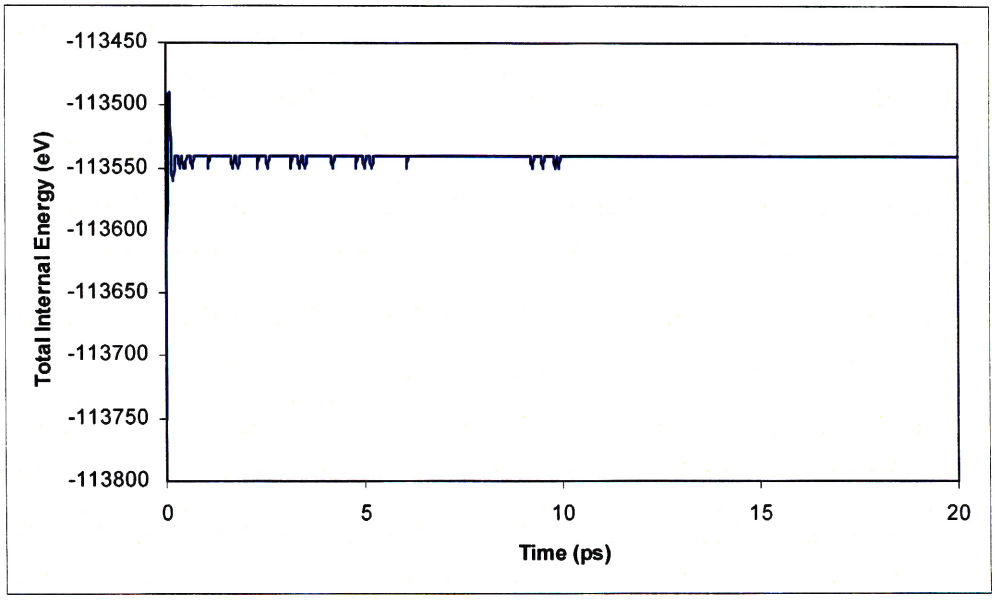

Figure 4.3: System total energy in a 300 K NPT zircon simulation. Total energy is not preserved during the first 10 ps of simulation, when velocity rescaling is performed periodically, but it is from 10 ps to 20 ps after velocity rescaling is turned off.

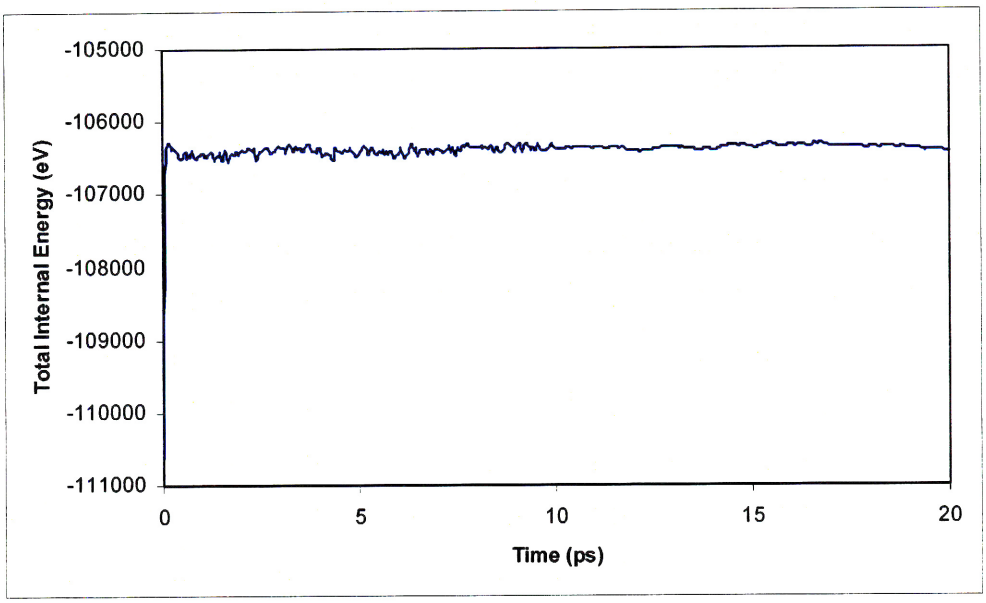

Figure 4.4: System total energy in a 5000 K NPT zircon simulation. The conservation of total energy from 10 ps to 20 ps is not as good as in 300 K simulation, shown in Figure 4.3, but nonetheless the perturbations are very small (less than 0.1%).

System total energy stabilizes at about -113540 eV and -106370 eV in 300 K and 5000 K simulations, respectively. Total energy at 5000 K is about 7170 eV higher than that at 300 K. According to the theorem of equi-partition of energy, an atom has on average about $\frac{3}{2}kT$ kinetic energy at temperature T, where k is the Boltzmann constant with a value of 8.617×10^{-5} eV/K. Thus at $T = 300$ and 5000 K, the kinetic energies per atom are

$$\frac{3}{2}kT = \frac{3}{2} \times 8.617 \times 10^{-5} \times 300 = 0.0388(\text{eV})$$

$$\frac{3}{2}kT = \frac{3}{2} \times 8.617 \times 10^{-5} \times 5000 = 0.646(\text{eV})$$

The difference is about 0.607 eV. With a total of 5184 atoms in the 6x6x6 supercell, the total kinetic energy difference should be $0.607 \times 5184 = 3147$

eV. This value is smaller than the 7170 eV difference observed from the simulations. The remaining 7170 - 3147 = 4023 eV energy is stored in the 5000 K zircon structure.

It is important to verify the system total internal energy in order to increase our confidence in the validity of the simulations. For constant energy simulations, the total internal energy should obviously be conserved, at least in theory. Even for constant temperature simulations – such as those performed in this section where the total energy is not expected to be conserved – verifying system total internal energy still has some usefulness. Total energy should be negative for the system to be stable, and should not have huge fluctuations toward the end of the simulation where average system properties are obtained; otherwise, the system itself is in a condition too unstable for any reasonable conclusion to be drawn.

An abnormal total internal energy behavior is one good indicator that an MD simulation has gone wrong, as will be seen in Section 5.4.

4.2.3 Dimensional changes

The volume of the simulation box is expected to change during the course of a simulation in which a constant pressure, not constant volume, ensemble is used. Dimensional changes of 300 and 5000 K simulations are shown in Figures 4.5 and 4.6, respectively. The dimensional changes shown include changes of lattice parameter *a*, lattice parameter *c* and the volume of the simulation cell. Lattice parameter *b* is not shown because it is equal to *a*.

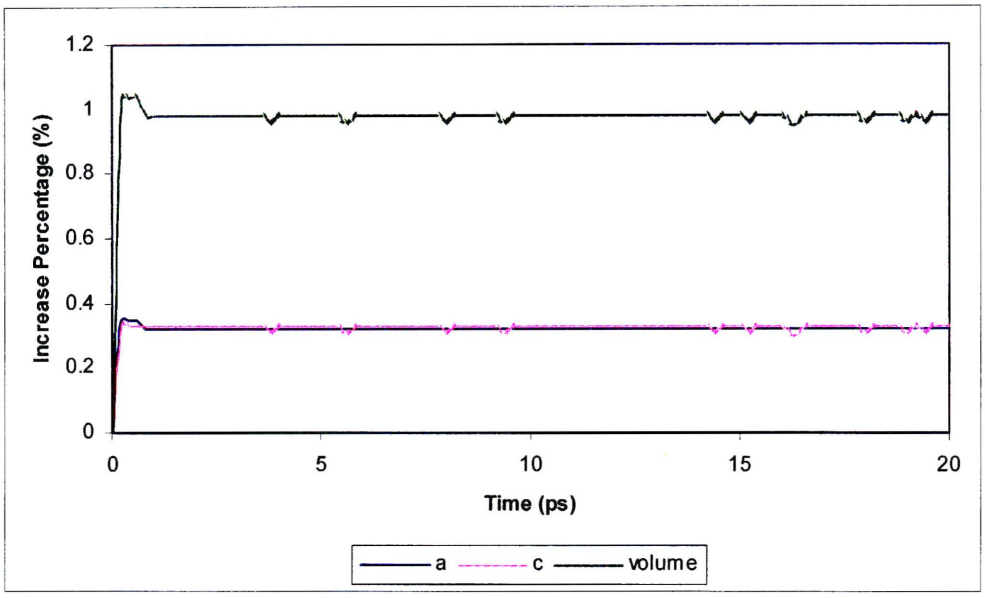

Figure 4.5: (Color) Dimensional changes of the simulation box in 300 K NPT zircon simulation.

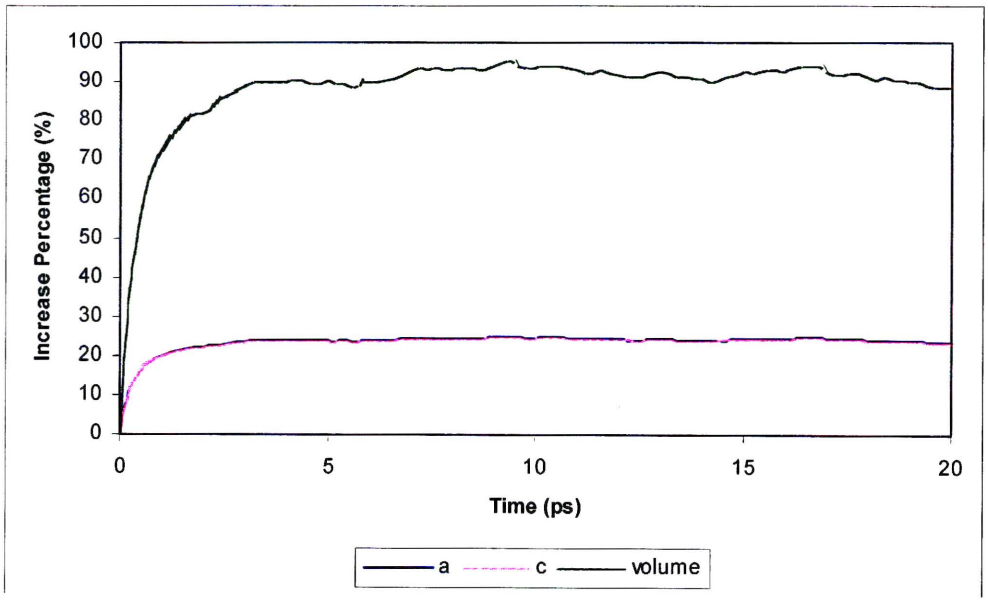

Figure 4.6: (Color) Dimensional changes of the simulation box in 5000 K NPT zircon simulation.

In Figure 4.5, the system dimensional changes at 300 K are seen to be very small. The starting structure for MD simulation is the structure resulting from GULP energy minimization at 0 K, so it is not surprising that MD

simulation at 300 K results in a volume expansion. Zircon's linear expansion coefficient at 300 K is about 1.18×10^{-5} K^{-1} [13]. If this coefficient is a constant (which it is not, but we'll assume it is the case for the sake of estimation) from 0 K to 300 K, the volume expansion should be $1.18 \times 10^{-5} \times 300 \sim 0.4\%$, close to the 1% observed in the simulation. Of course for a real calculation, we need to know the temperature dependence of the thermal expansion coefficient and integrate.

In Figure 4.6, it is seen that the system undergoes huge dimensional changes at 5000 K. Without looking at structural details, we cannot ascertain that the original crystal structure has been destroyed; but the huge volume increase is suggestive. The huge volume expansion of about 90%, however, is unrealistic. It is attributed to the unbalanced ion charges of the chosen potential with regard to decomposition products of zircon (*e.g.* SiO_2); see Section 6.6 for more details.

4.2.4 Final structures after simulation

Figure 4.7 shows the zircon structure before simulation; Figure 4.8 shows the same structure after 20-ps MD simulation at 300 K using the NPT ensemble; and Figure 4.9 shows the structure after 20-ps MD simulation at 5000 K using the NPT ensemble.

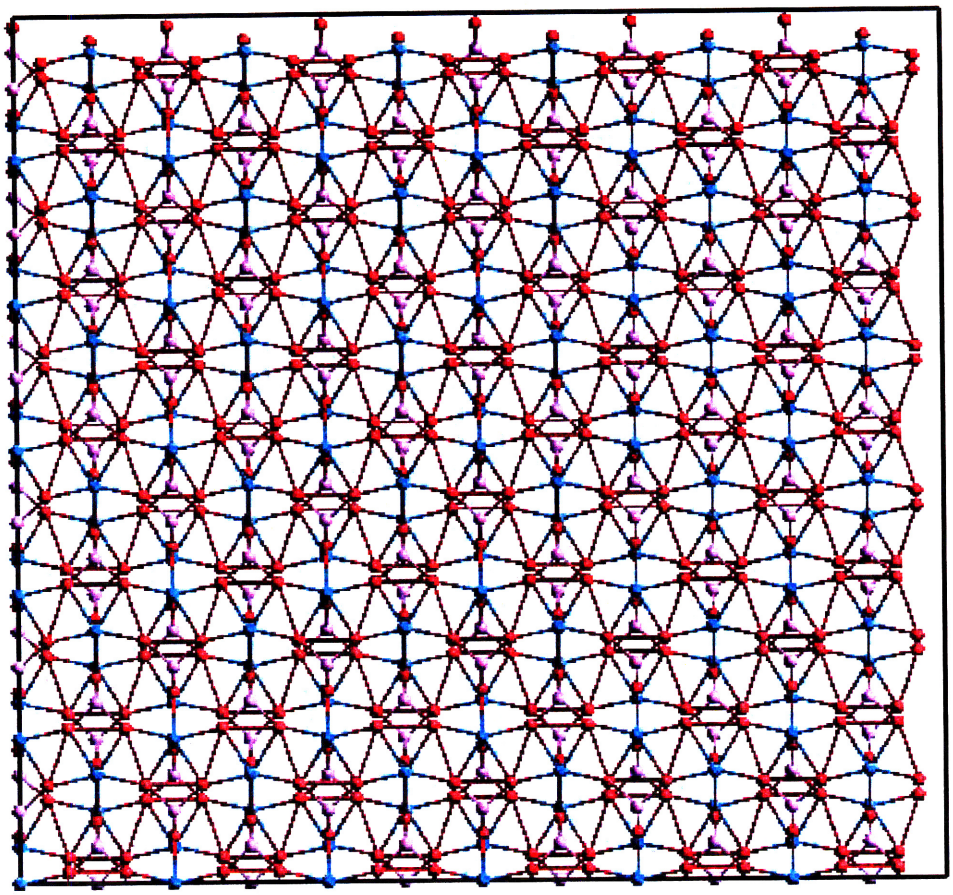

Figure 4.7: Zircon crystalline structure before simulation, viewed from $[0\bar{1}0]$ direction.

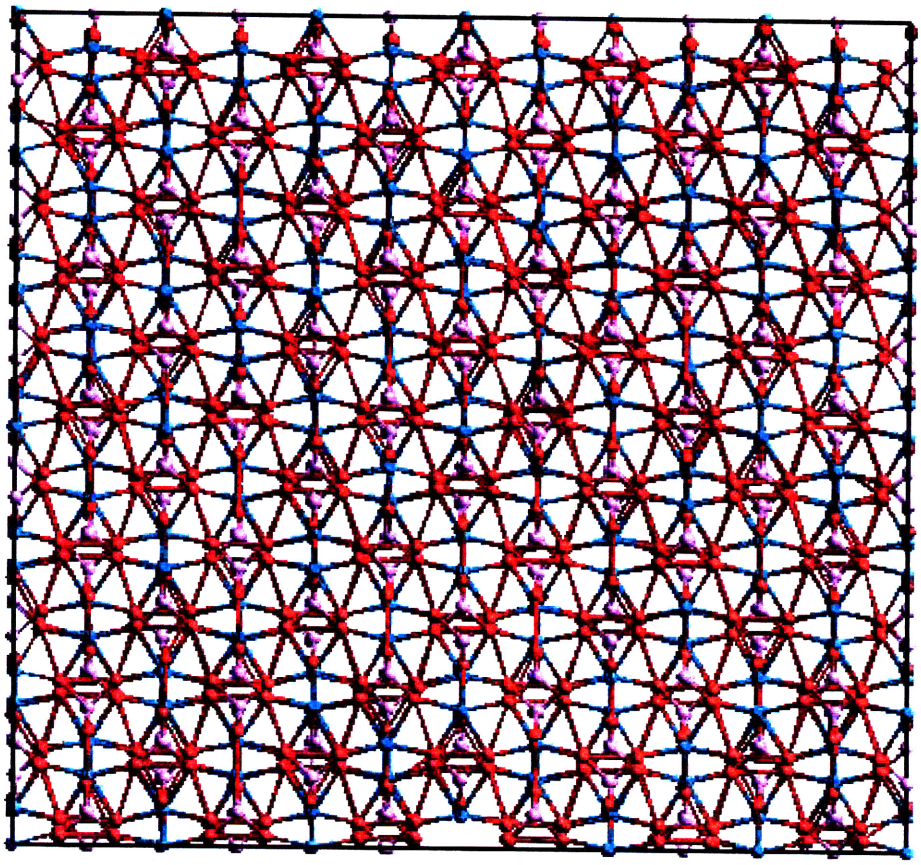

Figure 4.8: Zircon structure after 20-ps MD simulation at 300 K using the NPT ensemble, viewed from $[0\bar{1}0]$ direction.

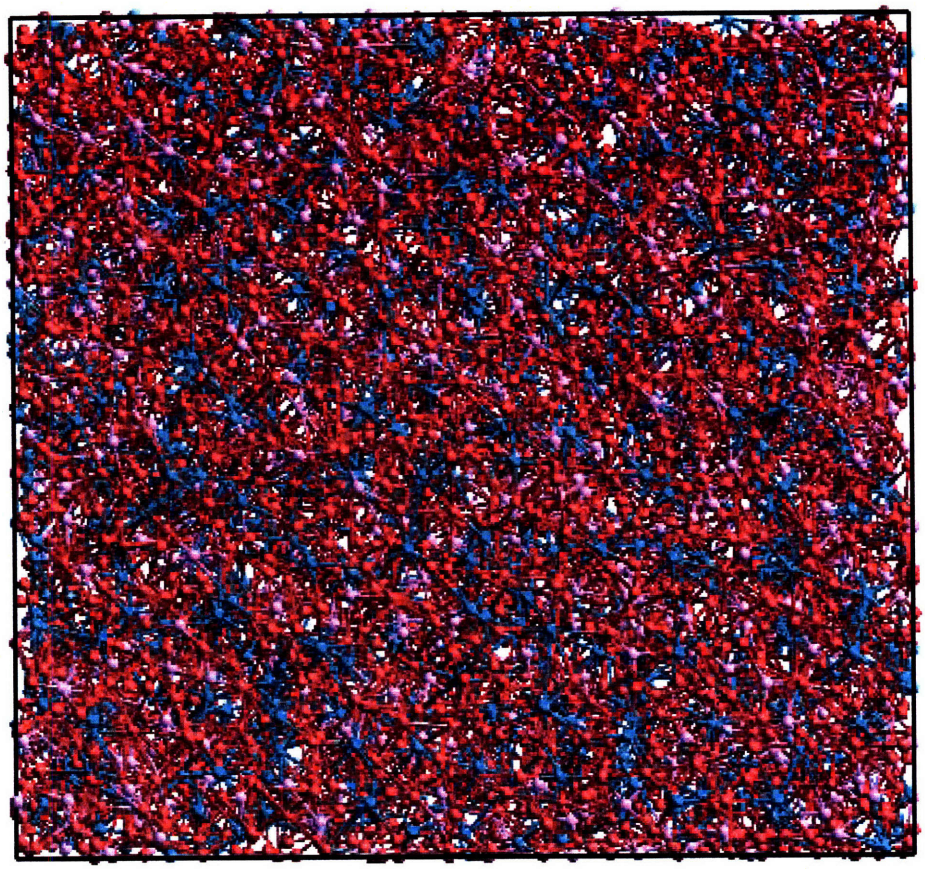

Figure 4.9: Zircon structure after 20-ps MD simulation at 5000 K using the NPT ensemble, viewed from $[0\bar{1}0]$ direction.

In Figure 4.7, the structure is in an unperturbed crystalline state with atoms at precisely the crystalline positions. In Figure 4.8 we can see the thermal vibrations of the atoms, but the structure is nonetheless still crystalline. In Figure 4.9, the structure has melted and the crystalline lattice has been destroyed.

4.2.5 Mean square displacements of atoms in the system

Later, we will use mean square displacements to calculate self-diffusion coefficients of Zr, Si and O in liquid zircon. Here, we calculate the mean

square displacements for both 300 K and 5000 K cases.

It is quite straightforward to calculate mean square displacements. At a given time step, for each atom in the system we can calculate the distance, taking periodic boundary conditions into consideration, between its current position and its original position at time step 0, whose square is the square displacement for this particular atom. Averaging over all atoms in the system yields the mean square displacements at this time step. The mean square displacement values thus calculated for 300 K and 5000 K cases are shown in Figures 4.10 and 4.11, respectively.

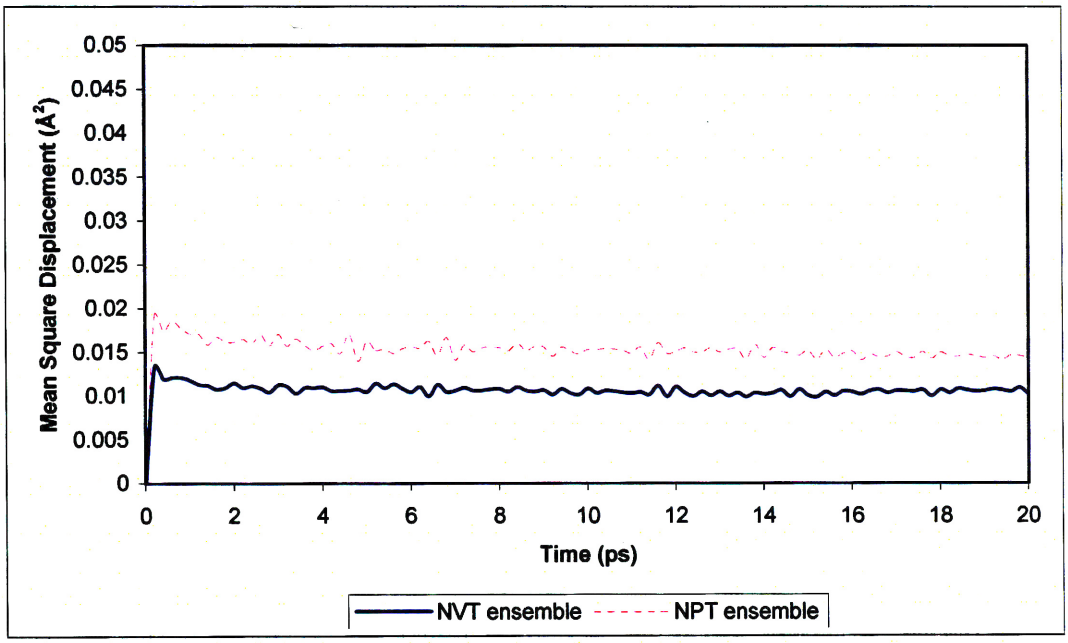

Figure 4.10: Mean square displacements in 300 K simulation.

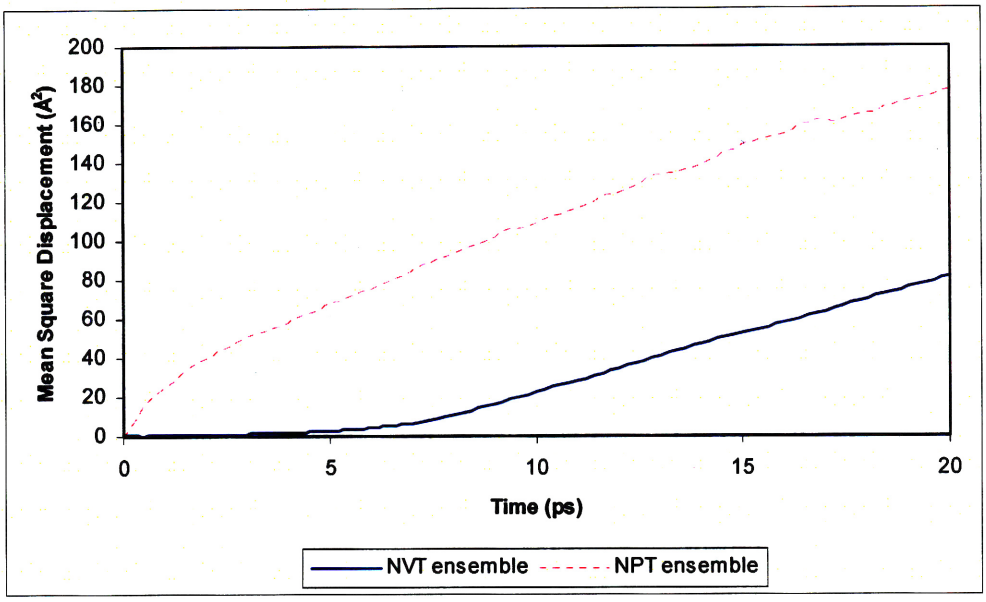

Figure 4.11: Mean square displacements in 5000 K simulation.

In Figure 4.10, the values of mean square displacements at 300 K are very small (around 0.01 $Å^2$ in the NVT ensemble case and 0.015 $Å^2$ in the NPT ensemble case) and do not increase with time. The atoms clearly do not have enough energy to escape the potential barriers surrounding their equilibrium sites.

At 5000 K, the values of mean square displacements are very large. For example, at time 20 ps in the NVT ensemble, the mean square displacement value is 81.767 $Å^2$. Thus, on average, each atom has traveled a distance of $\sqrt{81.767} \approx 9$ Å, which is several times of the interatomic distances in zircon. This value is even higher for the NPT ensemble. It is clear that atoms have left their sites and have started to diffuse, indicating a departure from the solid state.

Another feature seen in Figures 4.11 is that initially the mean square displacements value does not increase much when the NVT ensemble is

used. But once substantial disorder is introduced, mean square displacement values increase roughly linearly with time. For the NPT ensemble case, mean square displacement values increase almost linearly from the very beginning. It should be noticed that the slopes of the two linear increases in Figure 4.11 are roughly the same. In Section 4.4 we will use the relationship $\langle \Delta r^2 \rangle(t) = 6Dt + const.$ to calculate self-diffusion coefficient D from mean square displacements values. The equality of the slope values means we will obtain the same self-diffusion coefficient no matter which ensemble is used.

4.2.6 Radial distribution functions

In Chapter 2 we showed radial distributions functions for crystalline zircon. Long range periodicity exists in perfect crystalline structures, so the RDF has sharply distinguishable peaks even at very long distances. As the crystal structure is destroyed, such as when the solid melts, long range periodicity does not exist any more. Relative to any specific atom, other atoms at long distances appear to be more randomly located, so the RDF peaks at long distances flatten out and the value of RDF becomes close to 1. These features can be seen clearly from the 5000 K RDF curve in Figure 4.12.

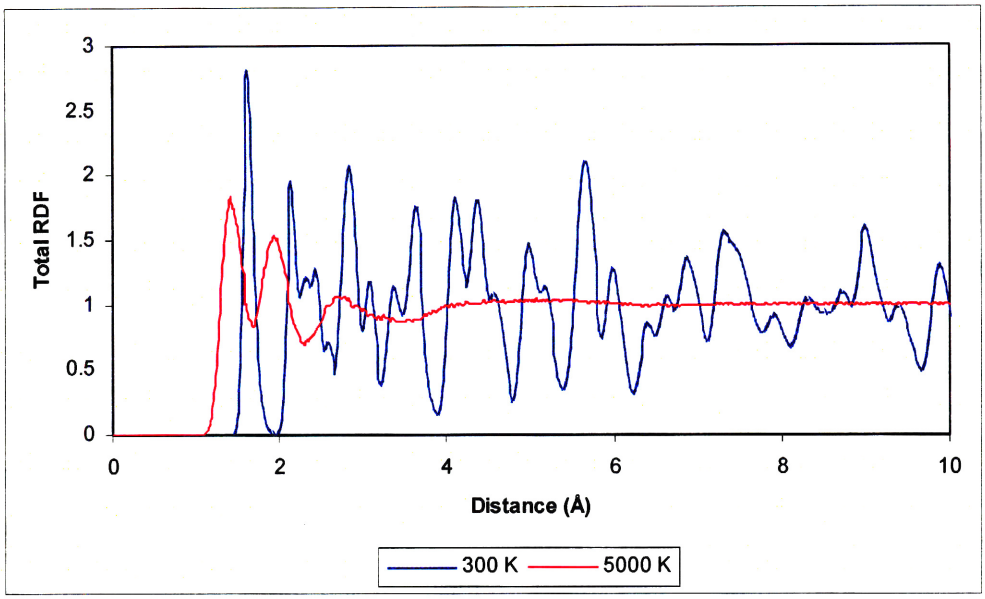

Figure 4.12: Total RDF of zircon calculated from 300 K and 5000 K simulations using NPT ensemble. RDFs are averaged over the last 5 ps of the simulations. The first peaks in both curves come from Si-O interatomic distances. The peak shifts from about 1.6 Å at 300 K to about 1.4 Å at 5000 K. This figure can be compared to Figure 2.19 where total RDF of perfect crystalline zircon is shown.

Comparing Figure 4.12 to Figure 2.19, we see that the peaks in the 300 K RDF are broadened compared to the RDF of the perfect (0 K) crystalline structure, but are nonetheless preserved even at long distances. The RDF curve for the structure at 5000 K has a value of 1 starting from about 4 Å, which means there is no unique correlation between atoms after this distance.

4.2.7 Summary of this section

This section presents simulations performed at 300 K and 5000 K. The temperatures have been shown to be well under control. The total internal energies are conserved after velocity rescaling is turned off. Using different metrics, such as system dimensional changes, final structures after

simulations, mean square displacements of atoms and total radial distribution functions, we have seen that the crystal structure is preserved at 300 K but lost at 5000 K, as would be expected from any realistic description of the system. Our zircon structure model and the chosen potential have thus passed the first minimum set of MD simulation tests.

4.3 Calculation of zircon melting temperature

In last section we have seen the huge differences of certain properties in 300 and 5000 K simulations, due to the fact that the structure has melted at 5000 K but not at 300 K. If we can determine at which temperature between 300 K and 5000 K these indicator properties change suddenly, we can determine the melting temperature of zircon.

There is some choice in indicator property used for detecting a first-order phase transformation, such as the melting of zircon. For example, system volume and enthalpy have sudden increases upon melting; heat capacity at constant pressure (C_p) has an infinite value at the melting temperature; mean square displacements value starts to increase with time once temperature is higher than the melting point. We can also plot radial distribution functions and try to detect the disappearance of RDF peaks at long distance. Bond angle distribution functions can also be used in the same way as the RDF for this purpose. Or, as we have done in Figures 4.8 and 4.9, we can even take a look at the positions of atoms directly and see whether the crystalline structure is preserved. Any of the indicators mentioned above can be used to determine the melting of zircon. Many of them are correlated with each other and will give the same result. The simplest one to use is probably system volume, since it needs no further calculation or data processing. This is what we used to determine the simulation melting temperature. We ran

the simulations at different temperatures and recorded system volumes. The melting temperature is located where the system volume exhibits a sudden change.

Table 4.1 shows the molar volume of zircon obtained at different temperatures. The data directly available from DL_POLY output file include supercell volume V. Because the supercell used has 6×6×6 unit cells, and each unit cell has four $ZrSiO_4$ formula units, there are in total 6×6×6×4 = 864 $ZrSiO_4$ formula units. The quantity V / 864 is then the volume per formula unit, which multiplied by Avogadro's number yields the molar volume values shown in Table 4.1. The same data are shown graphically in Figure 4.13.

Table 4.1: Zircon molar volumes at different temperatures between 300 and 5000 K

Temperature (K)	300	400	500	600	700	800
Molar volume (10^{-5} m^3/mol)	4.04	4.05	4.06	4.07	4.08	4.10
Temperature (K)	900	1000	1100	1200	1300	1400
Molar volume (10^{-5} m^3/mol)	4.11	4.13	4.14	4.16	4.17	4.19
Temperature (K)	1500	1600	1700	1800	1900	2000
Molar volume (10^{-5} m^3/mol)	4.21	4.22	4.24	4.26	4.29	4.31
Temperature (K)	2100	2200	2300	2400	2600	2800
Molar volume (10^{-5} m^3/mol)	4.33	6.77	6.78	6.93	7.00	7.14
Temperature (K)	3000	3400	3800	4200	4600	5000
Molar volume (10^{-5} m^3/mol)	7.09	7.29	7.28	7.45	7.52	7.67

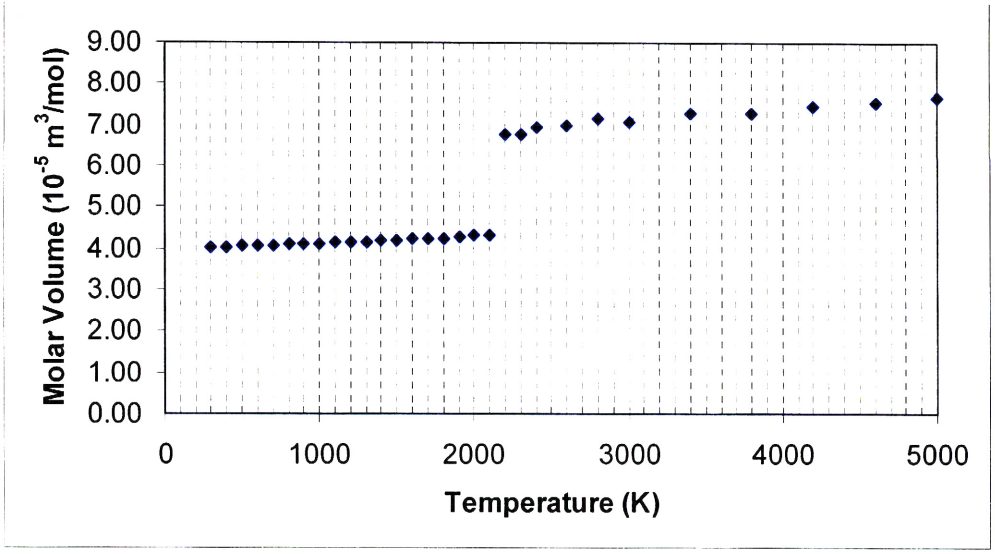

Figure 4.13: Zircon molar volumes at different temperatures between 300 and 5000 K in the NPT ensemble.

In Figure 4.13, the sharp jump in molar volume occurs between 2100 and 2200 K, within the experimental melting temperature range of 2000 ~ 2600 K. Figure 4.14 shows the total RDF plots at 2100 K and 2200 K. We can see that the peaks at long distances disappear in the RDF curve of 2200 K. So using different indicators (molar volume or RDF plot) yields the same melting temperature.

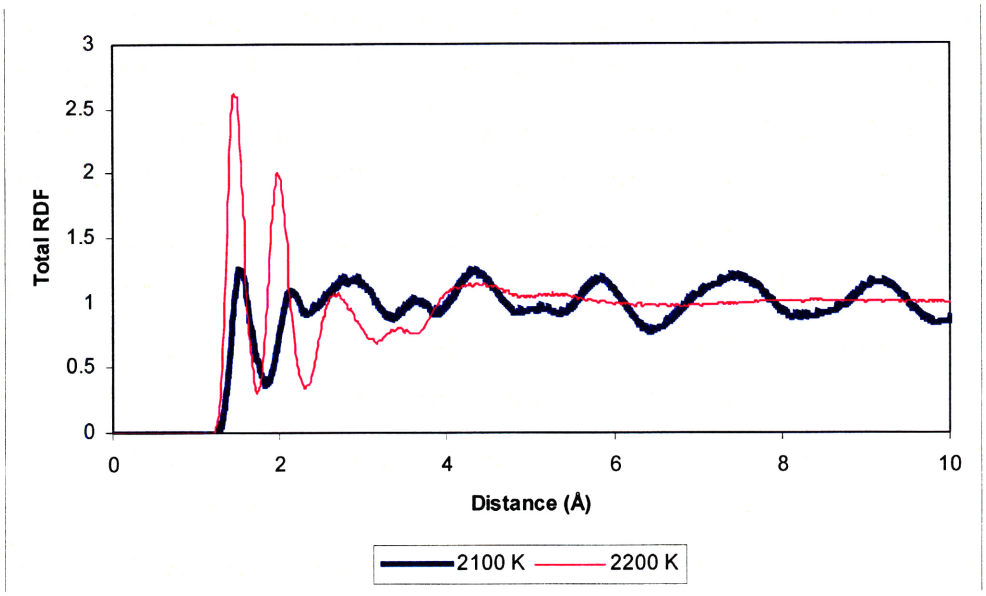

Figure 4.14: Total RDF plots at 2100 K and 2200 K, averaged over last 5 ps of simulations. Peaks at long distances are still present at 2100 K but not at 2200 K.

Repeating the same MD simulations at different temperatures at smaller intervals between 2100 K and 2200 K, the range of melting temperature can be further narrowed down. From the data in Table 4.2 and Figure 4.15, the melting temperature is found to be between 2120 K and 2130 K in our model.

Table 4.2: Zircon molar volumes at different temperatures between 2100 K and 2200 K

Temperature (K)	2110	2120	2130	2140	2150
Molar volume (10^{-5} m^3/mol)	4.34	4.34	6.76	6.71	6.73
Temperature (K)	2160	2170	2180	2190	
Molar volume (10^{-5} m^3/mol)	6.72	6.75	6.69	6.76	

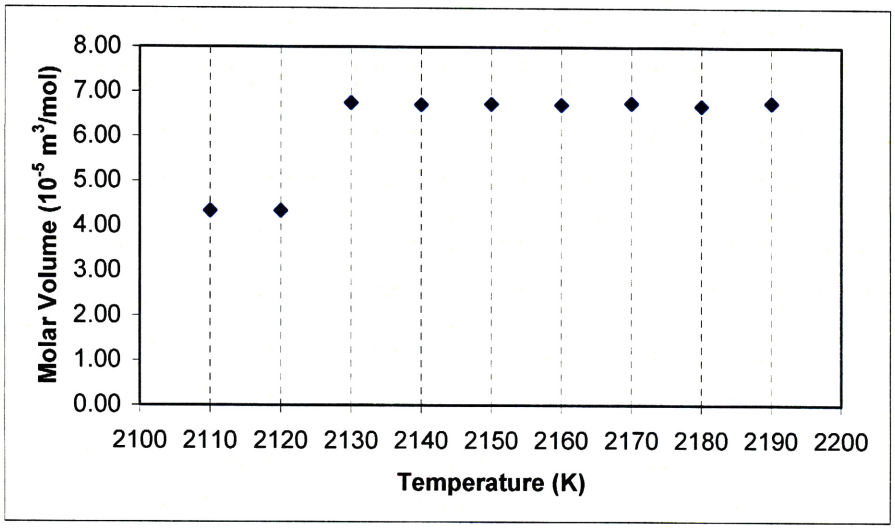

Figure 4.15: Zircon molar volumes at different temperatures between 2110 and 2190 K. The Melting temperature is found to lie between 2120 K and 2130 K.

4.4 Calculation of Zr, Si and O self-diffusion coefficients

There is a well-known relationship between atom mean square displacements and self-diffusion coefficients (see, for example, [14])

$$\frac{d\left\langle \Delta r^2 \right\rangle(t)}{dt} = 6D \Rightarrow \left\langle \Delta r^2 \right\rangle(t) = 6Dt + C, \tag{4.1}$$

where $\left\langle \Delta r^2 \right\rangle(t)$ is the mean square displacement at time t; D is the diffusivity or self-diffusion coefficient; and C is a constant. This relationship indicates that, for constant D, mean square displacement depends linearly on time.

We have calculated mean square displacements for the 300 K and 5000 K simulations in Section 4.2.5. At 300 K, the atoms do not leave their equilibrium sites and no detectable diffusion is present, so we are unable to calculate self-diffusion coefficients from this simulation. At 5000 K when

zircon has melted, however, we indeed saw that the value of mean square displacements increases linearly with time, from which we can calculate self-diffusion coefficients in liquid zircon.

The self-diffusion coefficients for Zr, Si and O were calculated separately. The mean square displacement data in Section 4.2.5 are not directly usable here, because they are average of all types of atoms in the system. The easy remedy is to average over specific species of atoms only. Details for calculating Si self-diffusion coefficient at 3000 K are given here. Calculations for other types of atoms or at other temperatures are similar.

MD simulation of zircon at 3000 K was performed for 20-ps using the NPT ensemble. Mean square displacement (MSD) values of Si at different simulation times were calculated and are shown in Table 4.3.

Table 4.3: Mean square displacements of Si at different simulation times of 3000 K NPT simulation

Time (ps)	0	0.2	0.4	0.6	0.8	1.0	1.2	1.4
MSD ($Å^2$)	0	0.844	1.036	1.041	1.137	1.167	1.279	1.413
Time (ps)	1.6	1.8	2.0	2.2	2.4	2.6	2.8	3.0
MSD ($Å^2$)	1.578	1.629	1.660	1.689	1.747	1.864	1.958	2.041
Time (ps)	3.2	3.4	3.6	3.8	4.0	4.2	4.4	4.6
MSD ($Å^2$)	2.086	2.161	2.143	2.258	2.377	2.347	2.328	2.414
Time (ps)	4.8	5.0	5.2	5.4	5.6	5.8	6.0	6.2
MSD ($Å^2$)	2.543	2.547	2.548	2.618	2.691	2.757	2.749	2.758
Time (ps)	6.4	6.6	6.8	7.0	7.2	7.4	7.6	7.8
MSD ($Å^2$)	2.936	3.117	3.154	3.279	3.332	3.458	3.486	3.563
Time (ps)	8.0	8.2	8.4	8.6	8.8	9.0	9.2	9.4
MSD ($Å^2$)	3.703	3.725	3.700	3.727	3.899	3.886	3.868	3.976
Time (ps)	9.6	9.8	10.0	10.2	10.4	10.6	10.8	11.0
MSD ($Å^2$)	4.191	4.174	4.113	4.296	4.356	4.455	4.593	4.527
Time (ps)	11.2	11.4	11.6	11.8	12.0	12.2	12.4	12.6
MSD ($Å^2$)	4.643	4.714	4.700	4.736	4.790	4.835	4.892	5.136
Time (ps)	12.8	13.0	13.2	13.4	13.6	13.8	14.0	14.2
MSD ($Å^2$)	5.257	5.338	5.372	5.460	5.519	5.611	5.682	5.831
Time (ps)	14.4	14.6	14.8	15.0	15.2	15.4	15.6	15.8
MSD ($Å^2$)	5.854	5.864	5.804	5.844	5.924	5.878	5.815	6.058
Time (ps)	16.0	16.2	16.4	16.6	16.8	17.0	17.2	17.4
MSD ($Å^2$)	6.126	6.287	6.091	6.147	6.454	6.377	6.374	6.543
Time (ps)	17.6	17.8	18.0	18.2	18.4	18.6	18.8	19.0
MSD ($Å^2$)	6.640	6.655	6.626	6.643	6.730	6.923	7.106	7.034
Time (ps)	19.2	19.4	19.6	19.8	20.0			
MSD ($Å^2$)	7.058	7.024	7.045	7.260	7.412			

We can fit the data in Table 4.3 to (4.1) using an implementation of the nonlinear least-squares (NLLS) Marquardt-Levenberg algorithm. Data for $\langle \Delta r^2 \rangle(t)$ are in the rows titled "MSD ($Å^2$)" in Table 4.3, and data for t are in the rows titled "Time (ps)". The fitting results are shown in Table 4.4.

Table 4.4: The results of fitting the data in Table 4.3 to the linear relationship $\langle \Delta r^2 \rangle(t) = 6Dt + C$

Parameter	Value	Standard Error
D (Å^2/ps)	0.0540	± 0.0004 (0.77%)
C (Å^2)	0.950	± 0.0289 (3.04%)

The resulting self-diffusion coefficient D is

$$D = 0.0540 \text{ Å}^2/\text{ps} = 5.40 \times 10^{-10} \text{ (m}^2/\text{s)}$$

The same calculations were done for Zr and O; these results, together with the result for Si, are shown in Table 4.5.

Table 4.5: Calculated self-diffusion coefficients of Zr, Si and O in zircon at 3000 K

Atom Name	Self-diffusion coefficient (10^{-10} m^2/s)
Si	5.40
Zr	2.70
O	5.37

No experimental study of self-diffusion coefficients for Zr, Si or O in zircon exists, so direct comparison with experimental values is not possible. There exist studies of Si and O self-diffusion coefficients in other types of systems, however. For example, Lesher, Hervig and Tinker [15] performed silicon and oxygen self diffusion studies in naturally occurring basaltic liquid between 1593 K and 1873 K. They found that at 1 GPa the self diffusivities for both Si and O are well described by the Arrhenius relationship

$$\ln D^*_{(Si,O)} = (-12.5 \pm 0.2) - (170000 \pm 2000)/RT \,, \qquad (4.2)$$

where T is temperature in K; R is the universal gas constant in J / (K mol) and D^* is the self-diffusion coefficient expressed in units of m^2/s. Using this empirical formula, with R = 8.314 and T = 3000 K, we can calculate D^* to be 4.09 × 10^{-9} (m^2/s). The values in Table 4.5 for Si and O are 5.4 × 10^{-10}

(m^2/s), about 7.6 times smaller.

4.5 Calculation of activation energy for self-diffusion

We calculated the activation energy for self-diffusion from the Arrhenius relationship

$$D = D_0 e^{-\frac{E_{self}}{kT}}, \tag{4.3}$$

where D_0 is a constant; E_{self} is the activation energy for self-diffusion; k is the Boltzmann constant; and T is absolute temperature. This relationship can be rearranged as

$$\ln D = \ln D_0 - \frac{E_{self}}{k}(\frac{1}{T}), \tag{4.4}$$

The signature linear dependence of ln$D$ on inverse temperature ($1/T$) is apparent in 4.4. To calculate the value of E_{self}, we can first calculate diffusivity D at different temperatures, from which we obtain ln$D$ versus ($1/T$) data; a linear fitting yields the value of activation energy E_{self}.

In Section 4.4 we calculated diffusivity D at 3000 K. Diffusivities calculated at other temperatures are shown in Table 4.6.

Table 4.6: Zr, Si and O self-diffusion coefficients at different temperatures

Self-diffusion coefficients (m^2/s)	Atom Name		
Temperature (K)	Zr	Si	O
3000	2.70×10^{-10}	5.40×10^{-10}	5.37×10^{-10}
3400	8.31×10^{-10}	1.53×10^{-9}	1.52×10^{-9}
3800	2.04×10^{-9}	3.63×10^{-9}	3.60×10^{-9}
4200	3.78×10^{-9}	6.95×10^{-9}	6.25×10^{-9}
4600	5.90×10^{-9}	1.06×10^{-8}	9.80×10^{-9}
5000	8.64×10^{-9}	1.54×10^{-8}	1.42×10^{-8}

The Arrhenius plots for obtaining Zr, Si and O self-diffusion coefficients are shown in Figure 4.16, where the linear relationships between ln$D$ and ($1/T$) values are apparent.

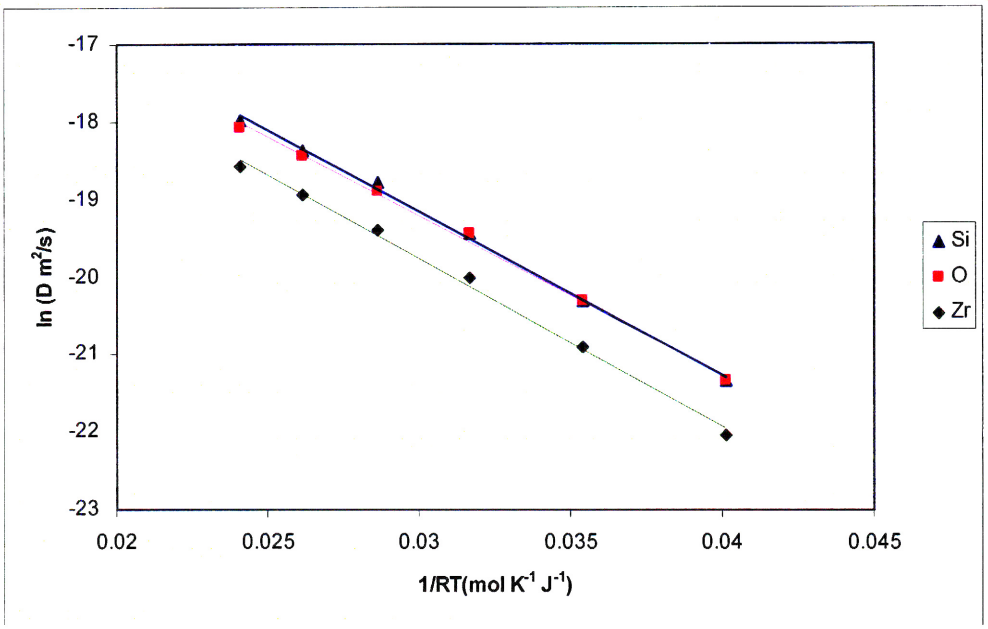

Figure 4.16: Arrhenius plots of Zr, Si and O self-diffusion coefficients.

Activation energies can be determined from the slopes of the lines in Figure 4.16, which, according to (4.1), equal $-E/k$. For example, the slope of the Zr line is -26083, so the activation energy for Zr self-diffusion is

$$
\begin{aligned}
E &= (-k) \times (-26083) \\
&= (-1.381 \times 10^{-23}) \times (-26083) \\
&= 3.602 \times 10^{-19}\ (\text{J}) \\
&= 216.9\ (\text{kJ/mol})
\end{aligned}
$$

Activation energies thus calculated for Zr, Si and O self-diffusion are shown in Table 4.7.

Table 4.7: Activation energies for Zr, Si and O self-diffusion

Atom Name	Activation energy for self-diffusion (kJ/mol)
Zr	216.9
Si	210.8
O	204.7

Geisler *et al.* [16] have performed experimental study of the kinetics of thermally-induced recovery and recrystallization of partially metamict zircon using Raman spectroscopy. They have empirically estimated the activation energy to be E = 2.24 ± 0.04 eV and believe this value is most likely related to recombination of point defects in the crystalline domains of partially metamict zircon. This activation energy is estimated from isothermal frequency curves. Two other activation energy values are reported in the same study: 2.6 ± 0.2 eV, estimated from Raman linewidth changes during transformation; and 3.8 ± 0.4 eV, obtained for epitaxial recrystallization by assuming Johnson-Mehl-Avrami growth kinetics as a first approximation. The authors did not estimate activation energies separately for different atom species, though we may conclude that the kinetics are determined as the slowest diffusing ion species diffusing by the fastest mechanism on its own sub-lattice.

Casting the experimental activation energy value of 2.24 eV into units of (kJ/mol) gives 2.24 eV = 3.589×10^{-19} Joules = 216.1 kJ/mol, close to the self-diffusion activation energies in Table 4.7. Getting realistic self-diffusion coefficients and activation energies for self-diffusion right is important for simulating the defect evolution process after a collision cascade.

4.6 Calculation of heat capacity

This section calculates the heat capacity of zircon at 300 K using MD simulations. There are two commonly used heat capacities: heat capacity at constant pressure C_p and at constant volume C_v. The definitions of them can be found in any good thermodynamics textbook (see, for example, [17]) and amount to

$$C_p = \frac{dH}{dT} \text{ at constant pressure,} \tag{4.5}$$

$$C_v = \frac{dE}{dT} \text{ at constant volume,} \tag{4.6}$$

In calculating C_p, enthalpy H can be calculated using its definition $H = E + PV$, where E is internal energy, P is pressure and V is volume. Constant pressure MD simulations with 1 atm. pressure were performed at 10 K intervals between 270 K and 330 K; relevant results from these simulations are recorded in Table 4.8.

Table 4.8: Data from MD simulations for calculation of C_p at 300 K

Temperature (K)	E (10^{-14} Joule)	P (Pascal)	V (10^{-26} m^3)	$H = E + PV$ (10^{-14} Joule)
270	-1.8198	155040	5.7877	-1.8198
280	-1.8196	100400	5.7893	-1.8196
290	-1.8194	33102	5.7907	-1.8194
300	-1.8191	81995	5.7923	-1.8191
310	-1.8190	115350	5.7939	-1.8190
320	-1.8186	81236	5.7955	-1.8186
330	-1.8185	503.52	5.7970	-1.8185

Figure 4.17 shows enthalpy values of the system at different temperatures, together with the linear fitting.

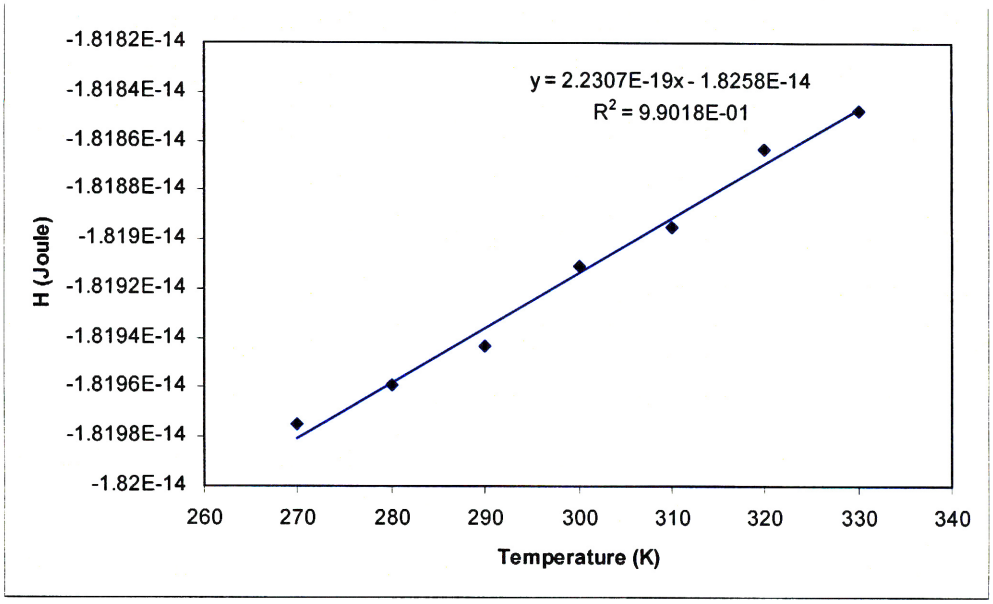

Figure 4.17: Enthalpy H at different temperatures for calculation of C_p.

The slope of the line shown in Figure 4.17 has a slope of 2.231×10^{-19} Joule/K/supercell. Convert the value into units of J/(K mol)

$$C_p = 2.231 \times 10^{-19} \text{ J K}^{-1} \text{ supercell}^{-1}$$
$$= 2.582 \times 10^{-22} \text{ J K}^{-1} \text{ (formula unit)}^{-1}$$
$$= 155.5 \text{ J K}^{-1} \text{ mol}^{-1}$$

The experimental value of C_p is 98.6 J/(K mol) and the C_p value calculated by GULP using the chosen potential is 102.1 J/(K mol) (Table 3.14). The C_p value calculated from MD simulation is thus 50% too large.

Calculation of C_v proceeded analogously. Table 4.9 presents system internal energies at different temperatures from the MD simulations, whose linear fitting is shown in Figure 4.18.

Table 4.9: Internal energies from MD simulations for calculation of zircon C_v at 300 K

Temperature (K)	270	280	290	300
Internal Energy (eV)	-113580	-113570	-113560	-113540
Temperature (K)	310	320	330	
Internal Energy (eV)	-113530	-113520	-113500	

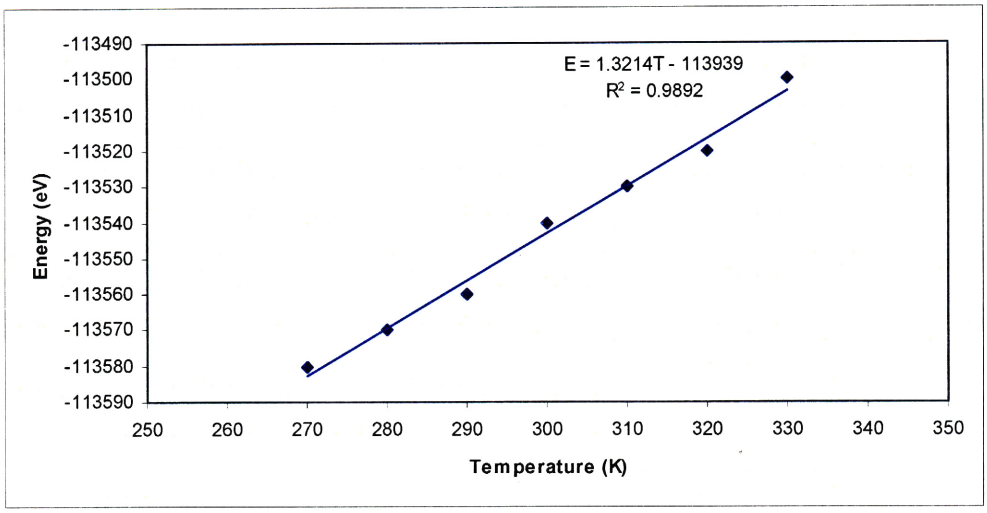

Figure 4.18: Internal energy E at different temperatures for calculation of C_v.

From the slope of the line in Figure 4.18, C_v was found to be

C_v = 1.321 eV K^{-1} supercell^{-1}

= 0.00153 eV K^{-1} (formula unit)$^{-1}$

= 147.6 J K^{-1} mol^{-1}

This value is again about 50% larger than the experimental value. It is smaller than C_p, as expected, but the difference of 7.9 J / (K mol) is much larger than the value of 0.372 calculated from $C_p - C_v = \frac{\alpha^2 TV}{\kappa_T}$ using experimental values in Chapter 3. These discrepancies reflect the limits of our model, as well as the limits of applying GULP's calculations in MD simulations, since we have apparently seen the heat capacities calculated by

GULP and by MD simulations are different. As discussed in Chapter 3, we should not expect to be able to reproduce every conceivable material property using simple two-body potentials and must be satisfied with being able to reproduce the key properties, which we presume to be sufficient for the present purpose.

4.7 Calculation of the coefficient of linear expansion

The coefficient of linear expansion was estimated from volume expansions at different temperatures. We have used values for system molar volume calculated at temperatures between 300 K and 1000 K in 100 K interval, together with the relationship

$$V = V_{300} + V_{300}\,\alpha\,\Delta T, \qquad (4.7)$$

where V is molar volume at a given temperature, V_{300} is molar volume at 300 K, α is the coefficient of linear expansion we wish to calculate, and ΔT is the difference in temperature.

Zircon molar volumes at different temperatures have already been recorded in Table 4.1. Molar volumes from this table in the temperature range from 300 K to 1000 K are plotted in Figure 4.19.

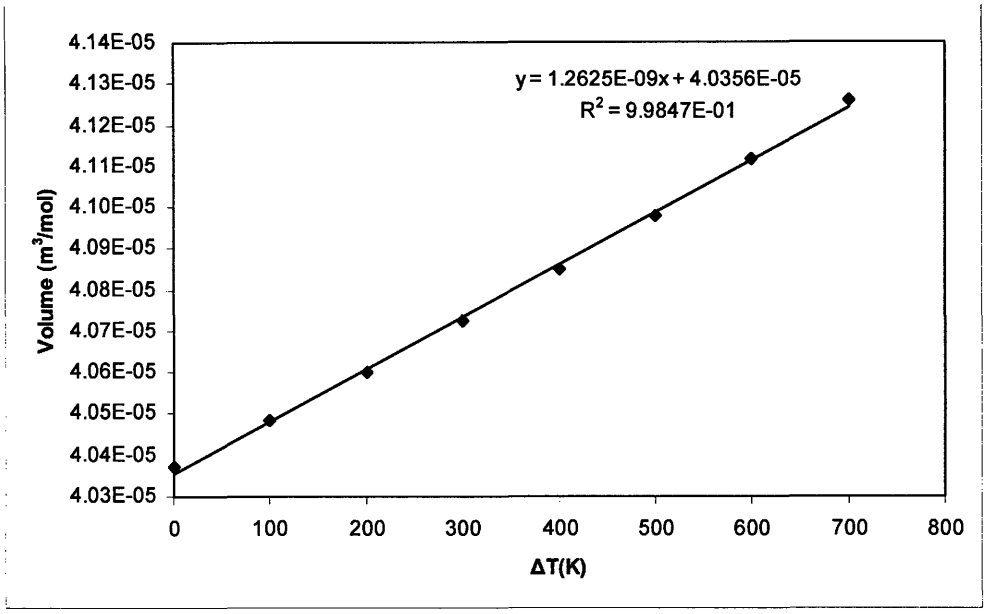

Figure 4.19: Molar volumes at different temperatures for calculation of the coefficient of linear expansion.

The slope of the line in Figure 4.19 is 1.263×10^{-9} m^3 / (K mol), from which the coefficient of linear expansion was calculated to be $\alpha = 3.13 \times 10^{-5} (K^{-1})$. This value is of the same order of magnitude as, but was three times the magnitude of, the experimental value of 1.18×10^{-5} (K^{-1}) [13].

4.8 Simulation of zircon melt-quenching

This section describes how melt-quenching of zircon is accomplished by MD simulation. First, the zircon structure was equilibrated at 300 K for 20 ps using the NPT ensemble, as in previous simulations. The final configuration from this first step was then used as the starting configuration for the next step, simulation at 5000 K for 10 ps.

The volume expansion at 5000 K was anomalously large when the NPT ensemble was used (shown in Figure 4.6 to be about 90%). To overcome

this anomaly (whose origin is discovered in Chapter 6, and a remedy supplied), the NVT ensemble was used for the simulation at 5000 K, with a manually imposed volume expansion. No experimental value of molar volume of "liquid" zircon exists, but the experimentally observed swelling in amorphous zircon is about 18% [18, 19]. To reproduce this swelling we set the volume to be 18% larger than the volume at 300 K by enlarging simulation cell parameters proportionally. If a is changed to $a(1+x)$, b is changed to $b(1+x)$ and c is changed to $c(1+x)$, the volume abc is changed to $abc(1+x)^3$. For the volume expansion to be 18%, $(1+x)^3$ should equal to 1.18, from which x is calculated to be 0.0567. Atom positions were adjusted proportionally after lengths of cell parameters a, b and c are increased.

In addition to the 18% expansion, 8% and 0% (no expansion) were also used. A volume expansion of 8% was used because Devanathan *et al.* [20] found that this swelling corresponds to that in a highly distorted zircon crystal at the onset of amorphization. The structures are topologically different when different volume expansions are imposed, as will be seen in Chapter 7.

After simulating at 5000 K for 10 ps, the system was fast-quenched to very low temperature. The quench was similar to that performed by Devanathan *et al.* [20]. The system was quenched from 5000 K to 30 K over 10 ps, corresponding to a quenching rate of 5.0×10^{14} K/s. The simulation of quenching used a constant volume ensemble so that the volume expansions we manually imposed were unchanged. The DL_POLY code was modified to decrease temperature after every time step in accordance with the chosen quenching rate.

After quenching, the system was equilibrated at 300 K for another 10 ps

using the NVT ensemble. Melt-quenched zircon structures thus obtained were analyzed in Chapter 7, where they are topologically compared to structures of crystalline zircon, liquid zircon and radiation amorphized zircon.

References of chapter 4

[1] M.L. Massie, B.N. Chun and D.E. Culler. The Ganglia Distributed Monitoring System: Design, Implementation, and Experience. Parallel Computing 30, 817 (2004).

[2] W. Smith and T.R. Forester. DL_POLY_2.0: A General-Purpose Parallel Molecular Dynamics Simulation Package. J. Mol. Graphics 14, 136 (1996).

[3] W. Smith, M. Leslie and T.R. Forester. The DL_POLY 2 User Manual. Daresbury Laboratory, Daresbury, England. April, 2003.

[4] W. Smith. The DL_POLY 3 User Manual. Daresbury Laboratory, Daresbury, England. April, 2003.

[5] W. Smith. Molecular Dynamics on Hypercube Parallel Computers. Comput. Phys. Commun., 62, 229 (1991).

[6] W. Smith. Molecular Dynamics on Distributed Memory (MIMD) Parallel Computers. Theoretica. Chim. Acta., 84, 385 (1993).

[7] W. Smith and T.R. Forester. Parallel Macromolecular Simulations and the Replicated Data Strategy: I. The Computation of Atomic Forces. Comput. Phys. Commun., 79, 52 (1994).

[8] W. Smith and T.R. Forester. Parallel Macromolecular Simulations and the Replicated Data Strategy: II. The RD-SHAKE Algorithm. Comput. Phys. Commun., 79, 63 (1994).

[9] M.R.S. Pinches, D. Tildesley and W. Smith. Large Scale Molecular Dynamics on Parallel Computers using the Link Cell Algorithm. Molecular Simulation, 6, 51 (1991).

[10] D.C. Rapaport. Multi-Million Particle Molecular Dynamics: II. Design

Considerations for Distributed Processing. Comput. Phys. Commun., 62, 217 (1991).

[11] W. Butterman and W.R. Foster. Zircon Stability and the ZrO_2-SiO_2 Phase Diagram. Am. Mineral. 52, 880 (1967).

[12] E.M. Levin, C.R. Robbins and H.F. McMurdie. Phase Diagrams for Ceramists. The American Ceramic Society, 1985.

[13] R.S. Carmichael, editor. Handbook of Physical Properties of Rocks, Vol. 3. Boca Raton, Fla.: CRC Press, 1982.

[14] R.W. Balluffi, S.M. Allen and W.C. Carter. Kinetics of Materials. John Wiley & Sons, 2005.

[15] C.E. Lesher, R.L. Hervig and D. Tinker. Self Diffusion of Network Formers (Silicon and Oxygen) in Naturally Occurring Basaltic Liquid. Geochimica et Cosmochimica Acta, 60, 405 (1996).

[16] T. Geisler, R.T. Pidgeon, W.V. Bronswijk and R. Pleysier. Kinetics of Thermal Recovery and Recrystallization of Partially Metamict Zircon: a Raman Spectroscopic Study. European Journal of Mineralogy, 13, 1163 (2001).

[17] H.B. Callen. Thermodynamics and an Introduction to Thermostatistics, 2nd Ed. New York, Wiley, 1985.

[18] B.D. Begg, N.J. Hess, W.J. Weber, S.D. Conradson, M.J. Schweiger, and R.C. Ewing. XAS and XRD Study of Annealed ^{238}Pu- and ^{239}Pu-Substituted Zircons ($Zr_{0.92}Pu_{0.08}SiO_4$). J. Nucl. Mater. 278, 212 (2000).

[19] W.J. Weber, R.C. Ewing and L.M. Wang. The Radiation-Induced Crystalline-to-Amorphous Transition in Zircon. J. Mater. Res. 9, 688 (1994).

[20] R. Devanathan, L.R. Corrales, W.J. Weber, A. Chartier and C. Meis. Molecular Dynamics Simulation of Disordered Zircon. Phys. Rev. B 69, 064115 (2004).

Chapter 5: Collision cascade MD simulations: methodology

This chapter discusses how collision cascade simulations should be conducted. There are many aspects of collision cascade simulations that should be carefully considered. Imprudently chosen parameters can make required computation time of simulation longer than necessary, such as when simulation systems are too large or time step sizes too small. In worst-case scenarios, poorly chosen parameter can render a simulation totally invalid and conclusions based on it meaningless, as will be seen in this chapter.

5.1 Starting zircon structure

Up to now, there are three candidate structures presented that can be used as the starting zircon structure for collision cascade simulations. One is the zircon structure developed from experimental data in Chapter 2. Another is that developed in Chapter 3, the structure resulting from GULP energy minimization of the experimental structure using the chosen empirical potential model. For convenience, we number these two structures #1 and #2, respectively. However, neither of these two was chosen as the starting structure. Instead, we have chosen the third one (referred to as structure #3), the zircon structure after constant-pressure MD simulation at 300 K for 20 ps, starting from structure #2. The three structures are schematically described in Figure 5.1.

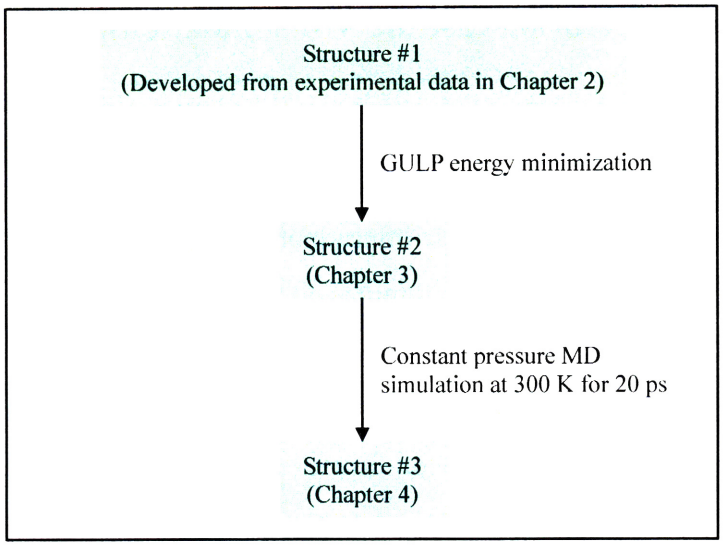

Figure 5.1: Schematic illustration of how the starting structure for collision cascade simulation is obtained.

Structure #1 is the most accurate replicate of the real zircon structure, but it cannot be precisely reproduced using the chosen potential. Structure #2, the minimal-energy structure under the potential, is different from, but very close to, structure #1, as seen in Table 3.12. During this energy minimization process, there are only very limited number of variables that can be changed, which include cell parameters a, b and c, and oxygen position parameters u and v. Atom positions are calculated from these parameters. This GULP energy minimization was performed at 0 K. Once MD simulation is performed on this structure at 300 K, however, every atom begins to vibrate under the constraint of the potential. It is therefore not surprising that structure #3 is slightly different from structure #2. Structure #3 has a volume about 1% larger than that of structure #2, which can be attributed to thermal expansion.

After comprehensive comparisons of dimension, mean square displacement, radial distribution function, *etc.*, it was found in Section 4.2 that the difference between structure #2 and structure #3 is quite small. Zircon

crystal structure connectivity is preserved in structure #3. Structure #3 is a natural choice as the starting structure for collision cascade simulations, because it is the most stable one under the current dynamic potential model.

5.2 Initial velocities of atoms

In MD simulations, the initial velocities of atoms can be generated according to Maxwell-Boltzmann distribution at the specified simulation temperature. Usually, a random number generator is involved in this process. As a result, simulations performed using exactly the same input parameters will not have exactly the same results if initial velocity generation is used; atoms won't have the same velocities and won't be at the same positions during the course of the simulations. Fortunately, one of the beauties of simulation is that physically important properties will not be significantly changed by this uncertainty for any well-performed simulation.

This velocity generation procedure, while necessary when no atom velocities are available at the start of simulation, will be detrimental to collision cascade simulations, where the velocity of the primary knock-on atom (PKA) must be set according to the desired PKA energy and initial direction. A Maxwell-Boltzmann distribution velocity generation will compromise the chosen PKA parameters.

Fortunately, the velocity generation is not needed for our purpose. The structure #3 used as the starting structure for collision cascade simulations is the resulting structure at the end of an MD simulation at 300 K. In addition to the atom positions, atom velocities are also available from this MD simulation and they are the natural choices for the starting atom velocities. Only the PKA velocity then needs to be changed in accordance with the

desired PKA initial energy.

The PKA already has a velocity at the end of the 300 K equilibration simulation. This velocity is simply discarded. A typical particle at 300 K, according to the theorem of equi-partition, will have kinetic energy $\frac{3}{2}kT = \frac{3}{2} \times 8.617 \times 10^{-5} (eV/K) \times 300K \approx 0.039(\text{eV})$, which is indeed negligible comparing to the PKA energies used in collision cascade simulations, which range from about 20 eV up to several keV.

The PKA velocity was calculated from desired initial energy and PKA mass using the simple formula $v = \sqrt{\frac{2E_{Kinetic}}{m}}$. For example, suppose we have chosen to use a Zr atom as the PKA and want the initial PKA energy to be 1 keV; the calculated PKA velocity will be 45993 m/s. The direction of the PKA initial velocity also needs to be chosen. If we want the PKA to have an initial velocity direction of [100], for example, the initial PKA velocity vector is then (45993 m/s, 0, 0).

The PKA velocity will change during the course of the simulations, as will velocities of all other atoms in the system. In the ideal situation, the velocities of atoms within or near the collision cascade should change only through influence of other atoms under the chosen potential, following Newton's equations. There are two places in the code where atom velocities can be changed artificially: one is the above-mentioned initial velocity generation using the Maxwell-Boltzmann distribution; the other is when atom velocities are rescaled to keep the system at a desired temperature. Both of these velocities changes must be suppressed or carefully changed in such a way that velocities of the PKA and other atoms involved in the

collision cascade are not affected. Thus the velocity rescaling mechanism provided by DL_POLY, which scales velocity of every atom in the system, cannot be used. In this study, the DL_POLY code was modified to suppress both the initial velocity generation and the velocity rescaling. This means, however, that we needed to find other means to control system temperature. Section 5.5 provides further details.

5.3 Choosing the PKA

The chemical compositional formula for zircon is $ZrSiO_4$. U and Th replace Zr at low concentrations (up to 5000 ppm) in naturally occurring zircon. In general, more highly-substituted compositions $(Zr,A)SiO_4$ can also be synthesized, where A can be Hf, Th, Pa, U, Np, Pu and Am.

In the context of nuclear waste confinement, Zr can be replaced with radioactive nuclear waste isotopes we want to confine. For example, zircon with 9.2 at.% Zr replaced by plutonium (8.1% ^{238}Pu; 1.1% ^{239}Pu) has been synthesized [1, 2]. This represents a waste loading of about 10 wt.% Pu.

Most zircon structural damage comes from the recoil heavy ion produced by α-decay events of incorporated radioactive isotopes. For example, a typical α particle produced by an average α-decay event within the ^{238}U decay series has energy from 4.5 to 7.5 MeV, and displaces less than about 100 atoms. The recoil nucleus, however, has energy of about 100 keV or less but displaces thousands of atoms [3].

We can choose a Zr, Si or O atom as the PKA. Because Zr sites are those the incorporated nuclear waste isotopes occupy, most of the time a Zr atom was chosen as the PKA in this study. Some authors (e.g. Trachenko *et al.* [4])

have used U as the PKA, on the grounds that this substitution represents the most realistic simulation of the actual recoil event when zircon is used to confine plutonium isotopes. U is much heavier than Zr, so there are some differences between the cascades produced by a U PKA and by a Zr PKA, even with the same energy. We have also used U as the PKA in this study by replacing one of the Zr atoms in the system with U. However, potentials have not been developed for U-O, U-Si and U-Zr interactions, so we have decided to use Zr potentials. That is, we have assumed U-O, U-Si and U-Zr interactions that are the same as Zr-O, Zr-Si and Zr-Zr interactions, respectively. U is treated as a "super-mass" Zr.

To minimize the system size required to contain the radiation event, we choose a Zr atom on one side of the simulation box and give it an initial velocity toward the center, as shown in Figure 5.2.

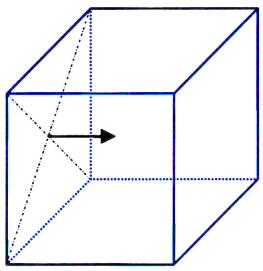

Figure 5.2: Location and initial velocity direction of the PKA. The PKA locates at the tail of the arrow, which shows the initial direction of PKA velocity. (The PKA needs to be moved away from simulation box boundary after energy removal is introduced there. Section 5.6 provides details.)

The desired location for the PKA is the center of the left boundary plane of the simulation cell. Of course in most cases there is no atom of the desired PKA type at exactly that location, in which case an atom of the same type nearest to that location is used. This is not the final configuration, however. After a heat bath is introduced at the simulation cell boundary as an energy

removal mechanism, the PKA must be moved away from where temperature is controlled. Section 5.6 provides details.

5.4 Choosing time step size

In Chapter 4 we have used a time step size of 1 fs (10^{-15} seconds) without much discussion or justification. We tested the simulations conducted in that chapter from different points of view: system temperature was shown to be controlled at the desired level; system total internal energy was found to behave normally and was conserved when velocity rescaling was turned off; physical properties derivable from the simulations were found to be reasonable compared to experimental values, *etc.* Although by no means a direct proof that the conducted simulations were valid, the generally good agreement between simulation and experimental properties confirms the physicality of the simulations. However, unphysical simulations can occur if unthinking choices of simulation parameters, such as the 1 fs time step size, are made.

To illustrate the problem of using too large a time step size, we have carried out an MD simulation with a 1-keV Zr PKA using 2 fs as the time step size. As before, a 6×6×6 supercell was used with 5184 atoms inside. A Zr atom near the center of simulation box's left boundary was chosen as the PKA and was given an initial velocity in the [100] direction (toward the right in Figure 5.2). The PKA had an initial velocity of (45993 m/s, 0, 0), corresponding to a 1-keV Zr PKA traveling in the [100] direction. The DL_POLY code was modified to suppress initial velocity generation. A constant volume, constant energy ensemble was used for the simulation.

Normally, one needs to run a simulation long enough so that the system is

stabilized. Most of the simulations in Chapter 4 were run to either 10 or 20 ps. From Figures 4.2, 4.3, 4.4 and 4.5, we have seen that system properties change little toward the end of the simulations (in fact, in the cases illustrated, the systems have stabilized long before the full 10 or 20 ps simulation times). How to determine when it is safe to stop the collision cascade simulations is discussed in Section 5.8. In this study, we have run most of the simulations to 10 ps. This time is extended if, at the end of the 10 ps simulation, we find that the system is not stable enough by the criteria given in Section 5.8.

However, here we simulate the system for just 1.0 ps, which is sufficient to manifest the problem we want to describe. Figure 5.3 shows the zircon structure achieved after the 1.0 ps of simulation, where the crystalline structure is found to be totally destroyed. Something must have gone wrong since a 1-keV Zr PKA shouldn't be so destructive.

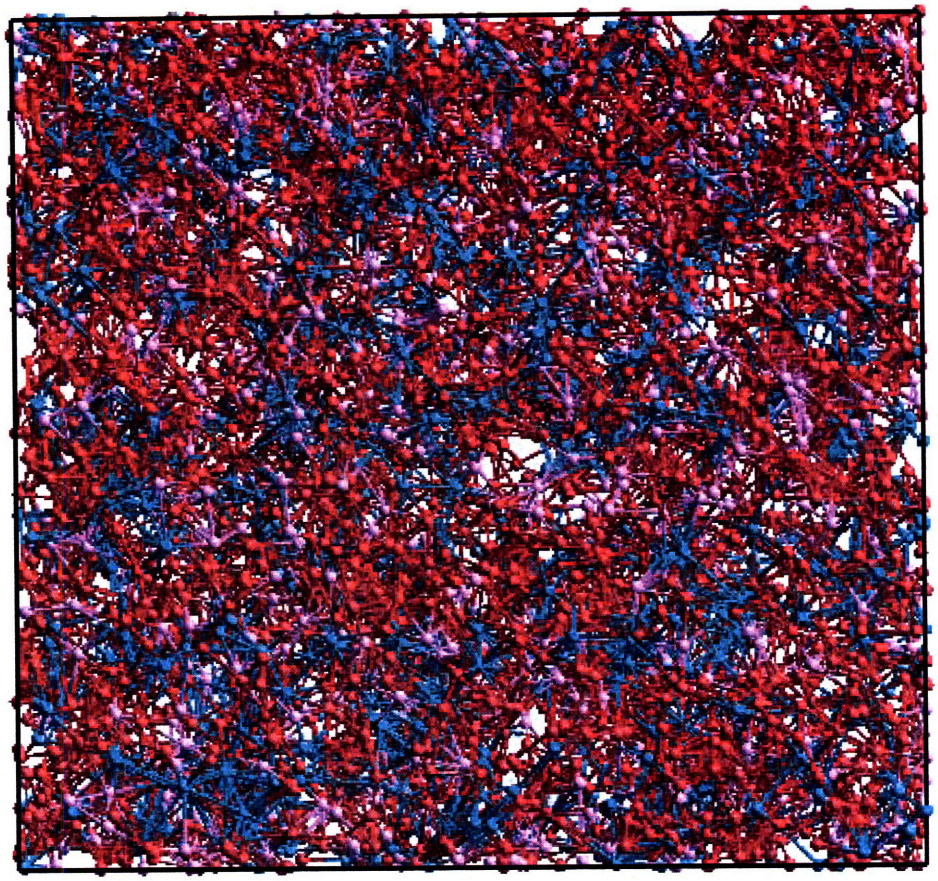

Figure 5.3: Zircon structure after 1.0 ps of invalid MD simulation with a 1-keV Zr PKA using a 2 fs time step. This time-step size is too large.

It is very instructive to plot the curve of system total energy against simulation time. Figure 5.4 shows system total energy in the first 0.04 ps of this invalid simulation. Figures 4.3 and 4.4 have shown what system total energy against simulation time curves should look like for valid MD simulations.

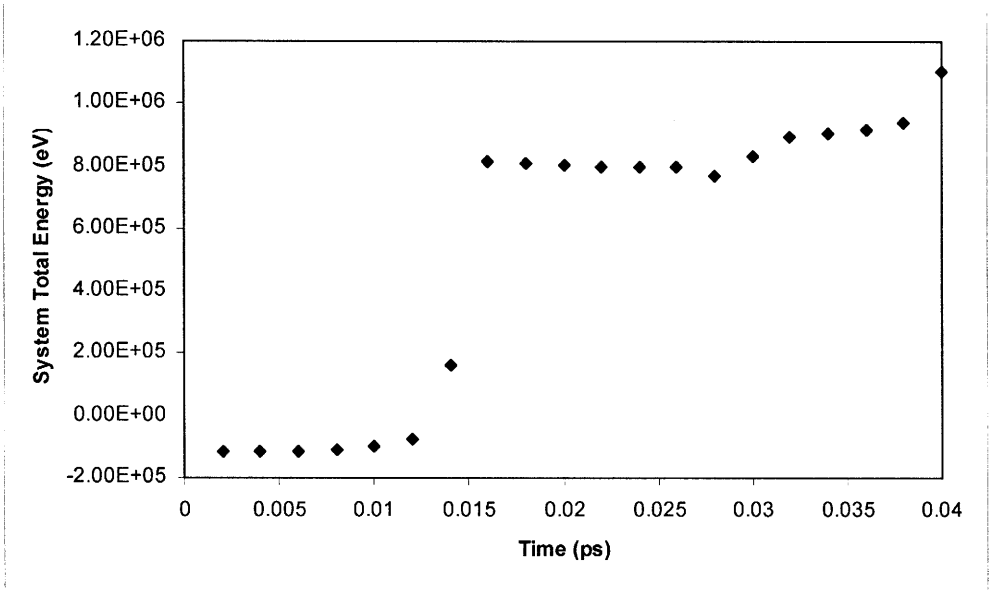

Figure 5.4: System total energy in the first 0.04 ps of an invalid MD simulation with a 1-keV Zr PKA using a 2 fs time step. This time-step size is too large.

Initially, the system total energy has a value of about -1.13×10^5 eV. A negative energy is necessary for a system to be stable. However, as can be seen from Figure 5.4, at about 15 fs system total energy suddenly increases to about $+8 \times 10^5$ eV. This is very abnormal. In fact, system total energy increase doesn't stop there. Figure 5.5 shows evolution of the system total energy over the full 1.0 ps of the simulation.

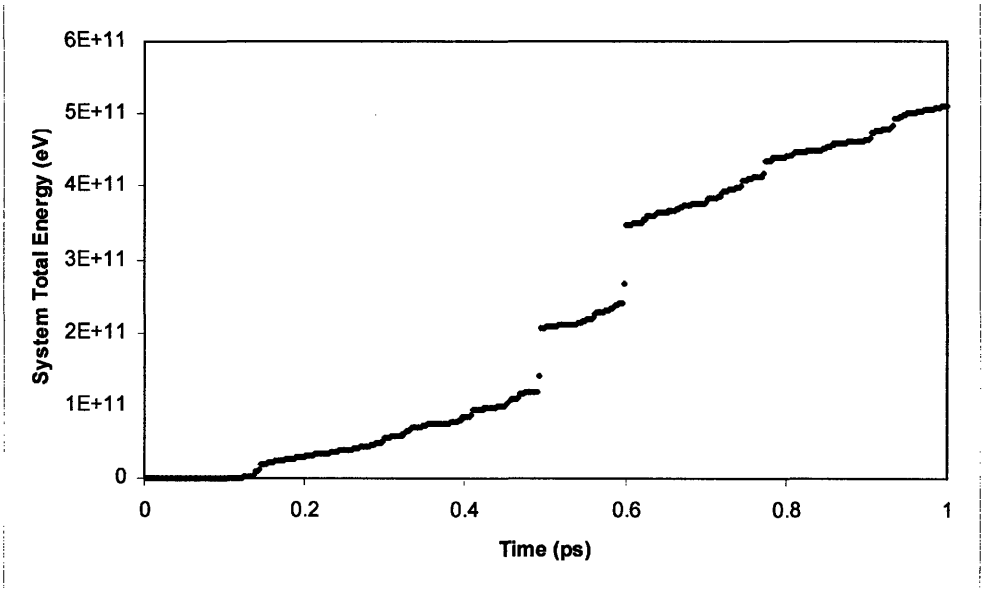

Figure 5.5: System total energy in the first 1.0 ps of invalid MD simulation with a 1-keV Zr PKA using a 2 fs time step. This time-step size is too large.

At the end of the 1.0-ps simulation, the system total energy has increased to more than 5.0×10^{11} eV and has shown no sign of stopping. For a valid simulation, system total energy should be conserved at about -1.13×10^{5} eV, since a constant energy ensemble is used. In reality, some small fluctuations are probably inevitable and are acceptable, but the huge increases seen in Figures 5.4 and 5.5 are a clear sign of trouble.

In addition to total energy, it is also very instructive to have a look at system temperatures at different simulation times. Figure 5.6 shows system temperature during the first 0.04 ps of simulation.

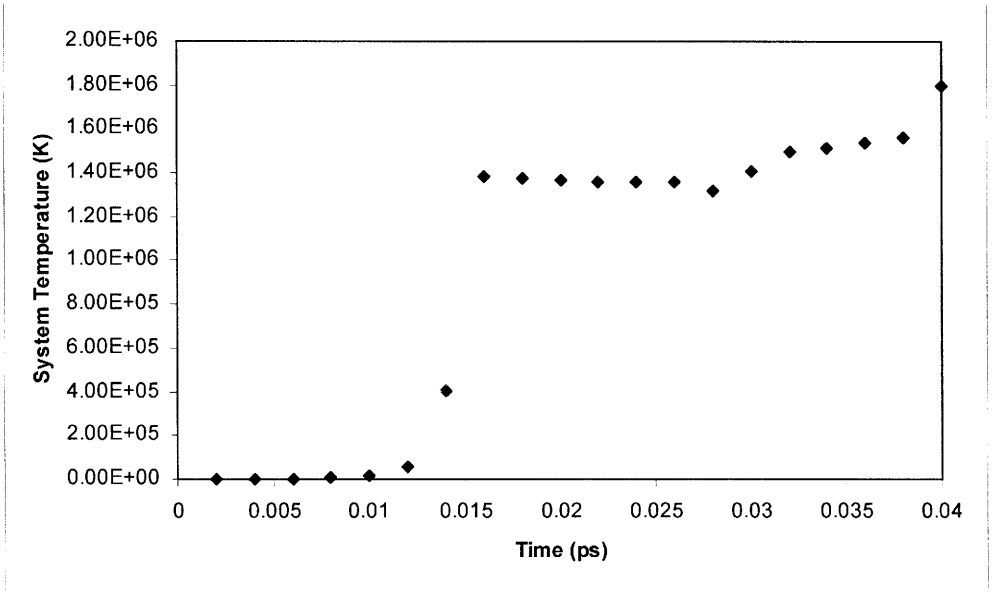

Figure 5.6: System temperature in the first 0.04 ps of invalid MD simulation with a 1-keV Zr PKA using a 2 fs time step. The time-step size is too large.

The system temperature suddenly increases to about 1.4×10^6 K at about 15 fs, and continues to increase from this absurdly high value, as shown in Figure 5.7.

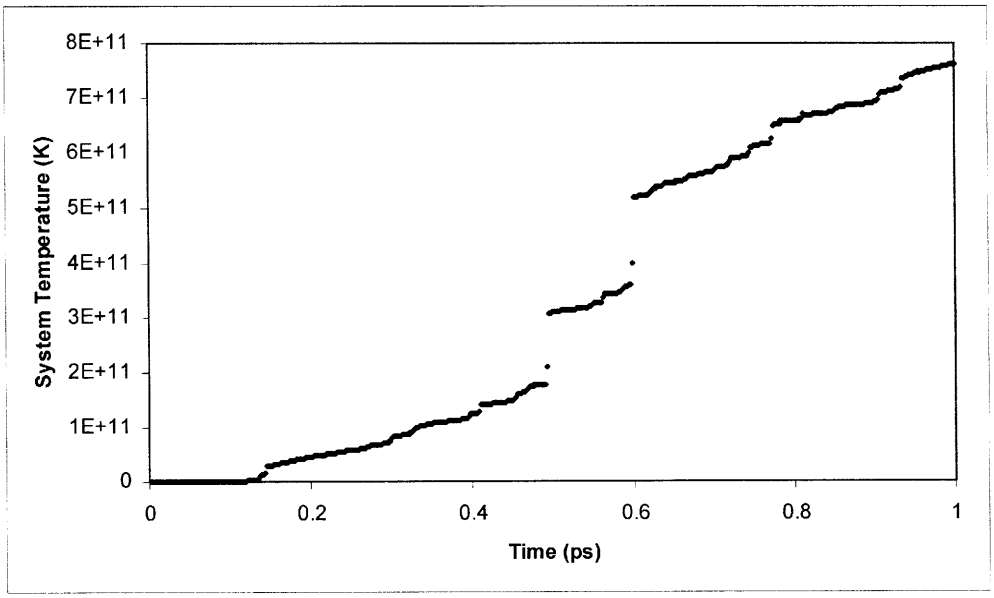

Figure 5.7: System temperature in the first 1.0 ps of invalid MD simulation with a 1-keV Zr PKA using a 2 fs time step. The time-step size is too large.

The similar trends in system temperature and system total energy shown in Figures 5.6 and 5.7 arise because they are correlated. In MD simulations, temperature is calculated from kinetic energies of atoms, which are of course components of the total energy. Kinetic energy turns out to be the dominant component of the total energy in this specific case, which is why total energy and system temperature curves have the same shape. Figure 5.8 shows system configurational energy. We can see that system configurational energy is of the order of 10^5 eV, indeed negligible compared to the total energy, which is of order 10^{11} eV. System configurational energy has increased from the initial -1.1×10^5 eV value to about 4.0×10^5 eV, another sign that the system has blown up and the simulation is invalid.

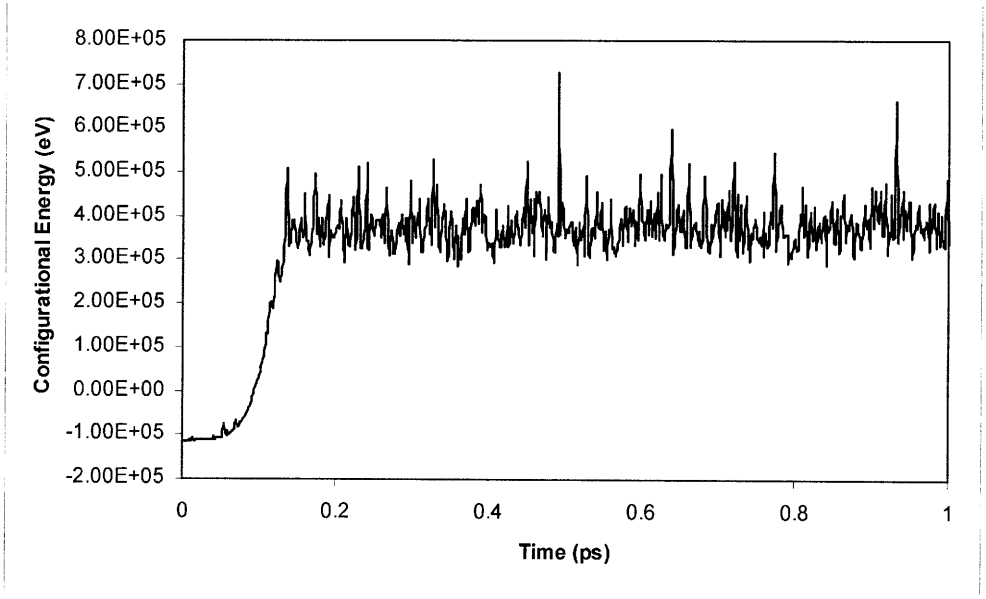

Figure 5.8: System configurational energy in the first 1.0 ps of invalid MD simulation with a 1-keV Zr PKA using a 2 fs time step. The time-step size is too large.

To see how simple it is to remedy this problem, we perform the same simulation again using a time step size of 1 fs. It is surprising how much

difference it makes by simply halving the time step size. The total number of time steps run was doubled so that the total simulation time was still 1.0 ps. Figure 5.9 shows the system structure after this 1.0-ps simulation.

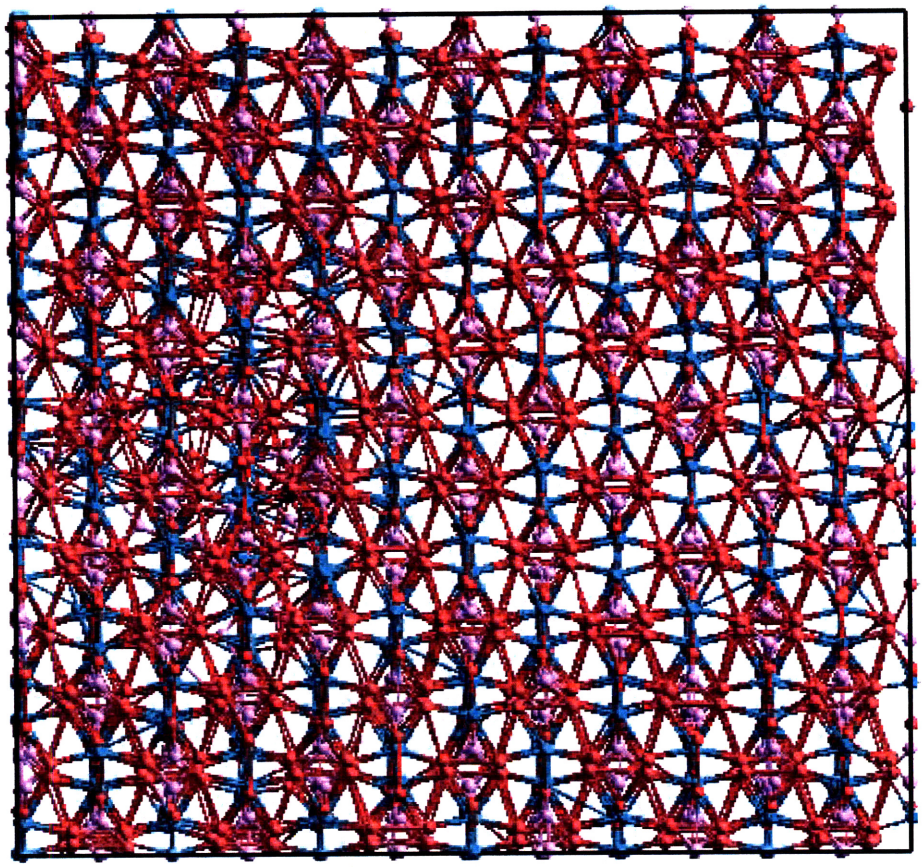

Figure 5.9: Zircon structure after 1.0 ps of MD simulation with a 1-keV Zr PKA using a 1 fs time step. The resulting configuration should be compared to that in Figure 5.3.

Since the PKA was started from the center of left boundary and has an initial velocity toward right, most of the structural changes are in the left part of Figure 5.9. The zircon crystalline structure in the remaining regions appears to be intact.

The system total energy and temperature at different simulation times are shown in Figures 5.10 and 5.11, respectively

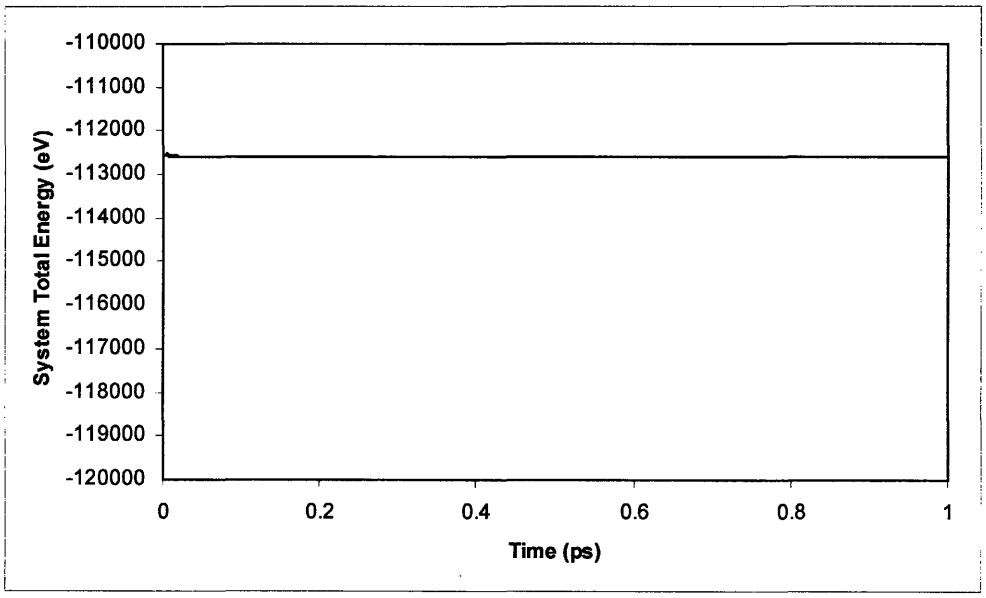

Figure 5.10: System total energy in the first 1.0 ps of MD simulation with a 1-keV Zr PKA using a 1 fs time step. This figure should be compared to Figures 5.4 and 5.5. The initial perturbation of total energy would disappear if a smaller time step size were used, so that the fastest atom in the system travels no more than about 0.1 Å in one time step, in accordance with the criterion for choice of time step specified later.

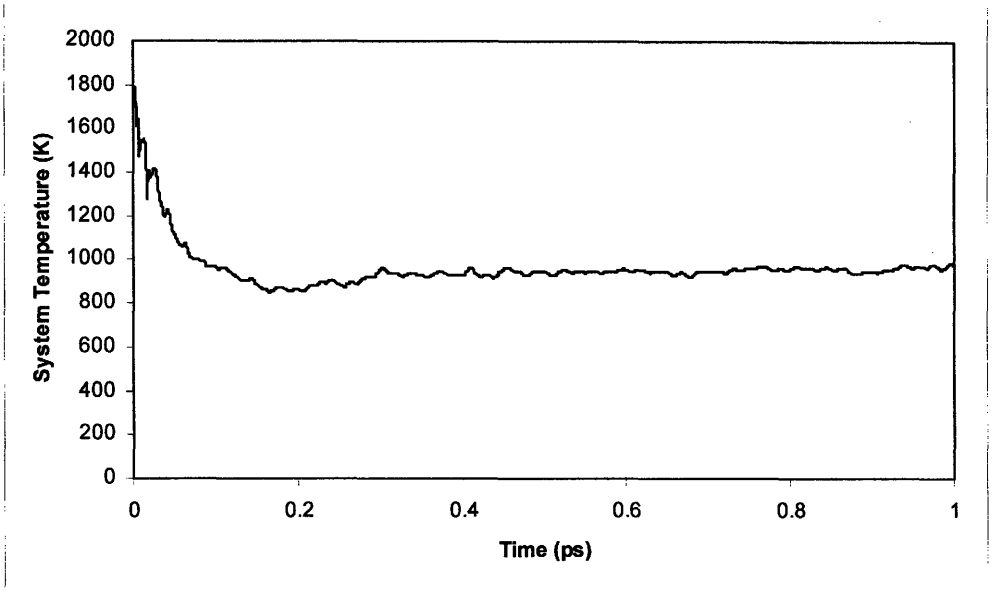

Figure 5.11: System temperature in the first 1.0 ps of MD simulation with a 1-keV Zr PKA using a 1 fs time step. This figure should be compared to Figures 5.6 and 5.7.

In Figure 5.10, the system total energy stabilized quickly at about -1.125 × 10^5 eV. This is the behavior we would expect for a valid simulation. The temperature changes in Figure 5.11 are more interesting. As discussed in Section 5.2, we started the simulation using atom velocities at the end of the 20-ps MD simulation at 300 K, except the velocity of the PKA. The system temperature should remain at 300 K if nothing were changed. However, because the PKA is given extra energy and we have not provided any temperature controlling mechanism, the system temperature is expected to increase. This is indeed what has happened, in Figure 5.11.

The system temperature started from about 1800 K and gradually stabilized toward a value between 900 and 1000 K, all of which are well above the initial 300 K. At 300 K, a typical atom will have kinetic energy of 3/2 kT ~ 0.039 (eV). If the 1 keV energy of the PKA were to be distributed evenly among all 5184 atoms in the system, each atom would gain an energy of

1000/5184 ~ 0.193 eV. This is (0.193 / 0.0388) ≈ 5 times the average atom kinetic energy at 300 K. From this rough estimate, the initial system average temperature should be 300 + 5 × 300 = 1800 K, in agreement with what appears in Figure 5.11. During the course of system evolution, some kinetic energy is transferred to configurational energy and stored in the structure. As a result, the system average temperature decreases.

Figure 5.12 shows the evolution of system configurational energy with simulation time. The configurational energy stabilizes at a negative value, signaling a stable system. The initial configurational energy was about -113740 eV, and final configurational energy about -113230 eV. The increase is 510 eV, so roughly half of the PKA energy (1 keV) is stored in the structure.

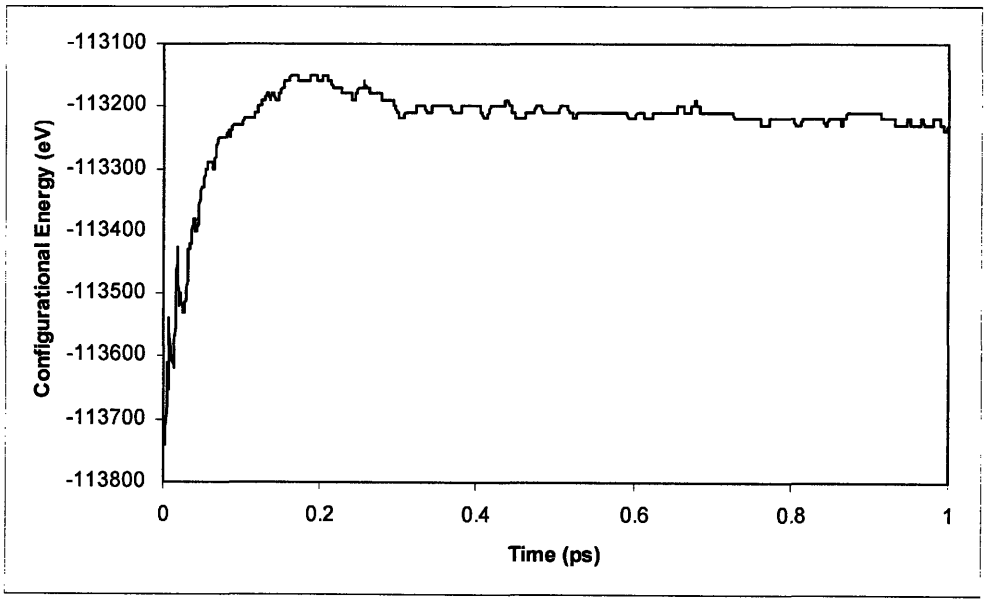

Figure 5.12: System configurational energy in the first 1.0 ps of MD simulation with a 1-keV Zr PKA using a 1 fs time step. This figure should be compared to Figure 5.8.

We have just seen that the simulation using a 1-keV Zr PKA is made valid

by reducing time step size from 2 fs to 1 fs. Choosing a time step size of 1 fs, however, is not always going to result in a valid simulation. To demonstrate this, the same simulation was performed once again, but with PKA energy increased to 5 keV. The time step size used was, again, 1 fs. All other parameters were the same as before. The simulation was found to be invalid: the system final structure shows a complete destruction of crystalline lattice, similar to what is shown in Figure 5.3; the system total energy and temperature increase to absurdly high values, similar to the trends shown in Figures 5.4, 5.5, 5.6 and 5.7; the system configurational energy becomes positive, similar to what's shown in Figure 5.8.

It is not very difficult to explain what went wrong. The 1-keV Zr PKA has an initial velocity of 45993 m/s, so when a time step size of a 2 fs is used, it can travel $45993 \times 2 \times 10^{-15} \approx 0.92$ Å in a single time step; the 5-keV Zr PKA has an initial velocity of 102843 m/s, so when a time step size of 1 fs is used, it can travel about 1.03 Å in a single time step. These distances, 0.92 and 1.03 Å, are comparable to interatomic distances in crystalline zircon. For example, in zircon the Si-O bond length is 1.62 Å and Zr-O bond length is 2.13 Å. Traveling such a large distance in one single time step is the root cause of all the anomalous behavior. MD simulations are essentially to solve Newton's equations discretely for 3-D multi-body systems. A fine grid partition of time *and* space is a necessity for the discrete solution to be numerically close to reality. The partitions using 2 fs as time step size in the 1-keV Zr PKA simulation and 1 fs as time step size in the 5-keV Zr PKA simulation are obviously too coarse when a particle can travel about 1 Å in a single time step. For the simulations to be accurate, atoms need to have opportunities of adjusting their trajectories more often than that.

Choosing a smaller time step size can solve the problem. For the 1-keV Zr

PKA case, we have seen that simply halving the time step size from 2 fs to 1 fs enables a valid simulation to be made. After the change, the PKA initially can travel about 0.5 Å in a single time step. 0.5 Å could still be too large in some cases. For example, we expect system total energy to be conserved when a constant energy ensemble is used. However, we can clearly see some perturbations in the initial part of the system total energy curve in Figure 5.10. A further decreasing in time step size will eliminate these fluctuations. An empirical rule for a valid zircon cascade simulation is that *the fastest atom in the system can travel no more than about 0.1 Å in any single time step.*

For the simulation of 5-keV Zr PKA, which has an initial speed of 102843 m/s, the above-mentioned rule demands a time step size of $\frac{0.1\times10^{-10}}{102843}\approx 0.1\,\text{fs}$ or less. Choosing a time step size of 0.1 fs indeed makes the simulation valid. System total energy, temperature and configurational energy curves look similar to those in Figures 5.10, 5.11 and 5.12. The system total energy conservation is perfect up to the simulation's numerical limit: the total energy remains at -108540 eV throughout the entire simulation. This behavior can be compared to that in Figure 5.10, where the system total energy has some perturbations initially. The conservation is not perfect in Figure 5.10 because initially the PKA can still travel about 0.5 Å in a single time step. If we were to decrease the time step such that the PKA can travel only about 0.1 Å in a single time step, the total energy conservation would be perfect. We can also see that, in Figure 5.10, the total energy conservation is very good after the initial part of the simulation. This can be explained by the fact that the velocity of the PKA is reduced very quickly. After some very short time, the fastest atom in the system has a velocity much smaller than the initial PKA velocity, so even though the time step

size is unchanged, the distance the fastest atom in the system can travel in a single time step has decreased dramatically, to a value much less than 0.1 Å. That's why the energy conservation turns out much better in latter part of that simulation.

In collision cascade simulations, using only one time step size is never the optimal choice. Table 5.1 shows the total number of time steps necessary to make 10 ps of MD simulation for different Zr PKA energies. For more energetic PKAs, a larger simulation cell is needed to contain the collision cascade, in addition to a smaller time step size, both of which contribute to longer computation time. For simulation using a 10-keV Zr PKA, a simulation supercell size of at least 12×7×7 (total of 14112 atoms) is required. On our computational facility, for a 12×7×7 supercell every 1,000 time steps of simulation costs about 16.8 hours of computation time. The 145442 time steps required to run 10 ps thus requires a computation time of about 2443 hours, or about 100 days, which is unacceptably long.

Table 5.1: Total number of time steps necessary to carry out a 10 ps of MD simulation using the time step size required by the empirical rule

Zr PKA Energy (keV)	Zr PKA Speed (m/s)	Required time step size according to the empirical rule (fs)	Total time steps needed to run 10 ps of MD simulation
0.1	14544	0.69	14,544
0.5	32522	0.31	32,522
1	45993	0.22	45,993
5	102843	0.10	102,843
10	145442	0.07	145,442

Fortunately, we do not need to stick with the small initial time step size. Figure 5.13 shows the velocity of the fastest atom of the simulation using a 1-keV Zr PKA. The velocity of the fastest atom decreased quickly from 45993 to less than 10000 m/s within less than 0.1 ps, at which time a time

step size of 1 fs is sufficiently small. Thus an effective way to keep computation time short is to use different time step sizes at different stages of the simulation – a variable time step. In this study, time step size used is never greater than 1 fs.

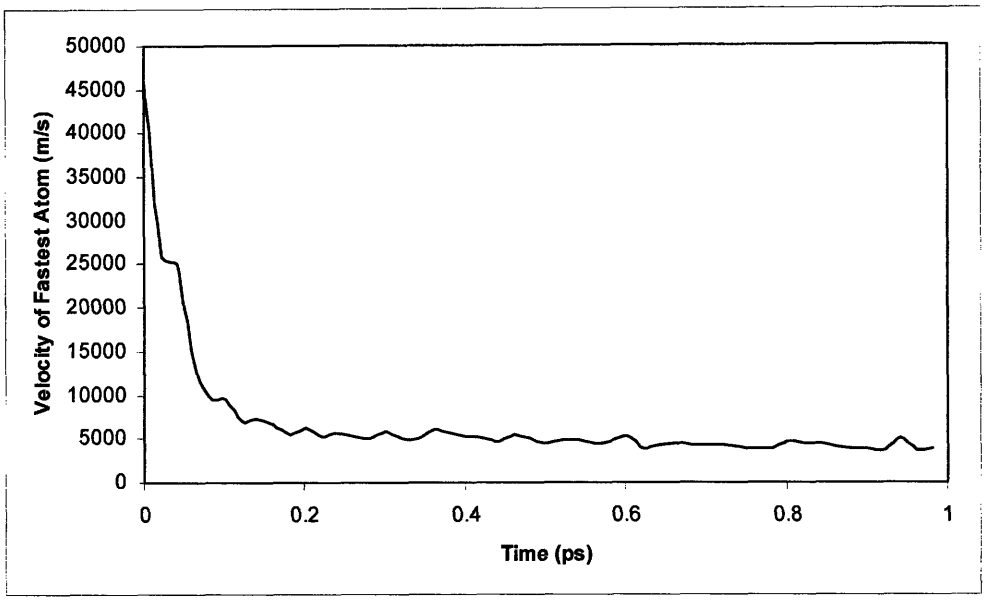

Figure 5.13: Velocity of the fastest atom of in a simulation using a 1-keV Zr PKA.

5.5 Energy removal at boundary of simulation cell

As seen in Figure 5.11, the system temperature stabilized between 900 and 1000 K in the MD simulation using 1-keV Zr PKA. However, for the simulation using the 5-keV Zr PKA, the final system temperature was about 3500 K, which is above the melting point of zircon. The structure will melt, making it very difficult, if not impossible, to isolate structural changes brought about by the collision cascade initiated by the PKA. This shows the necessity of having a control mechanism to keep the system temperature in check, by either enlarging simulation cell size or somehow removing the

excess energy from the system.

Velocity rescaling is the mechanism used to control temperature in MD simulations. The original velocity rescaling algorithm comes with DL_POLY, which rescales velocities of every atom in the system, is suppressed so that velocities of the PKA and other atoms in or near the collision cascade do not dominate the rescaling and are not altered by the rescaling. However, because no other temperature controlling mechanism is present, the extra energy brought in by the PKA will increase the overall system temperature. A 5-keV Zr PKA introduced into a 6×6×6 supercell is able to increase the system temperature from 300 K to about 3500 K, higher than zircon's melting point.

There are at least two methods to solve this problem. One is to increase system size so that the extra energy brought in by the PKA has less influence on the overall system. But of course, larger systems would mean longer computation time. For example, Devanathan *et al.* [5] used a simulation cell that contains about 20 atoms per eV of PKA energy. The temperature rise of the simulation cell as a result of the extra energy of the PKA is about 200 K in this particular setting. The initial temperature of their simulation cell is 30 K, so the end temperature is near the room temperature. Their scheme, however, is too computationally demanding to be adopted in this study. In Chapter 6, our simulation with 5-keV Zr PKA uses a simulation cell of 12,936 atoms (11×7×7 supercell), yet still requires about 1 week to finish. According to their methodology, a simulation with a 5-keV PKA would require a simulation cell with 10^5 atoms, which is about 8 times the number of atoms in our simulation cell, and would require roughly 60 times as long to finish the same simulation, since the computational time needed is found to scale roughly as N^2, where N is the number of atoms in

the system. Devanathan and co-workers have a 1960-processor massively parallel computer in the Environmental Molecular Sciences Laboratory at Pacific Northwest National Laboratory, whereas we have only about 30 processors at our disposal.

Another method is to carefully remove from the system the extra energy brought in by the PKA in such a way that the collision cascade is not significantly influenced. In this study, energy was removed from the simulation cell boundary. A 2-Å layer at each of the six sides of the simulation cell was kept at constant temperature using velocity rescaling. This is the same velocity rescaling algorithm used to keep the entire system under constant temperature by DL_POLY (which is suppressed in collision cascade simulations), but confined to the atoms in the boundary layers only. Of course, the PKA initial position, previously located right at the boundary, needs to be changed; otherwise, the PKA will inevitably be influenced by the newly introduced temperature control. Details are provided in Section 5.6.

The interatomic distances in zircon are about 2 Å, so there is only about one layer of atoms under temperature control. The effectiveness of controlling only one layer of atoms is remarkable, as can be seen below. Cascade simulations using 5-keV Zr PKA were performed with and without boundary temperature control; the resulting system temperatures are compared in Figure 5.14.

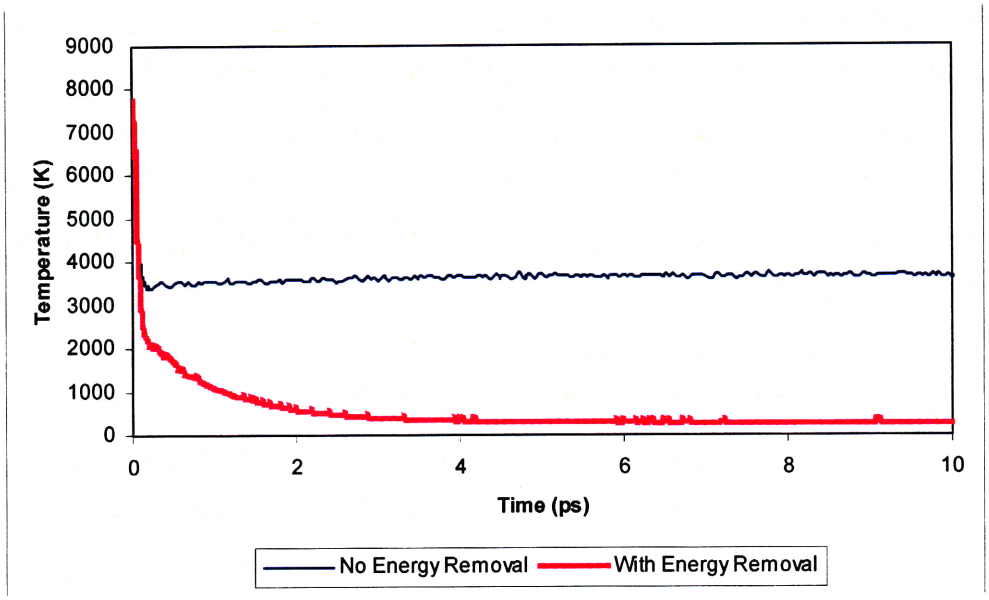

Figure 5.14: System temperatures of MD simulations using a 5-keV Zr PKA, both with and without boundary energy removal.

System temperature is kept successfully at 300 K when energy removal is applied. This has a profound influence on the final structure, because 300 K is below melting point, whereas 3500 K (the system final temperature when energy removal is not used) is well above melting point. The structural differences can be appreciated by comparing Figure 5.15 to Figure 5.16.

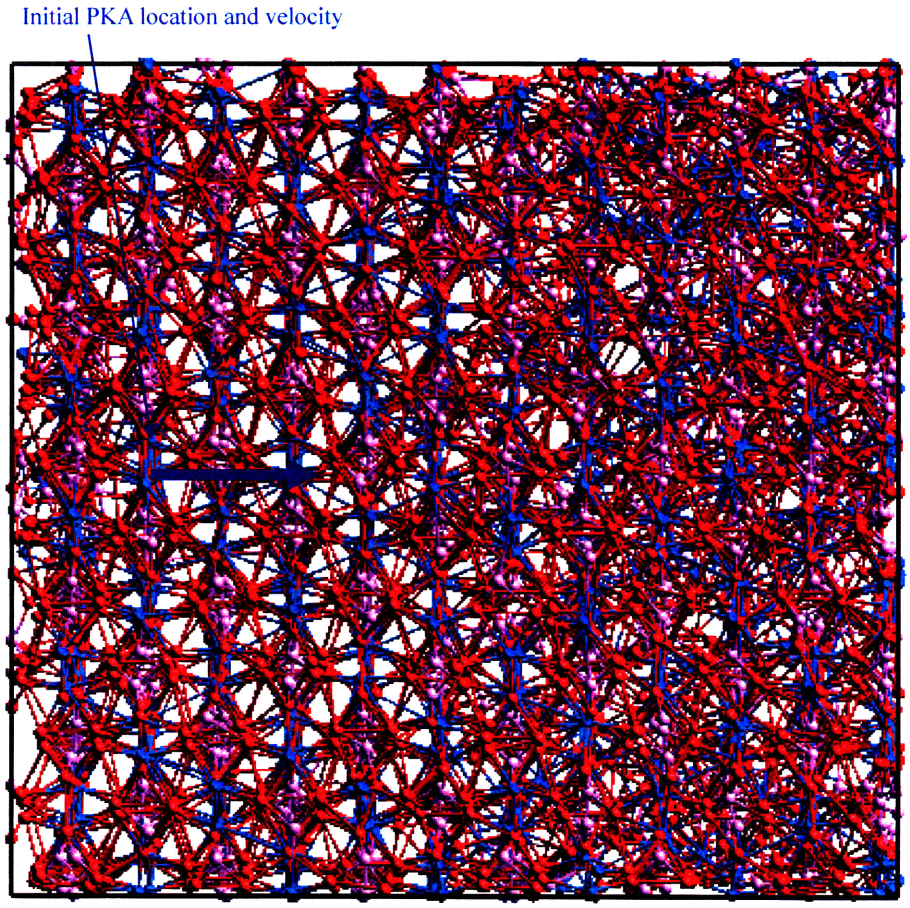

Figure 5.15: Zircon structure after 10-ps MD simulation using a 5-keV Zr PKA without energy removal at the boundary. The thick arrow in the middle of the figure shows the initial velocity direction of the PKA. The tail of this arrow is where PKA is located at time step 0 before simulation started.

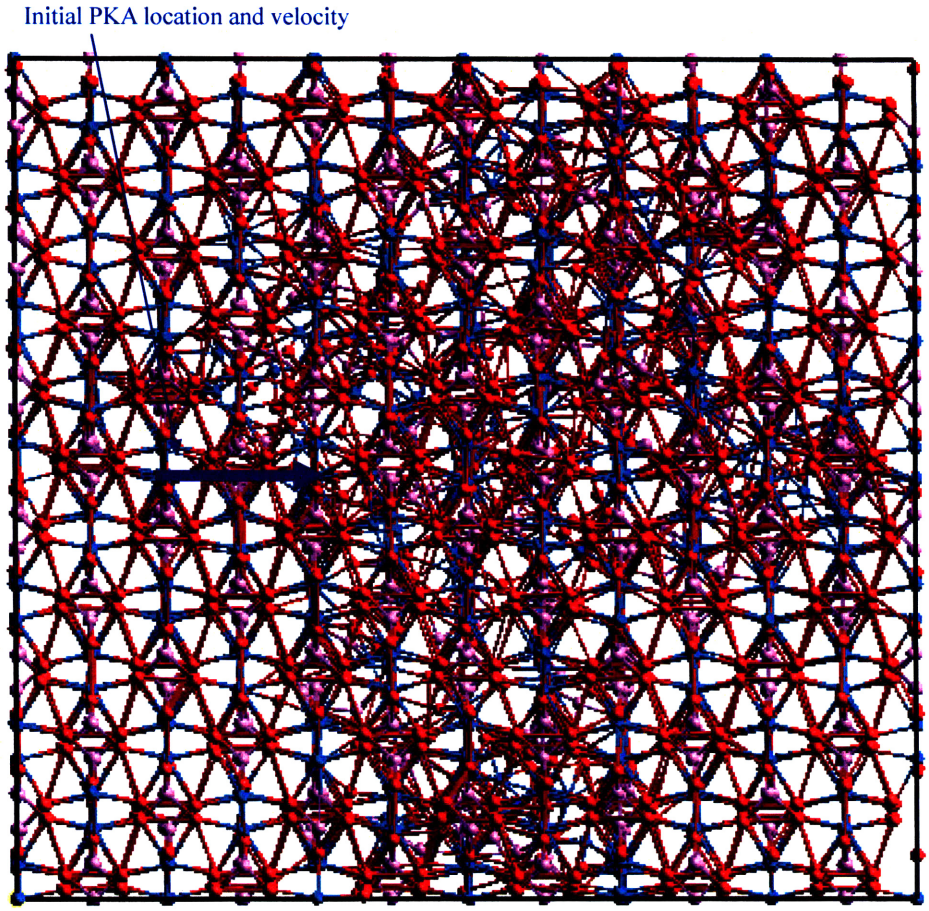

Figure 5.16: Zircon structure after 10-ps MD simulation using a 5-keV Zr PKA with energy removal at the boundary. The thick arrow in the middle of the figure shows the initial velocity direction of the PKA. The tail of this arrow is where PKA is located at time step 0 before simulation started. This figure should be compared to Figure 5.15.

It is much clearer in Figure 5.16 than Figure 5.15 which part of the structure has undergone significant changes due to the collision cascade. Figure 5.16 reveals another problem about system size, however. Simply by looking at the structure, it can be seen that the cascade region touches the boundary of the simulation cell and thus is influenced by the velocity rescaling applied there. A larger simulation cell would be more appropriate. The current system size, however, appears to be sufficiently large for the 1-keV PKA

simulation, as can be seen in Figure 5.17.

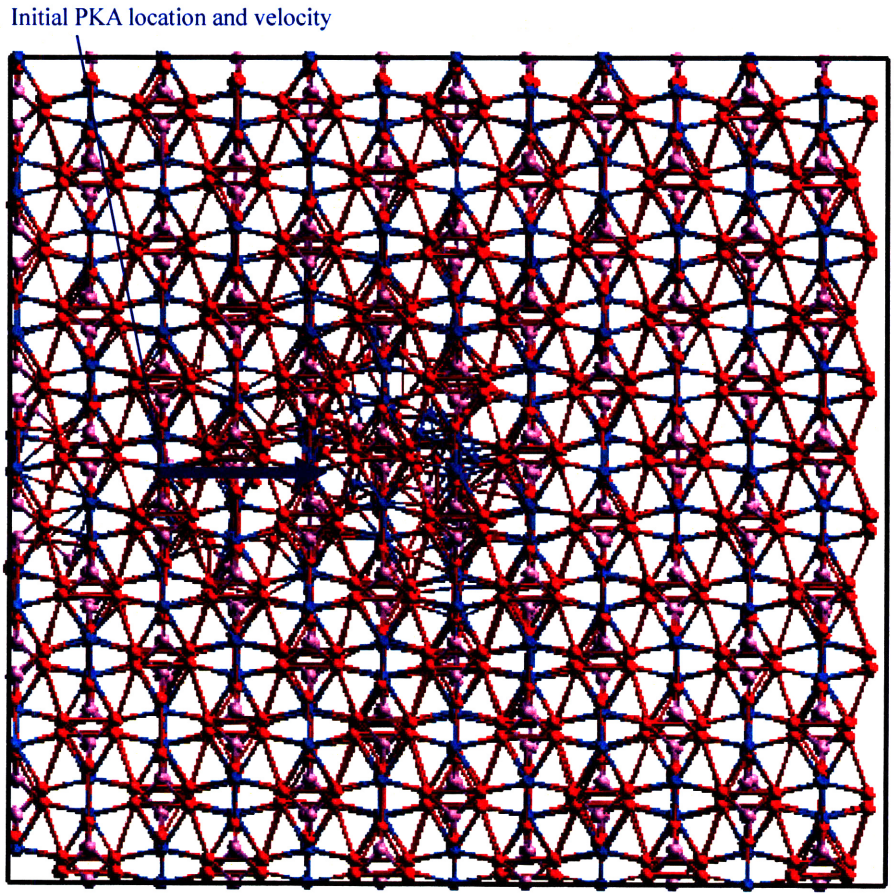

Figure 5.17: Zircon structure after 10-ps MD simulation using a 1-keV Zr PKA with energy removal at the boundary. The thick arrow in the middle of the figure shows the initial velocity direction of the PKA. The tail of this arrow is where PKA is located at time step 0 before simulation started. The supercell appears to be large enough for containing this radiation event.

The issue of choosing simulation cell size is discussed in Section 5.7, where a quantitative criterion is developed to determine the extent of the collision cascade, instead of relying on the qualitative appearance of the structure, which, though integrative, can be very subjective.

System total energies of MD simulations using a 5-keV Zr PKA are shown in Figure 5.18. About 4820-eV energy is removed from the system (950 eV in the 1-keV PKA case). The remaining 180-eV energy (50 eV in the 1-keV PKA case) is stored in the structure. Using stored energy as a crude indicator, we can say that the zircon structure suffered more distortion in the 5-keV PKA case than in the 1-keV PKA case, as would have been expected.

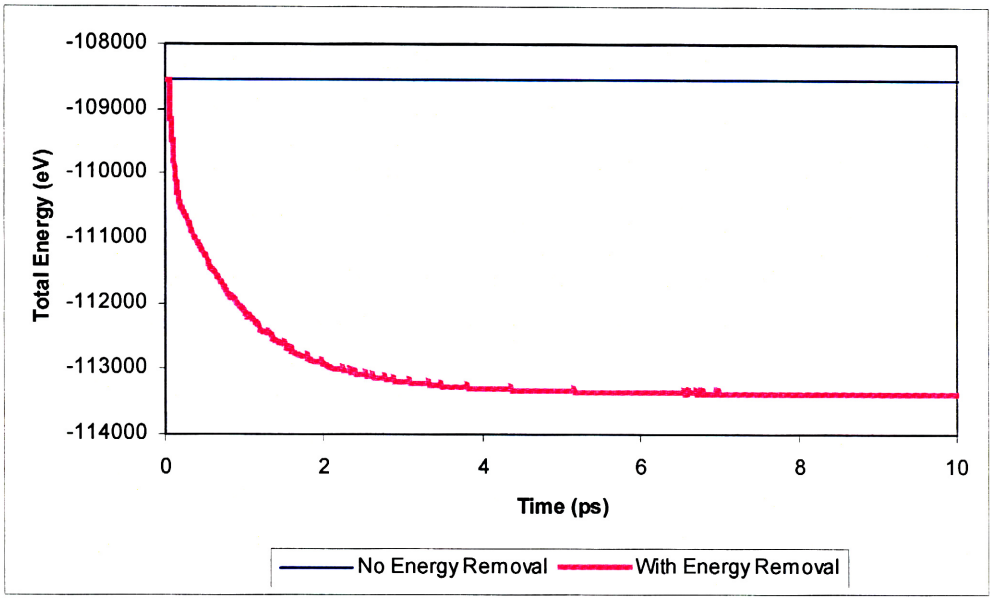

Figure 5.18: System total energies of MD simulations using a 5-keV Zr PKA, both with and without boundary energy removal.

5.6 Choosing the PKA, revisited

Section 5.3 discussed choosing location and initial velocity direction for the PKA. However, because of the boundary energy removal mechanism introduced in Section 5.5, the PKA initial location needs to be changed to avoid being influenced by the velocity rescaling at the boundary.

We move the PKA to the right (toward the supercell center). The boundary layer coupled to a constant temperature heat bath has a thickness of 2 Å.

Obviously the PKA needs to be moved out of this layer. Simply moving the PKA 2 Å, however, is not enough, since there can still be significant interactions between the constant temperature layer and the PKA or other atoms in the cascade. We were more conservative and moved the PKA at least 6 Å away, as shown in Figure 5.19. This movement of PKA left a gap of at least 4 Å between the constant temperature boundary layer and the PKA. For Zr in crystalline zircon, the closest Si particle is 3.05 Å away; closest O 2.14 Å away; and closest Zr 3.64 Å away. So a gap of at least 4 Å ensures that the first layer of neighbors of the PKA resides outside the boundary heat bath.

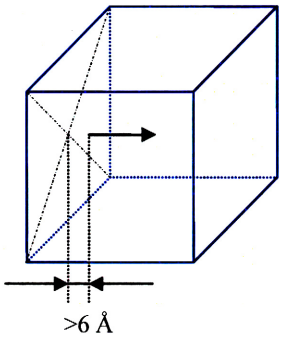

Figure 5.19: Location and initial velocity direction of PKA. PKA locates at the tail of the arrow, which shows the initial velocity direction. This figure can be compared to Figure 5.2 where PKA location and initial velocity direction for simulations with no energy removal are shown.

It is found that some atoms to the left of the PKA are also greatly influenced and sometimes displaced by the influence of the PKA, and thus should be considered part of the collision cascade. To make sure these atoms do not end up within the boundary heat bath, sometimes it is necessary to move the PKA even further away from the boundary. For example, in the cascade simulation using a 6-keV Zr PKA in Chapter 6, the initial location of the PKA was chosen about 14 Å away from the left boundary.

5.7 Choosing supercell size

This section aims to determine the right simulation cell (or supercell) size to use for collision cascade simulations. The simulation cell should be large enough to contain the collision cascade but not larger, to avoid unnecessary increase of computation time.

To determine simulation cell size, an empirical relationship developed by Foreman, Phythian and English [6] for metals recommends that the number of atoms in the cell should be about 16 times the recoil energy in eV. For example, for 1 keV recoil, the number of atoms in the cell should be 16 × 1000 = 16000. Devanathan *et al.* [5] prefer to include 20 atoms per eV of recoil energy, instead of the 16 recommended by Foreman *et al.* [6]. As discussed in Section 5.5, these rules generally give a simulation cell too large to be used in this study due to the constraint imposed by our limited computation facility.

Corrales *et al.* [7] have calculated the longitudinal range and lateral dispersion for Zr recoils with different energies using a modified SRIM (Stopping and Range of Ions in Matter) code. The SRIM code [8] uses a Monte-Carlo binary collision approximation based on the ZBL potential to describe elastic scattering. The original SRIM code also includes electronic stopping power as an energy loss mechanism. The modified version used by Corrales *et al.* [7] calculates particle ranges based only on the screened ZBL potential. This is more relevant in estimating ranges in MD simulations, for which electronic stopping power is unavailable. Their results are shown in Table 5.2.

Table 5.2: Average longitudinal and lateral ranges for energetic Zr atoms and the minimum tetragonal volume needed to contain the cascade. Calculations based only on nuclear stopping processes defined by the ZBL potential. Data copied from Corrales *et al.* [7].

Zr Recoil Energy (keV)	Longitudinal (nm)	Lateral or Radial (nm)	Minimum Volume (nm^3)	Minimum Volume (atoms)
1	2.1	0.9	7	644
30	15.2	5.9	2,116	194,713
70	29.0	10.9	13,782	1,267,940

Two unnecessary approximations are used in this methodology, which can easily be dispensed with when using MD simulations. The first is using only the screened ZBL potential. Other parts of the potential model are incorporated in MD simulations naturally. The second is the binary collision approximation, which is generally not quantitative enough for investigating collision cascade details.

The methods described thus far aim to estimate required supercell size before any MD simulation is performed. This study, however, adopts an iterative strategy. A supercell size is first chosen based on experience. MD simulation is performed and the extent of the cascade is assessed. The supercell size is then enlarged if it is found to be too small to contain the collision cascade. Using this strategy, the cascade extent is assessed in real simulations, with no need for unnecessary approximations.

In Section 5.5, layers 2 Å thick at each side of the simulation cell were kept at a constant temperature of 300 K. For collision cascades to be uninfluenced by velocity rescaling performed in these layers, the simulation cell needs to have a size large enough so that all the atoms of the collision cascade are never present inside these layers at any time. That is, all atoms of the collision cascade should be at least 2 Å away from each of the six

boundaries of the simulation cell at any given time. To determine whether this is the case, we first need to identify which atoms belong to the collision cascade.

The atoms in the cascade are those atoms that are significantly influenced by the energy brought in by the PKA. A first try is to include all the atoms which gain excess energy because of the collision cascade. At 300 K, an average atom has a kinetic energy of 3/2 kT ≈ 0.039 eV. Figure 5.20 shows the energy of the most energetic atom in the system of zircon MD simulation at 300 K.

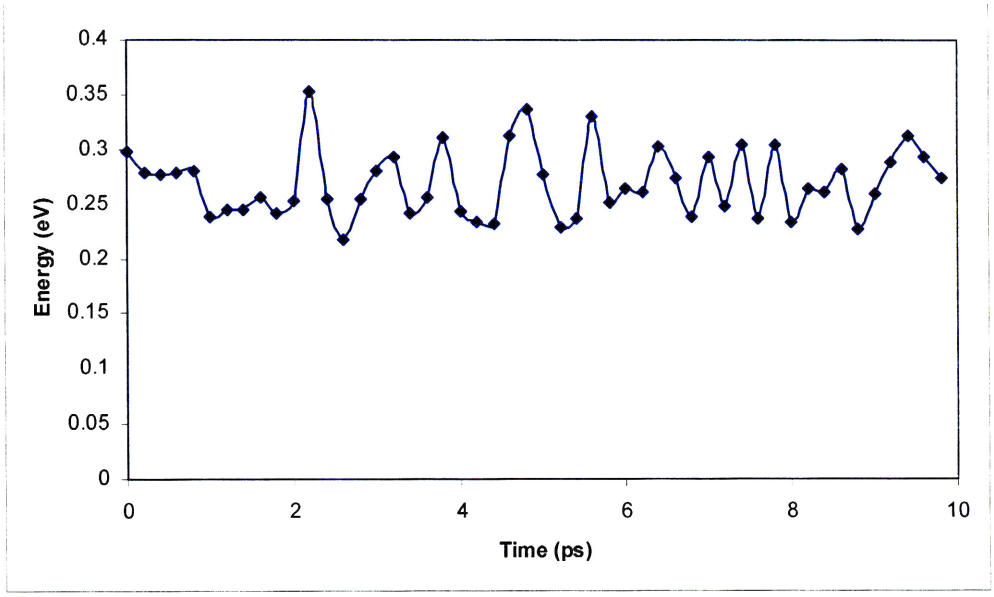

Figure 5.20: Energy of the most energetic atom in the system at different simulation times of zircon MD simulation at 300 K (after stability is attained).

In Figure 5.20, the most energetic atom in the system never has an energy value higher than about 0.35 eV. During collision cascade simulation, if an atom ever attains an energy value much higher than 0.35 eV at any time, it must have gained its excess energy because of the influence of the collision

cascade and therefore should be considered part of the cascade.

The only difficulty with this method of determining the extent of cascade is to choose an appropriate threshold energy. What energy should be considered sufficient for an atom to be considered part of the cascade? 0.35 eV? 1 eV? 5 eV? ... In light of the difficulty in choosing the appropriate threshold, we turn to another method of determining the extent of cascade described below.

Another criterion, other than energy, by which to quantify the influence on an atom from the collision cascade is to measure the displacement of the atom from its original site. At a temperature of 300 K, atoms thermally vibrate around their crystalline sites but do not have enough energy to leave. Figure 5.21 shows the largest displacement among all atoms in the system at different simulation times of a MD simulation performed at 300 K. No atom ever makes excursions more than about 0.5 Å away from its equilibrium site at any given time. Thus, if an atom ever leaves its site at any time during the collision cascade simulation, it can be considered part of the cascade. Unlike the case where energy is used as the quantitive criterion, here we have a natural threshold displacement distance reference: the interatomic distances in crystalline zircon.

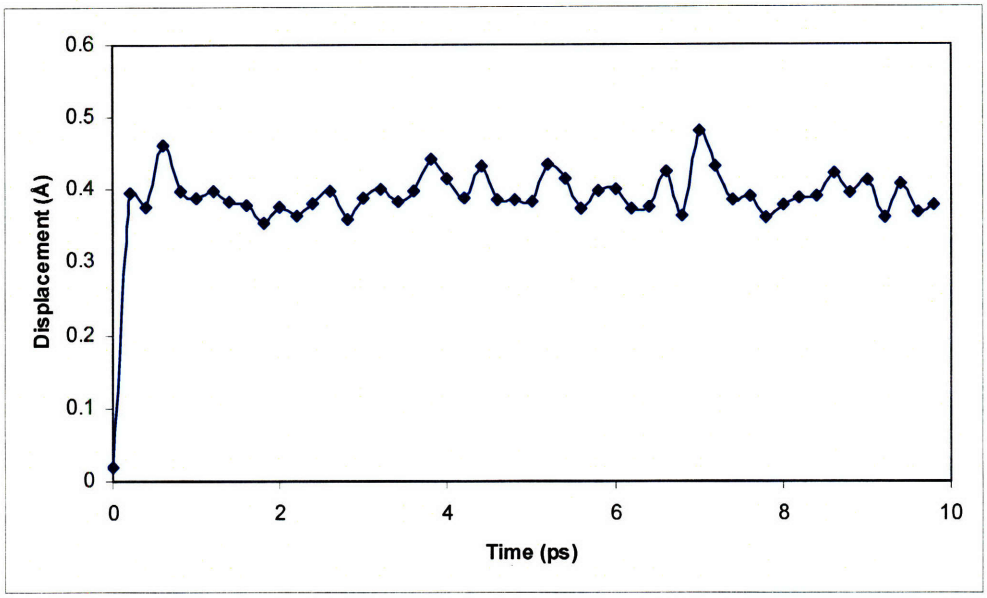

Figure 5.21: The largest displacement from their equilibrium sites among all atoms in the system at different simulation times of zircon MD simulation at 300 K.

For Si in crystalline zircon, the closest O neighbor is at a distance of 1.62 Å away; the closest Zr 3.05 Å away; and the closest Si 3.63 Å away. Therefore the closest neighbor of a Si atom is an O atom at a distance of 1.62 Å, which is then used as the threshold distance for Si. Threshold distances for O and Zr atoms are determined similarly. Table 5.3 givens the threshold distances for Zr, Si and O atoms.

Table 5.3: Threshold distances for Zr, Si and O atoms. If an atom has ever traveled longer than the threshold distance shown here away from its equilibrium site at any time during the collision cascade simulation, it is considered part of the cascade.

Particle Name	Zr	Si	O
Threshold Distance (Å)	2.13	1.62	1.62

We can see that the threshold values shown in Table 5.3 are all much larger than the highest peak displacement value in Figure 5.21 (less than 0.5 Å). So if we apply this rule to the equilibration simulation at 300 K, we find that

no atom belongs to a (here non-existent) collision cascade, as expected.

The number of atoms in the cascade is a non-decreasing function of time, because once an atom leaves its original site longer than its threshold distance, it will always be considered part of the cascade afterwards. It may come back to its original site later on, but this does not change the fact that this atom has been highly influenced by the collision cascade.

Using the threshold distance values in Table 5.3, we can determine at each time step of the simulation which atoms are part of the collision cascade. If any of the atoms in collision cascade is within 2 Å of the simulation cell boundary, the size of the simulation cell is not big enough. The cell size is then increased and the simulation is re-done. This process is repeated until the simulation cell is large enough. The simulation cell does not have to have equal number of unit cells on each side. For example, an 11x7x7 supercell is used for the 5-keV Zr PKA cascade simulation in Chapter 6.

5.8 Determine when to stop simulation

MD collision cascade simulations need to be run long enough that the system is stabilized. Stabilization means different things depending on the phenomena one wants to investigate. There are multiple stages in collision cascades with different time scales, so the time it takes to stabilize depends on which stages the phenomena under investigation belong to.

At least three stages in a collision cascade can be identified. In the first stage, the energy of the PKA is redistributed among atoms in the cascade by ballistic collisions. This process results in a very high local temperature in a very short time. The second stage is a relaxation phase during which the

"hot" collision cascade regions gradually attain equilibrium with the ambient crystalline structure. Connectivity disorder and defects are meta-stabilized during this stage. The last stage is the evolution of the defect structure, involving defect migration, recombination, *etc*. This stage takes a very long time and is usually not feasible to be investigated by MD simulations for complex ceramics systems with current computational power. Other methods, such as the Kinetic Monte Carlo approach, can be used in macroscopic simulations of the evolution of radiation damage.

MD simulations of collision cascades should run long enough to make sure at least the first two stages have finished. There are several properties that can be used to determine whether the system is meta-stabilized or not. The properties used in this study are system temperature, system total internal energy, energy of the most energetic atom in the system, and the number of atoms in the cascade. A cascade simulation using a 1-keV Zr PKA is used as an example here. System temperature and total internal energy at different simulation times are shown in Figures 5.22 and 5.23, respectively. We can see that, at about 4 ps, system temperature and total energy have been stabilized.

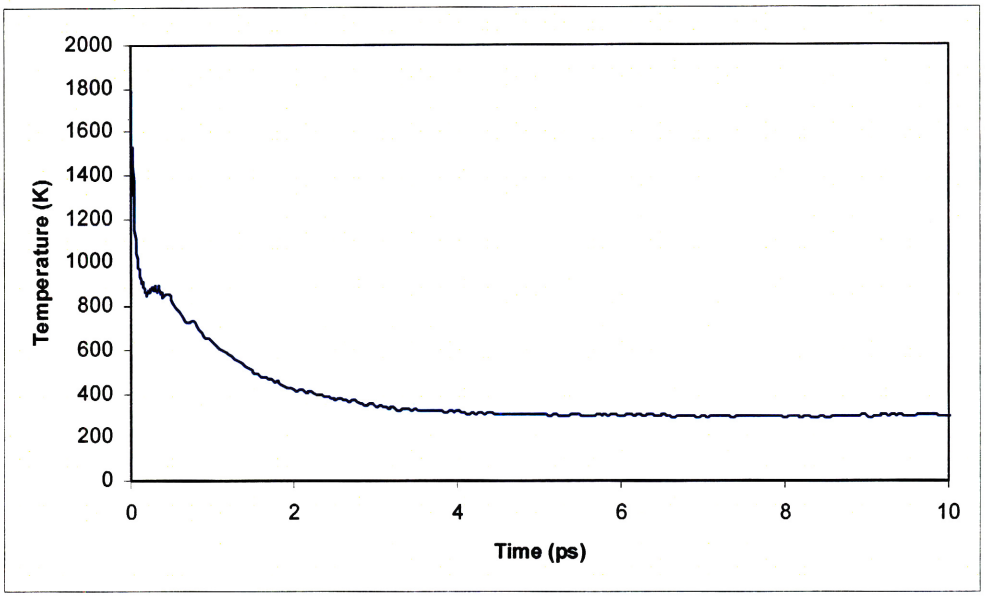

Figure 5.22: System temperature of an MD simulation using a 1-keV Zr PKA with boundary energy removal.

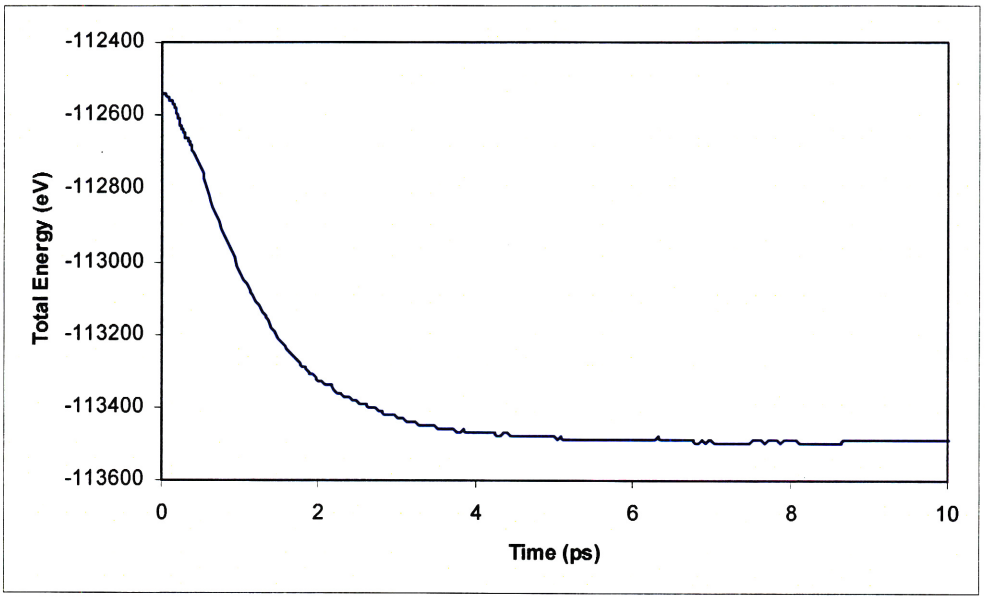

Figure 5.23: System total energy of an MD simulation using a 1-keV Zr PKA with boundary energy removal.

Figure 5.24 shows the energy of the most energetic atom in the system and the average atom energy at 300 K, with no PKA and thus no collision

cascade. Figure 5.25 shows the same information for a cascade simulation using a 1-keV Zr PKA. In Figure 5.25, we can see that, starting from about 3.0 ps, the energy of the most energetic atom in the system and the average atom energy have stabilized, and their values and trends are similar to what's shown in Figure 5.24 for zircon at 300 K. We can say that the system has stabilized at about 3.0 ps from an energetics viewpoint.

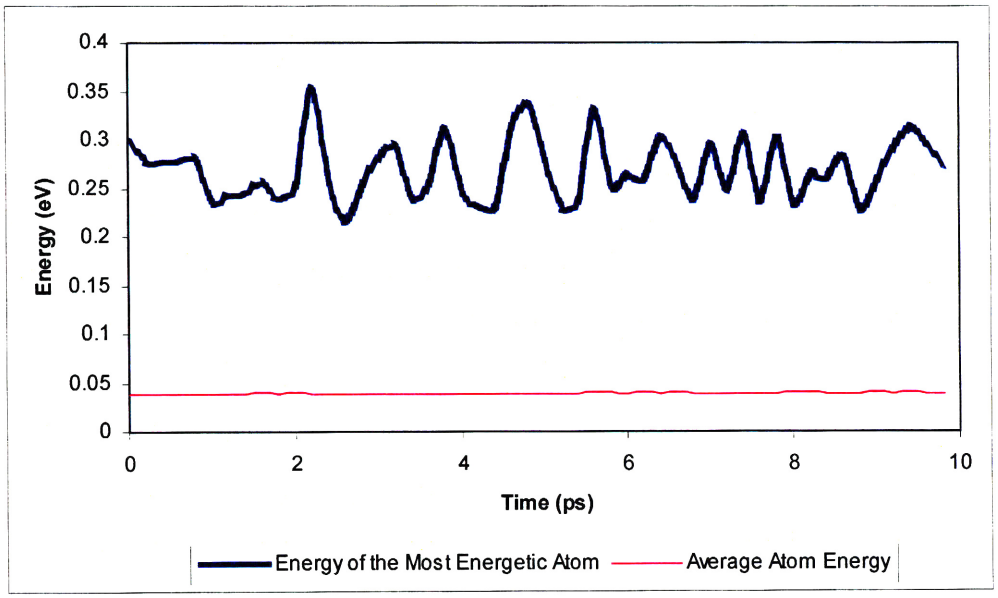

Figure 5.24: Energy of the most energetic atom in the system and average atom energy in an MD equilibration simulation of zircon at 300 K.

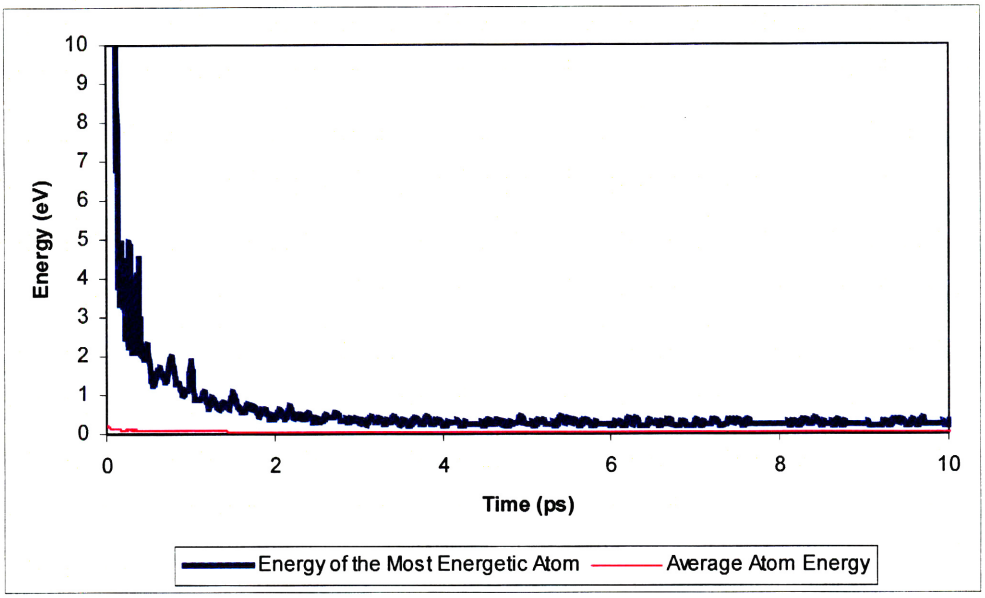

Figure 5.25: Energy of the most energetic atom in the system and average atom energy of MD cascade simulation using a 1-keV Zr PKA.

We note that one must look at the energy of the most energetic atom, not the energy of the original PKA, to determine whether the system has stabilized. The reason is that the PKA transfers its energy to other atoms in a very short time. Even when the energy of the initial PKA becomes very small, secondary knock-ons, tertiary knock-ons, *etc.* can still have high energies and the collision cascade could well still be under way. Figure 5.26 shows PKA energies at different simulation times of cascade simulation using a 1-keV Zr PKA. It can be seen that, starting from about 0.5 ps, the PKA has an energy less than 1 eV; and starting from about 1.0 ps, the PKA has the energy of a typical atom at 300 K. We cannot conclude based on this figure that the collision cascade has finished at about 1.0 ps.

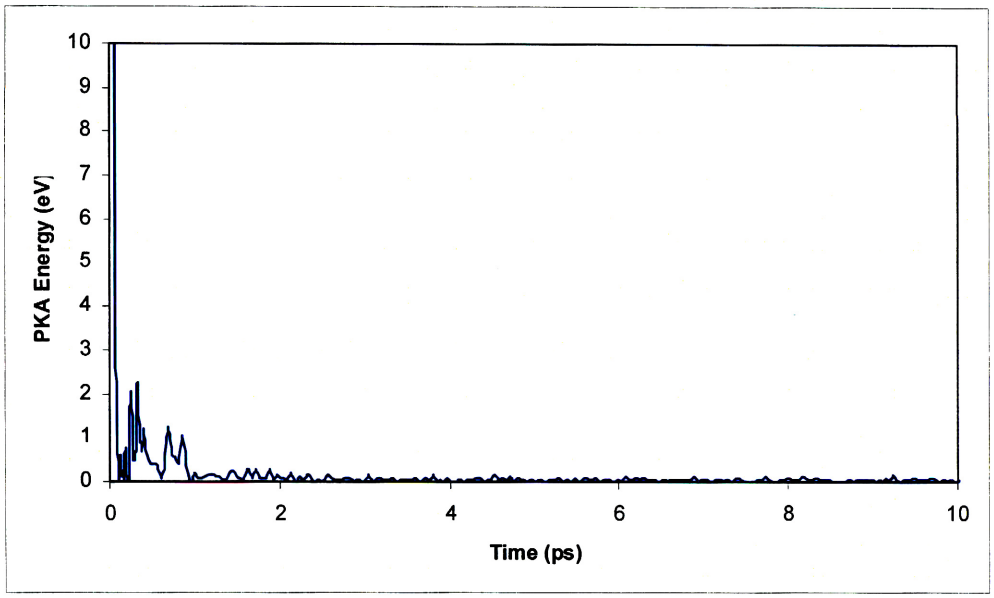

Figure 5.26: PKA energies at different simulation times of cascade simulation using a 1-keV Zr PKA.

In section 5.7, a method based on displacements of atoms from their original sites is developed to determine which atoms belong to the cascade. Using that method, we can plot the curve of the number of atoms in the cascade against simulation time. This curve must have stabilized for the system to be considered stabilized. The number of atoms in the cascade for a simulation using a 1-keV Zr PKA is shown in Figure 5.27. As discussed before, the number of atoms in the cascade is a non-decreasing function of time. The number of atoms in the cascade does not increase after about 2.0 ps, and the final count is 132.

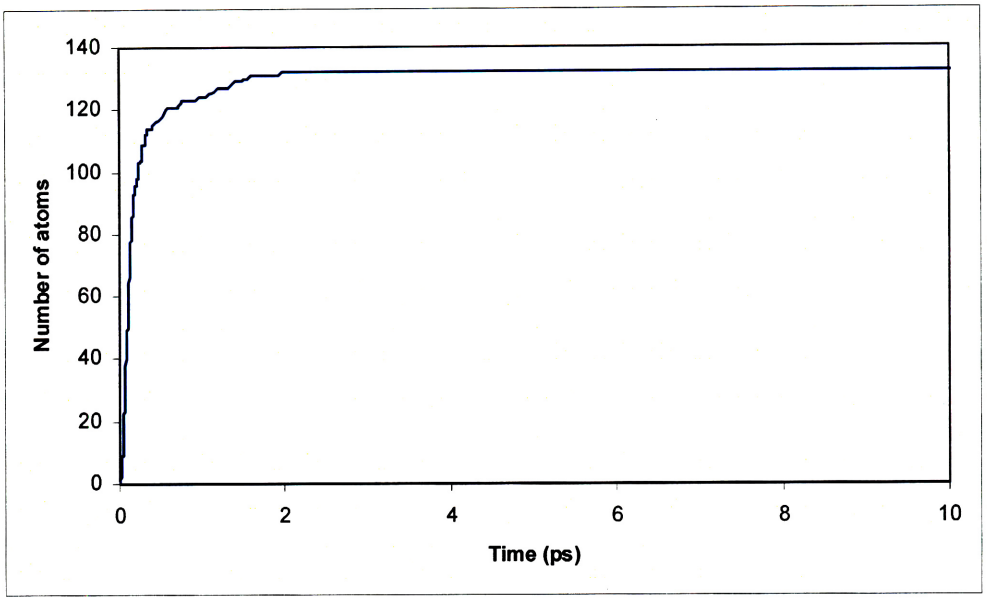

Figure 5.27: Number of atoms in the cascade for a simulation using 1-keV Zr PKA.

From all the discussions above, we can conclude that a cascade simulation using a 1-keV Zr PKA is stabilized after about 4.0 ps.

For all collision cascade simulations performed in this study, we have always performed the checks introduced in this section to make sure the systems have stabilized. If systems were found not to be stabilized, simulations were extended until they were.

5.9 The chosen cascade simulation setup

In previous sections, we have described how collision cascade simulations should be conducted. This section offers a brief summary.

The starting system configuration was the system after equilibration at 300 K, as depicted in Figure 5.1. A PKA was chosen and given an initial velocity

direction according to Figure 5.19. In most cases the PKA was a Zr atom or a U atom residing on one of the Zr sites. U was treated as a super-mass Zr in this study. Its interactions with Zr, Si and O atoms were the same as a Zr atom's interactions with them.

A variable time step size was used (Section 5.4). The time step size was chosen in such a way that the fastest atom in the system did not travel more than about 0.1 Å in a single time step. The time step size used in this study was never greater than 1 fs. A heat bath at 300 K was applied at simulation cell boundaries as the method to remove the excess energy introduced by the PKA from the system (Section 5.5).

After the simulation, two validations were performed. One is to make sure the simulation cell is large enough to contain the radiation event; the other is to make sure the simulation has been run long enough for the system to have stabilized.

In section 5.7, a method based on displacements of atoms from their original sites was developed to determine which atoms belong to the collision cascade. The extent of cascade was determined by applying this method. If the extent of cascade overlapped with the boundary layer coupled to constant temperature heat bath, the simulation cell was considered too small. As a result, its size was increased and the simulation was re-performed.

For each collision cascade simulation, we also checked system temperature, system total internal energy, energy of the most energetic atom in the system and the number of atoms in the cascade to make sure the simulation system had stabilized (Section 5.8).

References of chapter 5

[1] W.J. Weber. Radiation-Induced Defects and Amorphization in Zircon. J. Mater. Res. 5, 2687 (1990).

[2] W.J. Weber. Self-Radiation Damage and Recovery in Pu-Doped Zircon. Radiat. Eff. Defects in Solids 115, 341 (1991).

[3] C.S. Palenik, L. Nasdala and R.C. Ewing. Radiation Damage in Zircon. American Mineralogist 88, 770 (2003).

[4] K. Trachenko, M.T. Dove, T. Geisler, I. Todorov and B. Smith. Radiation Damage Effects and Percolation Theory. J. Phys.: Condens. Matter 16, S2623 (2004).

[5] R. Devanathan, L.R. Corrales, W.J. Weber, A. Chartier and C. Meis. Molecular Dynamics Simulation of Defect Production in Collision Cascades in Zircon. Nuclear Instruments and Methods in Physics Research B 228, 299 (2005).

[6] A.J.E. Foreman, W.J. Phythian and C.A. English. The Molecular Dynamics Simulation of Irradiation Damage Cascades in Copper using a Many-Body Potential. Philos. Mag. A 66, 671 (1992).

[7] L.R. Corrales, W.J. Weber, A. Chartier, C. Meis and J. Crocombette. Comment on "Large Swelling and Percolation in Irradiated Zircon". J. Phys.: Condens. Matter 15, 6447 (2003).

[8] J.F. Ziegler, J.P. Biersack and U. Littmark. The Stopping and Range of Ions in Solids. Vol. 1 of: The Stopping and Ranges of Ions in Matter. ed. J.F. Ziegler. New York, Pergamon, 1985.

Chapter 6: MD simulations of radiation effects in zircon

This chapter uses MD simulations to investigate radiation effects in zircon. Collision cascade simulations using Zr and U PKAs with energies up to 10 keV were conducted and cascade details were analyzed. When U was used as the PKA, it replaced a Zr atom and occupied its site. In this study, no separate potential is developed for U's interactions with other atoms. Instead, U was treated as a "super-mass" Zr. U-Zr, U-Si and U-O interactions were the same as Zr-Zr, Zr-Si and Zr-O interactions, respectively. The effects of PKA mass on collision cascade were investigated within this framework.

Not all simulations conducted in this chapter involve collision cascades, such as when determining threshold displacement energies where low-energy PKAs were used and normally no cascades were produced.

Only one PKA was used in most of the simulations, but multi-PKAs were used in Sections 6.5 and 6.6 to render the zircon structure amorphous.

Most analysis of the collision cascades is done in this chapter, but some analysis is delayed to Chapter 7, where topological methods are used.

6.1 Threshold displacement energies

The displacement of atoms from their crystalline sites is one of the primary material responses to irradiation. It is responsible for damage production and has profound implications for changes of material properties.

In the most basic theoretical models, a sharp threshold energy E_d is defined. A lattice atom is permanently displaced if it receives kinetic energy equal to

or greater than E_d. If it receives less than E_d, however, it may leave its site temporarily but will eventually return [1, 2].

Analytical models based on this definition of E_d typically assume that the medium is homogeneous and isotropic. Crystalline structure and the heterogeneity due to the existence of multiple sub-lattices in certain materials are neglected. These simplifications, although mandatory in many cases in order to make analytical models tractable, are totally unnecessary in MD simulations, where crystallographic structure and the effects of multiple sub-lattices are incorporated naturally.

There are many experimental methods to measure E_d. One of them is to put the material whose E_d value is sought under controlled irradiation. Material properties sensitive to the defects created when atoms are displaced are closely monitored. Radiation energy is then gradually increased and the energy level which causes sudden change in the monitored material property is recorded. From this recorded incoming particle energy and masses of the particles involved in the collision, we can calculate the threshold displacement energy E_d.

The above described method is just one example of displacement threshold determination. Experimental techniques available for measuring E_d in ceramics include optical and thermally stimulated spectroscopies, electron paramagnetic resonance, positron annihilation, and electron microscopy [3].

Threshold displacement energies have been measured for some ceramics, such as alumina, MgO, and ZnO. However, accurate E_d values are not available for many other ceramics due to experimental difficulties or the effort and expense required to overcome these difficulties. No experimental

values are found for zircon in the literature.

Advances in computer modeling and computational power have provided new methods for determining threshold displacement energies. Williford, Devanathan and Weber [3] used energy minimization methods to obtain estimates of displacement energies. They used the computer code GULP, which uses a Mott-Littleton [4] approximation to simulate isolated defects in extended solids. Energy minimization methods are less realistic and less accurate than are MD methods, but are also much faster.

Calculations of zircon threshold displacement energies using MD simulations have been carried out by Park, Weber and Corrales [5]. However, the potential they used, the potential #5 described in Section 3.2.5, yields a negative elastic constant C_{66}. Furthermore, the stable zircon structure using this potential has an *a*/*c* ratio on the wrong side of unity compared to the experimental zircon structure. Thus, it is not simply a repetition of work elsewhere to determine E_d values in this study. In addition, we determine E_d values along more directions to better define a displacement energy surface.

Conceptually, it is very easy to determine threshold displacement energies using MD simulations. The main process involves giving an atom an initial energy along a certain direction and see whether or not it is displaced. In zircon, certainly we would expect the threshold displacement energies of Zr, Si and O to be different and highly dependent on crystallographic directions. Thus, E_d values of Zr, Si and O are determined separately along many directions in Sections 6.1.1 through 6.1.3. All the directions used in [3] and [5] are also included in this study for the purpose of comparison. In addition, E_d values along directions directly toward neighboring atoms and toward

"open spaces" are also determined. The meaning of "toward neighboring atoms" and "toward open spaces" will be explained in more detail in Section 6.1.1.

6.1.1 Threshold displacement energies of Zr

As before, simulations used the structure #3 of Figure 5.1 as the initial structure. A 6x6x6 supercell was used, which is large enough to contain the low energy collision events in this section. A Zr atom near the center of the simulation cell was selected to be the PKA. Figure 6.1 shows this Zr atom and its immediate neighbors. The eight surrounding O atoms are numbered for convenience of reference. The coordinates of the atoms in Figure 6.1 are shown in Table 6.1.

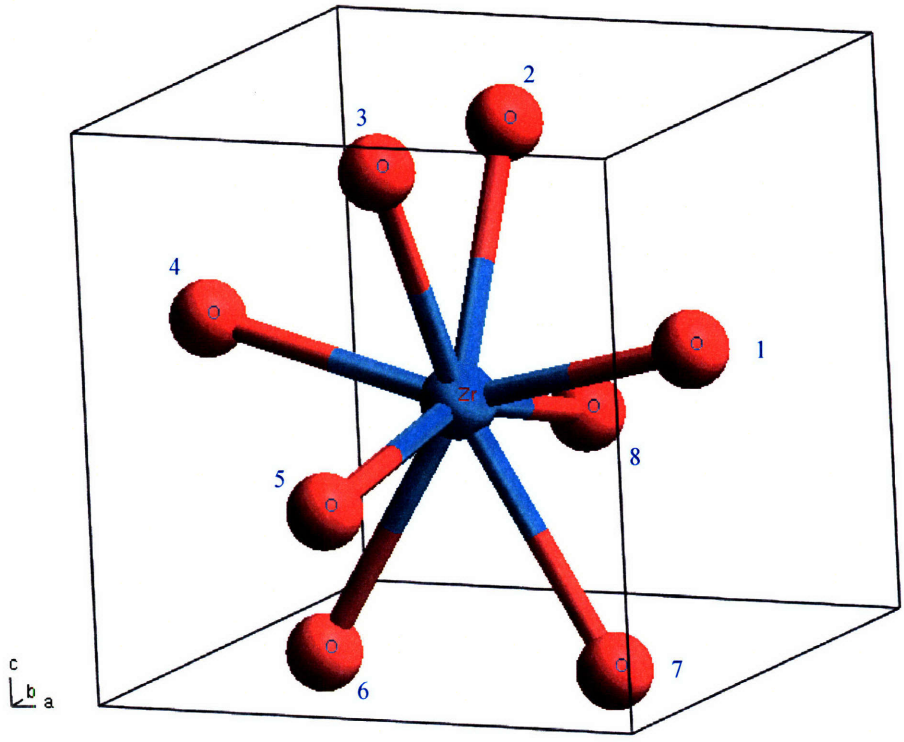

Figure 6.1: A Zr atom near the center of the 6x6x6 simulation supercell and its surrounding O atoms. The relative positions of the surrounding O atoms are slightly different from those in experimental zircon crystalline structure, as the atoms shown here are from the structure after 20-ps MD equilibration simulation at a temperature of 300 K.

Table 6.1: Coordinates of the atoms shown in Figure 6.1. The location of the origin is unimportant, since only the relative positions are needed for determining directions.

Atom Name	Atom Number	Coordinates as (x, y, z) (Unit: Å)
Zr	N/A	(0.0225, 0.0498, 0.0355)
O	1	(2.0416, 0.0267, 0.5294)
O	2	(-0.0294, 1.1753, 1.9518)
O	3	(0.0403, -1.2172, 2.0637)
O	4	(-2.1107, 0.0756, 0.5705)
O	5	(-0.0891, -2.1392, -0.3766)
O	6	(-1.2092, 0.0044, -1.9599)
O	7	(1.2999, -0.0475, -1.9767)
O	8	(0.0721, 2.1550, -0.4856)

Two kinds of initial directions for the Zr atom in Figure 6.1 are considered. One is directly toward one of the neighboring O atoms; the other is toward open spaces. The directions toward open spaces will be discussed shortly below. For directions toward neighboring atoms, there are in total 8 possibilities, since there are 8 neighboring O atoms. The direction towards O #i will be denoted as NB_i (NB for neighbor). For example, the direction towards O #5 will be denoted as NB_5.

The directions can be easily calculated from atom coordinates given in Table 6.1. For example, coordinates of Zr and O #1 are (0.0225 Å, 0.0498 Å, 0.0355 Å) and (2.0416 Å, 0.0267 Å, 0.5294 Å), respectively. The vector pointing from Zr to O #1 is then (2.0191 Å, -0.0231 Å, 0.4939 Å). The length of this vector is $\sqrt{2.0191^2+(-0.0231)^2+0.4939^2} \sim 2.0788$ Å, so the direction cosines ($\cos\alpha$, $\cos\beta$, $\cos\gamma$) for this direction are $(\frac{2.0191}{2.0788}, \frac{-0.0231}{2.0788}, \frac{0.4939}{2.0788}) \sim (0.9713, -0.0111, 0.2376)$. These are the direction cosines for direction NB_1. If Zr's initial kinetic energy is T, its velocity v is then $\sqrt{\frac{2T}{m}}$, where m is the mass of Zr. The initial velocity vector given to Zr at the beginning of the simulation will then be ($0.9713v$, $-0.0111v$, $0.2376v$) for NB_1 direction. Calculations for other directions are similar.

From the example above, it is clear that giving direction cosines is sufficient to specify a direction. Direction cosines of directions NB_1 through NB_8 for the Zr atom in Figure 6.1 are given in Table 6.2.

Table 6.2: Direction cosines of directions NB_1 through NB_8 for the Zr atom shown in Figure 6.1

Direction Symbol	Direction Cosines
NB_1	(0.9713, -0.0111, 0.2376)
NB_2	(-0.0233, 0.5063, 0.8620)
NB_3	(0.0074, -0.5298, 0.8481)
NB_4	(-0.9699, 0.0117, 0.2432)
NB_5	(-0.0500, -0.9815, -0.1848)
NB_6	(-0.5252, -0.0194, -0.8508)
NB_7	(0.5355, -0.0408, -0.8435)
NB_8	(0.0229, 0.9705, -0.2402)

The directions toward open spaces are those that avoid collisions head-on with neighboring atoms. Figure 6.2 shows the direction toward the open space between O #1, #2 and #3. The space seems to be quite open in Figure 6.2. However, if we drew the structure as a close-packed figure, as was done in Figure 2.4, the space would look much more crowded. The "openness" of spaces is thus only in a relative sense.

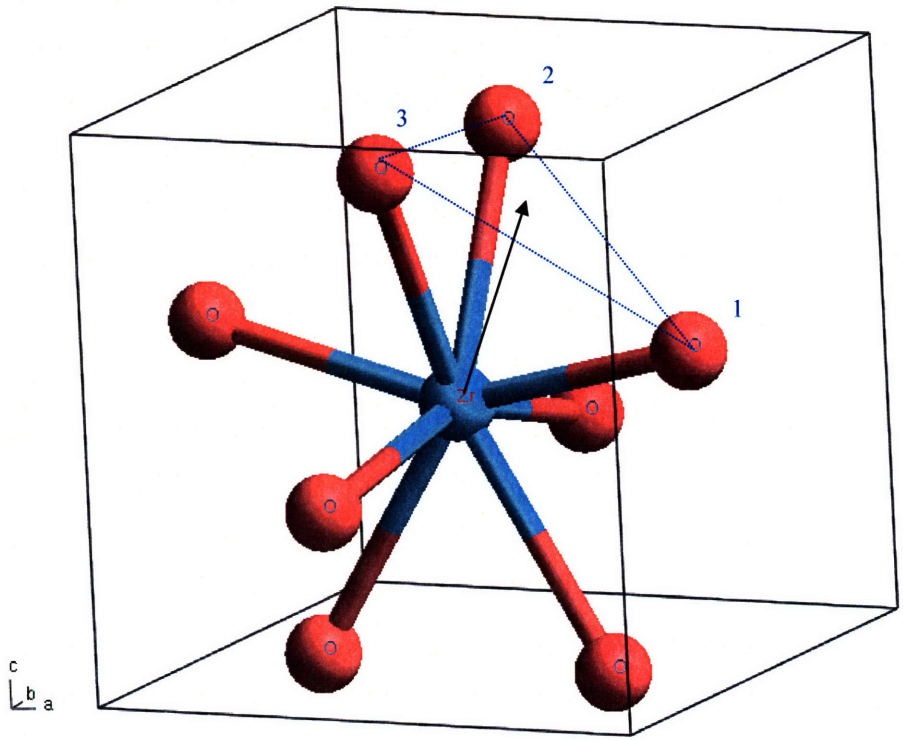

Figure 6.2: Illustration of direction OS_{123} for the Zr atom in Figure 6.1.

The direction shown in Figure 6.2 is denoted as OS_{123} (OS for open space), since it is the direction toward the center of the triangle with vertices at O #1, #2 and #3. Similarly, the direction towards center of the triangle with vertices at O #i, #j, and #k will be denoted OS_{ijk} in this study.

There are numerous definitions of triangle centers, such as centroid, incenter, circumcenter, orthocenter, *etc*. Centroid (shown in Figure 6.3) is the one we will use. In physics terms, a centroid point is also called a center of mass or center of gravity.

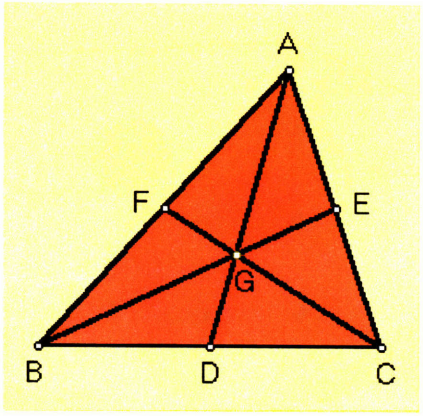

Figure 6.3: Illustration of triangle centroid. D is the midpoint of side BC; E is the midpoint of side CA; and F is the midpoint of side AB. G is the centroid of triangle ABC. Picture is from [6].

The centroid of triangle with vertices at (x1, y1, z1), (x2, y2, z2), and (x3, y3, z3) is located at ((x1+x2+x3)/3, (y1+y2+y3)/3, (z1+z2+z3)/3). After getting the coordinates of the centroid point, the direction from the Zr atom in Figure 6.1 to it can be calculated the same way directions NB_1 through NB_8 are calculated. They are just directions from one known point to another.

A direction toward open spaces can be determined for every triplet of surrounding O atoms. However, not all triplets of O atoms are worth considering. For example, referring to Figure 6.1, the triplet of O #3, #6 and #8 is probably not a good choice, as the direction OS_{368} is not much different from NB_4. Of course it does not hurt to calculate an E_d value along this direction; it is just unnecessary since it provides no new information. In this study, the following directions toward open spaces were considered: OS_{123}, OS_{128}, OS_{135}, OS_{137}, OS_{138}, OS_{157}, OS_{167}, OS_{234}, OS_{248}, OS_{345}, OS_{346}, OS_{357}, OS_{456}, OS_{468}, OS_{567}, and OS_{678}. These account for 16 out of a total of 56 possible triplets. Direction cosines for these directions are given in Table 6.3.

Table 6.3: Direction cosines of directions toward open spaces for the Zr atom in Figure 6.1

Direction Symbol	Direction Cosines
OS_{123}	(0.4080, -0.0338, 0.9123)
OS_{128}	(0.4764, 0.7576, 0.4462)
OS_{135}	(0.4277, -0.7729, 0.4687)
OS_{137}	(0.9133, -0.3823, 0.1405)
OS_{138}	(0.6947, 0.2714, 0.6662)
OS_{157}	(0.7268, -0.5270, -0.4405)
OS_{167}	(0.5062, -0.0406, -0.8614)
OS_{234}	(-0.4354, -0.0232, 0.8999)
OS_{248}	(-0.4913, 0.7492, 0.4441)
OS_{345}	(-0.4819, -0.7423, 0.4655)
OS_{346}	(-0.9219, -0.3544, 0.1564)
OS_{357}	(0.3143, -0.9435, -0.1052)
OS_{456}	(-0.7684, -0.4882, -0.4139)
OS_{468}	(-0.7553, 0.4751, -0.4514)
OS_{567}	(-0.0132, -0.4666, -0.8844)
OS_{678}	(0.0193, 0.3975, -0.9174)

In addition to the directions given in Tables 6.2 and 6.3, the following directions were also considered for the purpose of comparison with threshold displacement energies published in [3] and [5]: [110], [111], [001], [120], [011], [010], [101] and [100]. This set of directions is the union of the sets of directions considered in [3] and [5].

We have to be very careful when comparing directions in this study with those in [3] or [5]. We can deduce the direction labeling convention used in [5] by studying the figures therein. The figures in [5] are drawn using this convention: the paper is the plane containing the x and y axis, with x horizontal and y vertical. $+x$ direction is toward right and $+y$ upward. The direction pointing out of the paper is the $+z$ direction. Determined using some characteristic features of zircon structure shown in such figures as Figure 1 and Figure 7 in [5], we can conclude that the x, y and z directions in

this study correspond respectively to the *y*, *x*, and *z* directions in [5]. The alternating ZrO_8 triangular dodecahedra and SiO_4 tetrahedra are along the *z* direction in Figures 1 and 7 of [5], and they are also along the *z* direction in this study, so the *z* directions match in the two studies. Another distinctive feature of zircon structure is the plane containing each O atom and its neighboring Si and Zr atoms. Each O atom has 1 neighboring Si atom and 2 neighboring Zr atoms. The O atom and its neighboring Si and Zr atoms are roughly on the same plane. This plane is perpendicular to the *x* direction in this study (see Figure 6.7), but perpendicular to the *y* direction in [5], judged from Figure 7 of [5]. Thus the *x* direction in this study corresponds to the *y* direction in [5]. Because of the different labeling of directions, the E_d value along direction [210] determined here, for example, should be compared to E_d value along direction [120] in [5]. This is how we will compare E_d values in Table 6.4 and other similar tables where E_d values are reported. For reference [3], the direction labeling convention used is not mentioned in the original paper, and there are no figures or other hints to enable such information deduced. We will assume [3] used the same convention as that used in this study.

Intuitively, if $b > a$ and the PKA is displaced with initial energy *a*, it should also be displaced with initial energy *b*. If this is the case, when determining E_d value along a given direction, a procedure similar to what's called "binary search" in computer science can be used. Assuming we have already narrowed down E_d to the range $[a, b]$ (that is, $a \leq E_d \leq b$; initially *a* can be 0 and *b* can be a sufficiently large value), to narrow down the range further, a simulation can be performed with PKA energy $(a + b) / 2$. If the PKA is permanently displaced, the new range is $[a, (a + b) / 2]$; otherwise, it is $[(a+b) / 2, b]$. Either way, the width of the range is halved. This process is continued until we reach satisfactory accuracy. The width of the range

decreases exponentially. For example, assume the original range spans 400 eV. After 9 simulations, the width of the range will be reduced to $400/2^9 \sim$ 0.8 eV.

However, the assumption that if $b > a$ and the PKA is displaced with initial energy a, it is also displaced with initial energy b does not hold for certain directions (see discussion in Section 6.1.4). As a result, the process to determine E_d values takes certain guesses and is more *ad hoc* than algorithmic.

In this study, E_d values are reported as ranges. For example, if the E_d value is reported as [100 eV, 200 eV], it means the PKA is not permanently displaced with initial energy 100 eV or less, but is permanently displaced with initial energy 200 eV or more. For energies between 100 and 200 eV, the PKA may or may not be permanently displaced. If a single value is desired, the average of the two can be used. In the example above, the value is 150 eV, with an uncertainty of ±50 eV. This method of reporting E_d values is necessary for certain directions, as discussed in Section 6.1.4.

Each simulation was performed using a constant volume ensemble for 10 ps. (See Chapter 5 on how collision cascade simulations were conducted in this study.) At the end of the simulation, if the PKA was displaced from its original site more than a pre-chosen threshold distance away, it was considered permanently displaced; otherwise, it was not. The threshold distance values used for Zr, Si and O atoms are halves of those values shown in Table 5.3, which are the distances of closest neighbor atoms. The values in Table 5.3 are divided by two before used as threshold values here because interstitial sites are half-way between two neighboring sites. However, the determination of E_d values is not very sensitive to the

threshold distances chosen. It was found that the final position of the PKA was almost always either very close to the initial site (displacement much less than half of interatomic distance) or very far away (displacement comparable to or greater than interatomic distances).

As an example, Figure 6.4 shows the displacement of the Zr PKAs with initial velocities toward [101] direction and initial energies of 21 eV and 22 eV. We can see that initially the two PKAs had similar displacements, but after about 1.0 ps, the 21-eV PKA did not have enough energy to penetrate the potential barrier and returned to near its original site, while the 22-eV PKA was energetic enough to displace itself about 2.7 Å away. In this specific case, the difference between the two final displacements (0.3 Å for 21-eV PKA and 2.7 Å for 22-eV PKA) is huge, and we have much freedom in choosing threshold displacement values.

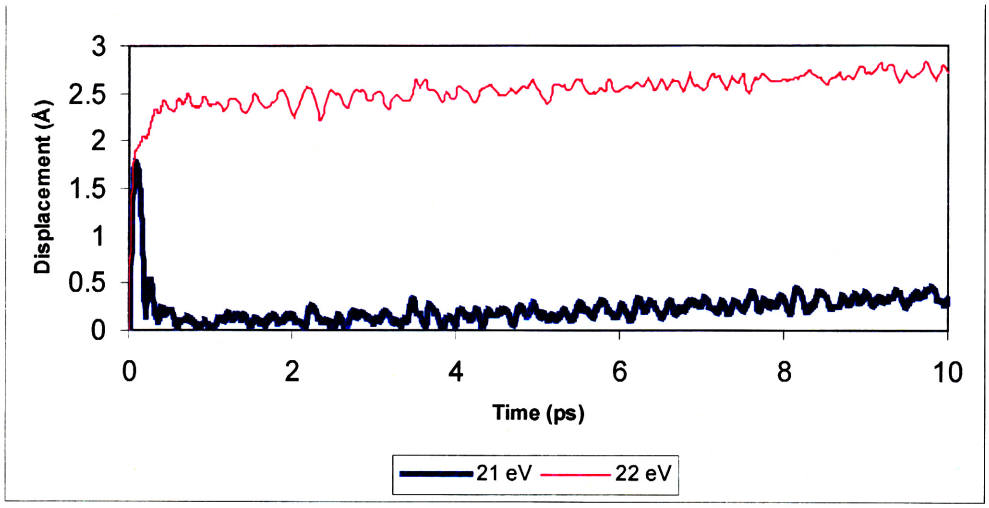

Figure 6.4: Displacement of Zr PKAs with initial velocities toward [101] direction and initial energies of 21 eV and 22 eV.

E_d values of Zr are given in Tables 6.4 and 6.5. The values in Table 6.4 are for those directions that appeared in either [3] or [5], such as [001], [111],

etc. E_d values along these directions are compared to those reported in [3] and [5]. The values in Table 6.5 are for directions toward neighboring atoms and open spaces (NB and OS directions), which have no other published values to compare with. A significant result is that surprisingly small values of E_d for Zr displacement exist (E_d ~ 21-29 eV) in several quite different directions ([101], OS_{234} and OS_{678}). More discussion of the results can be found in Section 6.1.4.

Table 6.4: Threshold displacement energies of Zr along those directions that appeared in either [3] or [5]

Direction		E_d (eV)		
In [3] and this study	In [5]	This study	[3]	[5]
[110]	[110]	[99, 100]	N/A	98
[111]	[111]	[120, 121]	N/A	110
[001]	[001]	[181, 186]	N/A	119
[120]	[210]	[150, 180]	78.8	122
[011]	[101]	[161, 162]	N/A	143
[010]	[100]	[120, 251]	103.2	146
[101]	[011]	[21, 22]	N/A	166
[100]	[010]	[126, 127]	89.2*	N/A

*Metastable. Full-equilibrium not achieved in [3].

Table 6.5: Threshold displacement energies of Zr for directions toward neighboring atoms and open spaces

Direction	NB_1	NB_2	NB_3	NB_4
E_d (eV)	[55, 56]	[110, 180]	[120, 121]	[52, 53]
Direction	NB_5	NB_6	NB_7	NB_8
E_d (eV)	[120, 121]	[99, 100]	[119, 144]	[84, 85]
Direction	OS_{123}	OS_{128}	OS_{135}	OS_{137}
E_d (eV)	[126, 127]	[133, 134]	[133, 148]	[112, 113]
Direction	OS_{138}	OS_{157}	OS_{167}	OS_{234}
E_d (eV)	[34, 35]	[118, 119]	[126, 168]	[24, 25]
Direction	OS_{248}	OS_{345}	OS_{346}	OS_{357}
E_d (eV)	[119, 120]	[80, 81]	[129, 160]	[144, 145]
Direction	OS_{456}	OS_{468}	OS_{567}	OS_{678}
E_d (eV)	[108, 181]	[99, 100]	[48, 49]	[28, 29]

6.1.2 Threshold displacement energies of Si

The process for determining threshold displacement energies of Si is similar to that for Zr. A Si atom near the center of the simulation cell is selected and is shown in Figure 6.5 together with its neighboring O atoms, which are numbered for convenience of reference.

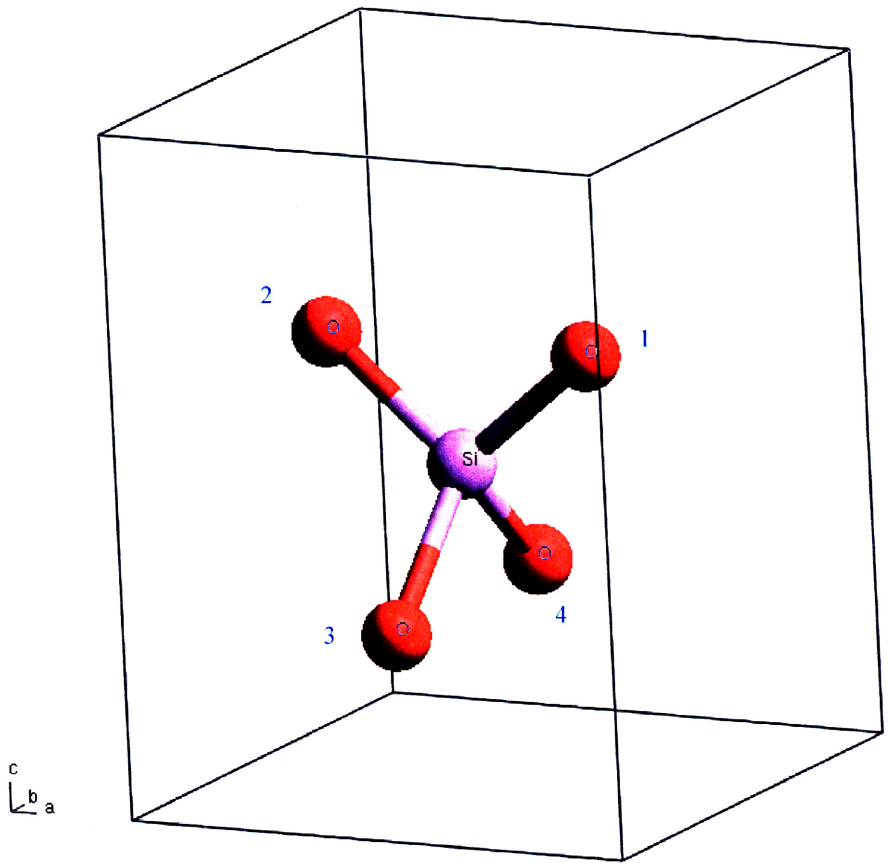

Figure 6.5: A Si atom near the center of the 6x6x6 simulation supercell and its surrounding O atoms. The relative positions of the surrounding oxygen atoms are slightly different from those in experimental zircon crystalline structure, as the atoms shown here are from the structure after 20-ps MD equilibration simulation at temperature of 300 K.

The coordinates of the atoms in Figure 6.5 are given in Table 6.6.

Table 6.6: Coordinates of the atoms shown in Figure 6.5. The location of the origin is insignificant since only the relative positions are important for determining directions.

Atom Name	Atom Number	Coordinates (Unit: Å)
Si	N/A	(0.0386, -0.0105, -3.0015)
O	1	(1.2999, -0.0475, -1.9767)
O	2	(-1.2092, 0.0044, -1.9599)
O	3	(-0.0194, -1.2046, -4.2042)
O	4	(0.0596, 1.2170, -4.1064)

E_d values for Si were determined along the four directions toward neighboring O atoms, NB_1 through NB_4, and four directions toward the most obvious open spaces, OS_{123}, OS_{124}, OS_{134} and OS_{234}. In addition, E_d values along the following crystallographic directions were also determined for the purpose of comparison with those values reported in [3] and [5]: $[0\bar{1}\bar{1}]$, $[11\bar{1}]$, $[111]$, $[101]$, and $[100]$. Direction cosines of all these directions are given in Table 6.7.

Table 6.7: Direction cosines of the directions along which threshold displacement values of the Si atom in Figure 6.5 will be determined

Direction	Direction Cosines
NB_1	(0.7759, -0.0228, 0.6304)
NB_2	(-0.7677, 0.0092, 0.6408)
NB_3	(-0.0342, -0.7042, -0.7092)
NB_4	(0.0127, 0.7432, -0.6690)
OS_{123}	(-0.0298, -0.8150, 0.5788)
OS_{124}	(0.0224, 0.7816, 0.6234)
OS_{134}	(0.6904, -0.0020, -0.7234)
OS_{234}	(-0.7120, 0.0268, -0.7016)
$[0\bar{1}\bar{1}]$	(0.0000, -0.7071, -0.7071)
$[11\bar{1}]$	(0.5774, 0.5774, -0.5774)
$[111]$	(0.5774, 0.5774, 0.5774)
$[101]$	(0.7071, 0.0000, 0.7071)
$[100]$	(1.0000, 0.0000, 0.0000)

Results for Si E_d values are given in Tables 6.8 and 6.9. The values in Table 6.8 are for those directions that appeared in either [3] or [5], such as [100], [111], *etc.* E_d values along these directions are compared to those reported in [3] and [5]. The values in Table 6.9 are for directions toward neighboring atoms and open spaces (NB and OS directions), which have no other published values to compare to. At least three directions ($[11\bar{1}]$, [111] and [100]) yield low E_d values (29-56 eV). More discussion of the results can be found in Section 6.1.4.

Table 6.8: Threshold displacement energies of Si along those directions that appeared in either [3] or [5]

Direction		E_d (eV)		
In [3] and this study	In [5]	This study	[3]	[5]
$[0\bar{1}\bar{1}]$	$[\bar{1}0\bar{1}]$	[140, 251]	N/A	48
$[11\bar{1}]$	$[11\bar{1}]$	[29, 30]	N/A	48
[111]	[111]	[28, 29]	N/A	52
[101]	[011]	[112, 113]	N/A	65
[100]	[010]	[55, 56]	22.6	N/A

Table 6.9: Threshold displacement energies of Si for directions toward neighboring atoms and open spaces

Direction	NB_1	NB_2	NB_3	NB_4
E_d (eV)	[129, 252]	[235, 253]	[209, 272]	[128, 251]
Direction	OS_{123}	OS_{124}	OS_{134}	OS_{234}
E_d (eV)	[76, 77]	[71, 176]	[65, 66]	[88, 89]

6.1.3 Threshold displacement energies of O

The situation for O atoms is a little more complex than that for Zr and Si. An O atom in zircon crystalline structure has one neighboring Si and two neighboring Zr atoms (see, for example, Figure 2.1 in Chapter 2). There are also neighboring O atoms, but their count depends on the chosen O-O cutoff value. The O-O partial RDF plot is shown in Figure 2.18, where the first

three peaks are at distances of 2.431 Å, 2.495 Å and 2.753 Å, respectively. If we include the first peak but not the second (by defining the O-O cutoff value between 2.431 Å and 2.495 Å, such as 2.46 Å), there is only 1 neighboring O atom; if the first two peaks are included, there are 2 neighboring O atoms; if the first three peaks are included, the number of neighboring O atoms becomes 4.

All O atoms are not equivalent in crystalline zircon. For example, in Chapter 2 we discussed that in ZrO_8 triangular dodecahedron four O atoms are closer to Zr than the other four (however, because a simple pair-potential is used to model Zr-O interaction, this fact is not able to be accurately reflected in our model).

For better comparison of E_d values of O with those in [3] and [5], we should choose an O atom near the center of the simulation cell that has the same local environment as the O atoms chosen in [3] and [5]. Reference [3] does not give any information about which O atom was chosen, but Figure 7 of [5] shows the immediate vicinity of the chosen O atom. The chosen O atom in this study, together with all the atoms within 4 Å distance from it, is shown in Figure 6.6. The chosen O atom is the one with the "O" label besides it. It has the same local environment as the O atom in Figure 7 of [5] because the [010] direction of the O atom shown in Figure 6.6 is more or less toward a neighboring O atom, and the O atom in Figure 7 of [5] has the same O atom neighbor in the [100] direction (remember, as discussed in Section 6.1.1, the x and y directions in this study correspond respectively to the y and x directions in [5], so [010] in this study is equivalent to [100] in [5]).

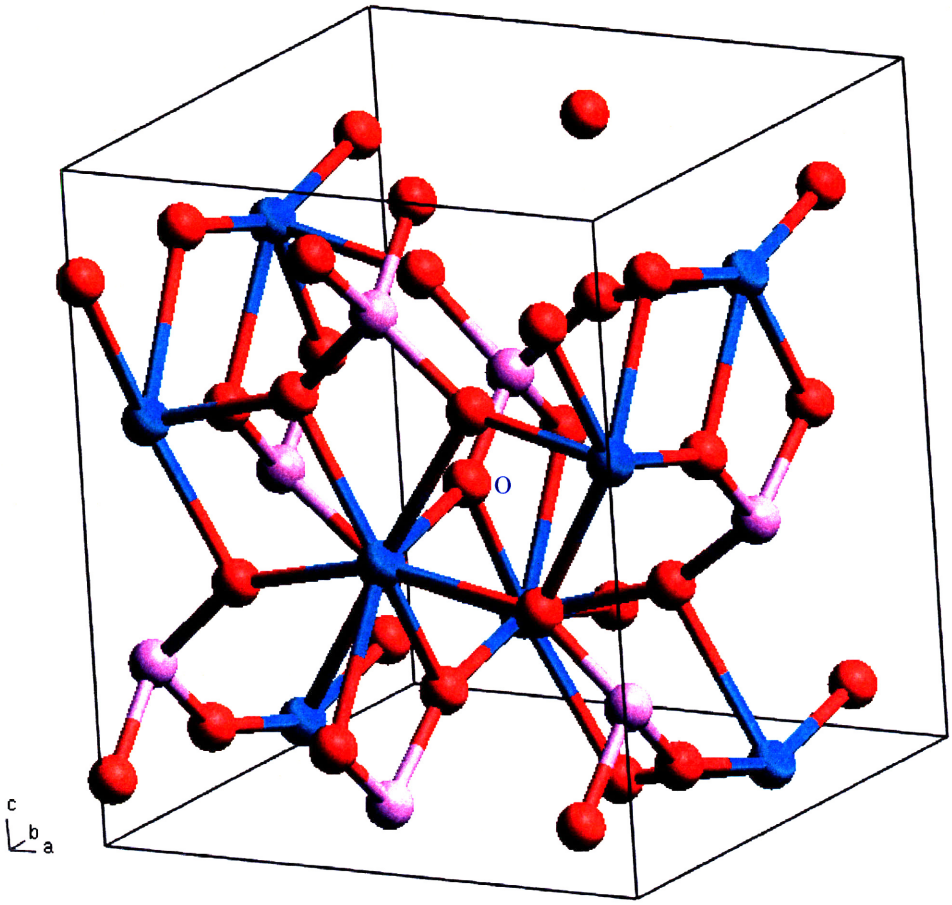

Figure 6.6: An O atom near the center of the simulation cell and all atoms within 4 Å. The O atom in the center with a label "O" is the chosen one.

For the purpose of denoting directions, Figure 6.7 shows the immediate neighborhood of the chosen O atom, with the neighboring Si and Zr atoms numbered for convenience of reference.

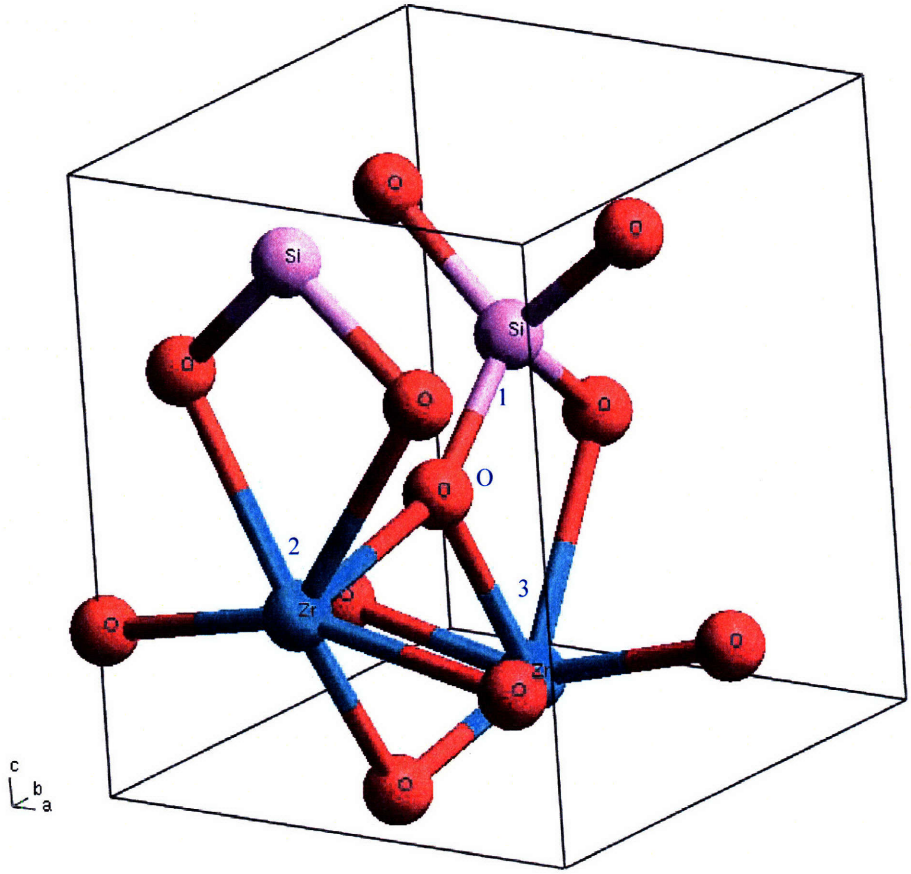

Figure 6.7: An O atom near the center of the simulation cell and all atoms within 3 Å. The O atom in the center with a label "O" is the reference O. Its neighboring Si and Zr atoms are numbered 1, 2, and 3 for convenience of reference and direction labeling.

The O atom and its one Si neighbor and two Zr neighbors are roughly on a plane perpendicular to the x direction. Both in-the-plane and out-of-the-plane directions should be sampled when calculating E_d values. Some obvious choices are the three in-the-plane directions toward neighboring Si and Zr atoms, and [100] and [$\bar{1}$00] directions that are out-of-the-plane and toward very open spaces (the openness of these two directions is apparent in Figure 6.6). In addition, all of the directions considered in [3] and [5] are included for the purpose of comparison. The three directions toward

neighboring Si #1, Zr #2, and Zr #3 are called NB_1, NB_2 and NB_3, respectively. Table 6.10 shows all the directions along which E_d values were determined for O and their corresponding direction cosines.

Table 6.10: Direction cosines of the directions along which threshold displacement energies of the O atom shown in the center of Figure 6.6 were determined

Direction	Direction Cosines
NB_1	(0.0159, 0.7238, 0.6898)
NB_2	(-0.0114, -0.9772, -0.2119)
NB_3	(-0.0145, 0.5220, -0.8528)
[100]	(1.0000, 0.0000, 0.0000)
$[\bar{1}00]$	(-1.0000, 0.0000, 0.0000)
$[20\bar{1}]$	(0.8944, 0.0000, -0.4472)
[111]	(0.5774, 0.5774, 0.5774)
[021]	(0.0000, 0.8944, 0.4472)
[001]	(0.0000, 0.0000, 1.0000)
[010]	(0.0000, 1.0000, 0.0000)
$[0\bar{1}1]$	(0.0000, -0.7071, 0.7071)
[252]	(0.3482, 0.8704, 0.3482)
$[02\bar{1}]$	(0.0000, 0.8944, -0.4472)

Table 6.11 shows the calculated E_d values of the O atom shown in the center of Figure 6.6. A significant number of directions yield low E_d values for O. More discussion of the results can be found in Section 6.1.4.

Table 6.11: Threshold displacement values of O

Direction		E_d (eV)		
In [3] and this study	In [5]	This study	[3]	[5]
NB_1	N/A	[391, 400]	N/A	N/A
NB_2	N/A	[106, 243]	N/A	N/A
NB_3	N/A	[123, 124]	N/A	N/A
$[\bar{1}00]$	$[0\bar{1}0]$	[28, 29]	N/A	N/A
[100]	[010]	[26, 27]	N/A	34
$[20\bar{1}]$	$[02\bar{1}]$	[33, 34]	N/A	23
[111]	[111]	[27, 28]	N/A	44
[021]	[201]	[171, 205]	N/A	68
[001]	[001]	[117, 118]	N/A	82
[010]	[100]	[61, 62]	N/A	93
$[0\bar{1}1]$	$[\bar{1}01]$	[142, 143]	N/A	107
[252]	[522]	[44, 45]	69.4	N/A
$[02\bar{1}]$	$[20\bar{1}]$	[70, 71]	47.3	N/A

6.1.4 Discussion

E_d values of Zr shown in Table 6.4 agree reasonably well with values in [3] or [5], except along direction [101]. The [101] direction is toward very open space, as can be seen in Figure 2.2 of Chapter 2. Along this direction, the Zr atom will be displaced 2.7 Å away from its original site at the end of the 10-ps MD simulation if it is given 22-eV initial energy (see Figure 6.4), so 22-eV energy is indeed enough to displace it. The E_d value along this direction (21.5 eV) is the minimum E_d value of Zr. We don't know why [5] got a much higher E_d value of 166 eV along this direction.

The maximum E_d value of Zr occured along the [010] direction and has a value of 185.5 eV.

Table 6.5 shows the E_d values of Zr along all the NB and OS directions. In this table, all the E_d values that are less than 50 eV are along directions in

the OS series, confirming a simple proposition that E_d values increase as the local environment becomes more closely-packed. But the average values along NB and OS directions, 101.19 eV for NB and 102.97 eV for OS directions, are contrary to this proposition. This may due to over-sampling of certain directions. There is not much justification that we can simply average over the directions we considered, as we have not taken measures to sample directions evenly.

For most directions, E_d values of Zr are reported as ranges with 1-eV width, such as the range [55 eV, 56 eV] for NB_1 direction. However, for certain directions, the ranges reported are much wider, such as the range [129 eV, 160 eV] for the OS_{346} direction. This is not because we didn't perform further simulations to narrow the range down; the ranges simply couldn't be further refined. We'll take the OS_{346} direction as an example. Table 6.12 shows the final displacement of the Zr PKA at the end of the simulation when it is given different initial energies along direction OS_{346}.

Table 6.12: Final displacement of the Zr PKA at the end of the simulation when it is given different initial energies along direction OS_{346}

Energy (eV)	Final Displacement (Å)	Displaced?
125	0.7291	No
126	0.7308	No
127	0.6590	No
128	0.6682	No
129	0.7256	No
130	3.2304	Yes
140	3.3950	Yes
141	4.5528	Yes
142	4.4817	Yes
143	4.4489	Yes
144	4.5776	Yes
145	4.4567	Yes
146	4.5067	Yes
147	4.4481	Yes
148	0.8336	No
149	2.6665	Yes
150	0.8229	No
151	0.7021	No
152	4.7183	Yes
153	0.7837	No
154	4.8090	Yes
155	0.7822	No
156	3.0896	Yes
157	4.4033	Yes
158	4.2388	Yes
159	0.7236	No
160	6.5078	Yes
161	4.1761	Yes
162	3.9476	Yes
163	3.2375	Yes
164	8.3217	Yes
165	8.2318	Yes

The values in the "Displaced?" column of Table 6.12 alternate between "Yes" and "No" in the energy range from 129 eV to 160 eV. Many simulations in which the Zr atom is given initial energies other than those shown in Table 6.12 are also conducted. It is found that whenever the initial

energy is less than 129 eV, the Zr atom is not permanently displaced, whereas whenever the initial energy is greater than 160 eV, it is. So an E_d value for Zr for direction OS_{346} is best reported as [129 eV, 160 eV], as was done in Table 6.5.

The reason for the alteration between displaced and not-displaced in the energy range from 129 eV to 160 eV is probably because of the multiplicity of options for the coordinated displacements of the surrounding atoms without significant energy difference. Besides, atoms are not static. The OS_{346} direction is toward the center of the triangle with vertices at the O atoms #3, #4 and #6. These O atoms are constantly moving. The level of openness of the aperture surrounded by these O atoms can be higher or lower at different times; thus the height of the potential barrier is constantly changing.

This phenomenon not only occurs for Zr PKA and directions toward open spaces, it also happens for other types of directions, such as direction NB_2 of Zr, and other types of PKAs, such as direction OS_{124} of Si and direction NB_2 of O. Since it is a general feature, reporting E_d as a single value, even for a specific direction, is only a simplification of the reality in many cases.

The minimum E_d value of Si occured along direction [111] (28.5 eV) and maximum along direction NB_2 (244 eV). In Table 6.9, the difference between E_d values along the NB directions and those along the OS directions are obvious, with E_d values along NB directions much higher. Compared to those of Zr, the OS directions of Si are toward more open spaces since there are only four O atoms surrounding each Si atom, whereas there are eight surrounding each Zr.

The minimum E_d value of O occurs along direction [100] (26.5 eV). E_d values along direction $[\bar{1}00]$ comes as a close second (27.5 eV). From Figure 6.6 or 6.7, we can see that both these two directions are perpendicular to the plane containing the O atom and its neighboring Si and Zr atoms and are toward very open spaces; they are also symmetric. That's why the E_d values along these two directions are very small and similar. The maximum E_d value of O (395.5 eV) occurs along direction NB_1. This value is unusually high and deserves a closer investigation. The O atom is not permanently displaced with initial energy up to 391 eV. However, damage to the lattice is produced even though the O atom itself returns to its original site. The NB_1 direction is toward the neighboring Si atom (Si #1 in Figure 6.7). Figure 6.8 shows the displacements of the O and Si #1 atoms at different simulation times when the O atom is given an initial energy of 300 eV toward Si #1.

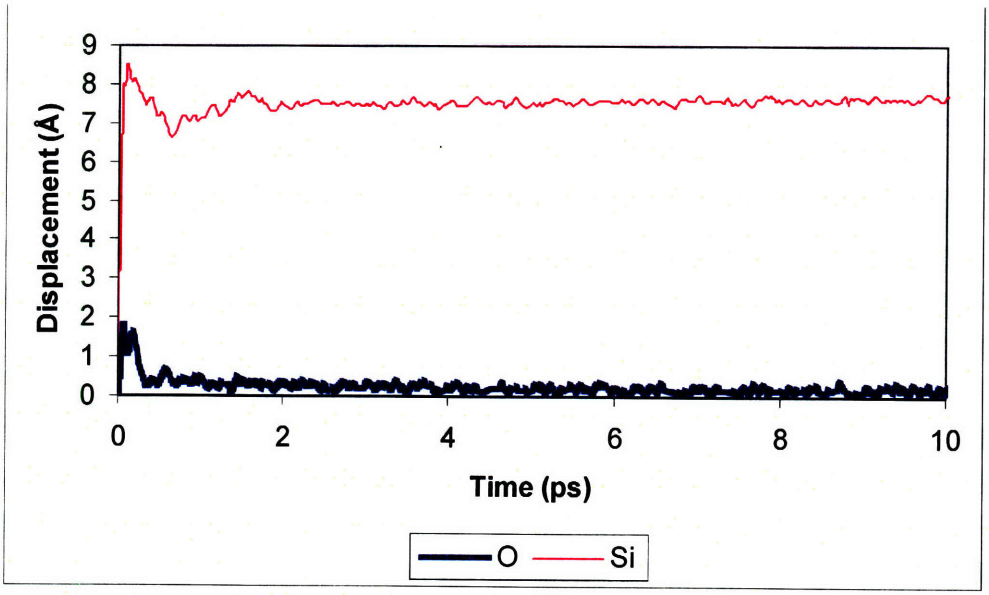

Figure 6.8: Displacements of the O atom in the center of Figure 6.7 and Si #1 at different simulation times when the O atom is given an initial energy of 300 eV toward Si #1. The O atom returned to its original site but the Si atom is displaced about 7.7 Å.

The interatomic distance between O and Si in crystalline zircon is about 1.62 Å. From Figure 6.8, we can see clearly that the maximum displacement of the O atom is roughly the interatomic distance between O and Si. Thus the O atom collided with the Si atom, and then came back to its original site. The Si site is an unstable site for an O atom (see Table 6.14). The Si atom, however, with the energy transferred from the O atom upon colliding, is displaced about 7.7 Å from its original site. So although the O atom is not permanently displaced, displacive damage has been produced in the material lattice. One could argue that, based on this observation, 300 eV is greater than the E_d value of O atom along the NB_1 direction.

Overall, in zircon E_d values are highly direction dependent and tend to be higher in those directions toward more compact local environment. In addition, although not apparent from the E_d values, in zircon Zr is harder to be displaced than Si, and O is the easiest to be displaced (Section 6.11).

6.2 Channeling

One of the advantages of MD simulations over other theoretical damage production models is that the channeling effects are naturally incorporated. Channeling happens when atoms are deflected into open channels in the crystalline structure surrounded by close-packed lines or planes of atoms. Channeled atoms experience reduced nuclear and electronic stopping and, consequently, have long ranges and produce few displacements [7]. Channeling was observed in one of the earliest MD simulations of metals [8].

There are open channels in crystalline zircon structure, such as the obvious one along the *c* direction seen in Figure 2.6. To investigate whether

channeling occurs in this open channel, MD simulations were conducted with a Zr PKA selected according to Figure 6.9. The initial velocity of the PKA was along the $+z$ direction.

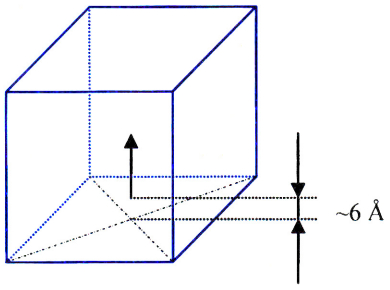

Figure 6.9: Location and initial velocity direction of the PKA for investigating channeling effects. PKA initial location is at the tail of the arrow, which shows PKA's initial velocity direction.

The Zr PKA at its equilibrium site is not in the open channel. For the purpose of our investigation, it is moved manually to the center of the open channel, as shown in Figure 6.10, before the simulation is started. An MD simulation with the PKA at its original site is also conducted for comparison. We will label the simulation with the PKA moved to the open channel as "open-channel", and the simulation without the artificial initial moving of the PKA as "normal". PKA initial energies were 1 keV in both cases.

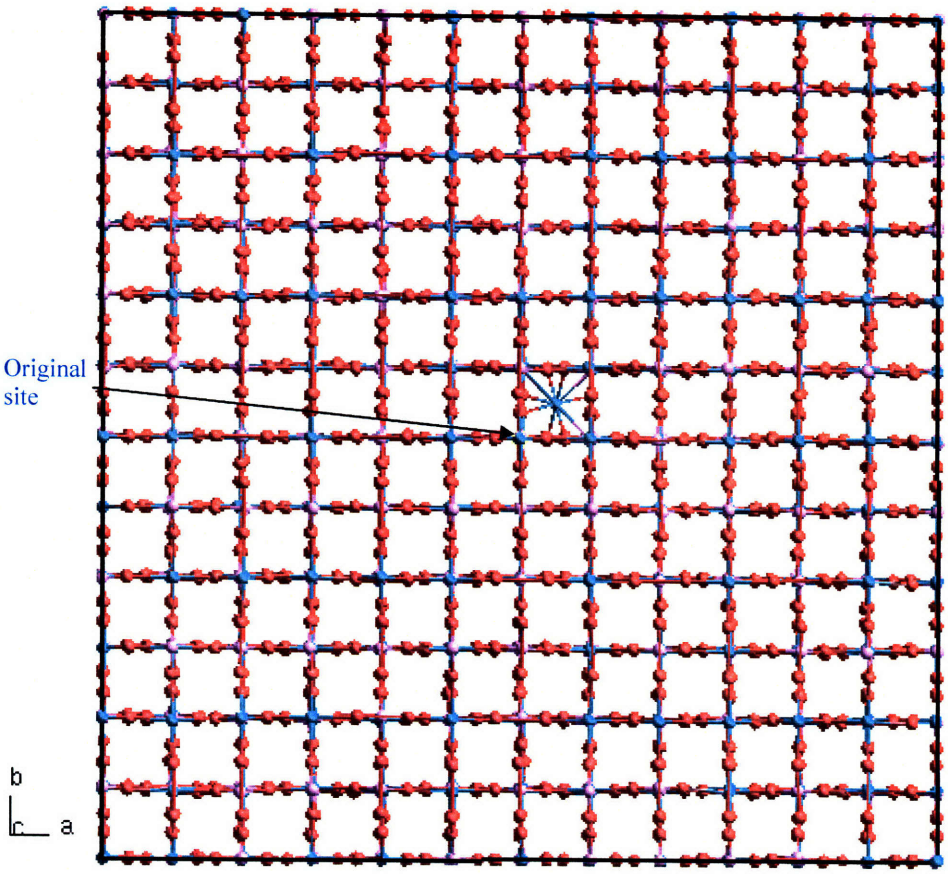

Figure 6.10: The Zr PKA is moved manually from its original site to the center of the open channel. Its nearby original site is also shown.

In Figure 6.10, the channeling walls surrounding the PKA in the open channel have boundaries at $x = 0$, $x = 3.318$, $y = 0$ and $y = 3.318$ Å. If channeling were to happen, the PKA should be confined within the open channel and its x and y coordinates should always be in the range of [0, 3.318 Å]. The z coordinate of the PKA should increase over time because the initial direction is along the $+z$ direction. Table 6.13 shows the PKA locations at different times during the simulation.

Table 6.13: PKA location at different simulation times for both normal and open-channel cases

Time (ps)	Location (Å)	
	Normal Case	Open-channel Case
0.0000	(-0.0289, -0.0059, -12.2106)	(1.6592, 1.6592, -12.2106)
0.0030	(-0.0291, -0.0048, -10.8390)	(1.6505, 1.6493, -10.8350)
0.0060	(-0.0430, -0.0023, -9.5938)	(1.6360, 1.6152, -9.4741)
0.0090	(-0.1339, 0.0034, -8.8275)	(1.6162, 1.5659, -8.1267)
0.0120	(-0.2025, 0.0104, -8.1796)	(1.5895, 1.5222, -6.7907)
0.0150	(-0.2235, 0.0199, -7.5926)	(1.5711, 1.4964, -5.4678)
0.0180	(-0.2312, 0.0292, -7.0330)	(1.5680, 1.4885, -4.1548)
0.0210	(-0.2308, 0.0357, -6.4940)	(1.5853, 1.4789, -2.8530)
0.0240	(-0.2222, 0.0368, -5.9708)	(1.5991, 1.4733, -1.5638)
0.0270	(-0.2071, 0.0328, -5.4599)	(1.6029, 1.4805, -0.2857)
0.0300	(-0.1896, 0.0295, -4.9700)	(1.6030, 1.4912, 0.9799)
0.0330	(-0.1765, 0.0389, -4.5191)	(1.5995, 1.5051, 2.2298)
0.0360	(-0.1755, 0.0650, -4.1174)	(1.5944, 1.5197, 3.4680)
0.0390	(-0.1953, 0.0950, -3.7655)	(1.5876, 1.5392, 4.6967)
0.0420	(-0.2425, 0.1207, -3.4595)	(1.5789, 1.5749, 5.9145)
0.0450	(-0.3147, 0.1452, -3.1842)	(1.5801, 1.6307, 7.1209)
0.0480	(-0.4034, 0.1762, -2.9273)	(1.5942, 1.6894, 8.3159)
0.0510	(-0.5005, 0.2207, -2.6868)	(1.6123, 1.7387, 9.4981)
0.0540	(-0.6025, 0.2828, -2.4675)	(1.6204, 1.7785, 10.6660)
0.0570	(-0.7079, 0.3617, -2.2684)	(1.6179, 1.8199, 11.8170)
0.0600	(-0.8132, 0.4515, -2.0819)	(1.6218, 1.8659, 12.9490)
0.0630	(-0.9154, 0.5454, -1.9023)	(1.6342, 1.8956, 14.0580)
0.0660	(-1.0143, 0.6381, -1.7284)	(1.6589, 1.9026, 15.1420)
0.0690	(-1.1108, 0.7258, -1.5602)	(1.6772, 1.8825, 16.2080)
0.0720	(-1.2060, 0.8062, -1.3986)	(1.6751, 1.8668, 16.6070)
0.0750	(-1.3018, 0.8782, -1.2449)	(1.6538, 1.8544, 16.8740)
0.0780	(-1.4017, 0.9424, -1.1010)	(1.6195, 1.8478, 17.1030)
0.0810	(-1.5100, 1.0013, -0.9689)	(1.5851, 1.8489, 17.3000)
0.0840	(-1.6303, 1.0588, -0.8510)	(1.5620, 1.8582, 17.4740)
0.0870	(-1.7633, 1.1179, -0.7478)	(1.5534, 1.8748, 17.6280)
0.0900	(-1.9060, 1.1786, -0.6574)	(1.5545, 1.8975, 17.7700)
0.0930	(-2.0535, 1.2389, -0.5767)	Reached Simulation Cell Boundary

Although both simulations are run to 10 ps, Table 6.13 only shows coordinates up to 93 fs, because that was when the Zr PKA in the open-

channel case reached the simulation cell boundary. We could have increased the simulation cell size and redone the simulation, but this proved unnecessary, since the current simulations were already sufficient to demonstrate the channeling effects. In the normal case, the PKA's x and y coordinates changed quite a bit due to collisions with neighboring atoms. From the data in Table 6.13, at time 93 fs the PKA had already moved 2.02 Å in the x direction and 1.24 Å in the y direction. At the end of the entire 10-ps simulation, the PKA moved from initial position (-0.0289 Å, -0.0059 Å, -12.2106 Å) to final position (-3.2029 Å, 3.0966 Å, 0.2242 Å). The displacements along x, y, and z directions were 3.17 Å, 3.10 Å, and 12.43 Å, respectively. The PKA was never close to the simulation cell boundary during the entire course of the simulation. For the open channel case, however, the PKA was unable to move significant distances along either x or y direction due to the potential barrier imposed by the atoms in the channel wall. In fact, before reaching the simulation cell boundary, the PKA's displacements along x and y directions were never greater than 0.1 Å and 0.3 Å, respectively.

Figure 6.11 shows the displacements along the z direction of both open-channel and normal cases. The channeling effect is apparent from the comparison of the two curves.

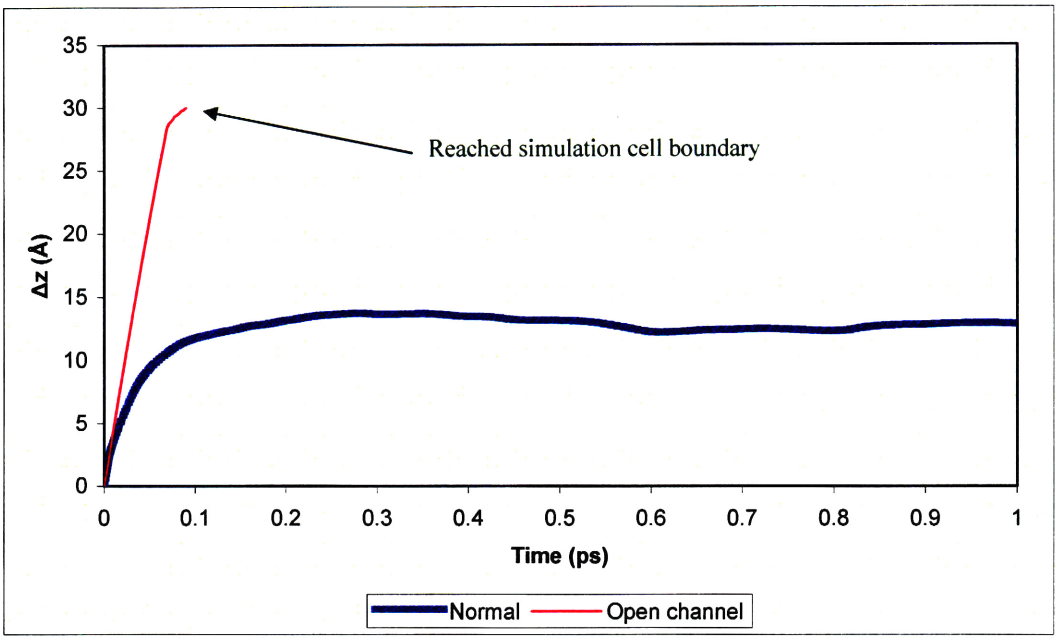

Figure 6.11: Displacements along the z direction of the PKAs in normal and open-channel simulations. After about 0.1 ps, the PKA in the open-channel case reached simulation cell boundary and its displacement along the z direction was already about 30 Å. In the normal case, however, the PKA was stabilized after about 0.5 ps and its displacement along the z direction was about 14 Å. It never came close to the simulation cell boundary.

Channeling makes it easier for atoms to travel longer distance, thus results in Frenkel pairs with longer separations. It also takes energy away from the location where the PKA is produced. When traveling in the open channels, atoms graze off the atoms on the channel wall, transferring so little energy that most of the atoms are not displaced. Figure 6.12 compares the number of ever-displaced atoms (see definition in Section 6.9) in normal and open-channel cases.

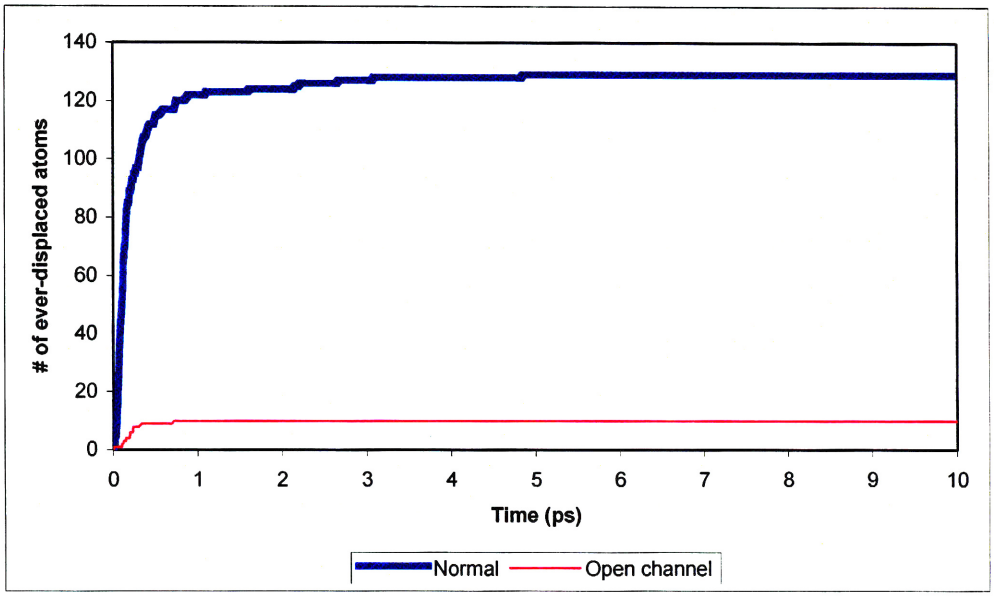

Figure 6.12: The number of ever-displaced atoms for both normal and open-channel cases. When channeling occurs, the number of ever-displaced atoms dramatically reduces.

Figure 6.12 shows that the number of ever-displaced atoms dramatically decreased when channeling occurred. Channeled atoms moved long distances while producing little damage. Thus, theoretical models that don't take channeling effects into consideration may overestimate radiation damage to material lattices.

6.3 Stability of anti-site defects

In zircon, an anti-site defect can be either a cation-cation or a cation-anion replacement. There is no anion-anion anti-site in zircon since there is only one type of anion, O, in the structure. There are in total six possible anti-site configurations: Zr on Si site, Zr on O site, Si on Zr site, Si on O site, O on Zr site, and O on Si site.

A MD simulation is run for each type of anti-site defect. For example, to

investigate the stability of the anti-site of a Zr atom on a Si site, a Si atom near the center of a 6x6x6 simulation cell was selected and its identity was changed to Zr. To keep the overall balance of atom species and charges, a Zr atom near the simulation cell boundary was chosen and its identity was changed to Si. This location is as far away as possible from where we have changed a Si to Zr so the interaction between the two anti-sites is minimized. A 10-ps MD simulation was then performed and the displacement of the Zr atom residing on a Si site is recorded. Depending on the value of this displacement, we can determine whether this anti-site is stable or not. Simulations for investigating the stability of other kinds of anti-site defects are similar. Results are given in Table 6.14.

Table 6.14: Stability of anti-site defects

Anti-site type	Displacement at the end of 10-ps simulation (Å)	Stable?
Zr on Si site	0.2153	Yes
Zr on O site	1.4181	No
Si on Zr site	1.1904	No
Si on O site	1.6929	No
O on Zr site	0.2730	Yes
O on Si site	2.0708	No

Two types of anti-sites were stable in our current model: Zr on Si site and O on Zr site. The latter one is especially interesting since it is an anion residing on a cation site. Further investigation of such intriguing defect possibilities would need to take specific account of the probability of strong O-O molecule bonding stabilizing such defect configurations.

6.4 Linear collision sequence

At low recoil energies, the cascade event may be dominated by linear collision sequences [7]. Linear collision sequences were predicted by R.H.

Silsbee [9] and were shown to arise in the first MD simulations of damage production [8].

A focuson and a dynamic crowdion are two kinds of focused linear collision sequences. A focuson can transfer a large amount of energy away from the PKA site while a dynamic crowdion transports matter as well as energy. A dynamic crowdion is a series of replacement events occurring along straight rows of atoms. Both focusons and crowdions significantly reduce the amount of damage produced.

Figure 6.13 shows a linear sequence of atoms in zircon crystalline structure along y direction. Unlike in simple structures such as bcc and fcc, these atoms are not exactly on a straight line. In addition, this sequence is heterogeneous, containing both Zr and O atoms.

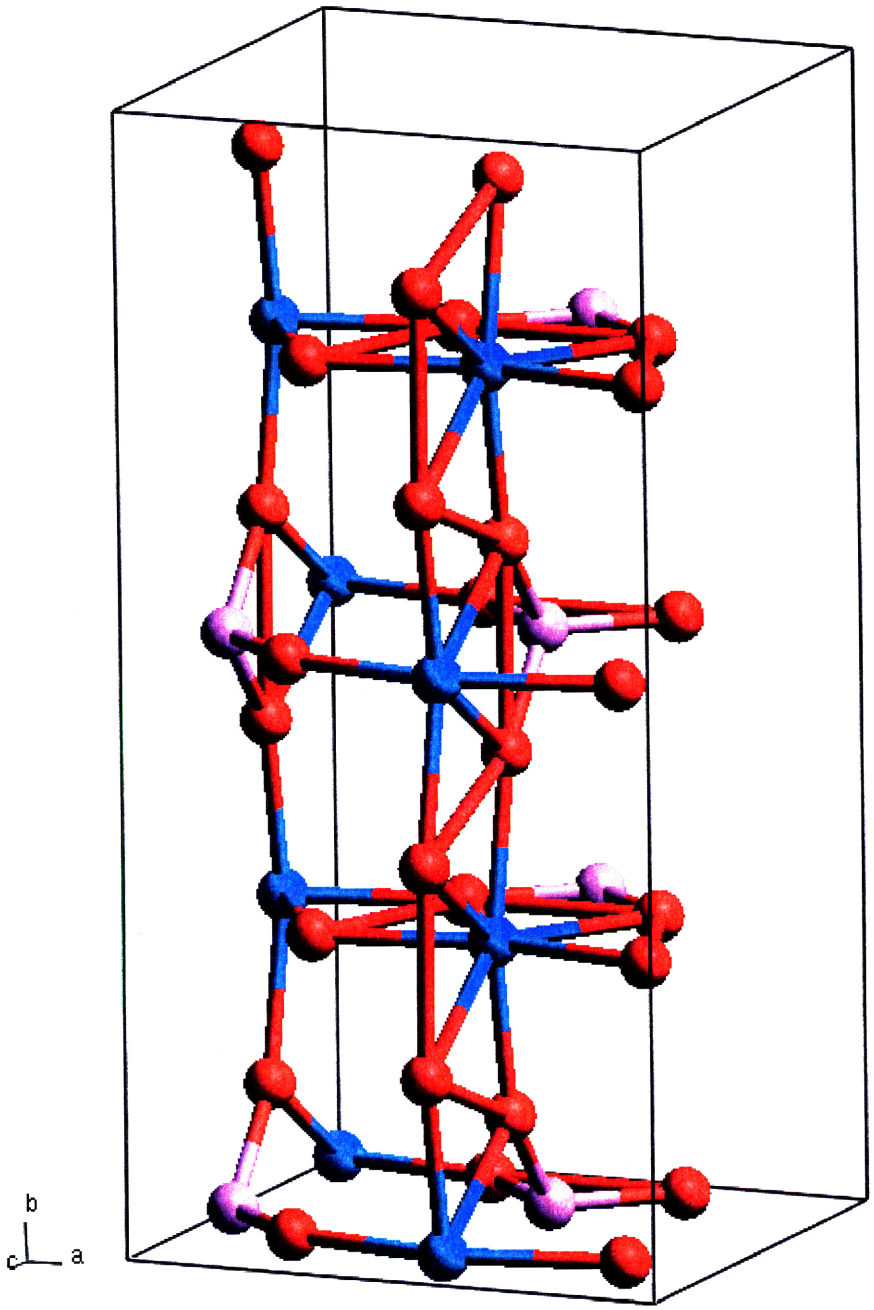

Figure 6.13: The linear sequence of Zr and O atoms along *y* direction

To investigate whether linear collision sequences occur, a Zr atom was selected as the PKA, similar to what's shown in Figure 5.19 except instead

of selecting a Zr atom near the left boundary, a Zr atom was selected near the "front" boundary. The PKA was given an initial velocity toward $+y$ direction. The initial energy of the PKA was 200 eV.

For convenience of reference, the Zr PKA and the atoms that are on the linear sequence along the $+y$ direction are numbered. The Zr PKA is numbered 0, and it is called Zr-0; the O atom next to it in the linear sequence along the $+y$ direction is numbered 1, and it is called O-1; the next O atom is called O-2, the next Zr atom Zr-3, and so on and so forth. Figure 6.14 shows the y coordinates of atoms from Zr-0 through O-13 at different simulation times.

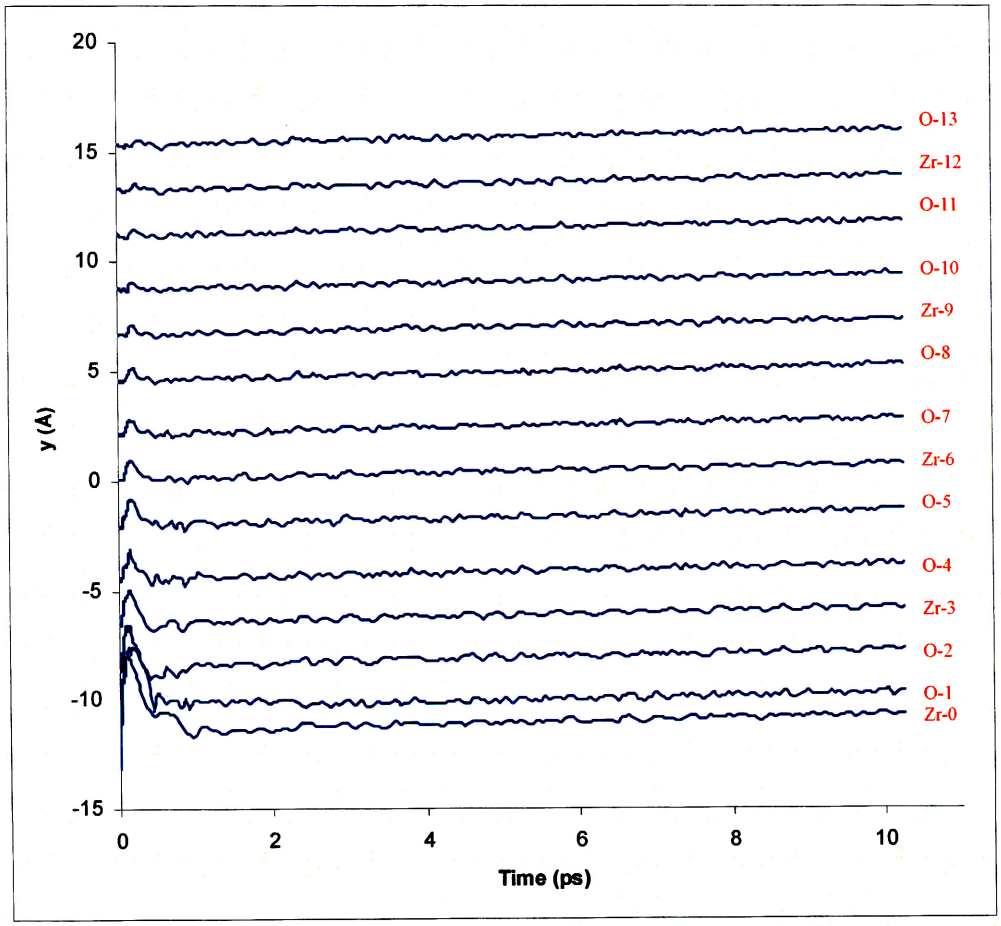

Figure 6.14: The y coordinates of atoms in the linear sequence

The linear collision sequence is apparent in Figure 6.14. Every atom in the linear sequence has moved synergically along $+y$ direction. The first few atoms (Zr-0 through about O-5) initially had surges of displacements (the peaks in Figure 6.14) along $+y$ direction, but eventually retreated about half-way back. The higher numbered atoms, starting roughly from O-8, initially had a small displacement along $-y$ direction, but once they felt the energy transferred from the PKA, they were displaced along $+y$ direction for about 0.8 Å. The atom O-13 in Figure 6.14 moved about 0.74 Å along $+y$ direction at the end of the 10-ps simulation. O-13 was already 28.5 Å away from the PKA Zr-0, so the PKA's energy was transferred far away by the linear collision sequence.

Figure 6.15 shows the angle between directions of atom displacements and the $+y$ direction for atoms Zr-0, O-4, Zr-9 and O-13. The general trend is increase of focus (decrease of the angle between direction of displacement and the $+y$ direction) along the linear collision sequence from atom Zr-0 to atom O-13. The increase of focus is not strict, as can be seen by the relative positions of curves for Zr-9 and O-13 near the end of the simulation in Figure 6.15, but the general trend is valid.

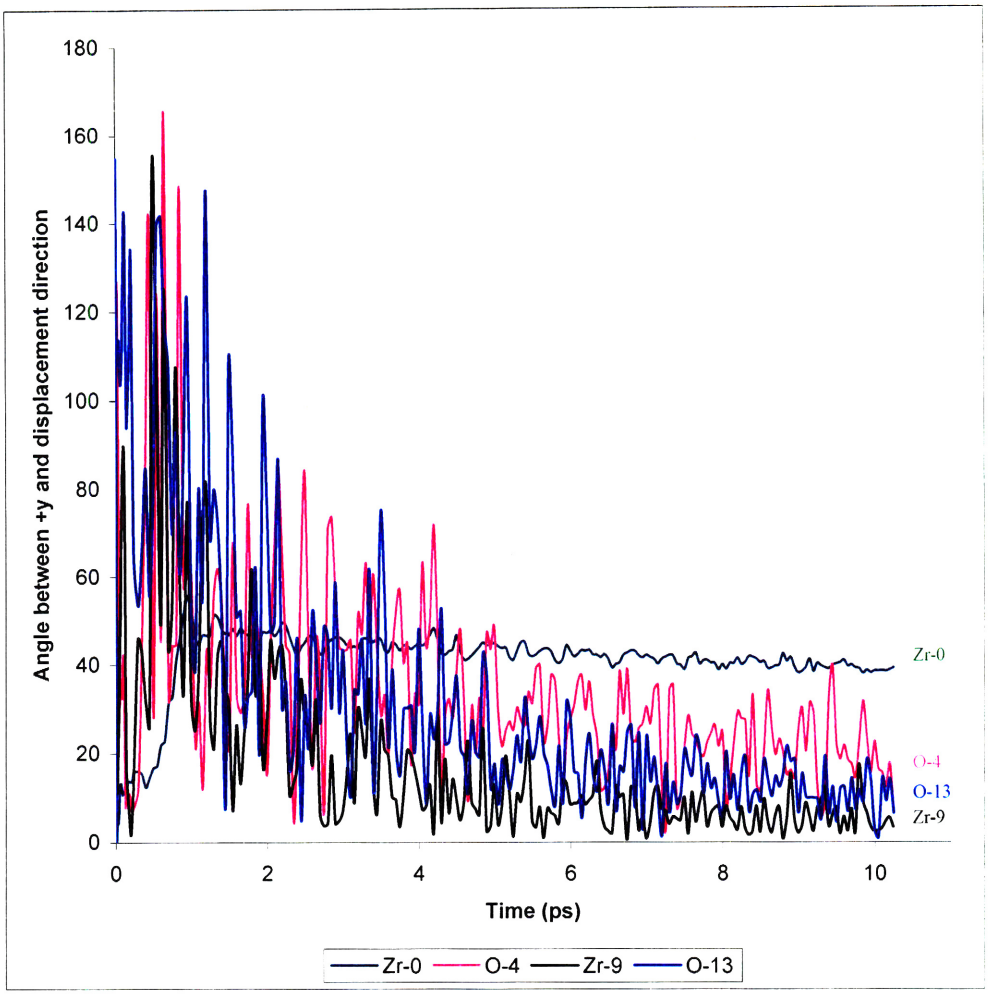

Figure 6.15: (Color) Angle between displacement direction and +*y* direction for atoms Zr-0, O-4, Zr-9 and O-13. The general trend is increase focusing along the linear collision sequence from Zr-0 to O-13.

Thus we have seen that a linear collision sequence has indeed occurred along the [010] direction. It started as a chain of quasi-replacement sequences but later degraded into a focuson which transfers energy without additional displacements or damage production. The starting portion of the linear collision sequence transferred matter as well as energy, as Zr-0 was displaced 2.5 Å along the +*y* direction, O-1 was displaced 1.5 Å, O-2 was displaced 1.0 Å, *etc*. However, it may be called "quasi-replacement sequence" instead of "replacement sequence" because, for example, Zr-0

does not take O-1's site. Zr-0 is displaced 2.1 Å laterally relative to $+y$ direction and its displacement has a 40° angle with $+y$ direction. This agrees with the fact that Zr is not stable on an O site, as shown in Table 6.14.

6.5 Radiation-induced amorphization

This section simulates zircon's amorphization by irradiation. Multiple 5-keV Zr PKAs were used to render a 6x6x6 supercell amorphous. Simulations were conducted using constant volume ensemble. The simulation cell is not big enough to contain the entire cascade engendered by the PKA. The parts of the cascades that entered the constant temperature boundary layer were subdued by the velocity rescaling there. The cascades were thus "cut off" by the constant temperature layer and only parts of the cascades are kept. The overlap of cascades and the boundary layer is unavoidable, since we want to use collision cascades to amorphize the entire structure, including those parts near the constant temperature boundary. However, since we are not investigating the shapes or extents of the cascades, this should not be a problem. In this instance we are only interested in the final zircon structure as the aftermath of the (partial) cascades.

The PKA initial locations were just outside the constant temperature boundary layer and their initial velocity directions were toward the center of the simulation cell to maximize their damages to the structure. The PKAs used were not from the same initial location. Four PKAs were fired near each of the six boundaries of the simulation cell. They were evenly spaced on a plane just outside the constant temperature layer, as shown in Figure 6.16.

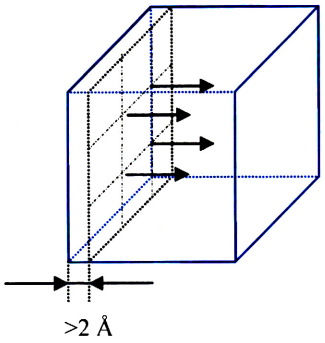

Figure 6.16: Four PKAs near the *-x* boundary of the simulation cell. The PKA initial locations are at the ends of the arrows, which denote PKA's initial velocity directions. Four PKAs are introduced near each of the six boundaries.

Figure 6.16 shows the four PKAs used near the left boundary of the simulation cell. Each PKA, except the first one, was introduced 2 ps after its previous PKA. Similar to what's shown in Figure 6.16, four PKAs were introduced near each of the six boundaries. In total, 24 PKAs were used. At 2 ps after introducing the 24^{th} PKA, the structure was equilibrated at 300 K for 10 ps.

The number of ever-displaced atoms (see definition in Section 6.9) at the end of the final equilibration simulation was 3310. Out of a total number of 5184 atoms, this corresponds to a radiation dose of 0.64 dpa. Since we did not count multiple displacements of an atom during the calculation of the number of ever-displaced atoms, the real dose is likely to be higher. Nonetheless, both 0.64 dpa and the undetermined higher real dose value should be enough to complete the disordering transformation of zircon, but are still one or two orders of magnitude lower than the dose required for other radiation-damage phenomena, such as void swelling [10]. Figure 6.17 shows the final structure at the end of the final 10-ps equilibration simulation at 300 K. It appears to be largely amorphous, except for the

boundary layers.

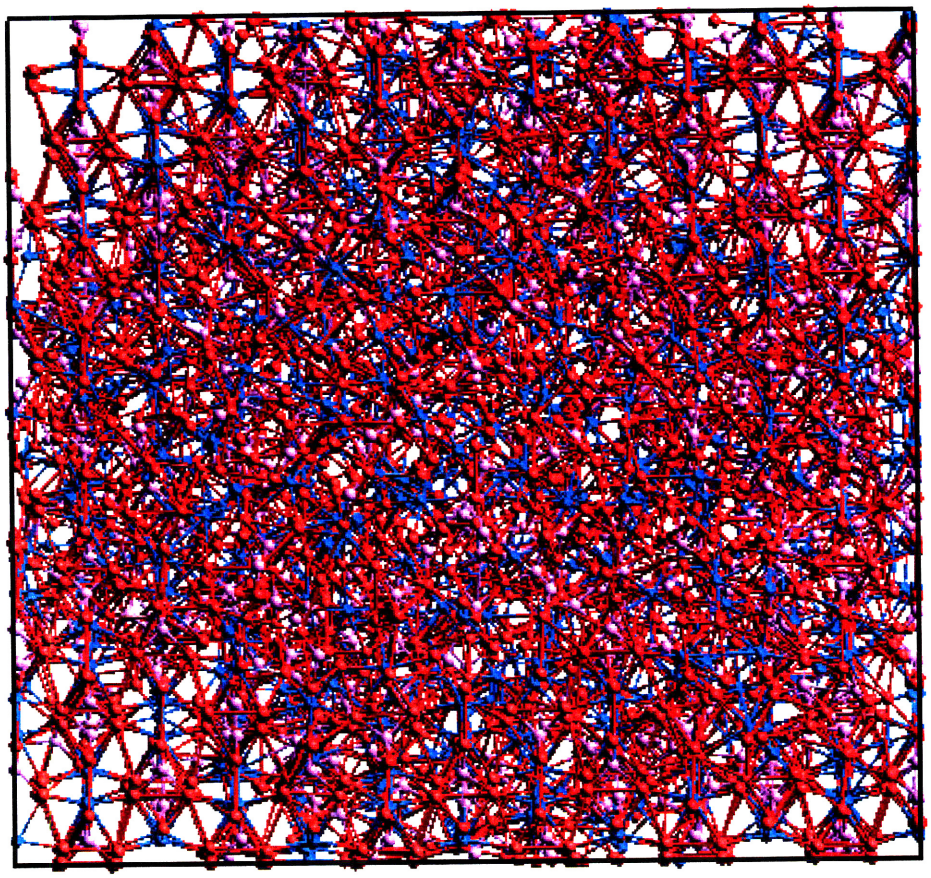

Figure 6.17: Zircon structure after 24 5-keV PKAs and the final 10-ps equilibration simulation at 300 K using constant volume ensemble.

We mentioned above that there were altogether 3310 atoms ever-displaced, which means there are still 1874 atoms that were never displaced. These atoms are shown in Figure 6.18. As expected, they are all near simulation cell boundaries where velocity rescaling was applied to keep the temperature at 300 K.

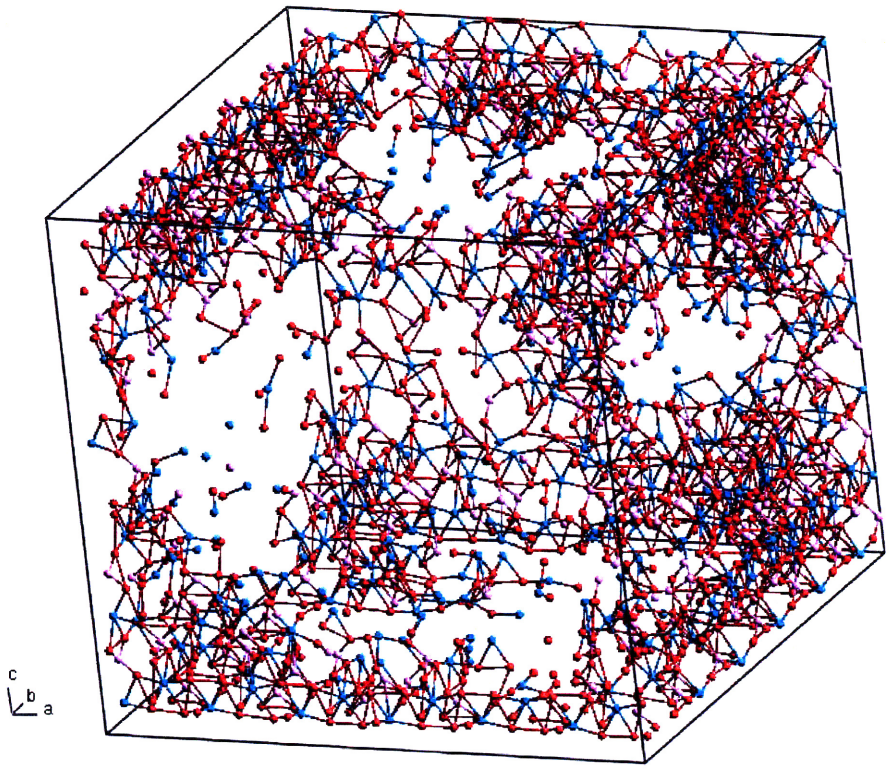

Figure 6.18: Atoms of Figure 6.17 that are not displaced. They are all near simulation cell boundaries where velocity rescaling was applied to keep temperature at 300 K.

The structure shown in Figure 6.17 was analyzed and topologically compared to crystalline, melt and melt-quenched zircon structures in Chapter 7.

6.6 Radiation-induced swelling

In Section 6.5, simulations were conducted using a constant volume ensemble. The zircon structure was rendered amorphous by multiple PKAs. In theory, we can also investigate radiation-induced swelling by using the same PKAs to amorphize zircon, but this time using constant pressure instead of constant volume ensemble. However, things did not work quite as

expected. Figures 6.19 and 6.20 plot volume expansions of the system during the first and second PKAs, respectively.

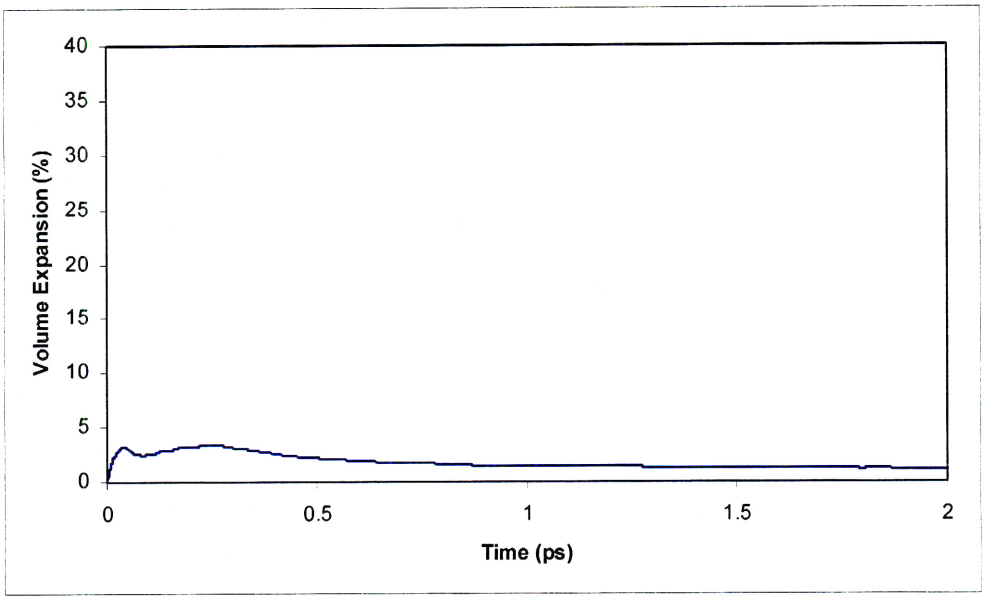

Figure 6.19: Volume expansion during simulation of the first PKA when using constant pressure ensemble. Expansion seems to be reasonable.

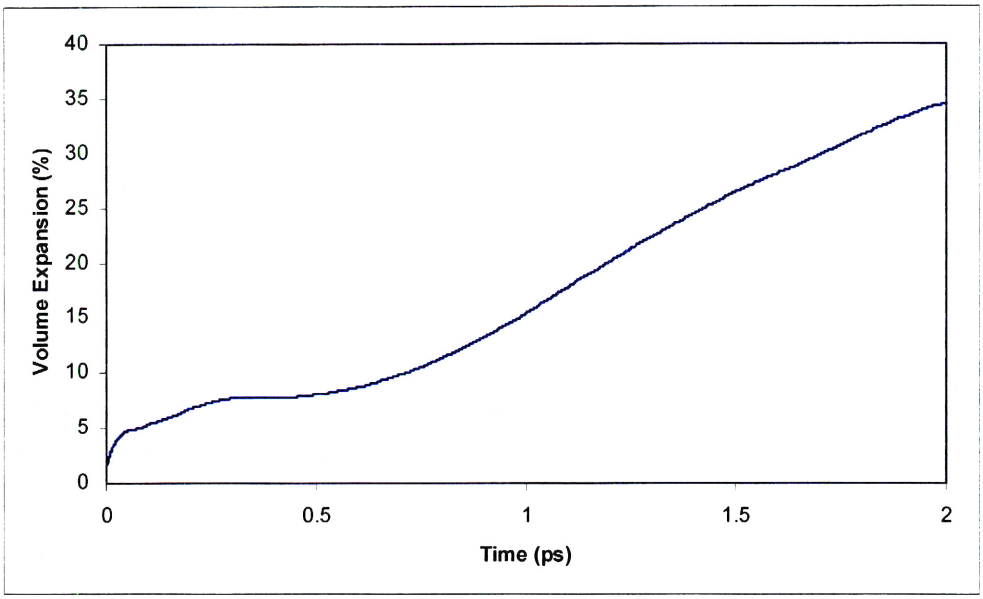

Figure 6.20: Volume expansion during simulation of the second PKA when using constant pressure ensemble. Expansion seems to be too large.

The volume expansion due to the first PKA was about 1.2%. Although there are no experimental data to compare to, this value at least seems to be reasonable. However, starting from the second PKA, the system broke down. In Figure 6.20, volume expansion soared to about 35%, much more than the 18% of experimentally observed swelling in amorphous zircon [11, 12].

In Section 6.5 when investigating radiation-induced amorphization, we used 24 PKAs to amorphize the structure before finally equilibrated the structure for 10 ps, all using constant volume ensemble. Another method to investigate radiation-induced swelling is to keep using a constant volume ensemble in the simulations with the 24 PKAs, but then use a constant pressure ensemble in the final equilibration step. The volume expansion during the final equilibration step is shown in Figure 6.21. Once again the large volume expansion (about 42%) is seen. So the abnormal volume expansion is unlikely to have been caused by the way we combined a constant pressure ensemble and collision cascades together, since the volume expansion in Figure 6.21 is still very large when the combination is not used.

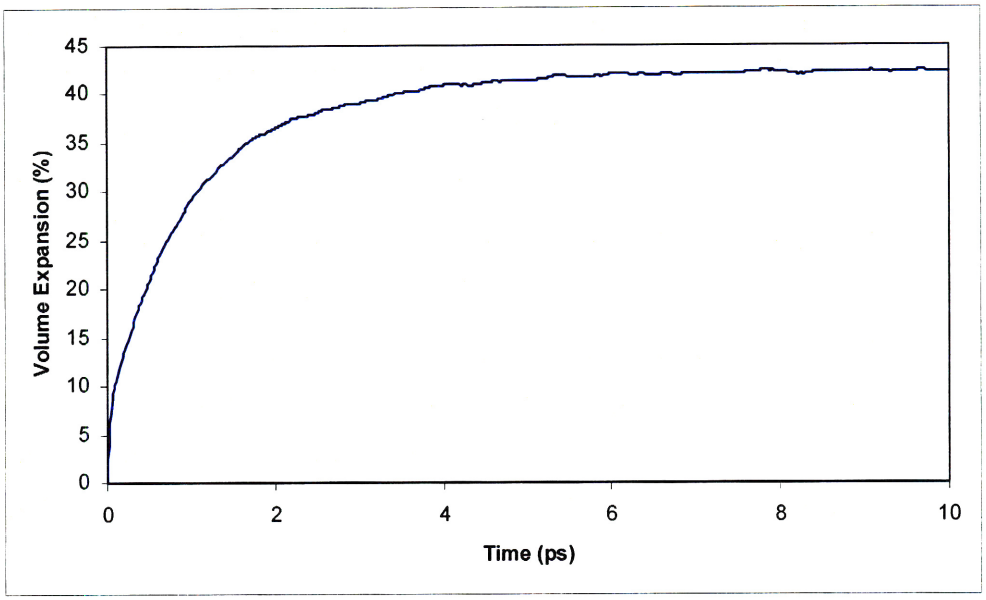

Figure 6.21: The volume expansion during the final equilibration step when constant pressure ensemble is used. The simulations for the collision cascades of the 24 PKAs are conducted using constant volume ensemble.

This abnormal volume expansion reminds us of Figure 4.6, where the volume expansion of zircon at 5000 K was shown to be about 90%. All these unrealistic huge volume expansions may come from the same source, namely unbalanced ion charges, as explained below. In our potential model, Zr, Si and O have charges of +3.8, +2.0, and -1.45, respectively. From experiments, we know that at high temperatures zircon decomposes into ZrO_2 and SiO_2 (Figure 4.1). This phase separation also happens when zircon is amorphized by irradiation. In the current model, ZrO_2 and SiO_2 will not be charge neutral, but have charges of +0.9 and -0.9, respectively. The Coulomb repulsive forces within phases of ZrO_2 and SiO_2 are likely the driving force of the huge volume expansion.

The solution is to choose ion charges so that ZrO_2 and SiO_2 maintain charge neutrality. We chose O's charge to be -1.0, -1.2, -1.4, -1.6, -1.8 and -2.0, respectively. The charges of Zr and Si are fixed once O's charge is chosen, if

ZrO_2 and SiO_2 are to remain charge-neutral. After changing ion charges, other potential parameters also need to be changed. This was done by using code GULP to do a fitting of potential parameters to zircon crystalline structure and elastic constants, starting from parameters in the current potential (potential #4 in Chapter 3) and using the new ion charges. The newly obtained potentials are called charge-balanced potentials and were used to determine stable zircon crystalline structure and to calculate some of zircon's equilibrium properties. Results are given in Table 6.15.

Table 6.15: Zircon structure parameters, elastic constants and other properties using charge-balanced potentials

Property	Experi-mental	Original Potential	Charge of O in charge-balanced potential					
			-1.0	-1.2	-1.4	-1.6	-1.8	-2.0
Volume ($Å^3$)	261.13	265.59 +1.71%	262.48 +0.52%	262.33 +0.46%	263.51 +0.91%	264.56 +1.31%	264.77 +1.39%	265.19 +1.55%
a (Å)	6.607	6.602 -0.08%	6.574 -0.50%	6.525 -1.24%	6.494 -1.71%	6.456 -2.29%	6.417 -2.88%	6.384 -3.38%
c (Å)	5.982	6.093 +1.86%	6.074 +1.54%	6.162 +3.01%	6.248 +4.45%	6.348 +6.12%	6.430 +7.49%	6.509 +8.81%
Bulk Modulus (GPa)	225.0	223.12 -0.84%	218.54 -2.87%	231.27 +2.79%	226.13 +0.50%	225.28 +0.12%	239.73 +6.55%	273.05 +21.36%
C_{11} (GPa)	424.0	445.36 +5.04%	440.18 +3.82%	455.29 +7.38%	460.42 +8.59%	482.16 +13.72%	516.19 +21.74%	566.56 +33.62%
C_{33} (GPa)	490.0	479.19 -2.21%	401.59 -18.04%	425.18 -13.23%	408.32 -16.67%	409.16 -16.50%	436.43 -10.93%	469.10 -4.27%
C_{44} (GPa)	114.0	84.35 -26.01%	53.64 -52.95%	76.95 -32.50%	59.52 -47.79%	29.37 -74.24%	4.61 -95.96%	18.84 -83.47%
C_{66} (GPa)	49.0	63.87 +30.35%	13.42 -72.61%	33.48 -31.67%	46.09 -5.94%	47.15 -3.78%	38.66 -21.10%	40.07 -18.22%
C_{12} (GPa)	70.0	64.08 -8.46%	87.77 +25.39%	104.91 -49.87%	115.17 +64.53%	103.46 +47.80%	91.91 31.30%	114.20 +63.14%
C_{13} (GPa)	149.0	133.17 -10.62%	127.34 -14.54%	133.97 -10.09%	120.14 -19.37%	113.84 -23.60%	127.25 -14.60%	158.16 +6.15%

No charge-balanced potential in Table 6.15 had a better overall performance, as far as zircon stable structure and equilibrium properties are concerned, than the original potential we used. The potential with an O charge of -1.2 was the best among all the charge-balanced potentials, because none of the properties calculated using it has a worse than 50% difference from experimental value. All other charge-balanced potentials gave one or more calculated properties more than 50% off the experimental values. We have

used the charge-balanced potential with an O charge of -1.2 and call it *the charge-balanced potential* hereafter.

Using the charge-balanced potential, zircon at 5000 K had a molar volume of 4.69×10^{-5} m^3/mol. In Section 3.3, the experimental molar volume of zircon was shown to be 3.92×10^{-5} m^3/mol, so the volume expansion is about 19.6%, much better than the 90% expansion using the original potential. However, at 300 K, the stable structure using the charge-balanced potential had a molar volume of 3.42×10^{-5} m^3/mol, which is about 12.8% less than the experimental value. (Because of this and the calculated properties shown in Table 6.15, the charge-balanced potential without further optimizations is not as good as the original potential we used, except perhaps in the cases when the structure amorphizes while a constant pressure ensemble is used.) Perhaps it is more meaningful to judge the charge-balanced potential using the volume expansion from 300 K to 5000 K, which is about 37.1%. This value is higher than experimental value but better than the value of 90% using the original potential. The volume expansion value could possibly be brought in line with the experimental value with further adjustment of the short-range potential parameters.

Radiation-induced swelling behaved very well under the charge-balanced potential, even without any further potential optimizations. The same process as in Section 6.5 was used to amorphize the zircon structure, with only two modifications: using the charge-balanced potential instead of the original potential; using the constant pressure ensemble instead of constant temperature. The huge volume swelling shown in Figure 6.20 did not occur in the new simulations. In fact, at the end of the final equilibration step, the molar volume stabilized at about 3.55×10^{-5} m^3/mol, which is about 4% more than the equilibrium molar volume of 3.42×10^{-5} m^3/mol at 300 K

using the charge-balanced potential.

The number of ever-displaced atoms when using the charge-balanced potential was similar to (although slightly smaller than) that when using the original potential, so the levels of amorphization of the radiation-induced amorphous structures using the two kinds of potentials were similar. The radiation-induced volume expansion of 4% integrated over the simulation cell is not close to the experimental value, which is about 18% [11, 12, 13]. However, it should be emphasized that our incentive for introducing the charge-balanced potential was the anomalously large volume expansion upon amorphization when the constant pressure ensemble was used with the original potential, and now the swelling is brought under control. Also, the volume change of 4% was that averaged over the whole cell and is less than the larger swelling value in the center of the overlapping cascades.

Thus, the anomalously large volume swelling shown in such figures as Figure 4.6, Figure 6.20 and Figure 6.21 was caused by the non-neutrality of SiO_2 and ZrO_2 units, which are created when zircon structure is amorphized either thermally or by irradiation. We tried to produce a charge-balanced potential with better overall performance than our original potential, to no avail. Consequently, the new charge-balanced potential was used only in amorphization of zircon structures using the constant pressure ensemble, while most of the simulations were still conducted using the original potential.

6.7 Time scale of collision cascade process

During the initial ballistic stage of collision cascade, the PKA energy is redistributed among hundreds or thousands of atoms in a very short time.

We can consider the initial ballistic stage finished once the energy of the most energetic atom in the system (call it E_{max}) falls below a chosen threshold energy (call it E_0). As seen in Figure 5.25, E_{max} reduces to just a few eV in a time of a fraction of 1 ps.

Often there were fluctuations in E_{max} values. E_{max} might be less than E_0 at time t1, but be greater than E_0 again at a later time t2 > t1. In this study, we used the last time that $E_{max} > E_0$ as the time at the end of ballistic stage (call it t_b). Figure 6.22 illustrates the methodology using a fictional (not from real simulation) E_{max} against time curve. Assume we have chosen $E_0 = 20$ eV. In Figure 6.22, E_{max} first becomes less than E_0 at about 0.1 ps, but the t_b value in this fictional setup is where the thick segment between 0.4 and 0.5 ps intersects with the E = 20 eV horizontal line, because this is the last time E_{max} is greater than E_0 (assuming E_{max} is always less than E_0 after 1 ps).

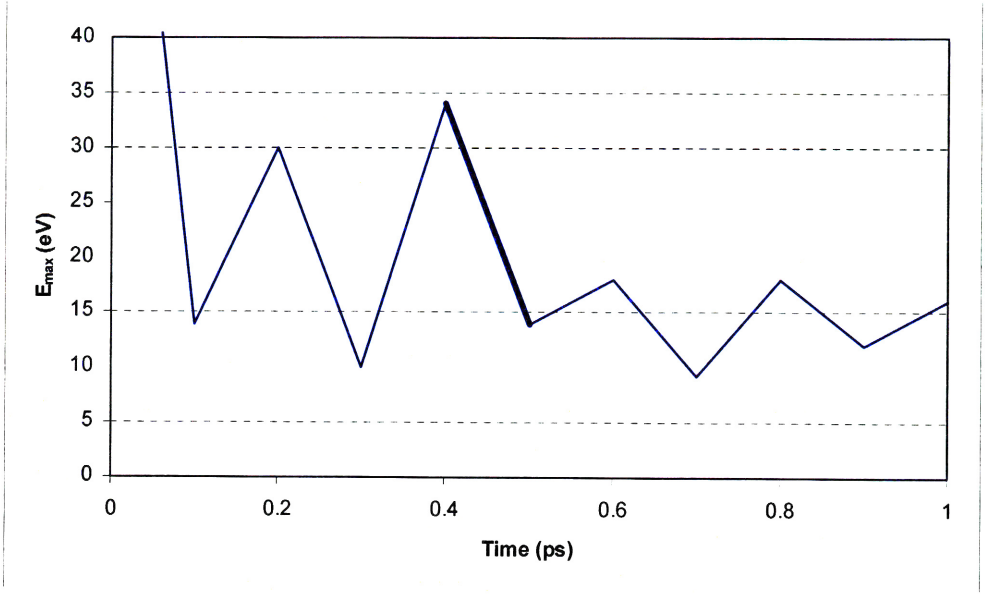

Figure 6.22: Fictitious E_{max} against simulation time curve to illustrate the methodology used to determine the time scale of ballistic stage. If threshold energy E_0 is chosen to be 20 eV, the last time $E_{max} > E_0$ is where the thick segment between 0.4 and 0.5 ps intersects with the E = 20 eV horizontal line,

which is the t_b value sought.

In Section 6.1, we have seen that the minimum energy required to displace an atom in zircon is about 20 eV, so 20 eV is a reasonable choice for the threshold energy E_0. E_0 values of 15 and 25 eV were also used to test t_b's sensitivity to E_0. Results of t_b values are shown in Figure 6.23 for simulations using both Zr and U PKAs, with PKA energies from 100 eV up to 10 keV.

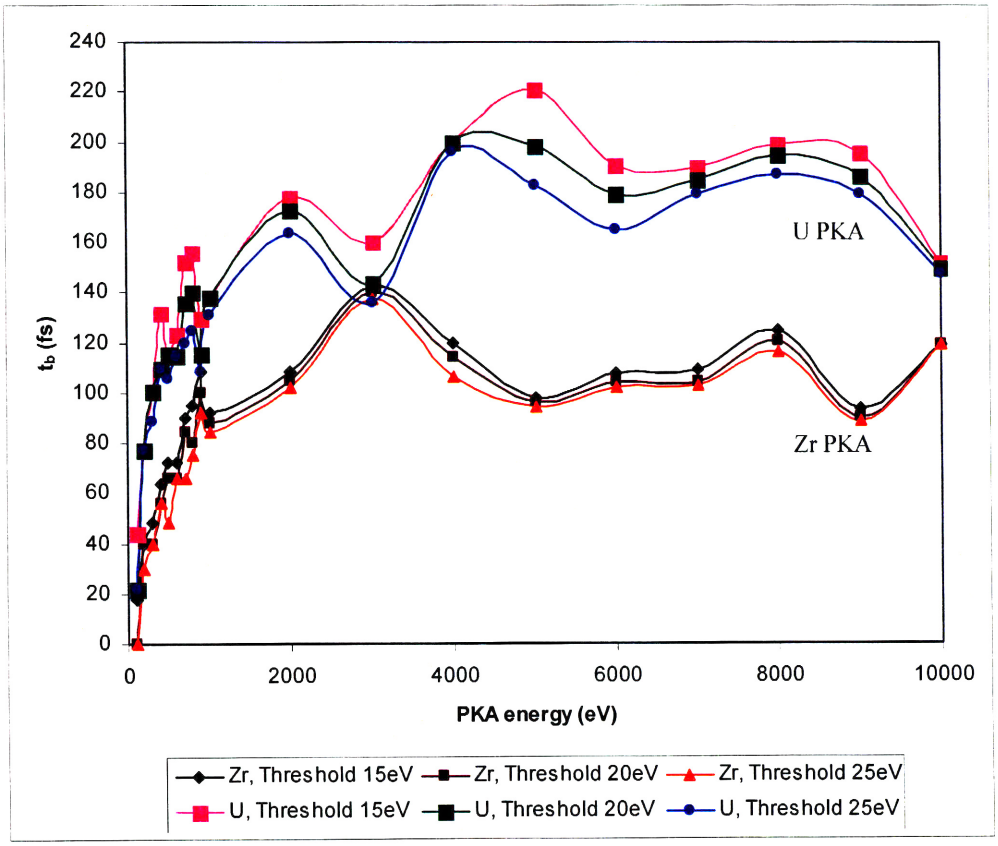

Figure 6.23: Time scale of the ballistic stage of collision cascades

Several conclusions can be made from the curves in Figure 6.23

1) When PKA energy is less than about 3 keV, t_b depends strongly on

PKA energy and is larger for more energetic PKAs. However, when PKA energy is greater than about 3 keV, t_b is more or less stable about a fixed value. For a U PKA, it stabilizes around 180 fs; for a Zr PKA, around 100 fs.

2) The t_b value is larger for heavier PKAs, since the curves for U PKA are above the curves for Zr. In other words, the ballistic stage of collision cascade is longer for more massive PKAs.
3) The t_b value is not very sensitive to changes in chosen threshold energy values. The curves for E_0 = 15, E_0 = 20 and E_0 = 25 eV are close to each other.

The ballistic stage lasts about 0.1 ps according to Figure 6.23. This value falls in the range of 10^{-15} to 10^{-12} seconds presented by Park *et al.* [5] and agrees very well with the ~100 fs value provided by Robinson [7]. The next stage of "cooling down" of the cascade region to ambient temperature takes one order of magnitude longer, in the range of a few pico-seconds, as shown in the figures of Section 5.8.

6.8 Extent of cascade

Using the criterion developed in Section 5.7, we can determine the atoms that are highly influenced by the collision cascade, from which the extent of the cascade can be determined. If the crystallographic features of the structure were ignored, we would expect the extent of the cascade to be longer along the longitudinal direction and shorter along the lateral direction, as in the results calculated by Corrales *et al.* [14] using modified SRIM (Stopping and Range of Ions in Matter) code [15] with only the ZBL potential [15]. A part of their results is shown in Table 5.2, and we can see that, for various PKA energies, the cascade extent along the longitudinal

direction is roughly three times the extent along the lateral direction. In our simulations, since the initial PKA direction was toward $+x$ direction, we would expect the extent of cascade to be larger along the x direction than along y and z directions, based solely on the SRIM calculations. However, it is not the case if crystallographic features of zircon are taken into account. The channeling effects along the z direction were discussed in Section 6.2 and the linear collision sequence along y direction discussed in Section 6.4 will contribute to the widening of cascade extent along those two directions, as evidenced by the results given in Table 6.16.

Table 6.16 Extent of cascade

Zr PKA Energy	Extent of cascade (Å)			U PKA Energy	Extent of cascade (Å)		
	x	y	z		x	y	z
100 eV	8.582	6.149	7.989	100 eV	8.852	8.030	9.553
200 eV	11.723	8.356	8.965	200 eV	16.023	7.168	20.881
300 eV	16.204	11.090	10.534	300 eV	15.585	10.693	10.330
400 eV	16.023	13.765	13.765	400 eV	19.133	14.272	12.941
500 eV	15.100	14.888	13.007	500 eV	16.801	13.104	15.293
600 eV	19.276	17.295	14.759	600 eV	22.548	13.952	14.599
700 eV	18.819	20.868	15.461	700 eV	22.726	17.166	15.511
800 eV	23.634	21.417	19.078	800 eV	23.359	17.268	14.990
900 eV	25.757	21.171	22.618	900 eV	24.845	18.781	17.207
1 keV	23.137	20.894	25.757	1 keV	25.887	22.731	21.798
2 keV	33.626	29.686	30.491	2 keV	26.881	27.263	28.406
3 keV*	>44.058	>27.126	>36.385	3 keV	40.569	31.457	30.575
4 keV*	>40.854	>32.039	>42.781	4 keV*	>37.224	>29.212	>42.788
5 keV*	>53.500	>45.429	>42.787	5 keV*	>46.674	>35.173	>42.561
6 keV*	>46.842	>37.069	>42.774	6 keV*	>46.587	>34.079	>42.790
7 keV*	>52.819	>46.363	>42.789	7 keV*	>48.072	>39.594	>42.789
8 keV*	>44.758	>30.632	>42.790	8 keV*	>50.349	>40.817	>42.788
9 keV*	>52.948	>37.517	>42.788	9 keV*	>54.337	>40.811	>42.786
10 keV*	>71.510	>46.363	>42.409	10 keV*	>54.994	>39.730	>42.788

* Simulation cell not large enough to contain the cascade along z direction

The data in Table 6.16 with a ">" sign are calculated from those simulations using simulation cells not large enough to contain the entire collision cascade along z direction. For example, for the simulation using Zr 10-keV PKA, a 12x7x7 supercell with altogether 14,112 atoms was used. This

simulation cell was not large enough to contain the cascade along z direction. For it to be large enough, we need to enlarge the simulation cell quite a lot along the z direction, because atoms are able to travel very long distances with very small energy losses along the open channels of z direction, as seen in Section 6.2. We didn't enlarge the simulation cell due to the huge extra computation time required. The simulations that used not-large-enough simulation cells are clearly marked in this study and their results should be viewed cautiously. However, we made sure that the simulation cell was always large enough along the x direction, which is the direction that absorbs the majority of the PKA's impact. Thus, we expect the approximations to be good enough; and most of the defects, which subsequently important in evaluating structural and property changes, are believed to have been captured.

According to the results in Table 6.16, the cascade extent along the longitudinal direction is still larger than along lateral directions in most of the simulations, but the differences are not as much as those predicted in [14], calculated using the SRIM code. When the PKA energy is large enough for channeling effects to occur along the z direction, the cascade extent along z direction sometimes is even larger than the extent along the x direction (Zr 1-keV PKA and U 2-keV PKA cases, for example).

The difference in cascade extent using Zr or U PKA is small, even though U has more than twice the mass of Zr. A more massive PKA thus does not dramatically either enlarge or shrink the spatial extent of the region affected by the collision cascade.

Channeling and linear collision sequences can bring a cascade's influence to very large distance and as a result enlarge the cascade extent data in Table

6.16. When the cascade extends a along the x direction, b along the y direction, and c along the z direction, it does not mean that every atom within the $a \times b \times c$ volume element is part of the cascade. In fact, only a small fraction of them are. From this perspective, the number of ever-displaced atoms might be a better criterion to describe cascade strengths than the extent of the cascade, which will be calculated in next section.

Sub-cascades were detected in more energetic simulations. For example, the final structure after 10-ps simulation of a cascade using a 10-keV Zr PKA is shown in Figures 6.24 and 6.25, viewed from two different angles. Two sub-cascades are apparent in the figures. The shapes of the sub-cascades look similar to those cascades bought about by PKAs with smaller energies. If higher-energy Zr PKAs always result in production of sub-cascades, a proposition neither proven nor disproven in this study, the cascades caused by Zr PKAs with energies up to 10 keV may contain all the relevant physics of single-cascade behaviors. No sub-cascades are detected for simulations using U PKA with energies up to 10 keV.

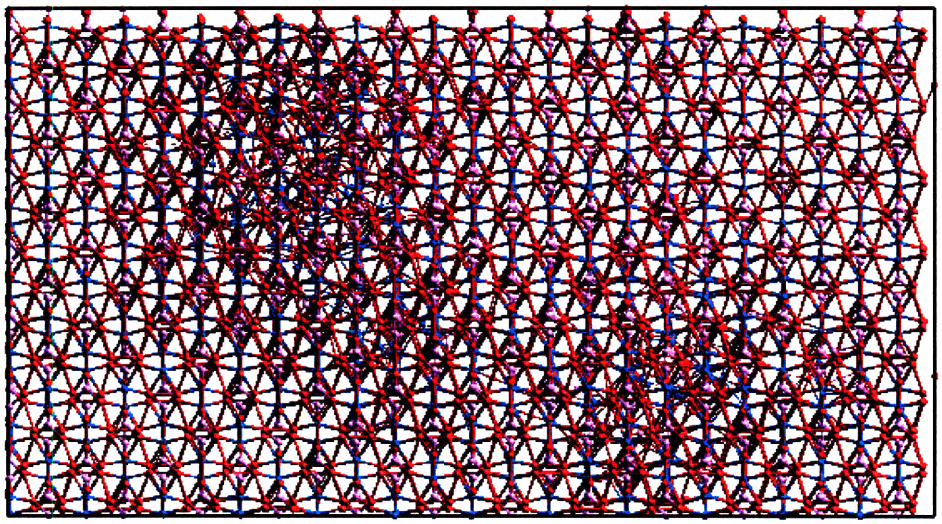

Figure 6.24: Zircon structure after 10-ps simulation using 10-keV Zr PKA, viewed from the $[0\bar{1}0]$ direction. Two sub-cascades can be discerned.

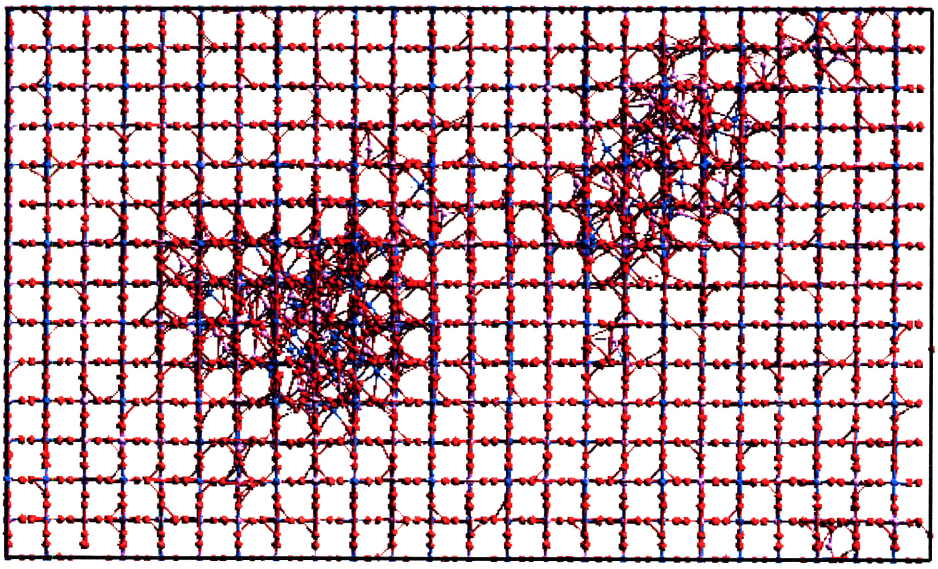

Figure 6.25: Zircon structure after 10-ps simulation using a 10-keV Zr PKA, viewed from the [001] direction. Two sub-cascades can be discerned.

PKA displacement is much different from cascade extent, since the PKA can transfer energy to other atoms which then continue to enlarge the cascade. Table 6.17 shows the displacements of Zr and U PKAs with various initial

energies. It can be seen that PKA displacement along the x direction is only about half of, or less than half of, the extent of the cascade along the x direction in Table 6.16. U travelled farther than Zr along the x direction, because U is much heavier and thus less prone to changing direction.

Table 6.17: Displacements of Zr and U PKAs with various initial energies. A displacement of (a, b, c) means at the end of the 10-ps simulation, the PKA has moved a in the x direction, b in the y direction and c in the z direction.

PKA	Displacement (Å)	PKA	Displacement (Å)
Zr, 100 eV	(0.9085, -0.0224, 0.1722)	U, 100 eV	(2.9450, 0.9655, 0.6763)
Zr, 200 eV	(3.8629, -1.7803, -0.5900)	U, 200 eV	(7.9745, -0.3816, -0.6898)
Zr, 300 eV	(7.4545, -0.0453, -2.2819)	U, 300 eV	(9.4366, 0.0461, -2.1310)
Zr, 400 eV	(7.9581, -0.8108, -2.5926)	U, 400 eV	(11.5209, 0.0689, -1.8907)
Zr, 500 eV	(7.8036, -1.5936, -0.9551)	U, 500 eV	(11.9644, -0.0363, -2.7994)
Zr, 600 eV	(8.7926, 0.0754, -1.7099)	U, 600 eV	(14.2117, 0.0108, -2.8197)
Zr, 700 eV	(6.0110, 0.1755, -1.9929)	U, 700 eV	(14.1107, -0.0063, -2.3881)
Zr, 800 eV	(6.8714, -0.2881, 2.6557)	U, 800 eV	(17.0073, 0.0533, -1.9507)
Zr, 900 eV	(7.7660, -0.0408, 2.7470)	U, 900 eV	(13.6637, -0.0076, -2.2575)
Zr, 1 keV	(10.4664, -3.4987, 3.1897)	U, 1 keV	(13.8165, -1.4817, -0.6176)
Zr, 2 keV	(23.8019, 0.2356, -4.2768)	U, 2 keV	(19.9733, -5.1453, 2.0826)
Zr, 3 keV*	(36.8776, 0.1969, -16.3870)	U, 3 keV	(20.1199, 3.3331, 7.0646)
Zr, 4 keV**	(26.9303, 7.9192, -20.2685)	U, 4 keV*	(29.0399, 4.1766, -15.7340)
Zr, 5 keV**	(20.3516, 6.6235, -21.1525)	U, 5 keV*	(39.7700, 6.9268, 15.4827)
Zr, 6 keV*	(29.6058, 2.4859, 14.9395)	U, 6 keV*	(24.5391, -5.1863, 14.9985)
Zr, 7 keV**	(35.1658, -0.0268, 21.9595)	U, 7 keV*	(30.0164, -3.5116, 11.8035)
Zr, 8 keV**	(33.4196, 1.8903, -20.5075)	U, 8 keV*	(30.7418, -4.7238, 17.8125)
Zr, 9 keV**	(26.5230, -5.7598, 20.3898)	U, 9 keV*	(35.0312, -12.7709, 19.2198)
Zr, 10 keV**	(39.7957, 7.2408, -19.8730)	U, 10 keV**	(34.3911, -10.5129, 20.0718)

* Simulation cell was not large enough to contain the entire cascade along the z direction

** Simulation cell was not large enough to contain the entire cascade along the z direction and PKA ended near simulation cell boundary and thus was affected by the velocity scaling there

PKA displacement along the y direction was much smaller than that along the x or z directions. The displacement was understandably large along the x direction, since this is the PKA's initial direction. It is also large along the z direction, due to the channeling described in Section 6.2, which is not available along the y direction. From the data in Table 6.17, we can see that channeling occurred for Zr PKAs with kinetic energy 3 keV and more, and for U PKAs with energy 4 keV and more.

Figure 6.26 plots PKA displacements along the x direction against PKA initial energy. When PKA energy is small, channeling doesn't occur and a U PKA travels farther along the x direction than a Zr PKA. When PKA energy is larger than about 3 keV, however, channeling occurs and the PKA propagation distance along the x direction becomes similar for U and Zr PKAs. PKAs never travel more than about 4 nm along the x direction in our simulations. Although simulations with more energetic PKAs were not conducted due to limited computing resources, we can reasonably expect that those PKAs would also be channeled into the open channels along the z direction and consequently would not be able to travel the longitudinal distances calculated by Corrales *et al.* [14] using the modified SRIM (Stopping and Range of Ions in Matter) code [15]. The latter totally ignores the crystalline structure and predicts, for example, that a 30-keV Zr PKA will travel 15.2 nm and a 70-keV PKA 29.0 nm along the longitudinal direction.

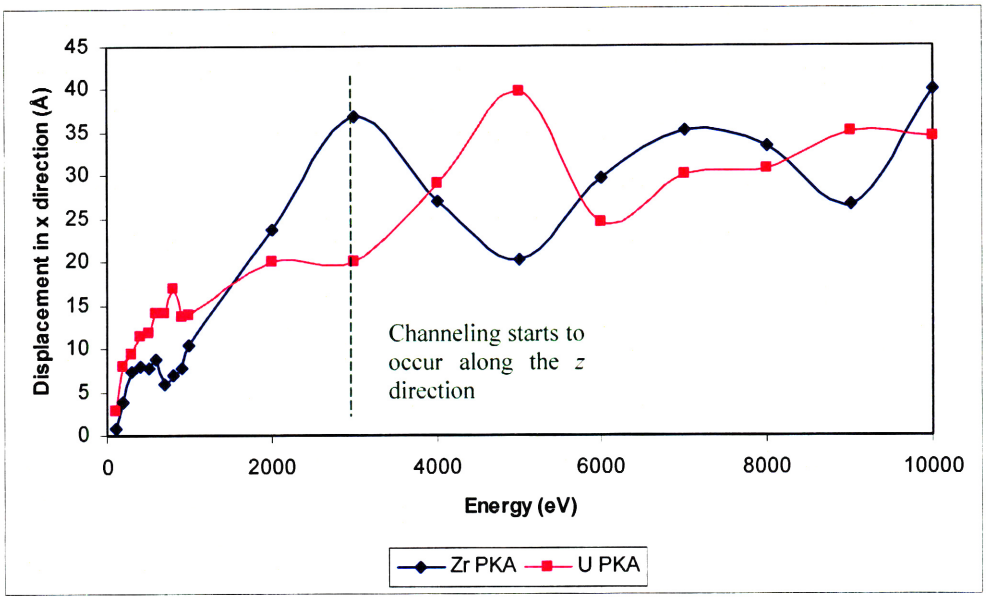

Figure 6.26: PKA displacement along the x direction. When PKA energy is small, channeling doesn't occur and U PKA travels longer distance along the x direction than a Zr PKA. When PKA energy is larger than about 3 keV, however, channeling occurs and the PKA propagation distance along the x direction becomes similar for U and Zr PKAs. PKAs never travel more than about 4 nm along the x direction in our simulations.

Thus far, we have talked about the extent of cascade without much discussion of the criterion used. We have used the method developed in Section 5.7 and threshold distance values given in Table 5.3, which are the distances of closest neighbors. Here we test the sensitivity of cascade extent on the threshold distance values. The threshold distance values given in Table 5.3 were scaled equally by a factor f and the extents of cascades re-calculated. Results are shown in Table 6.18.

Table 6.18: Sensitivity of cascade extent on the threshold distance values. The threshold distance values given in Table 5.3 are scaled equally by a scaling factor, *f*, and the extent of cascade is recalculated for the collision cascade caused by a 1-keV Zr PKA.

Scaling factor of threshold distance values, f	Extent of cascade (Å)		
	x	y	z
0.5	28.3420	26.8110	29.1840
0.6	26.4330	23.7320	28.7070
0.7	23.1370	22.7390	28.7070
0.8	23.1370	22.7390	28.7070
0.9	23.1370	20.8940	26.5580
1	23.1370	20.8940	25.7570
1.0	22.7540	20.7077	25.7570
1.1	22.2910	20.7077	21.5283

From Table 6.18, we can see that the extent of cascade depends on the threshold distance values we chosen, as expected, but is not too sensitive to their values, especially when the scaling factor *f* is around 1.0. Figure 6.27 shows the extent of cascade along the *x* direction, which is the initial velocity direction of the PKA. As we can see, around $f = 1$ there is little change of cascade extent when we change the value of *f*, which partially justifies why we can use the threshold distance values given in Table 5.3.

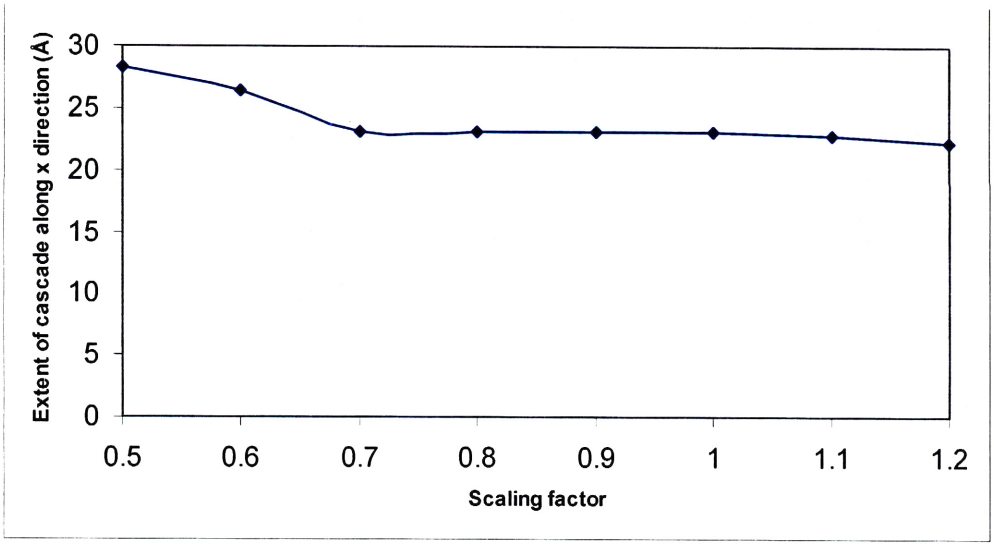

Figure 6.27: Sensitivity of cascade extent along the x direction on chosen threshold distance values, which are the original threshold distance values in Table 5.3 times the scaling factor.

6.9 Number of ever-displaced and displaced atoms

This section calculates the number of ever-displaced and displaced atoms during the collision cascade. During the collision cascade, many atoms will be displaced from their sites, all of which are "ever-displaced" atoms. Some of these ever-displaced atoms, however, may eventually return to their original sites. Only those atoms that do not return are displaced atoms. For example, the O atom whose displacement is shown in Figure 6.8 is ever-displaced but not permanently displaced. It is considered a displaced atom at time 0.1 ps, but not at 10 ps. The number of ever-displaced atoms is determined using the method developed in Section 5.7 and the threshold distance values given in Table 5.3.

Figure 6.28 shows the number of ever-displaced and displaced atoms when using Zr and U PKAs with different energies.

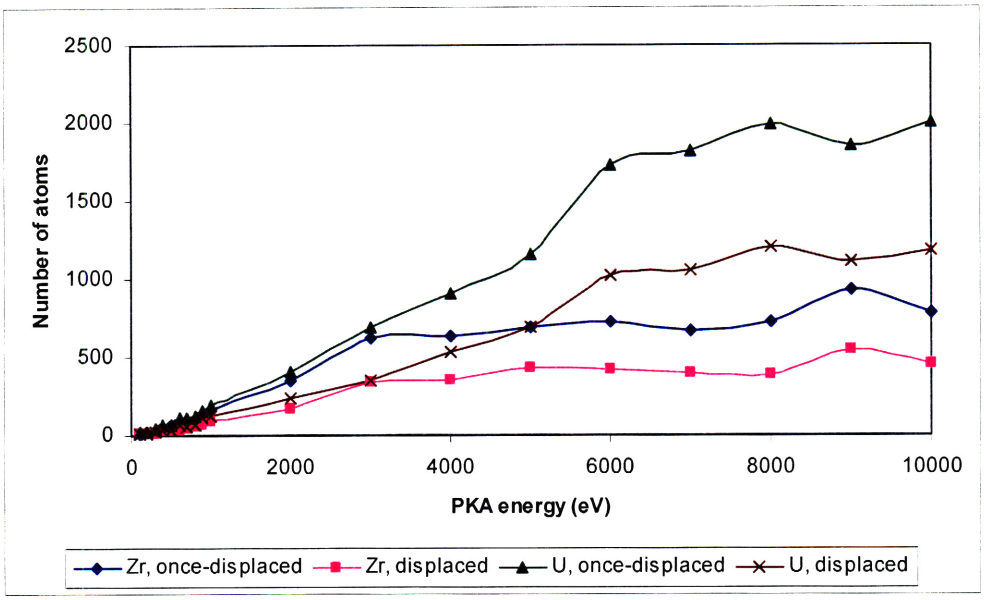

Figure 6.28: The numbers of ever-displaced and displaced atoms for simulations using Zr and U PKAs with different energies

We can see that more ever-displaced and displaced atoms are produced by U PKA than by Zr PKA. There are more ever-displaced atoms than displaced atoms, as expected. The percentage of ever-displaced atoms that went back to their original sites is shown in Figure 6.29. It can be seen that the percentage of ever-displaced atoms that went back has no clear dependency on the mass of the PKA.

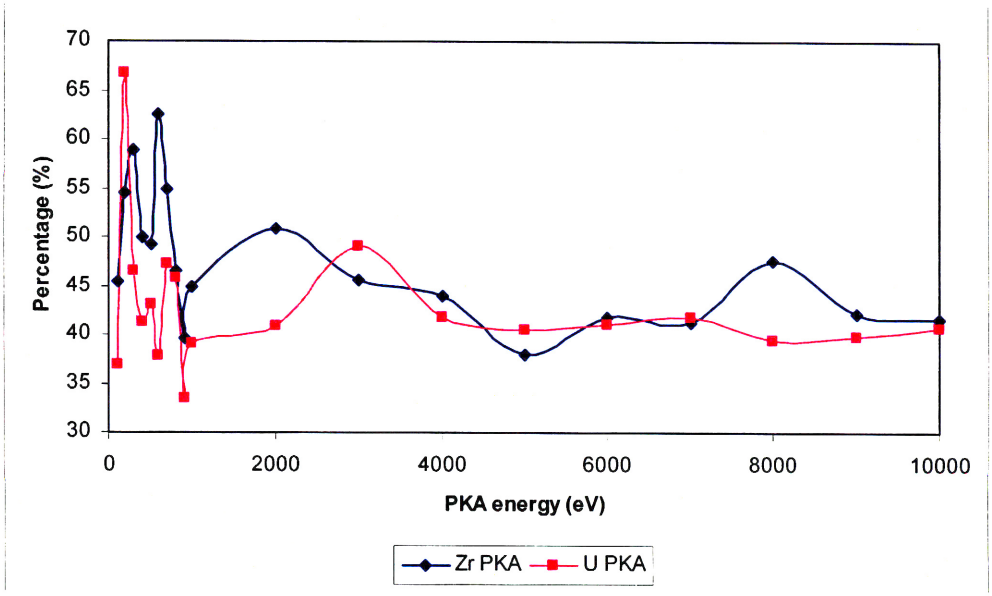

Figure 6.29: Percentage of ever-displaced atoms that returned back to their original sites for simulations using Zr and U PKAs with different energies

The fact that U PKAs displaced more atoms than Zr PKAs can be seen intuitively by looking at the damaged lattices directly. The zircon structures after 10-ps MD simulations using 5-keV Zr and U PKAs are shown respectively in Figure 6.30 and Figure 6.31. A casual comparison of these two figures clearly shows that the U PKA produced more damage. Because U is simply a super-mass Zr in this study, this simply confirms that heavier PKAs produce more damage to the lattice than lighter ones if their initial energies are the same.

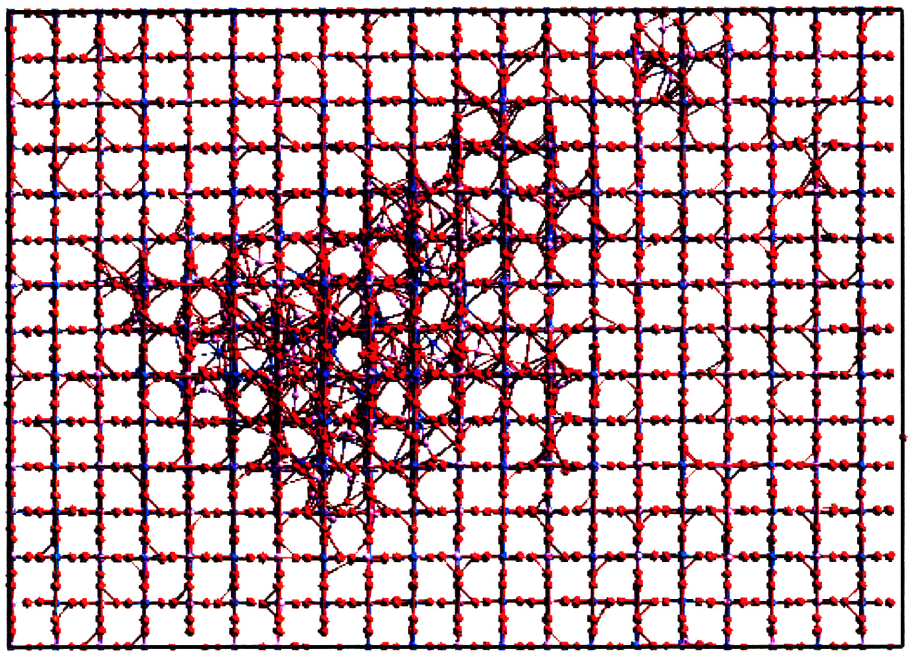

Figure 6.30: Zircon structure after 10-ps MD simulation using 5-keV Zr PKA.

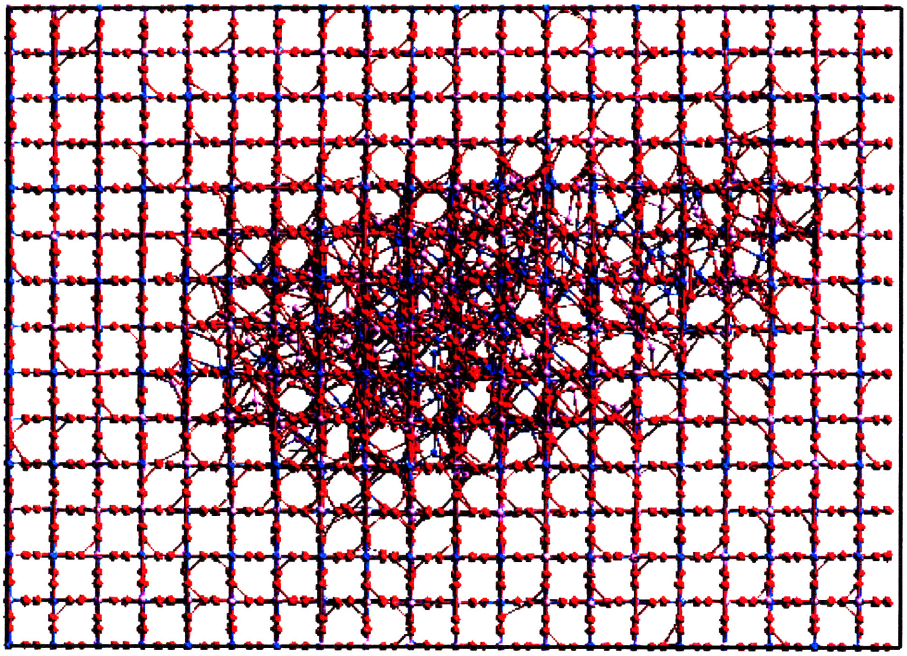

Figure 6.31: Zircon structure after 10-ps MD simulation using 5-keV U PKA.

Experimentally, an α-decay recoil in natural zircon displaces about 3800 atoms [16]. Th and Ra α-decay recoils in natural zircon have energies from 30 keV to 70 keV. Due to electronic energy-loss mechanisms, only about 50% of the recoil energy is dissipated in the nuclear collisions [14], or about 15~35 keV. U has similar mass to Th or Ra, so the number of atoms it displaces should be of the same order of magnitude as the numbers of atoms displaced by Th or Ra. The 10-keV U recoil in our simulation displaces about 1000 atoms (Figure 6.28), in reasonable agreement with experimental results.

The ever-displaced atoms constitute only a small fraction of all the atoms within the volume element of the cascade extent. For example, in Table 6.16 we have seen that the extent of the cascade caused by a 1-keV Zr PKA is 23.137Å by 20.8940 Å by 25.7570 Å. At the end of the simulation, there were in total 1083 atoms within this volume element, of which 165 were ever-displaced, accounting for only 15%. The percentage for a 1-keV U PKA is 17%.

6.10 Thermal spike

We investigate thermal spike in this section by calculating average temperatures of two different groups of atoms

1. Ever-displaced atoms.
2. All atoms within the volume element defined by the cascade extent.

These groups are not static. As simulation goes on, more atoms are displaced and added into group 1. Similarly, as the extent of the cascade

changes, the atoms belonging to group 2 also change. From the discussion in the last section, we know that the atoms in group 1 account only for a small fraction of all the atoms in group 2. Since the atoms in group 1 are those that are most influenced by the collision cascade, they tend to have more energies. Consequently, the average temperature of atoms in group 1 will be much higher than that of atoms in group 2, as shown in Figures 6.32 and 6.33. In Figure 6.33, the curve for average temperature of atoms in group 1 is labeled "Cascade Atoms" and the curve for the temperature of atoms in group 2 is labeled "Volume Element". Average temperatures are calculated for the simulations using 1-keV Zr and U PKAs.

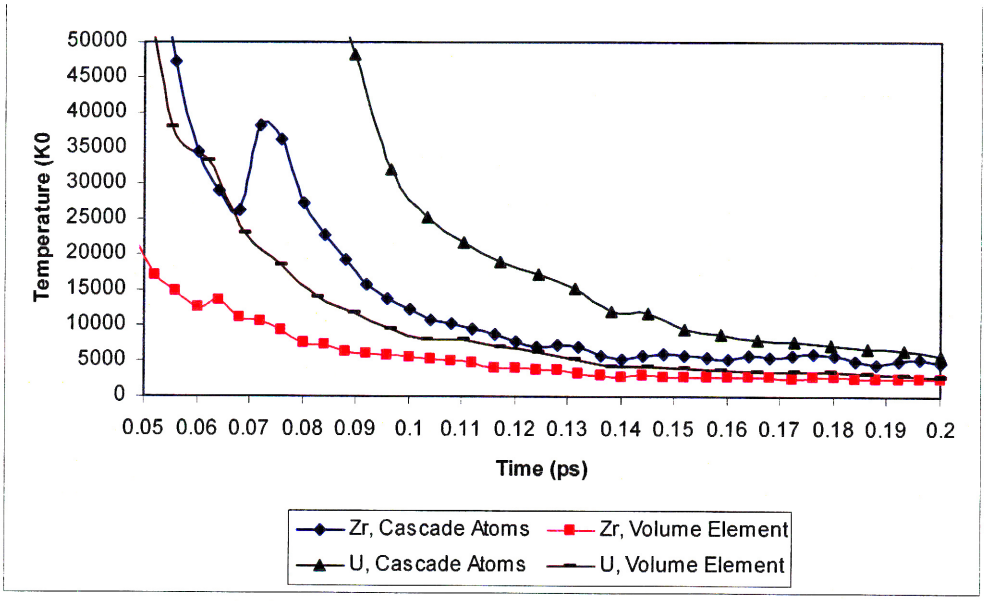

Figure 6.32: Thermal spike during the first 0.2 ps simulations using 1-keV Zr and U PKAs

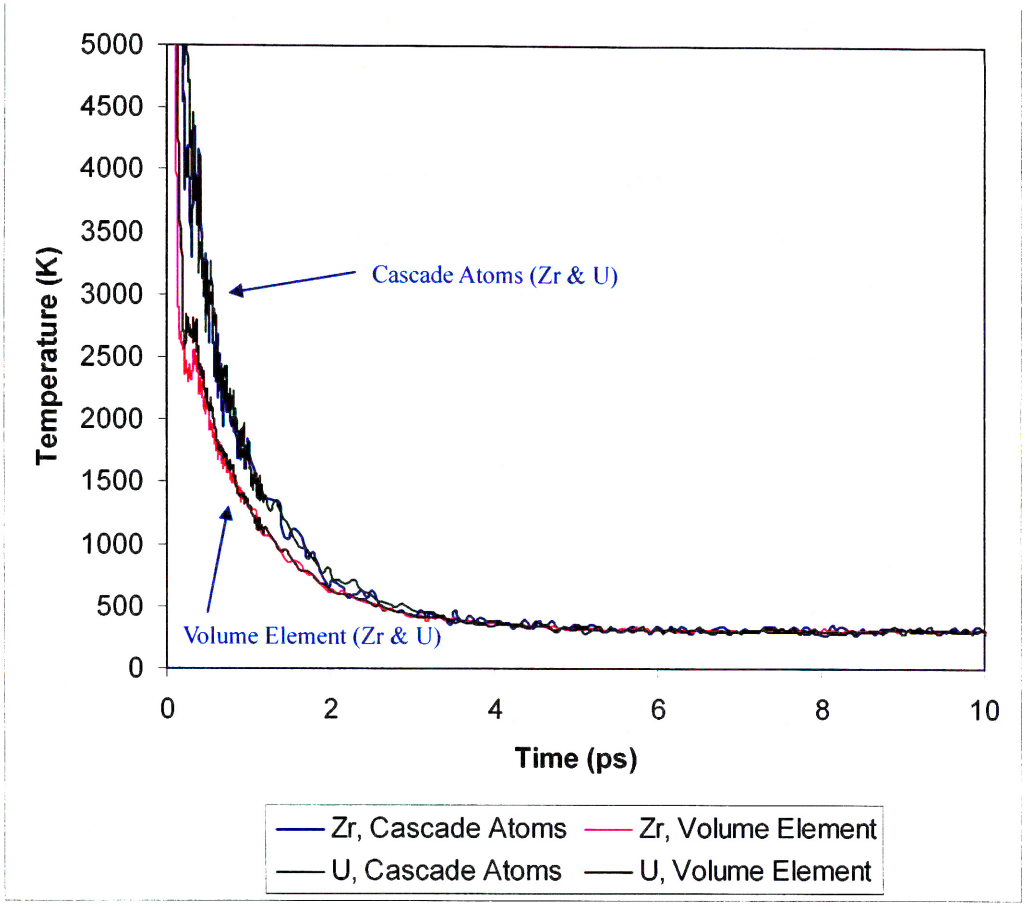

Figure 6.33: Thermal spike of simulations using 1-keV Zr and U PKAs

In Figure 6.32, during the initial 0.2 ps of the simulations, the thermal spike caused by a U PKA has a higher average temperature than that caused by a Zr PKA. At the end of 0.2 ps, both thermal spikes still comprise temperatures much higher than the melting point of zircon. Figure 6.33 shows that, after the initial short period, the temperatures of the thermal spikes caused by Zr and U PKAs are similar.

6.11 Distribution of PKA energy among sub-lattices

This section investigates the distribution of PKA energy among Zr, Si and O sub-lattices. Sub-lattice kinetic energy is the total kinetic energy of atoms

within this specific sub-lattice. For example, the kinetic energy of the O sub-lattice is the sum of the kinetic energies of all O atoms.

Before introducing any PKA, a specific sub-lattice has a certain amount of kinetic energy E_0 due to thermal vibration; after absorbing some of the PKA's energy, the kinetic energy of this sub-lattice becomes E_1. $E_1 - E_0$ is what we are interested in here and is called the "excess kinetic energy". The PKA itself was excluded from calculation of excess kinetic energies of sub-lattices.

Figures 6.34 and 6.35 plot the excess kinetic energy of each sub-lattice as a percentage of the total excess kinetic energy, which is simply the sum of the excess kinetic energies of all sub-lattices. Figure 6.34 shows the results for the simulation of a 5-keV Zr PKA and Figure 6.35 shows the results for the simulation of a 5-keV U PKA.

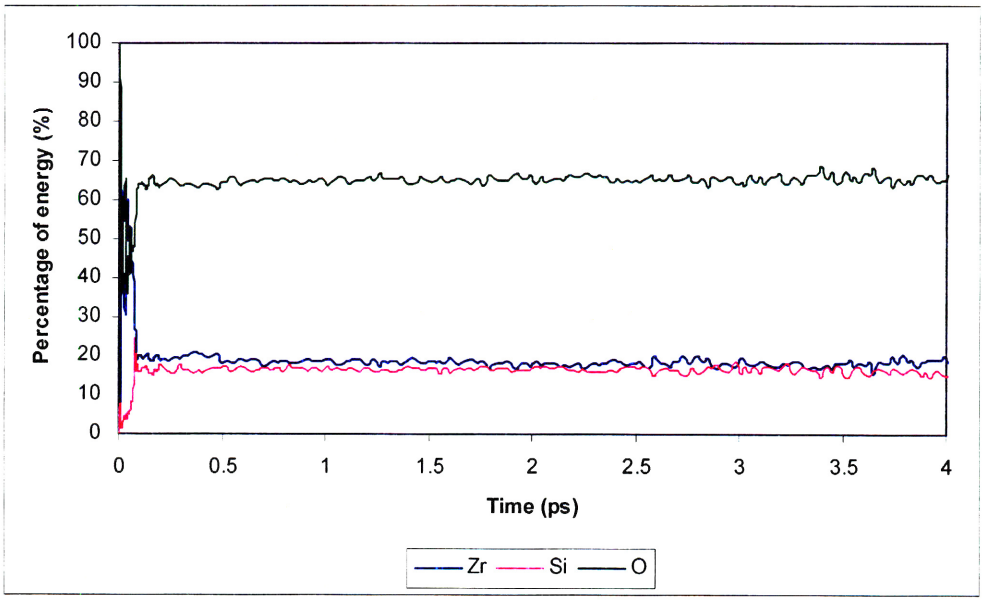

Figure 6.34: (Color) Excess kinetic energy of sub-lattices as a percentage of total excess kinetic energy, for the simulation using a 5-keV Zr PKA.

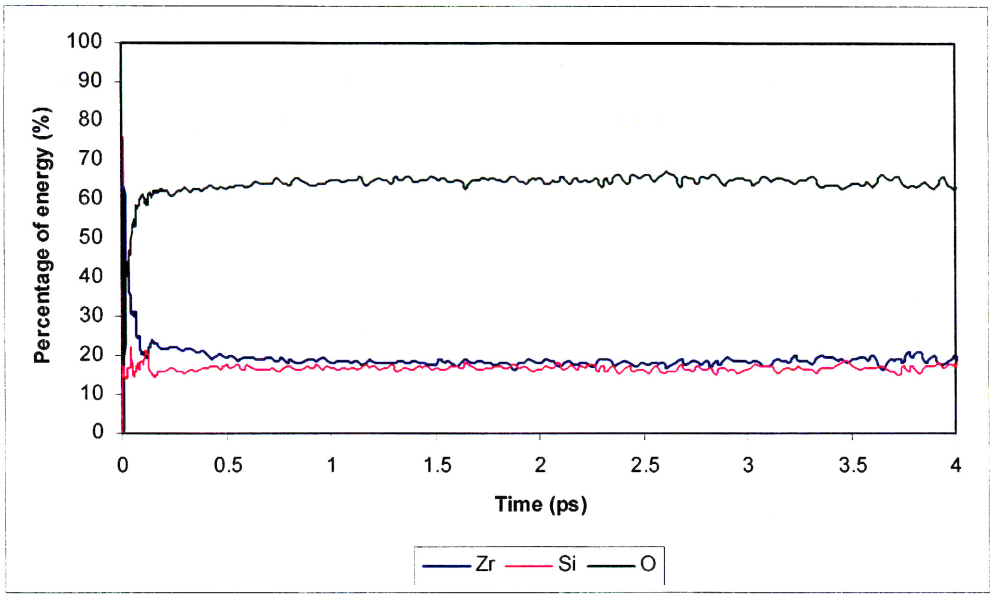

Figure 6.35: (Color) Excess kinetic energy of sub-lattices as a percentage of total excess kinetic energy, for the simulation using a 5-keV U PKA.

We saw similar trends in Figure 6.34 and Figure 6.35. The Zr sub-lattice absorbed a little more PKA energy than did the Si sub-lattice, and the O sub-lattice absorbed the majority, between 60% and 65%, of the excess energy. Stoichiometrically, Zr, Si and O account for respectively 16.7%, 16.7% and 66.7% of atoms in zircon lattice, so the distribution of PKA energy into sub-lattices is roughly proportional to atom ratios. We conducted simulations using 5-keV Si and O PKAs and constructed figures (not shown) similar to Figures 6.34 and 6.35 that again indicate that the distribution of excess energy into sub-lattices is roughly proportional to atom ratios, the Zr sub-lattice absorbing a little more excess energy than the Si sub-lattice. Thus, the specific pattern of distribution of excess energy into sub-lattices shown in Figures 6.34 and 6.35 is due to zircon's intrinsic response to collision cascades, not to energy transfers in individual collisions. (Otherwise, for example, we would expect the Si sub-lattice to absorb more energy than the

Zr sub-lattice when a Si PKA is used, since energy transfer from Si to Si is more efficient than from Si to Zr.)

Since zircon structures are dominated by the presence of O atoms, and the majority of the initial PKA energy is transferred to the O sub-lattice, we expect most of the ever-displaced atoms to be O atoms. This is indeed the case. For example, out of the 692 ever-displaced atoms caused by 5-keV Zr PKA, 40 (5.8%) are Zr, 150 (21.7%) are Si, and 502 (72.5%) are O atoms; out of the 1164 ever-displaced atoms caused by a 5-keV U PKA, 109 (9.4%) are Zr, 228 (19.6%) are Si, and 826 (71.0%) are O atoms. Although there are same number of Zr and Si atoms in zircon structure, the number of ever-displaced Zr was much smaller than that of Si, even though the Zr sub-lattice absorbs more energy. This proves that Zr atoms are harder to be displaced than Si in zircon. Over 70% of ever-displaced atoms are O, more than the stoichiometric ratio, since O is lighter and more easily displaced than the other two.

We saw above that Zr is harder to displace than Si in zircon, but this could be an artifact of using a larger threshold distance value for Zr (2.13 Å, Table 5.3) than that for Si (1.62 Å, Table 5.3). It is not. We re-calculated the number of ever-displaced atoms using 1.62 Å as the threshold distance for all three kinds of atoms in zircon. The results are shown in Table 6.19. As expected, when the threshold distance value of Zr is decreased from 2.13 to 1.62 Å, the number of ever-displaced Zr atoms increases. But fewer Zr atoms are nevertheless displaced than are Si atoms. So the conclusion remains the same: Zr is harder to displace than Si atom in zircon.

Table 6.19: Number of ever-displaced atoms in each sub-lattice for simulations using 5-keV Zr PKA and 5-keV U PKA

5-keV PKA	Threshold distance values (Å)			Number of once displaced atoms				
	Zr	Si	O	Zr	Si	O	U	Total
Zr	2.13	1.62	1.62	40 (5.8%)	150 (21.7%)	502 (72.5%)	0	692
	1.62	1.62	1.62	63 (8.8%)	150 (21.0%)	502 (70.2%)	0	715
U	2.13	1.62	1.62	109 (9.4%)	228 (19.6%)	826 (71.0%)	1	1164
	1.62	1.62	1.62	155 (12.8%)	228 (18.8%)	826 (68.3%)	1	1210

6.12 Recoil density

For a PKA with initial energy E, define the recoil density, n(T, E), as the mean number of atoms produced with kinetic energy from T to T + dT due to the PKA with energy E [7, 17]. Recoil density is fundamental to many theoretical collision cascade theories.

Completely ignoring energy loss due to electron excitation and the crystalline structure of the medium, n(T, E) has been estimated to satisfy the following relationship [7, 17]

$$\lim_{T/E\to 0} n(T,E) = c\frac{E}{T^2}, \tag{6.1}$$

where the constant c depends on the scattering law. For ideal hard-sphere scattering, $c = 1$ [7].

We can test the applicability of Equation (6.1) in zircon. The cascade simulation using 1-keV Zr PKA was investigated in detail for this purpose. In this case, E = 1000 eV. For each atom, the maximum energy at any simulation time was used as the recoil energy for this particular atom.

Equation (6.1) applies only for T << E, so T should be much smaller than 1000 eV. At 300 K, an average atom will have about 0.04 eV of energy due to thermal vibration, so T should also be much greater than 0.04 eV. Table

6.20 shows the number of recoils with energy from 1 eV to 2 eV, from 2 eV to 3 eV, ..., from 10 eV to 11 eV, and from 11 eV to 1000 eV. Figure 6.36 shows the number of recoils in different energy ranges.

Table 6.20: Count of recoils in different energy ranges

Recoil energy range (eV)	Recoil energy (eV)	Recoil count
[1, 2)	1.5	336
[2, 3)	2.5	86
[3, 4)	3.5	39
[4, 5)	4.5	23
[5, 6)	5.5	11
[6, 7)	6.5	11
[7, 8)	7.5	4
[8, 9)	8.5	7
[9, 10)	9.5	4
[10, 11)	10.5	1
Equal to or greater than 11	N/A	34

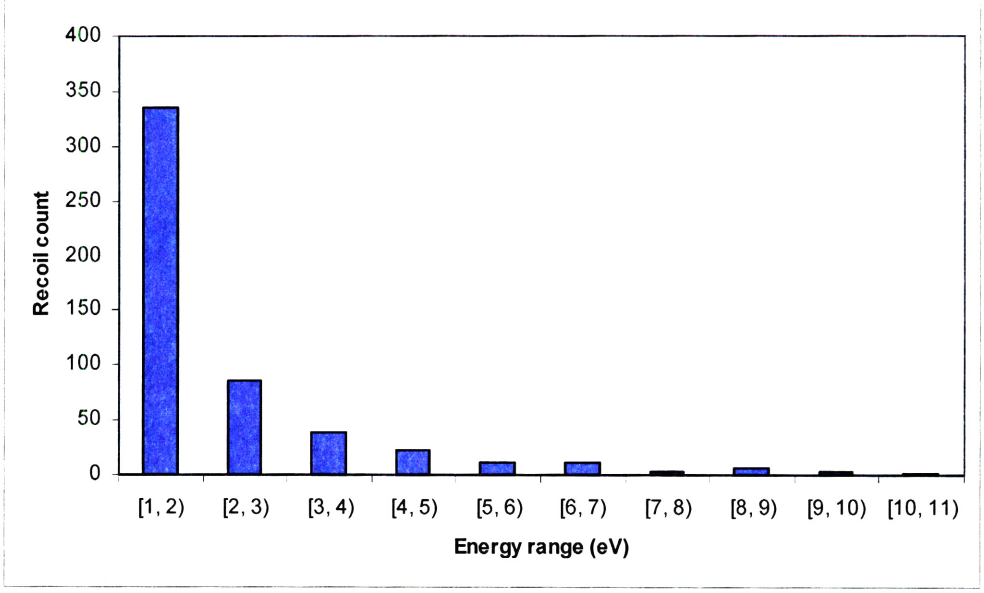

Figure 6.36: Count of recoils in different energy ranges

We can use the data in the second column of Table 6.20 as x, the data in the third column of Table 6.20 as y, and fit the data to an equation having the

form $y = a/x^2$. The result, fitted using code GnuPlot, yields $a = 717.216 \pm 30.69$ (4.279%).

From the value of a, we can obtain the value of c in Equation (6.1). From Equation (6.1), we also know that $n(T, E)\, dT = c\, E/T^2$. Here $dT = 1$ eV, since this is the width the energy range we have chosen, and $E = 1000$ eV; so $n(T, E) = 1000\, c/T^2$, which has the required form, from which we derive $a = 1000\, c$. Thus $c = a / 1000 \sim 0.72$

References of chapter 6

[1] G.H. Kinchin and R.S. Pease. The Displacement of Atoms in Solids by Radiation. Rep. Prog. Phys. 18, 1 (1955).

[2] G.H. Kinchin and R.S. Pease. Mechanism of the Irradiation Disordering of Alloys. J. Nucl. Energy 1, 200 (1955).

[3] R.E. Williford, R. Devanathan and W.J. Weber. Computer Simulation of Displacement Energies for Several Ceramic Materials. Nuclear Instruments and Methods in Physics Research B 141, 94 (1998).

[4] N.F. Mott and M.J. Littleton. Conduction in Polar Crystals. I. Electrolytic Conduction in Solid Salts. Trans. Faraday Soc. 34, 485 (1938).

[5] B. Park, W.J. Weber and L.R. Corrales. Molecular-Dynamics Simulation Study of Threshold Displacements and Defect Formation in Zircon. Phys. Rev. B 64, 174108 (2001).

[6] Retrieved in November, 2005 from http://faculty.evansville.edu/ck6/tcenters/class/centroid.html.

[7] M.T. Robinson. Basic Physics of Radiation Damage Production. J. Nucl. Mater. 216, 1 (1994).

[8] J.B. Gibson, A.N. Goland, M. Milgram and G.H. Vineyard. Dynamics of Radiation Damage. Phys. Rev. 120, 1229 (1960).

[9] R.H. Silsbee. Focusing in Collision Problems in Solids. J. Appl. Phys. 28, 1246 (1957).

[10] F.W. Clinard Jr. and L.W. Hobbs, in: Physics of Radiation Effects in Crystals, ed. R.A. Johnson and A.N. Orlov. Elsevier, Amsterdam, 1986.

[11] B.D. Begg, N.J. Hess, W.J. Weber, S.D. Conradson, M.J. Schweiger and R.C. Ewing. XAS and XRD Study of Annealed ^{238}Pu- and ^{239}Pu-Substituted Zircons ($Zr_{0.92}Pu_{0.08}SiO_4$). J. Nucl. Mater. 278, 212 (2000).

[12] W.J. Weber, R.C. Ewing and L.M. Wang. The Radiation-Induced Crystalline-to-Amorphous Transition in Zircon. J. Mater. Res. 9, 688 (1994).

[13] W.J. Weber. Alpha-Decay-Induced Amorphization in Complex Silicate Structures. J. Am. Ceram. Soc. 76, 1729 (1993).

[14] L.R. Corrales, W.J. Weber, A. Chartier, C. Meis and J.-P. Crocombette. Comment on "Large Swelling and Percolation in Irradiated Zircon". J. Phys.: Condens. Matter 15, 6447 (2003).

[15] J.F. Ziegler, J.P. Biersack and U. Littmark. The Stopping and Range of Ions in Solids (Volume 1 of: The stopping and ranges of ions in matter, edited by J.F. Ziegler.). New York, Pergamon, 1985.

[16] I. Farnan and E.K.H. Salje. The Degree and Nature of Radiation Damage in Zircon Observed by ^{29}Si Nuclear Magnetic Resonance. J. Appl. Phys. 89, 2084 (2001).

[17] P. Sigmund. On the Number of Atoms Displaced by Implanted Ions or Energetic Recoil Atoms. Appl. Phys. Lett. 14, 114 (1969).

Chapter 7: Topological analysis of crystalline, melted, melt-quenched and radiation-induced amorphous zircon structures

This chapter compares various zircon structures obtained in previous chapters in terms of their topological characteristics, which has not been attempted before. The structures investigated are: experimental (Section 2.2), simulated crystalline (Section 4.2), melt, melt-quenched with different volume swelling (Section 4.8), radiation-induced amorphous (Section 6.5), melt and melt-quenched using the new charge-balanced potential, and radiation-induced amorphous using the new charge-balanced potential (Section 6.6). For convenience of reference, each structure is given a symbol, as shown in Table 7.1.

Table 7.1: Symbols for zircon structures

Symbol	Description
Crys	Crystalline structure derived from experimental data (Section 2.2)
CrysSimu	MD simulation at 300 K using constant pressure ensemble (Section 4.2)
Melt	MD simulation at 5000 K using constant volume ensemble, starting from structure CrysSimu
Quen0%	Starting from structure CrysSimu, simulated at 5000 K for 10 ps; quenched from 5000 K to 10 K in 10 ps; and finally equilibrated at 300 K for 10 ps. All simulations use constant volume ensemble (Section 4.8)
Quen8%	Starting from structure CrysSimu, system volume increased manually by 8% and atom positions scaled proportionally; simulated at 5000 K for 10 ps; quenched from 5000 K to 10 K in 10 ps; and finally equilibrated at 300 K for 10 ps. All simulations use constant volume ensemble (Section 4.8)
Quen18%	Starting from structure CrysSimu, system volume increased manually by 18% and atom positions scaled proportionally; simulated at 5000 K for 10 ps; quenched from 5000 K to 10 K in 10 ps; and finally equilibrated at 300 K for 10 ps. All simulations use constant volume ensemble (Section 4.8)
RadiAmor	CrysSimu structure amorphized using 24 Zr PKAs and then equilibrated at 300 K for 10 ps. All simulations use constant volume ensemble (Section 6.5)
Melt-CB	MD simulation at 5000 K using constant pressure ensemble and the new charge-balanced potential. $\Delta V/V \approx 33.8\%$ compared to the structure at 300 K.
Quen-CB	Structure simulated at 300 K for 10 ps; simulated at 5000 K for 10 ps; quenched from 5000 K to 10 K in 10 ps; and finally equilibrated at 300 K for 10 ps. All simulations use constant pressure ensemble and the new charge-balanced potential. $\Delta V/V \approx 19.5\%$ compared to the structure at 300 K.
RadiAmor-CB	Using the new charge-balanced potential, Crys structure equilibrated at 300 K for 20 ps; then amorphized using 24 Zr PKAs and finally equilibrated at 300 K for 10 ps. All simulations use constant pressure ensemble (Section 6.6). $\Delta V/V \approx 4\%$ compared to the structure at 300 K.

7.1 Bond length

Bond length and interatomic distances were determined by looking for peaks in radial distribution functions (RDF), which were calculated using the algorithm described in Section 2.3.1. RDFs in this section were calculated averaging over the final 5.0 ps of simulations, except for structure Crys (Table 7.1) where no MD simulation was involved.

The important bond lengths to consider are Si-O and Zr-O bond lengths. The former contains information about structural changes in the SiO_4 tetrahedra; the latter in ZrO_8 triangular dodecahedra. The Si-O and Zr-O RDF plots of structures CrysSimu, Quen0% and RadiAmor are shown in Figure 7.1 and Figure 7.2, respectively.

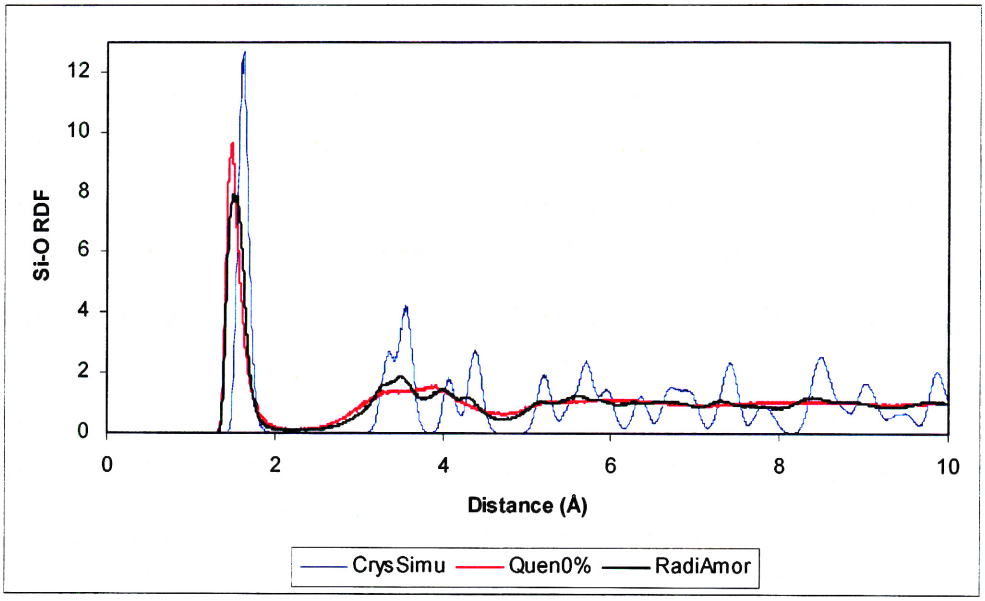

Figure 7.1: (Color) Si-O RDF plots of structures CrysSimu, Quen0% and RadiAmor

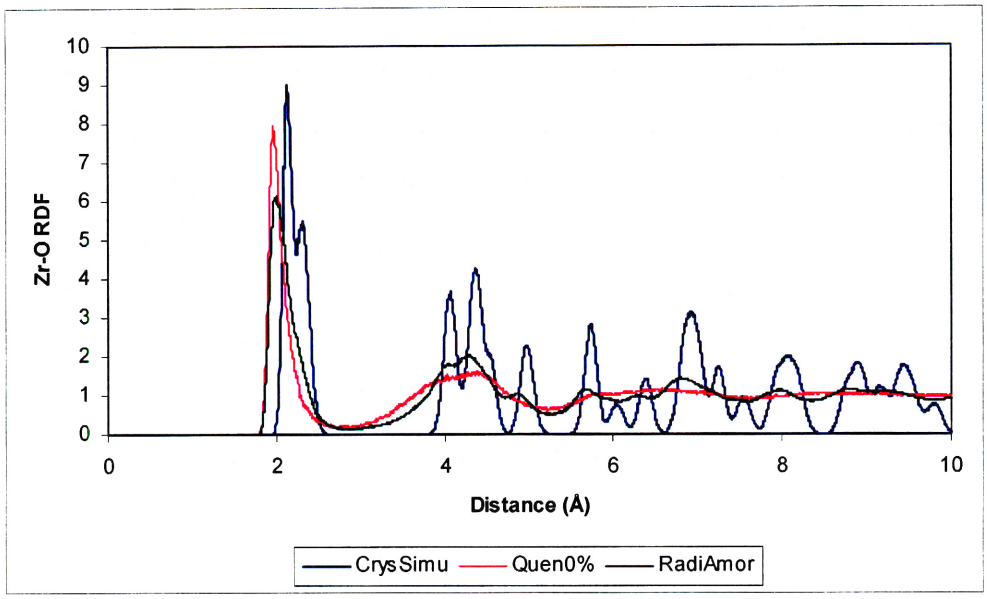

Figure 7.2: (Color) Zr-O RDF plots of structures CrysSimu, Quen0% and RadiAmor

The Si-O RDF plot for perfect crystalline zircon comprises many delta functions (Figure 2.13). We can see that in Figure 7.1 the Si-O RDF for CrysSimu has distinct peaks at locations corresponding to those delta functions. The first peaks of Si-O RDF plots for structures Quen0% and RadiAmor, however, occur at smaller Si-O interatomic distances, which means Si-O bond length decreases in both structures compared to crystalline zircon. Long-range peaks disappear in Si-O RDF plots of both Quen0% and RadiAmor, which means there are no long-range Si-O correlations and the structures are non-crystalline. Similar conclusions can be reached for Zr-O bond lengths from Figures 2.14 and 7.2.

Table 7.2 gives the Si-O and Zr-O bond lengths determined from RDF plots for all the structures in Table 7.1. The general trend is: Si-O and Zr-O bond lengths decrease as the zircon structure amorphizes using potential 4 without balanced charges. If the charge-balanced potential is used, however,

Zr-O bond length still decreases, but Si-O bond length increases.

Table 7.2: Si-O and Zr-O bond lengths

Structure Symbol	Crys	CrysSimu	Melt	Quen0%	Quen8%
Si-O bond length (Å)	1.62	1.62	1.42	1.48	1.46
Zr-O bond length (Å)	2.12, 2.27	2.12, 2.32	1.99	1.97	1.97
Structure Symbol	Quen18%	RadiAmor	Melt-CB	Quen-CB	RadiAmor-CB
Si-O bond length (Å)	1.45	1.51	1.66	1.70	1.67
Zr-O bond length (Å)	1.98	1.99	1.96	1.93	1.98

Zr-O bond lengths are roughly the same in the eight amorphous structures in Table 7.2. The amount of the decrease in Zr-O bond length is in general agreement with the 0.1 Å value observed experimentally in metamict zircon by Farges and Calas [1] using x-ray absorption spectroscopy.

Si-O bond lengths in the amorphous structures, however, strongly depend on the ion charges used. Si-O bond lengths are considerably larger when the charge-balanced potential is used, and more closely resemble Si-O bond lengths found in silica and silicates.

Among the three melt-quenched structures, Quen0%, Quen8% and Quen18%, it can be seen in Table 7.2 that the larger the specific volume, the smaller the Si-O bond length. Structures Quen0%, Quen8% and Quen18% are in the order of increasing specific volumes but decreasing Si-O bond lengths.

The relationship between the specific volume and Si-O bond length may seem to be counter-intuitive. The structures with smaller specific volumes have larger pressure (20.0 GPa for Quen0%, 13.2 GPa for Quen8%, and 7.6 GPa for Quen18% in our simulations), so the atoms should be more compacted together. Or, looking at this in another way, for structures with larger specific volumes, there is more space for atoms to spread out, so we

would expect the bond length to be larger. However, there are other structural changes which can affect bond lengths. The most important of these is the average coordination number of Si, which is smaller in the melt-quenched structure with a larger imposed specific volume (Table 7.4). The bond strength is larger when the coordination number is smaller, resulting in shorter bonds. This observation also applies in comparison of Si-O and Zr-O bond lengths. Zr atoms have more neighboring O atoms than Si in zircon, so Zr-O bond lengths are larger than Si-O. The correlation between coordination number and bond length is well known in the estimation of coordination-dependent ionic "radii" [2, 3].

7.2 Bond angle

Bond angles are determined by looking for peaks in bond angle distribution functions (BADF), which are calculated using the algorithm described in Section 2.3.2. Section 2.3.2 also gave a method for determining bond length cutoff values, which are required for BADF calculation. However, if the method is followed strictly, we will get different cutoff values for different structures of Table 7.1. Fortunately, the differences between these cutoff values are small. For the sake of simplicity and consistency, the same cutoff values are used for the same pair of atoms in all structures, which are somewhat in the middle of those cutoff values determined separately for different structures. The chosen cutoff value for the Si-O bond length is 2.3 Å and for the Zr-O bond length is 3.0 Å.

Bond angle values of O-Si-O and O-Zr-O contain information about structural changes in SiO_4 and ZrO_8 units, respectively. Figure 7.3 shows the O-Si-O BADF plots of structures CrysSimu, Quen0% and RadiAmor. It can be seen that even though we didn't use any three-body potential term to

control bond angles, the O-Si-O bond angle in Si coordination units is largely preserved .The O-Si-O BADF plot of CrysSimu has two distinctive peaks at about 97° and 116°, which are at the same locations as the peaks in O-Si-O BADF plot of structure Crys (Figure 2.21). The two peaks are still distinguishable in the O-Si-O BADF plot of RadiAmor. The peak with smaller angle is starting to disappear but nonetheless is still recognizable. For structure Quen0%, there is only one peak at about 113°. It can be seen in Figure 7.3 that the O-Si-O bond angle distribution is broadened when zircon amorphizes; all the angles are within the range from about 70° to 150°.

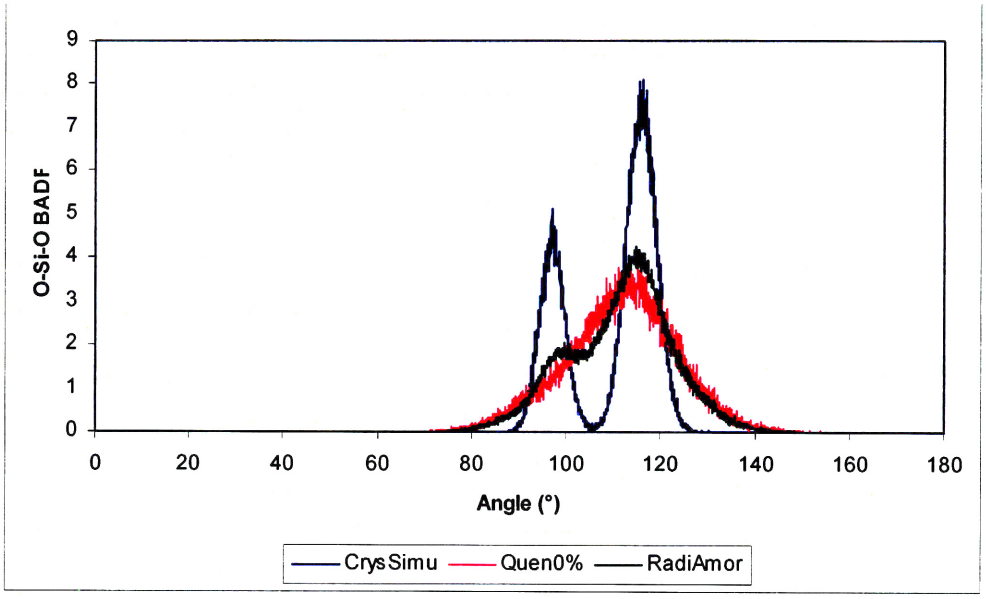

Figure 7.3: (Color) O-Si-O BADF of structures CrysSimu, Quen0% and RadiAmor.

Figure 7.4 shows the O-Si-O BADF plots of structures Quen0%, Quen8% and Quen18%. It can be seen that O-Si-O bond angle is larger in the structure with larger specific volume, which, just as is the decrease of Si-O bond length, might also be caused by a decrease in the coordination number

of Si atoms when specific volume increases (Section 7.3).

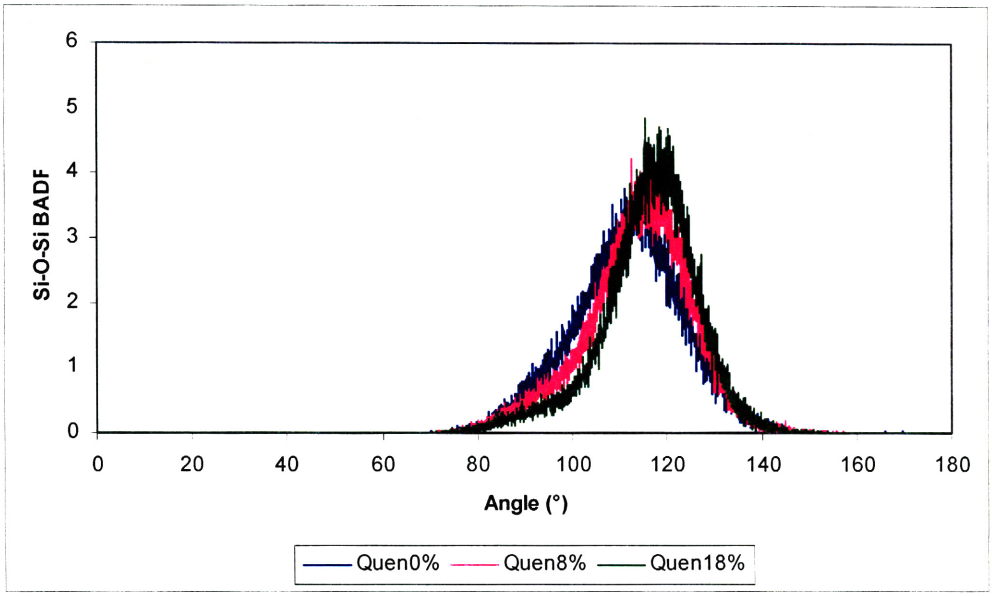

Figure 7.4: (Color) O-Si-O BADF of structures Quen0%, Quen8% and Quen18%.

Table 7.3 shows the O-Si-O bond angles in the structures of Table 7.1.

Table 7.3: O-Si-O bond angles

Structure Symbol	Crys	CrysSimu	Melt	Quen0%	Quen8%
O-Si-O bond angle (°)	97.0, 115.9	96.6, 115.6	108.5	113.3	114.4
Structure Symbol	**Quen18%**	**RadiAmor**	**Melt-CB**	**Quen-CB**	**RadiAmor-CB**
O-Si-O bond angle (°)	118.2	98.7, 114.4	87.5, 111,8	82.2, 106.3	86.6, 121.0

In zircon, the O-Zr-O bond angle distribution is more complex than O-Si-O (compare Figure 2.22 with Figure 2.21). There are seven different values of O-Zr-O bond angles corresponding to the seven peaks in Figure 2.22. Six of these peaks are preserved in the O-Zr-O BADF plot of structure CrysSimu, as can be seen in Figure 7.5. The two peaks at 134° and 135° have been combined into one. The most favored O-Zr-O angle in structure Quen0% is about 85°.

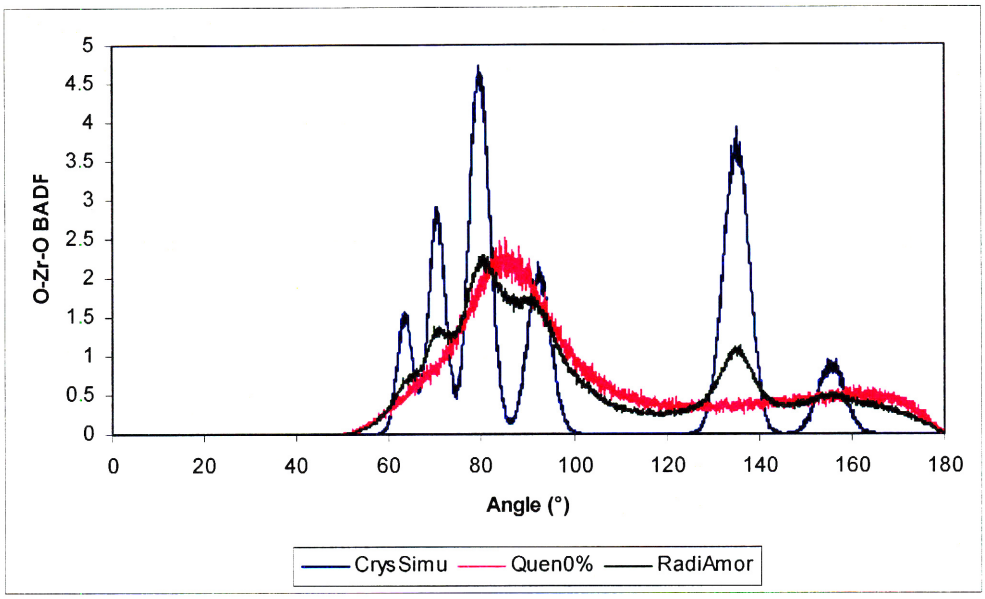

Figure 7.5: (Color) O-Zr-O BADF of structures CrysSimu, Quen0% and RadiAmor.

Figure 7.6 shows the O-Zr-O BADF plots of structures Quen0%, Quen8% and Quen18%. As for O-Si-O bond angles, we again see the shift of peaks toward larger angles as specific volume of the structure increases. This might be caused by the decrease of Zr coordination number as specific volume increases (Section 7.3).

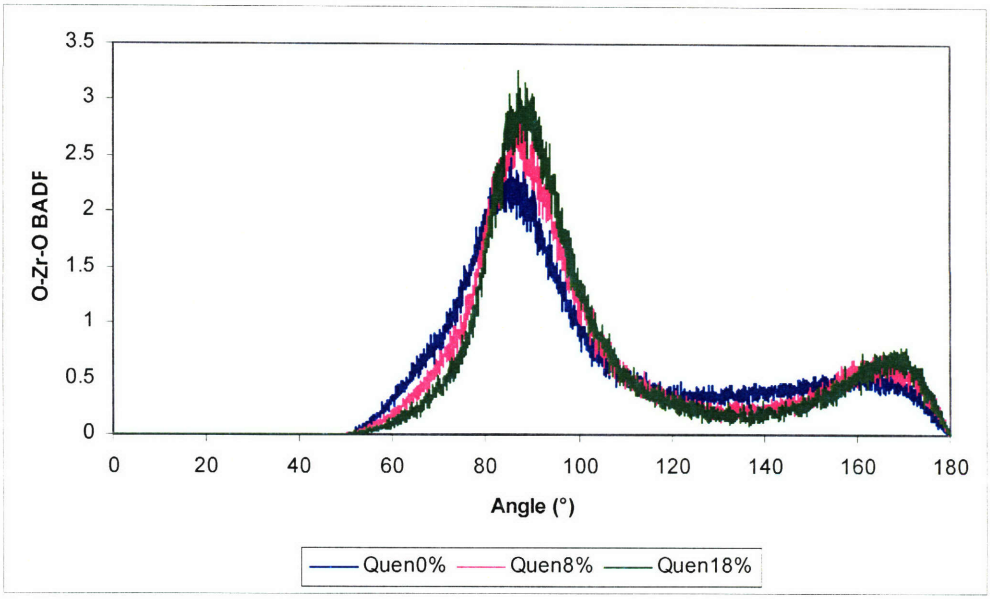

Figure 7.6: (Color) O-Zr-O BADF of structures Quen0%, Quen8% and Quen18%.

In crystalline zircon, there is no Si-O-Si bond angle since there is no bridging O atom between Si atoms. However, bridging O atoms between Si atoms appear in amorphous zircon structures. This phenomenon is investigated in more detail in Section 7.4. The Si-O-Si BADF plots of structures Quen0% and RadiAmor are shown in Figure 7.7. It can be seen that all Si-O-Si bond angles are greater than about 70°, and the most favored angle is about 120°. For comparison, the Si-O-Si BADF for melt-quenched fully polymerized silica peaks at around 146°; Hobbs *et al.* [4] have found no correlation between Si-O-Si BADF and density in the whole range of crystalline SiO_2 polymorphs.

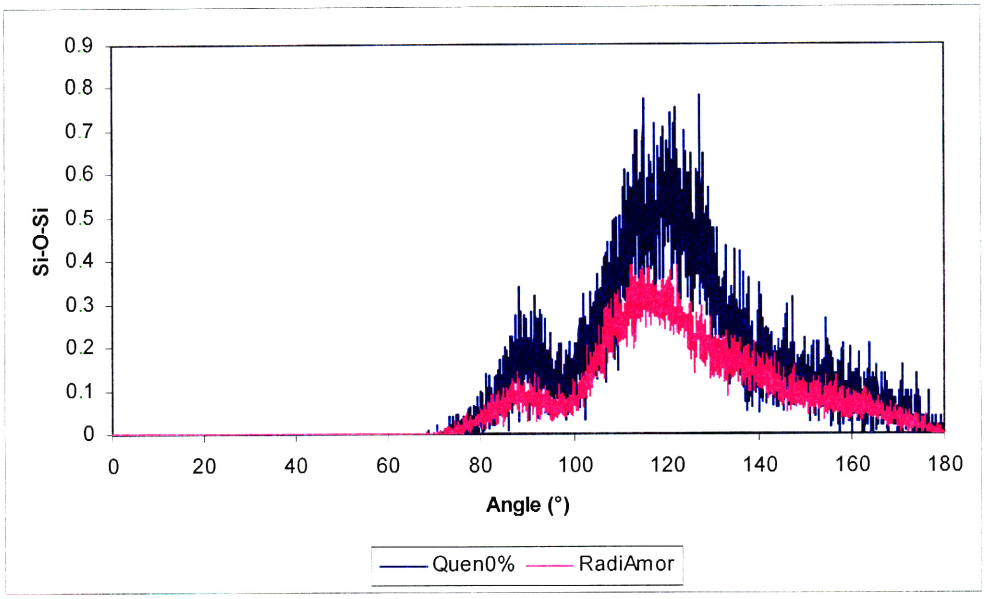

Figure 7.7: (Color) Si-O-Si BADF of structures Quen0% and RadiAmor.

7.3 Coordination number

Coordination number is the count of neighboring atoms. The same bond length cutoff values as in Section 7.3 are used in section, namely 2.3 Å for Si-O bond and 3.0 Å for Zr-O bond.

Table 7.4 gives coordination numbers of Si in various structures of Table 7.1. In structures Crys and CrysSimu, there are exactly 4 O atoms surrounding each Si atom, but Si atoms with other coordination numbers appear in amorphous zircon structures. In the structures amorphized, either thermally or by radiation, using the original potential (potential #4 in Section 3.2), the average coordination numbers of Si are less than 4, and 3-coordinated Si atoms appear in significant amount, sometimes even comprising the majority (structure Quen18%). This decrease of Si coordination number is caused by the ion charges used in this particular potential: +3.8 for Zr, +2.0 for Si and -1.45 for O. If the structure is composed of "pure" SiO_4 tetrahedra,

as in silica, the Si:O ratio will be 1:2 (each Si is surrounded by 4 O atoms, while each O is shared by 2 Si atoms). Thus, to keep charge neutrality, the charge of Si should be twice the absolute value of the oxygen charge. With a charge of -1.45 for O, this means Si should have a charge of +2.9. The charge of Si used in the potential, +2.0, is less than this value, and therefore Si has a tendency to lose O neighbors. When the new charge-balanced potential is used, the tendency for Si atoms to lose O neighbors does not exist anymore, as shown clearly in Table 7.4 for structures Melt-CB, Quen-CB and RadiAmor-CB. (The charge imbalance is also responsible for the huge volume expansion upon amorphization in constant pressure simulations; see Section 6.6 for details.)

Table 7.4: Number of O neighbors of Si. Si-O cutoff: 2.3 Å.

Structure	Percentage of Si atoms having number of O neighbors (%)						Average number of O neighbors
	2	3	4	5	6	7	
Crys	0	0	100	0	0	0	4.00
CrysSimu	0	0	100	0	0	0	4.00
Melt	0.73	28.4	65.0	5.7	0.20	0	3.76
Quen0%	0	27.0	72.6	0.39	0	0	3.73
Quen8%	0	47.8	52.1	0.031	0	0	3.52
Quen18%	0	**69.2**	30.8	0.013	0	0	3.31
RadiAmor	0	24.0	75.9	0.16	0	0	3.76
Melt-CB	0.30	11.1	71.5	15.8	1.3	0.014	4.07
Quen-CB	0	2.2	63.4	33.1	1.3	0	4.34
RadiAmor-CB	0	0.36	63.2	32.2	4.2	0.0045	4.40

Even though there is a tendency for Si atoms to reduce Si coordination number, the O atoms may not be able to move freely due to steric constraints. As the specific volume increases, it is easier for O atoms to move around and this will result in a decrease of Si coordination number. This point is clear in Table 7.4, where Si coordination number continuously decreases from structure Quen0% to Quen8% to Quen18%. Figure 7.8

shows percentages of Si atoms that are 3-coordinated, 4-coordinated and 5-coordinated in structures Quen0%, Quen8% and Quen18%. It is very clear from this figure that the number of 3-coordinated Si atoms increases when specific volume increases.

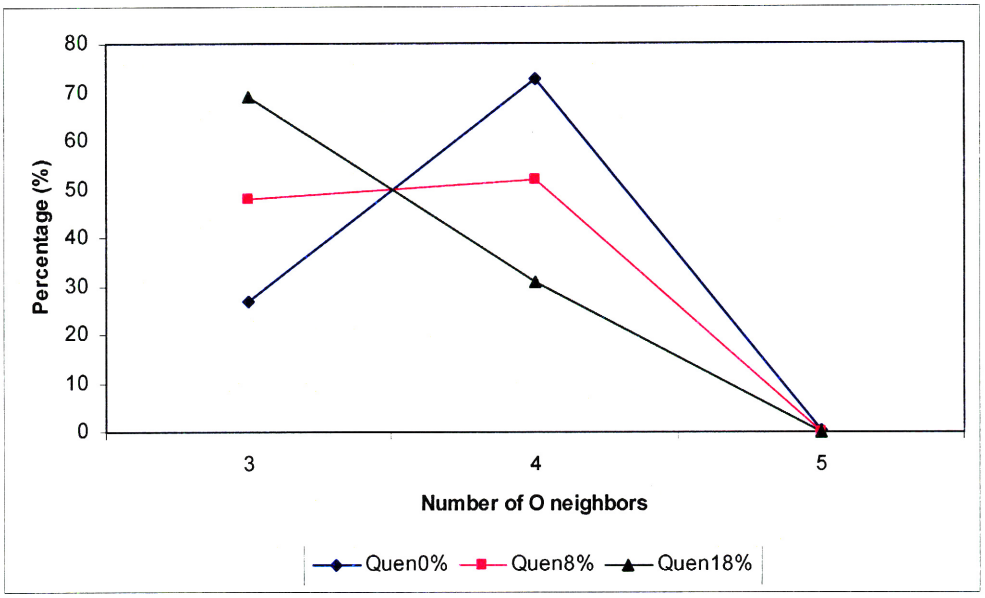

Figure 7.8: Percentages of 3-coordinated, 4-coordinated and 5-coordinated Si atoms in structures Quen0%, Quen8% and Quen18%.

Table 7.5 shows the number of O neighbors of Zr atoms in various structures. For structures Quen0%, Quen8%, Quen18% and RadiAmor, Table 7.5 shows that a very small fraction of Zr atoms keeps a coordination number of 8, while in Table 7.4 a much larger fraction of Si atoms retains a coordination number of 4. Thus Si atoms are better than Zr at maintaining the initial coordination numbers they had in crystalline zircon. It is worth noting that the coordination numbers in their respective pure oxides (most forms of SiO_2, monoclinic ZrO_2) are 4 and 7. The predominant coordination of 6 for oxygen about Zr in the Quen8% and Quen18% structures is quite unrealistic.

Table 7.5: Number of O neighbors of Zr. Zr-O cutoff: 3.0 Å.

Structure	Percentage of Zr atoms having number of O neighbors (%)								Average number of O neighbors
	4	5	6	7	8	9	10	11	
Crys	0	0	0	0	100	0	0	0	8.00
CrysSimu	0	0	0	0	100	0	0	0	8.00
Melt	0.031	1.5	14.0	35.1	45.6	3.6	0.18	0.0045	7.36
Quen0%	0	2.3	50.0	39.3	8.0	0.39	0	0	6.54
Quen8%	0.045	7.8	**70.4**	20.0	1.7	0	0	0	6.15
Quen18%	0.11	20.6	**71.5**	7.7	0.098	0	0	0	5.87
RadiAmor	0	1.9	34.0	24.8	38.8	0.49	0	0	7.02
Melt-CB	0.0061	0.90	8.7	27.1	60.1	3.2	0.059	0	7.56
Quen-CB	0	1.1	46.5	42.9	9.3	0.22	0	0	6.61
RadiAmor-CB	0	0.12	7.0	29.1	60.1	3.7	0.027	0	7.60

7.4 Polymerization of Si coordination units

In crystalline zircon structure, a SiO_4 tetrahedron does not share any vertex or edge with other SiO_4 tetrahedra. However, it is observed in the experiments of Farnan and Salje [5], using ^{29}Si nuclear magnetic resonance, that Si coordination units are polymerized by sharing oxygen atoms in natural metamitc zircon amorphized by α-decay events over geological time scale. The degree of polymerization increases with irradiation dose [5].

The polymerization has also been observed in our simulations. The Si-Si RDF plots of structures Crys, Quen0% and RadiAmor are shown in Figure 7.9. The appearance of new peaks at about 2.8 Å for both Quen0% and RadiAmor structures manifests the polymerization of Si coordination units in these structures. The location of the new peak, 2.8 Å, is close to the Si-Si distance in silicates, where SiO_4 tetrahedra are connected through vertex oxygen sharing. The new peak is the only peak in Si-Si RDF plots of structure Quen0%, while the Si-Si RDF plot of structure RadiAmor retains clear peaks at distances of 3.6 Å and 5.5 Å. Since the RDF for structure RadiAmor is the average over only those non-crystalline atoms (determined

using the method developed in Section 7.6), it means the radiation amorphized structure is different from the melt or melt-quenched structures, and is closer to the original crystalline structure.

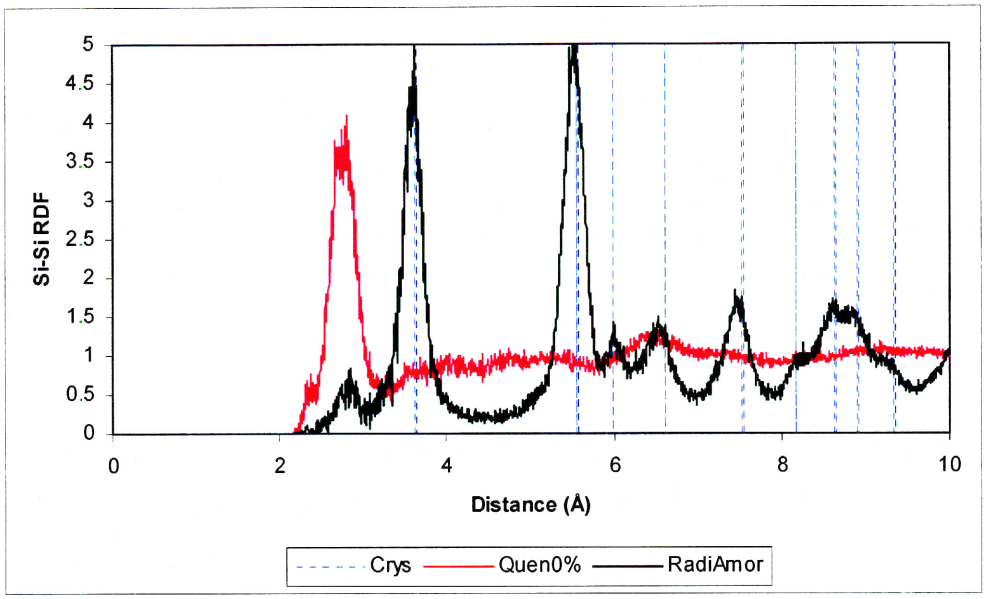

Figure 7.9: Si-Si RDF plots of structures Crys, Quen0% and RadiAmor. The appearance of new peaks at about 2.8 Å in RDF plots for both Quen0% and RadiAmor structures signals the polymerization of Si coordination units in these structures.

About 93.3% of Si atoms in structure Quen0% are connected to other Si through bridging O atoms. The average number of bridging O atoms per Si atoms (the "Q" value) is 1.95. Specific volume also plays an important role in polymerization of Si coordination units. Table 7.6 shows the fraction of Si atoms polymerized and the average number of bridging O atoms in structures Quen0%, Quen8% and Quen18%. It can be seen that Si units are less polymerized in structures with larger specific volume. This may simply due to the fact there is more space to spread out Si coordination polyhedra and the appearance of a larger fraction of 3-coordinated Si.

Table 7.6: The fraction of Si atoms polymerized and the average number of bridging O atoms per Si in structures Quen0%, Quen8% and Quen18%

Structure	Percentage of Si atoms Polymerized	Average number of bridging O atoms per Si
Quen0%	93.3%	1.94
Quen8%	91.2%	1.76
Quen18%	84.5%	1.45

Table 7.7 gives the degree of polymerization in structures Melt, Quen0%, Melt-CB and Quen-CB. It can be seen that the charge-balanced potential produces more polymerization and the degree of polymerization increases when zircon is quenched from liquid state.

Table 7.7: The fraction of Si atoms polymerized and the average number of bridging O atoms per Si in melt and quenched structures using the potential 4 and the new charge-balanced potential

Structure	Percentage of Si atoms Polymerized	Average number of bridging O atoms per Si
Melt	88.5%	0.93
Quen0%	93.3%	1.94
Melt-CB	91.3%	1.50
Quen-CB	97.5%	2.77

The increase in degree of polymerization with increase of irradiation dose (increasing number of overlapping cascades) is also observed in our simulations. Figure 7.10 and Figure 7.11 show respectively the percentage of Si atoms polymerized and the average number of bridging O atoms after the zircon structure endured progressively more dose (expressed in units of collisional energy per gram). The increase of polymerization with more irradiation dose is apparent in either figure. The curves in Figures 7.10 and 7.11 have very similar shape, which means the percentage of Si atoms polymerized and the number of bridging O atoms are highly correlated and they can be used equivalently as indicators of degree of polymerization. The collisional dose at which saturation of polymerization occurs is the same as

measured experimentally (1.7 ~ 8.1 × 10^4 J/g) for α-decay induced amorphization of natural zircon [6].

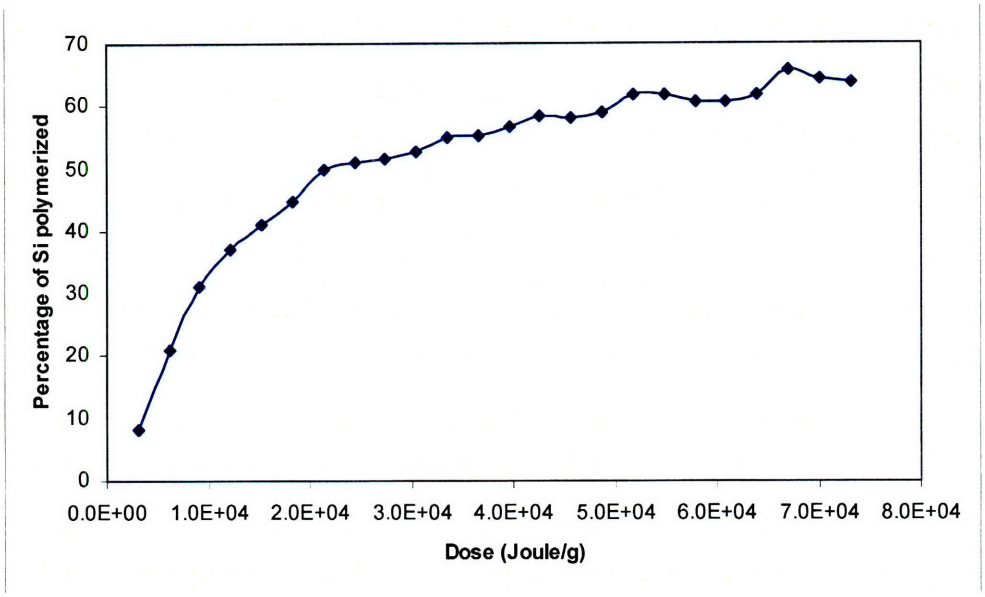

Figure 7.10: Percentage of Si atoms polymerized after the structure endured progressively more collisional energy in multiple cascades.

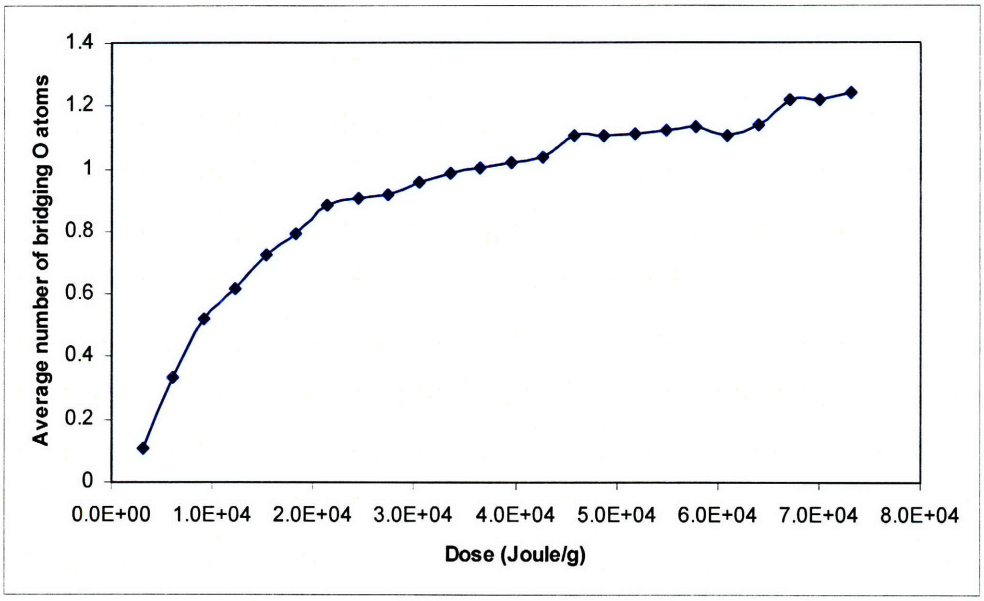

Figure 7.11: Average number of bridging O atoms per Si after the structure endured progressively more collisional energy in multiple cascades.

7.5 Ring, local cluster and topological modeling

Topology in the context of this study is the way atoms are interconnected with each other. Sometimes atoms are combined into structural units, such as SiO_4 tetrahedra in silica, before the connectivity is analyzed.

The language of symmetry has been firmly established for crystallographic descriptions, to which the topological description of connectivity is a useful alternative. In structures that do not have long-range translational and orientational orders, the language of symmetry is not applicable but topology still is. Topology is also believed to be central in describing network structures [7].

Topological connective has been successfully correlated with structural freedom from a purely geometrical viewpoint. Structures can be thought of as consisting of polytopes connected together by sharing corners, edges or faces. In some compounds, these polytopes can easily be identified. For example, in Chapter 2 we have demonstrated the edge-sharing SiO_4 tetrahedra and ZrO_8 triangular dodecahedra extending parallel to the *c* axis and the edge-sharing of ZrO_8 triangular dodecahedra along the *a* axis in zircon. For elemental solids such as Si, there is no obvious choice of polyhedron as the structural units, in which case fictional polyhedra centered on each atom and with vertices at mid-points between two neighboring atoms can be used. The degree of structural freedom, *f*, can be calculated from *V*, the number of vertices per polytope, and *C*, the number of polytopes sharing a vertex, using the formula derived by Gupta and Cooper [8, 9]:

$$f = d - C\{\delta - [\delta(\delta + 1)/2V]\}-(d-1)(Y/2)-[(p-1)d-(2p-3)](Z/p)$$

where d is dimensionality of the structure, δ is dimensionality of polytope, Y

is the fraction of edge-sharing vertices and Z is the fraction of vertices sharing p-sided faces. $f > 0$ means the structure has freedom to rearrange; $f < 0$ means the structure is rigid; and $f = 0$ means the structure is marginally constrained and changing boundary conditions provides more structural possibilities. Correlations have been established between structural freedom *f* and ease of metamictization under displacive irradiation [7, 10 and 11] and glass-forming ability [10].

The concept of *ring* is another cornerstone of topological analysis of material structures. A ring is simply a closed circuit of connected sequence of nodes, or, in our context, of atoms or polytopes. An extended structure consisting of self-similar units must have rings, since a connected graph with no rings, a tree, mandates impossible exponential increase of node density if only self-similar elements are allowed [12]. Thus rings are stated by Hobbs *et al.* as a "steric necessity" [12].

In an infinite network structure, there is an infinite number of rings. Naturally, attention should be focused on those rings that contain important information about the structure. To this end, a few definitions of rings have been created, including primitive rings [13, 14], "rings of interests" [15], minimal rings [16], strong rings [15] and very strong rings [15]. We will use primitive rings, which are the rings that are not sums of two or more smaller rings [13, 14], for ring-related topological modeling in this study.

A simplified version of the algorithm described in [17] is used in this study for primitive ring identification. For any pair of atoms in a ring, there are two paths from one atom to the other along the ring. A candidate ring is a primitive ring if and only if for any pair of atoms in the ring, the length of the shorter path along the ring from one atom to the other (or the length of

any one if the two paths along the ring have equal lengths) must equal the length of the shortest path or paths between these two atoms in the structure [17]. This is the basis for primitive ring identification. A "four-point-directed" path search method is used in [17] to reduce memory usage when searching for large-numbered rings. This method is not used in this study, since the amount of memory available in our current computer system is sufficient for holding the entire all-pairs shortest distance information required for identifying primitive rings in zircon. The algorithm used for calculating the all-pairs distance matrix is the Floyd-Warshall algorithm, which can be found in any good textbook on algorithms, such as the one by Cormen *et al.* [18].

From here on, we will use "ring" and "primitive ring" interchangeably, since non-primitive rings are never discussed in this study.

A concept related to primitive ring is *local cluster*, which is the set of all primitive rings passing through a given node in a graph. If individual atoms are used as graph nodes, the local cluster for a given atom is all the primitive rings that contain this atom; if polytopes consisting of multiple atoms are used as topological unit, the local cluster for a given polytope is the set of all primitive rings that pass through one of the edges of this polytope. The local cluster can also be defined as the union of all atoms belonging to all the primitive rings passing through a given node.

Determination of the local cluster is necessary for a complete description of local topology for certain structures, for which *statistics* of primitive rings are not by themselves sufficient. For example, both of the two silicon polymorphs, cristobalite and tridymite, have exactly twelve 6-rings passing through each node [12]. Based solely on statistics of primitive rings, these

two polymorphs cannot be differentiated topologically. However, the local cluster of cristobalite has 29 polytopes whereas that of tridymite has 27 [12]. Adding the information about local cluster enables us to distinguish cristobalite from tridymite.

The language of rings and local clusters has been successfully used to topologically describe the structure of silica polymorphs [12]. There are at least 7 known compact polymorphs of silica: cristobalite, tridymite, quartz, keatite, moganite, coesite and stishovite [19, 20]. Structures of these polymorphs can be uniquely described by rings and local clusters, which describe middle-range topological information that is hard to extract experimentally. Correlation between ring content and material density has also been found for silica polymorphs [12]. In addition, it is found that the number of N_{th} network neighbors is decreased by rings of order 2N or 2N-1 [12, 21].

Topology-based local rules have been successfully used for structural assembly. It is found that the same structural units, representing similar short-range connectivity, can be used to assemble both crystalline and amorphous silica polymorphs. A small change in the local assembly rule can result in dramatic changes in the final assembled structures [12, 22, and 23].

The local cluster is a characteristic structural unit, just as is a unit cell of a crystal in the language of crystallography. The local cluster contains both short- and middle-range topological information. It is an attractive alternative to the unit cell for describing crystalline structures and, unlike a unit cell, describes local topology instead of symmetry. Its usefulness is even more apparent in aperiodic structures where unit cells and symmetries are simply inapplicable. Local clusters can be used to uniquely characterize

all polymorphs of Si_3N_4 [24] and SiC [24], in addition to silica [12, 22]. A natural conjecture is that the local cluster or set of all local clusters in a non-crystalline network contains all topological information of a network structure [12].

For an intuitive impression of local clusters and their differences from unit cells, unit cells and local clusters of simple crystalline structures, including simple cubic, body-centered cubic and face-centered cubic, are shown in figures from 7.12 to 7.19.

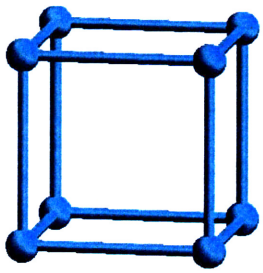

Figure 7.12: Simple cubic unit cell for a monatomic structure

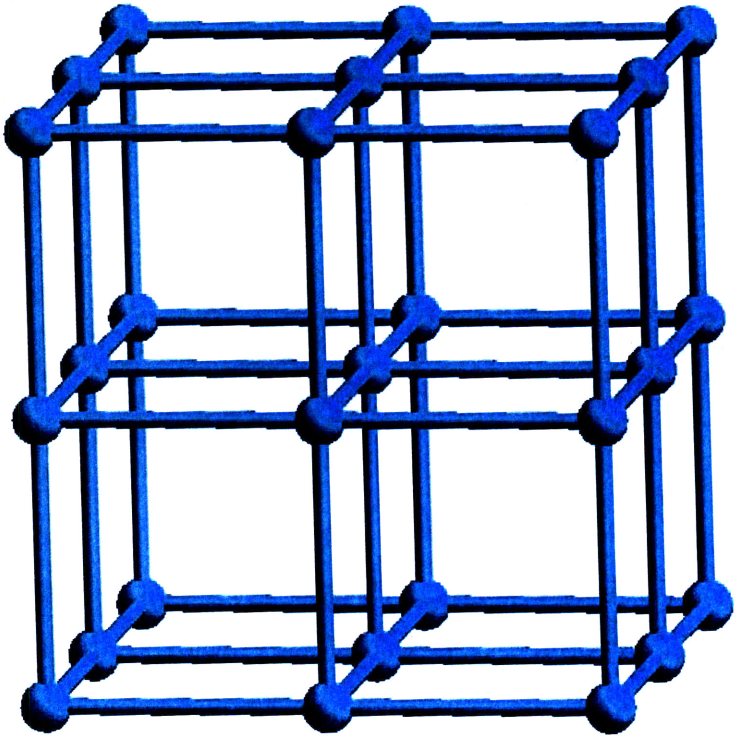

Figure 7.13: Local cluster of simple cubic monatomic structure when only nearest neighbors are considered connected. That is, if the lattice constant is a, the bond cutoff is infinitesimally larger than a. There is a total of 27 atoms in the local cluster, comprising 12 4-rings and 24 6-rings.

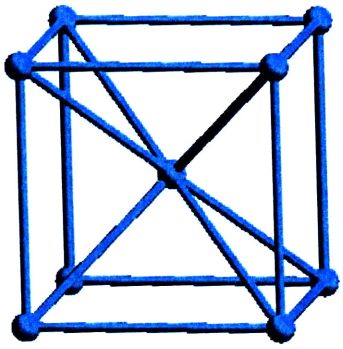

Figure 7.14: Bond-centered cubic unit cell for a monatomic structure

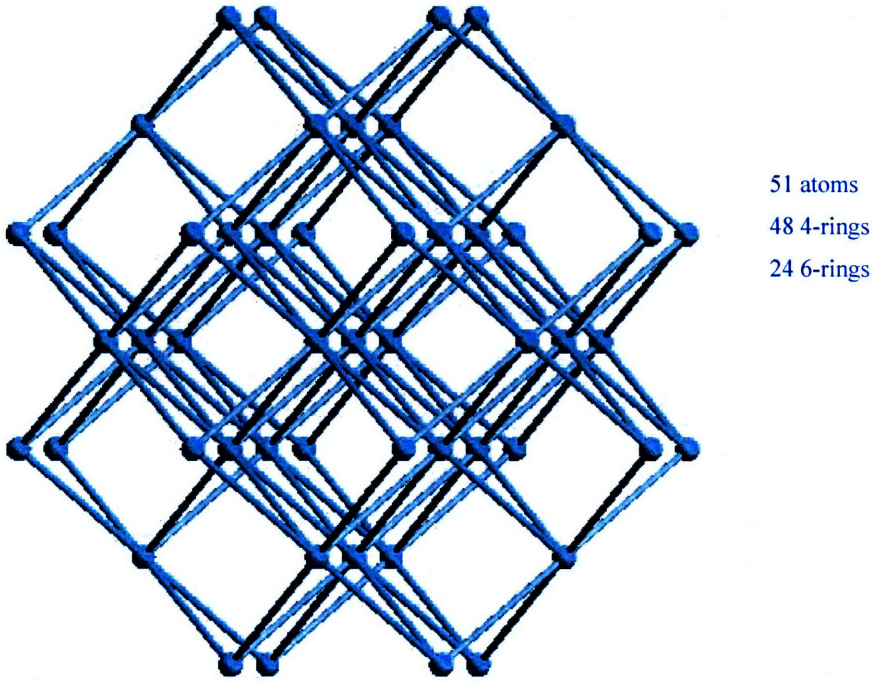

Figure 7.15: Local cluster of monatomic BCC structure when only nearest neighbors are considered connected. That is, if the lattice constant is a, the bond cutoff is infinitesimally larger than $\frac{\sqrt{3}}{2}a$. There is a total of 51 atoms in the local cluster, comprising 48 4-rings and 24 6-rings.

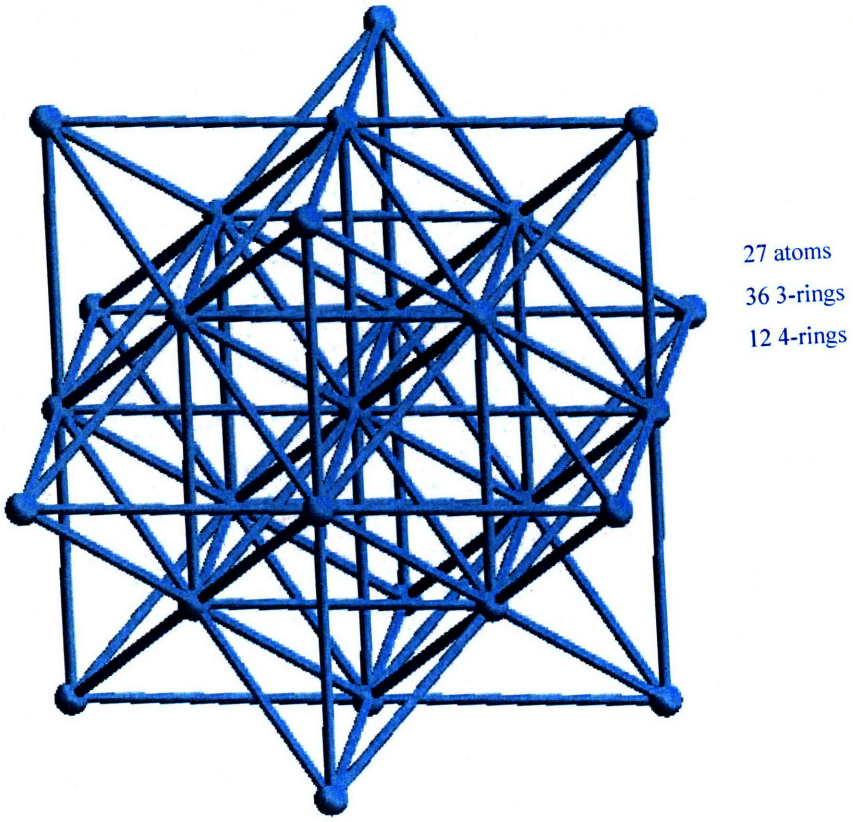

Figure 7.16: Local cluster of monatomic BCC structure when 1st and 2nd nearest neighbors are considered connected. That is, if the lattice constant is a, the bond cutoff is infinitesimally larger than a. There is a total of 27 atoms in the local cluster, comprising 36 3-rings and 12 4-rings.

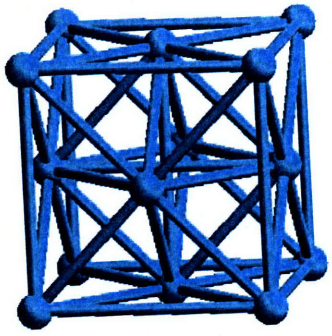

Figure 7.17: Face-centered cubic unit cell for a monatomic structure

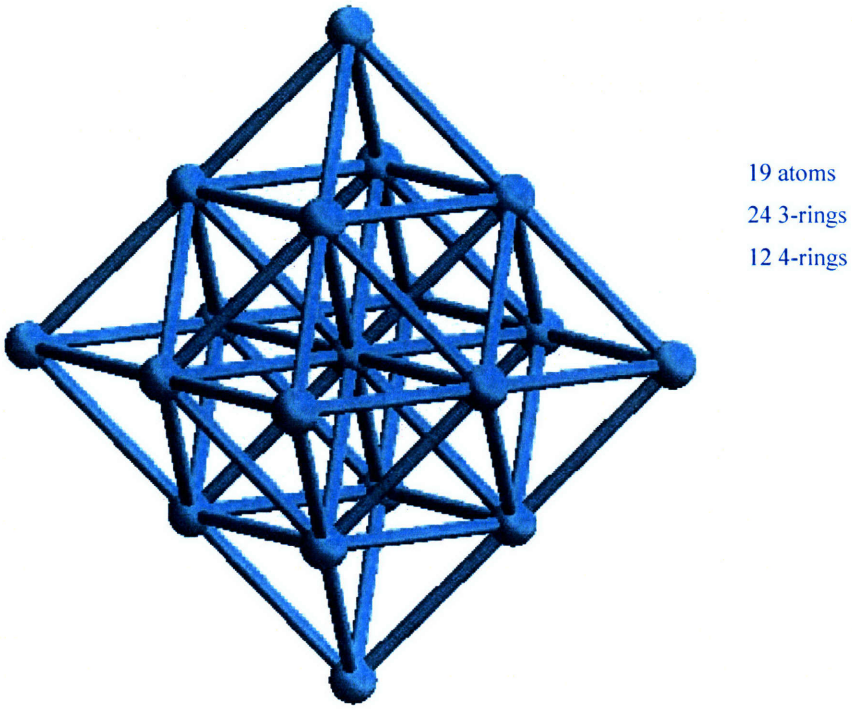

Figure 7.18: Local cluster of monatomic FCC structure when only nearest neighbors are considered connected. That is, if the lattice constant is a, the bond cutoff is infinitesimally larger than $\frac{\sqrt{2}}{2}a$. There is a total of 19 atoms in the local cluster, comprising 24 3-rings and 12 4-rings.

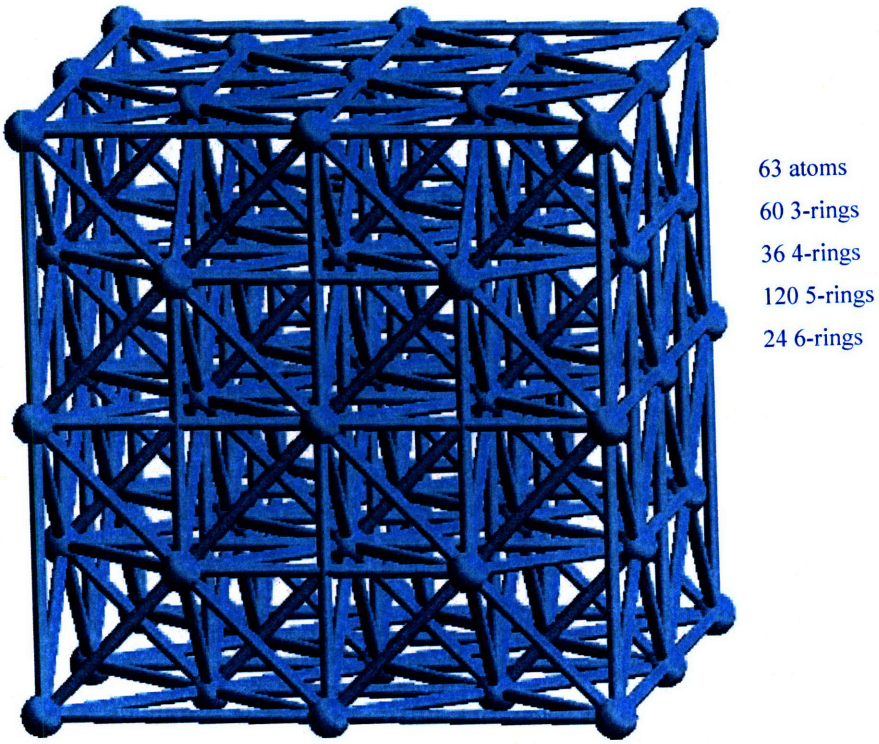

Figure 7.19: Local cluster of monatomic FCC structure when 1st and 2nd nearest neighbors are considered connected. That is, if the lattice constant is *a*, bond cutoff is infinitesimally larger than *a*. There is a total of 63 atoms in the local cluster, comprising 60 3-rings, 36 4-rings, 120 5-rings and 24 6-rings.

Unit cells only contain local information and only apply in crystalline structures. Local clusters apply in both crystalline and non-crystalline structures and contain information of both local and intermediate range. Local clusters for simple cubic, BCC and FCC structures all have 6-rings, which contain information about third neighbors. Larger rings have been found in other more complex structures, such as 12-rings found in silica [4] and rings with 28 Si nodes in sodium silicate glasses [17]. These rings contain connectivity information about even further neighbors.

The unit cell of zircon was shown in Chapter 2. Local clusters of Zr, Si and

O atoms in zircon are shown in figures from 7.20 to 7.22. Only cation-anion bonds are considered when determining rings in zircon. That is, for example, there are no O-O bonds or Zr-Si bonds. Due to this choice, only even-numbered rings are possible. The bond-length cutoff values used are the same as in previous sections: 2.3 Å for Si-O and 3.0 Å for Zr-O.

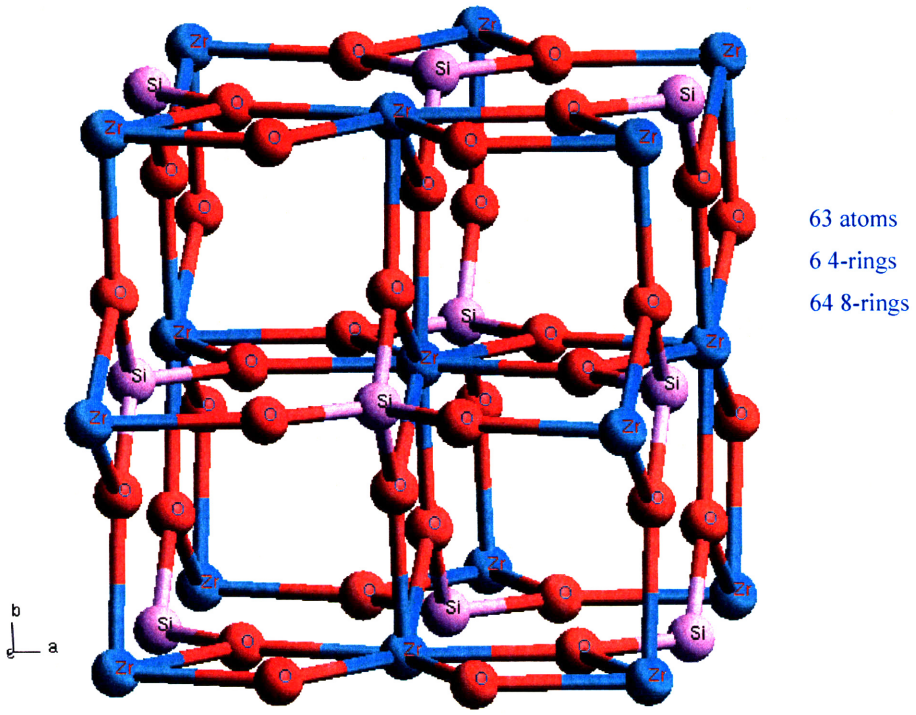

Figure 7.20: The local cluster of Zr atom in zircon. There is a total of 63 atoms in the local cluster, comprising 6 4-rings and 64 8-rings.

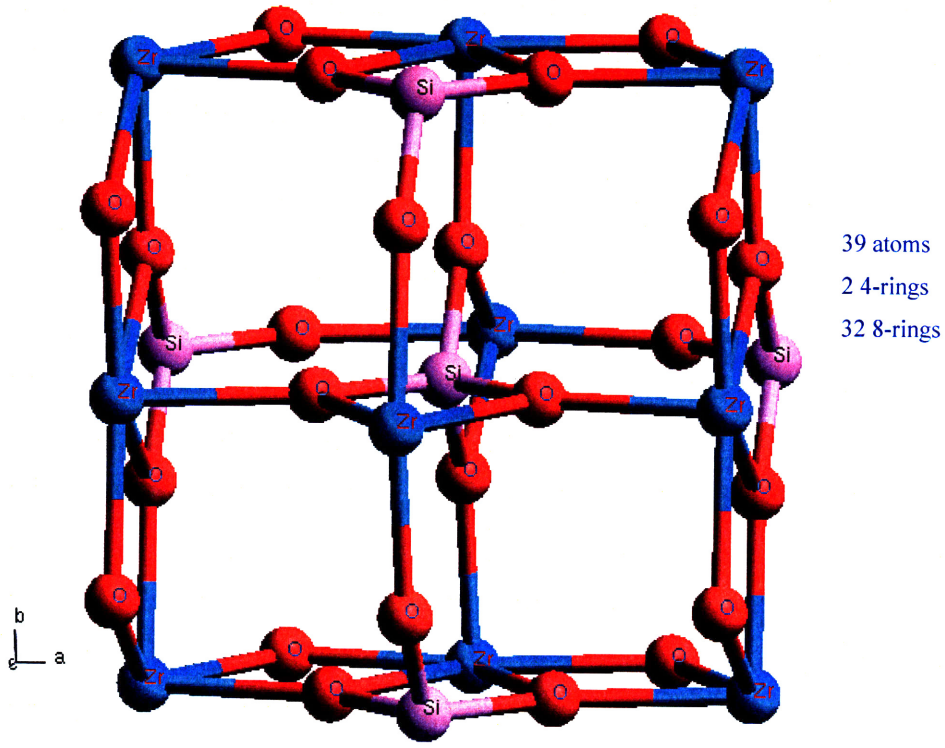

Figure 7.21: The local cluster of Si atom in zircon. There is a total of 39 atoms in the local cluster, comprising 2 4-rings and 32 8-rings.

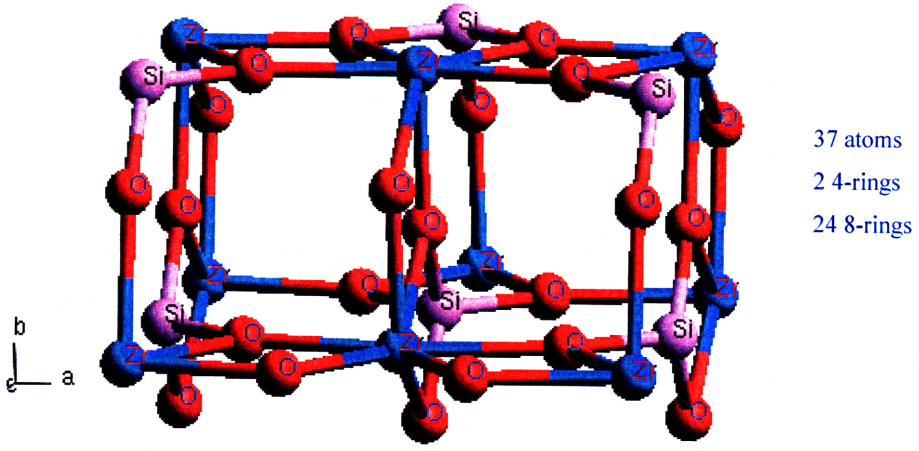

Figure 7.22: The local cluster of O atom in zircon. There is a total of 37 atoms in the local cluster, comprising 2 4-rings and 24 8-rings.

Average local clusters of Zr and Si atoms are given in Table 7.8 and Table

7.9, respectively, for the various structures of Table 7.1. Average local clusters are calculated by averaging the total number of atoms in the local cluster and the count of rings of specific sizes. For example, if the local cluster of Zr #1 has 63 atoms, 6 4-rings and 64 8-rings, and local cluster of Zr #2 has 64 atoms, 8 4-rings, 9 6-rings and 60 8-rings, then the average local cluster of these two Zr atoms will have 63.5 atoms, 7 4-rings, 4.5 6-rings and 62 8-rings.

Table 7.8: Average Zr local clusters in various structures

Structure	Average Zr local cluster		
	Number of atoms	Average ring size	Rings
Crys	63.0	7.657	6.000 4-rings, 64.000 8-rings.
CrysSimu	63.0	7.657	6.000 4-rings, 64.000 8-rings.
Melt	83.935	9.678	3.351 4-rings, 6.117 6-rings, 13.757 8-rings, 19.983 10-rings, 12.438 12-rings, 5.367 14-rings, 0.839 16-rings, 0.093 18-rings.
Quen0%	75.450	9.162	1.741 4-rings, 4.005 6-rings, 12.097 8-rings, 13.852 10-rings, 5.028 12-rings, 1.991 14-rings, 0.023 16-rings, 0.006 18-rings.
Quen8%	78.476	9.759	1.086 4-rings, 2.466 6-rings, 8.346 8-rings, 12.138 10-rings, 5.627 12-rings, 2.463 14-rings, 0.573 16-rings, 0.058 18-rings, 0.016 20-rings.
Quen18%	83.405	10.588	0.666 4-rings, 1.481 6-rings, 5.544 8-rings, 9.293 10-rings, 6.419 12-rings, 3.591 14-rings, 1.104 16-rings, 0.358 18-rings, 0.112 20-rings.
RadiAmor*	77.251	9.462	1.583 4-rings, 3.724 6-rings, 10.897 8-rings, 14.333 10-rings, 7.063 12-rings, 2.192 14-rings, 0.197 16-rings, 0.068 18-rings.
Melt-CB	83.549	11.567	3.169 4-rings, 3.953 6-rings, 7.322 8-rings, 13.181 10-rings, 14.313 12-rings, 15.270 14-rings, 4.902 16-rings, 2.697 18-rings, 1.227 20-rings.
Quen-CB	73.257	9.813	3.213 4-rings, 4.669 6-rings, 10.185 8-rings, 14.142 10-rings, 9.999 12-rings, 5.094 14-rings, 1.171 16-rings, 0.227 18-rings.
RadiAmor-CB*	73.175	9.743	5.471 4-rings, 7.805 6-rings, 17.691 8-rings, 20.596 10-rings, 7.958 12-rings, 6.008 14-rings, 3.588 16-rings, 2.446 18-rings.

*Averaged over non-crystalline Zr atoms determined in Section 7.6

Table 7.9: Average Si local clusters in various structures

Structure	Average Si local cluster		
	Number of atoms	Average ring size	Rings
Crys	39.0	7.765	2.000 4-rings, 32.000 8-rings.
CrysSimu	39.0	7.765	2.000 4-rings, 32.000 8-rings.
Melt	49.097	9.728	1.247 4-rings, 2.459 6-rings, 5.729 8-rings, 8.490 10-rings, 6.035 12-rings, 1.990 14-rings, 0.253 16-rings, 0.012 18-rings.
Quen0%	48.279	9.294	0.676 4-rings, 1.797 6-rings, 5.699 8-rings, 7.149 10-rings, 2.812 12-rings, 0.869 14-rings, 0.014 16-rings, 0.005 18-rings.
Quen8%	49.668	9.926	0.484 4-rings, 1.051 6-rings, 3.825 8-rings, 6.161 10-rings, 3.317 12-rings, 1.240 14-rings, 0.279 16-rings, 0.025 18-rings, 0.007 20-rings.
Quen18%	52.784	10.967	0.304 4-rings, 0.498 6-rings, 2.238 8-rings, 4.434 10-rings, 3.539 12-rings, 1.999 14-rings, 0.785 16-rings, 0.215 18-rings, 0.038 20-rings.
RadiAmor*	48.517	9.522	0.590 4-rings, 1.753 6-rings, 5.987 8-rings, 6.542 10-rings, 3.793 12-rings, 1.190 14-rings, 0.050 16-rings, 0.044 18-rings.
Melt-CB	53.706	11.468	1.616 4-rings, 2.013 6-rings, 3.664 8-rings, 6.131 10-rings, 6.938 12-rings, 6.605 14-rings, 2.867 16-rings, 1.074 18-rings, 0.509 20-rings.
Quen-CB	51.178	9.802	1.947 4-rings, 2.966 6-rings, 5.560 8-rings, 7.872 10-rings, 6.001 12-rings, 3.413 14-rings, 0.468 16-rings, 0.075 18-rings.
RadiAmor-CB*	49.479	9.355	2.819 4-rings, 4.372 6-rings, 11.477 8-rings, 10.105 10-rings, 3.845 12-rings, 2.982 14-rings, 0.966 16-rings, 0.966 18-rings.

*Averaged over non-crystalline Si atoms determined in Section 7.6

An immediate observation from Tables 7.8 and 7.9 is that although melt, melt-quenched and radiation-induced amorphous zircon structures are all amorphous, they have quite different ring contents in average Zr and Si local clusters. The ring contents in average Zr and Si local clusters are shown respectively in Figure 7.23 and Figure 7.24 for structures Melt-CB, Quen-CB and RadiAmor-CB.

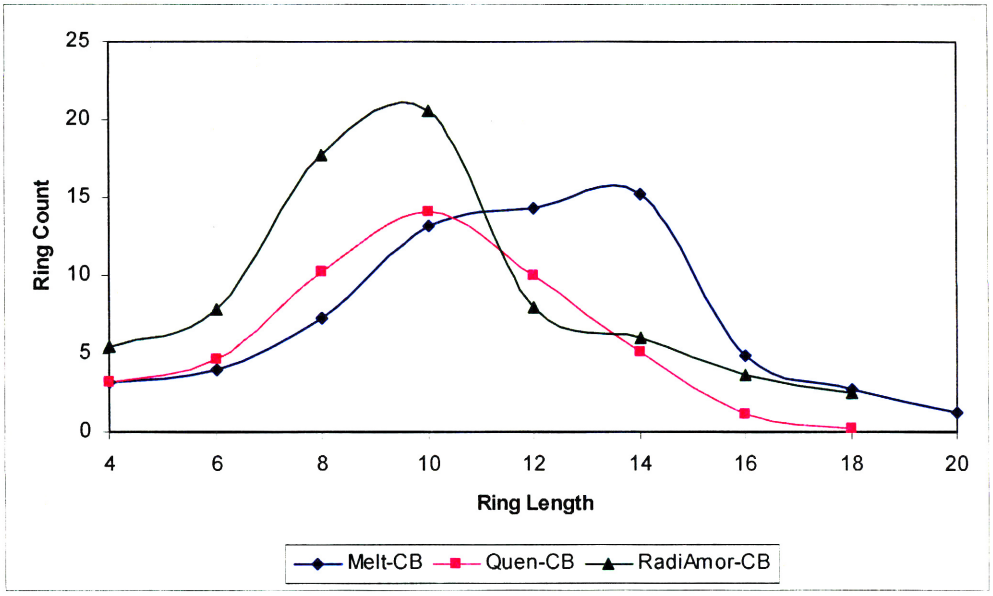

Figure 7.23: Ring contents of average Zr local clusters in structures Melt-CB, Quen-CB and RadiAmor-CB.

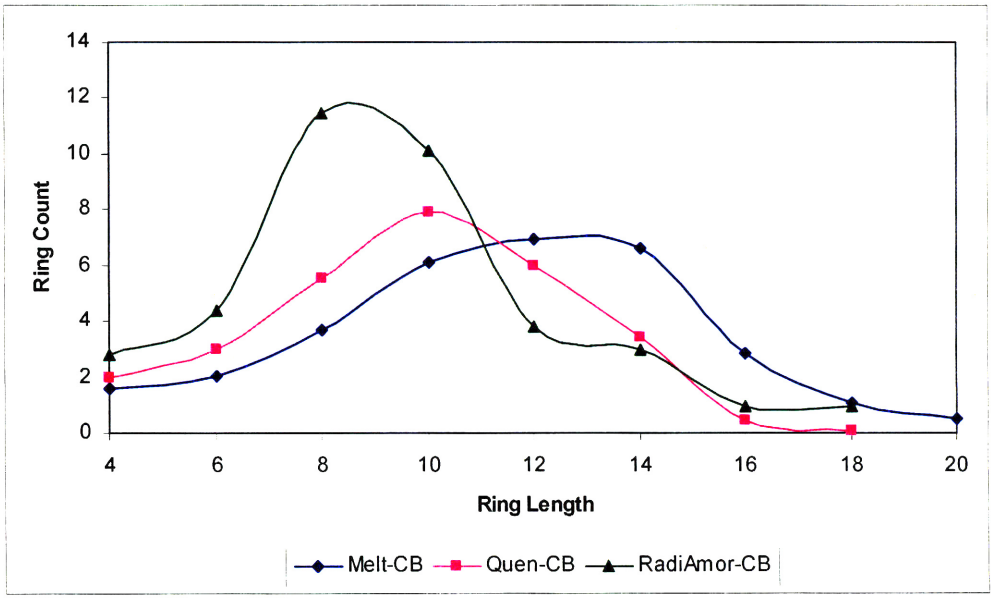

Figure 7.24: Ring contents of average Si local clusters in structures Melt-CB, Quen-CB and RadiAmor-CB.

From Tables 7.8 and 7.9, we can see that for average Zr and Si local clusters, the general trend is that the number of atoms in the average local cluster

increases as the average ring size increases. We can also see in Tables 7.8 and 7.9 that, as the system amorphizes, average ring size increases. Large rings with lengths of 18 and 20 start to appear in amorphous structures. Zr and Si atoms can have local clusters containing large 18- and 20-rings regardless of their individual coordination number. The local clusters of a Zr atom and a Si atom in structure RadiAmor that contain large 18-rings are shown in Figure 7.25 and Figure 7.26, respectively.

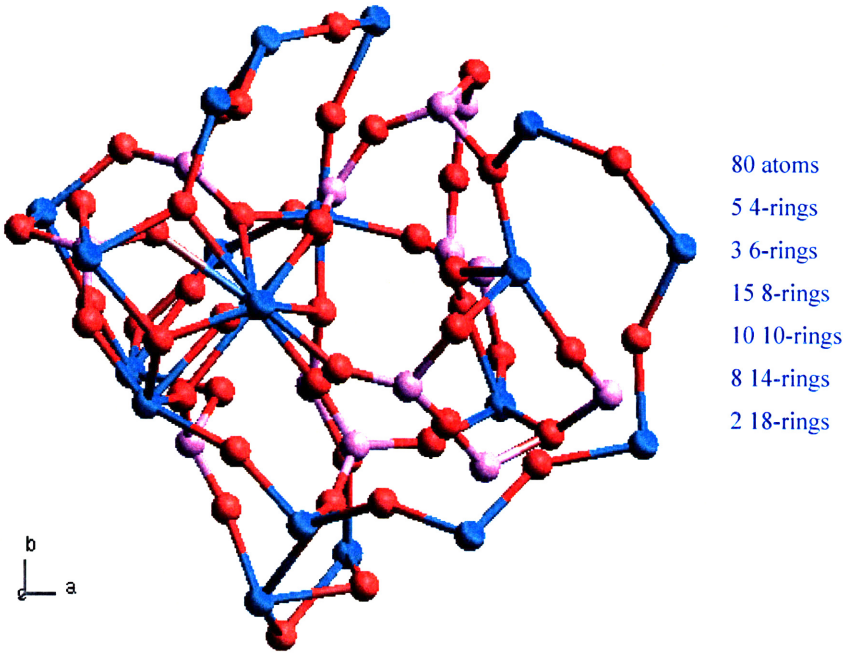

Figure 7.25: (Color) The local cluster of a Zr atom in structure RadiAmor that contains large rings. Blues atoms are Zr, pink atoms are Si, and red atoms are O.

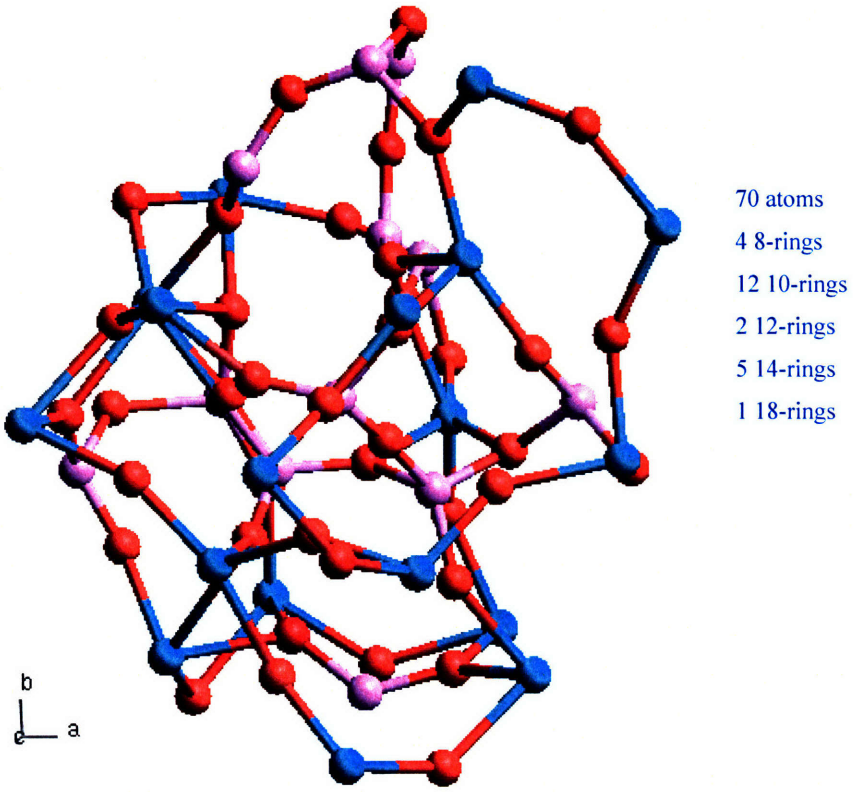

Figure 7.26: (Color) The local cluster of a Si atom in structure RadiAmor that contains large rings. Blues atoms are Zr, pink atoms are Si, and red atoms are O.

The extents of local clusters enlarge when zircon amorphizes. The extent of the Zr local cluster of crystalline zircon shown in Figure 7.20 is 6.607 Å by 6.607 Å by 8.973 Å, whereas the extent of the Zr local cluster of structure RadiAmor shown in Figure 7.25 is 13.539 Å by 11.709 Å by 10.737 Å; the extent of the Si local cluster of crystalline zircon shown in Figure 7.21 is 6.607 Å by 6.607 Å by 5.982 Å, whereas the extent of the Si local cluster of structure RadiAmor shown in Figure 7.26 is 10.670 Å by 11.524 Å by 11.014 Å.

In Tables 7.8 and 7.9, we can also see that for structures Quen0%, Quen8%

and Quen18%, average ring sizes for both Zr and Si local clusters increase with increase of imposed specific volume. This is contrary to what occurs in silica, where an increase of density (thus a decrease of specific volume) is found to be associated with an increase of average ring size [4, 12]. An increase of average ring size associated with an increase of specific volume is more intuitive. The counter-intuitive behavior found in silica is explained in [12] and [4] by the observation that larger rings can fold back on themselves and more effectively occupy space, while smaller rings which are more planar cannot. However, as shown in Figure 7.25 and Figure 7.26, the larger rings in zircon do not appear to fold back to themselves more severely than smaller rings.

7.6 Topological identification of remnant crystalline structure in amorphous zircon

This section develops a topological method to identify crystalline atoms in zircon structures. This method is based on the concept of local clusters in Section 7.5. As we have seen, each and every Zr atom in crystalline zircon has exactly the same local cluster, which is not surprising since every Zr atom is equivalent. The same also holds for local clusters of Si and O atoms. These local clusters provide accurate and unique topological signatures to identify crystalline atoms.

The topological method for identification of crystalline atoms is better than the often-used method based on a Wigner-Seitz partitioning of the space [25, 26]. The Wigner-Seitz cell method depends on a reference grid, which is no longer available in heavily damaged regions. Since the local clusters comprise both short and middle range information, the topological method is also better than those methods based only on local structures limited to

the first coordination shell. For many materials, the local structures are often very similar in crystalline and amorphous phases.

A crystal is an orderly periodic array of atoms. An atom by itself cannot be identified as either crystalline or amorphous. It is the relationships with other atoms that matter. From this perspective, topological identification of crystalline atoms adheres to the essential definition of a crystal, since it deals with the connectivity of atoms directly.

We check each atom in turn to see whether it should be considered a crystalline atom. The atom under investigation is called the "check atom". We can use the entire local cluster exactly as it is as the topological signature to identify crystalline atoms. For example, based on the local cluster of a Zr atom (Figure 7.20), we can define a Zr atom to be a crystalline atom if its local cluster has exactly 6 4-rings, 64 8-rings and no other rings. In addition, the rings must have the same order of atoms as those in crystalline zircon. Among the six 4-rings, four of them should be Zr-O-Zr-O rings while the other two should be Zr-O-Si-O rings. This topological signature, however, is too strict, since the criterion of "no other rings" means there must be no rings with lengths greater than 8. Larger rings can occur when there are nearby point defects in an otherwise crystalline environment. This situation will disqualify the check atom as a crystalline atom when it shouldn't.

A better signature is to only include part of the ring content of the local cluster, such as to only include ring contents up to 4-rings, 6-rings, 8-rings, *etc*. The signature becomes more restrictive when more ring contents are included. In this study, topological signatures including ring contents up to 6-rings are used for all of Zr, Si and O atoms, as shown in Table 7.10.

Table 7.10: Topological signature of Zr, Si and O atoms in locally crystalline zircon

Atom	Signature
Zr	4 Zr-O-Zr-O 4-rings, 2 Zr-O-Si-O 4-rings, 0 6-ring
Si	2 Si-O-Zr-O 4-rings, 0 6-ring
O	1 O-Si-O-Zr 4-ring, 1 O-Zr-O-Zr 4-ring, 0 6-ring

To speed up calculation, before checking ring content, the coordination number of the check atom is calculated. If it is different from the coordination number in crystalline zircon, no further ring content checking is performed. The algorithm for identification of crystalline atoms in zircon structures is summarized below.

1. Choose an atom in the system, which has not been checked before, as the check atom.
2. If the coordination number of the check atom is different from that in crystalline zircon, 8 for Zr, 4 for Si, and 3 (1 Si and 2 Zr neighbors) for O, go back to step 1 and choose the next check atom.
3. Calculate the local cluster of the check atom and compare it with the topological signatures given in Table 7.10. If they match, the check atom and all the atoms in the rings that are part of the topological signature are considered crystalline atoms.

Table 7.11 shows the results of applying this topological method of identifying crystalline atoms to the structures of Table 7.1. The radiation-induced amorphous simulation boxes, RadiAmor and RadiAmor-CB, have almost half of the atoms as crystalline atoms, almost all of which are close to the simulation cell boundary. Figure 7.27 shows the RadiAmor structure, Figure 7.28 shows only those crystalline atoms in the RadiAmor structure, and Figure 7.29 shows the non-crystalline atoms.

Table 7.11: Percentage of crystalline atoms in the simulation cells for strurctures in Table 7.1

Structure	Percentage of crystalline atoms in the simulation cell
Crys	100%
CrysSimu	100%
Melt	4.53%
Quen0%	5.44%
Quen8%	4.09%
Quen18%	2.64%
RadiAmor	41.51%
Melt-CB	6.08%
Quen-CB	5.57%
RadiAmor-CB	46.82%

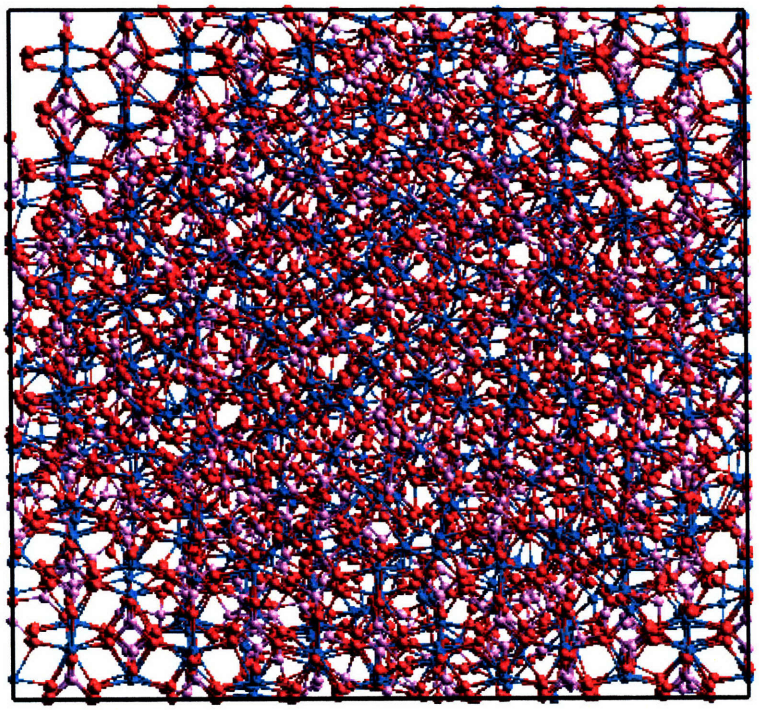

Figure 7.27: Structure RadiAmor

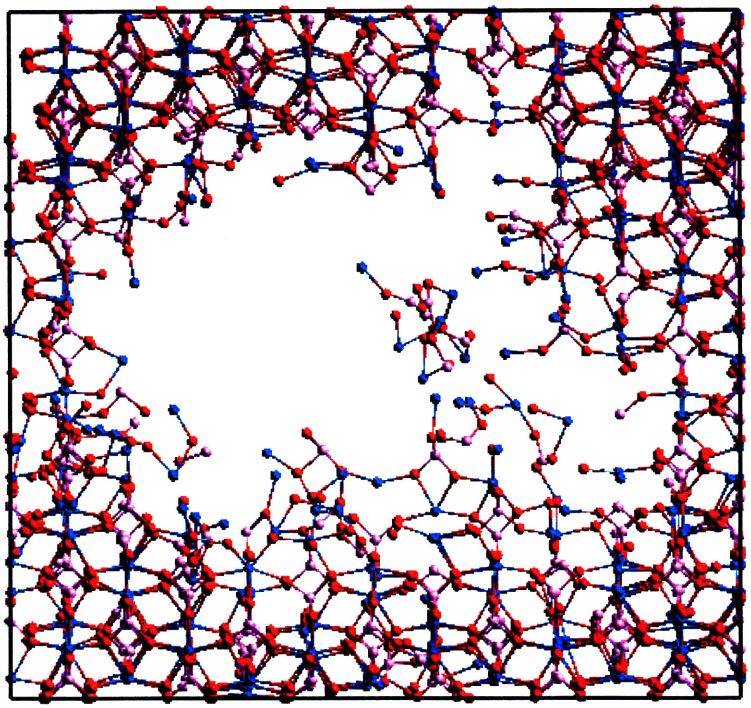

Figure 7.28: Crystalline atoms in structure RadiAmor

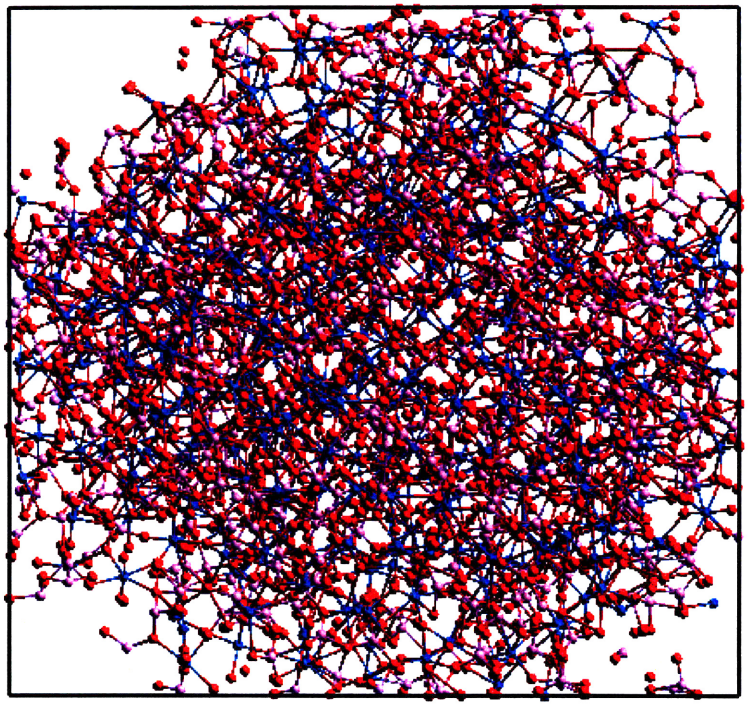

Figure 7.29: Non-crystalline atoms in structure RadiAmor

We can also use this topological method to differentiate crystalline and non-crystalline atoms at different times of collision cascade simulations. Figure 7.30 shows the number of non-crystalline atoms in the structure for the simulation using 1-keV Zr PKA, together with the number of ever-displaced atoms and the number of displaced atoms. Definitions of ever-displaced and displaced atoms were given in Section 6.9.

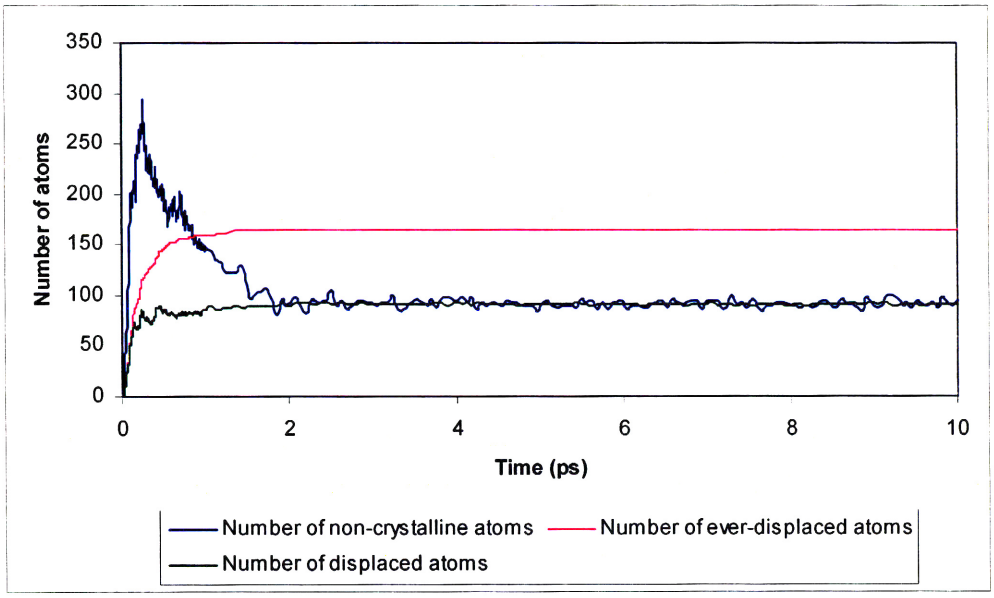

Figure 7.30: (Color) The numbers of non-crystalline atoms, ever-displaced atoms and displaced atoms of the collision cascade simulation using 1-keV Zr PKA.

At the end of the simulation, there are 165 ever-displaced atoms and 91 displaced atoms in Figure 7.30, so about 45% of ever-displaced atoms returned back to their original sites. The number of non-crystalline atoms in the structure peaked at a value of 294 at about 0.25 ps and then decreased and finally stabilized at about 90, so about 204 out of the peak 294 non-crystalline atoms (or almost 70%) are annealed. The annealing of most of the defects can be seen clearly in the movie showing the progress of the

collision cascade caused by the 1-keV Zr PKA. A movie file "Zr_1keV.mov" is available in the CD accompanying this thesis and can be opened by Apple QuickTime movie player.

It can also be seen in Figure 7.30 that the topologically determined number of non-crystalline atoms stabilized at roughly the same value as the number of displaced atoms, thus in lightly damaged structure (only 91 out of 5184, or about 1.8%, atoms are displaced in the simulation using 1-keV Zr PKA), the structural damage accessed by the topological method is more or less equivalent to that accessed by calculation of the number of displaced atoms. However, the calculation of the number of displaced atoms depends on the original reference crystalline grid. In heavily damaged structures where the original crystalline grid doesn't provide any useful reference, the topological method becomes indispensable.

References of chapter 7

[1] F. Farges and G. Calas. Structural Analysis of Radiation Damage in Zircon and Thorite: An X-Ray Absorption Spectroscopic Study. Am. Mineral. 76, 60 (1991).

[2] L. Pauling. The Nature of the Chemical Bond and the Structure of Molecules and Crystals: an Introduction to Modern Structural Chemistry. Cornell University Press, Ithaca, N.Y., 1960.

[3] R.D. Shannon and C.T. Prewitt. Revised Values of Effective Ionic Radii. Acta Cryst. B26, 1046 (1970).

[4] L.W. Hobbs and X. Yuan. Topology and Topological Disorder in Silica. in: Defects in SiO_2 and Related Dielectrics: Science and Technology, ed. G. Pacchioni, L. Skuja and D. Griscom. Kluwer, Dordrecht, Netherlands, 2000.

[5] I. Farnan and E.K.H. Salje. The Degree and Nature of Radiation Damage in Zircon Observed by ^{29}Si Nuclear Magnetic Resonance. J. Appl. Phys. 89,

2084 (2001).

[6] C.S. Palenik, L. Nasdala and R.C. Ewing. Radiation Damage in Zircon. American Mineralogist 88, 770 (2003).

[7] L.W. Hobbs. The Role of Topology and Geometry in the Irradiation-Induced Amorphization of Network Structures. J. Non-Cryst. Solids 182, 27 (1995).

[8] P.K. Gupta. Rigidity, Connectivity, and Glass-Forming Ability. J. Am. Ceram. Soc. 76, 1088 (1993).

[9] P.K. Gupta and A.R. Cooper. Topologically Disordered Networks of Rigid Polytopes. J. Non-Cryst. Solids 123, 14 (1990).

[10] L.W. Hobbs. Topology and Geometry in the Irradiation-Induced Amorphization of Insulators. Nucl. Instr. Meth. B 91, 30 (1994).

[11] L.W. Hobbs, A.N. Sreeram, C.E. Jesurum and B.A. Berger. Structural Freedom, Topological Disorder, and the Irradiation-Induced Amorphization of Ceramic Structures. Nucl. Instr. and Meth. B 116, 18 (1996).

[12] L.W. Hobbs, C.E. Jesurum and B. Berger. The Topology of Silica Networks. in: Structure and Imperfections in Amorphous and Crystalline Silicon Dioxide. ed. R.A.B. Devine, J.-P. Duraud and E. Dooryhee. John Wiley & Sons, 2000.

[13] C.S. Marians and L.W. Hobbs. A Language for the Study of Network Silica Glasses. Diffusion Defect Data 53/54, 31 (1987).

[14] C.S. Marians and L.W. Hobbs. Characterization of SiO_2 Surfaces as a Function of Network Connectivity. J. Non-Cryst. Solids 106, 317 (1988).

[15] K. Goetzke and H.-J. Klein. Properties and Efficient Algorithmic Determination of Different Classes of Rings in Finite and Infinite Polyhedral Networks. J. Non-Cryst. Solids 127, 215 (1991).

[16] L. Guttman. Ring Structure of the Crystalline and Amorphous Forms of Silicon Dioxide. J. Non-Cryst. Solids 116, 145 (1990).

[17] X. Yuan and A.N. Cormack. Efficient Algorithm for Primitive Ring Statistics in Topological Networks. Comp. Mater. Sci. 24, 343 (2002).

[18] T.H. Cormen, C.E. Leiserson, D.L. Rivest and C. Stein. Introduction to Algorithms, 2nd Ed. The MIT Press and McGraw-Hill Book Company, 2001.

[19] P.J. Heaney. Structure and Chemistry of the Low-Pressure Silica Polymorphs. Rev. Mineral. 29, 1 (1994).

[20] R.J. Hemley, C.T. Prewitt and K.J. Kingma. High-Pressure Behavior of Silica. Rev. Mineral. 29, 41 (1994).

[21] C.S. Marians and L.W. Hobbs. Network Properties of Crystalline Polymorphs of Silica. J. Non-Cryst. Solids 124, 242 (1990).

[22] L.W. Hobbs, C.E. Jesurum, V. Pulim and B. Berger. Local Topology of Silica Networks. Phil. Mag. A 78, 679 (1998).

[23] C.E. Jesurum. Local-Rules Based Topological Modeling of Ceramic Network Structures, PhD Thesis. Massachusetts Institute of Technology, Cambridge, MA, 1998.

[24] C.E. Jesurum, V. Pulim, and L.W. Hobbs. Topological Modeling of Amorphized Tetrahedral Ceramic Network Structures. J. Nucl. Mater. 253, 87 (1998).

[25] E. Wigner and F. Seitz. On the Constitution of Metallic Sodium. Phys. Rev. 43, 804 (1933).

[26] E. Wigner and F. Seitz. On the Constitution of Metallic Sodium. II. Phys. Rev. 46, 509 (1934).

Chapter 8: Summary of results and conclusions

8.1 Summary of prior simulations of amorphized zircon

8.1.1 Park *et al.* [1, 2]

The potential Park *et al.* [1, 2] used was the potential 5 in Chapter 3. The major problem with this potential is a negative C_{66} value (Park *et al.* [1, 2] did not report C_{66} value). Another problem is that $a < c$ in the stable zircon structure using this potential, whereas experimentally $a > c$ in zircon. The simulation cell used had 12,288 atoms in total. The largest PKA energy used was 200 eV. The authors' claim that the system size was not large enough for more energetic PKAs was too conservative and lead to the criticism from Trachenko *et al.* [3]. The MD simulations by Park *et al.* were only run to 2 ps, which was probably long enough for their low-energy cascades but must be extended for more energetic PKAs. Boundary energy removal was used. A limited set of threshold displacement energies was determined. It was found that silicon atoms maintained their tetrahedral coordination, while the coordination number of zirconium atoms was reduced. Channeling-like effects were found in the simulations. Amorphization was not investigated.

8.1.2 Crocombette and Ghaleb [4]

Crocombette and Ghaleb [4] calculated threshold displacement energies on a limited set of directions and performed collision cascade simulations in uranium-doped zircon. The potential they used was the potential 3 in Chapter 3, except that a supplementary dipolar interaction was introduced for the U-O pair. Uranium resided at zirconium sites. In simulations for

calculation of threshold displacement energies, a simulation cell with 5,184 atoms was used. The simulation was run to 0.3 ps using the NVE ensemble. For the collision cascade simulations, uranium PKAs with 4 and 5 keV initial energies were introduced in a simulation cell with 139,968 atoms. A constant volume ensemble was used. Boundary layers with 0.3 nm thickness were coupled to a constant temperature heat bath at 300 K. The simulations were run to 10 ps using variable time step size. The maximum time step size used was 2 fs.

Amorphous regions in the center of the cascades were found, based on the definition of "disordered" and "distorted" atoms. Disordered atoms were those atoms that had different coordination numbers from those in the crystalline structure. Distorted atoms had the same coordination numbers as those in the crystalline structure, but the angular distribution around them deviated from the perfect crystal. Both criteria were not really appropriate to characterize amorphization, since they were based only on the first neighbor shell. A decrease of coordination number was found for both Zr and U, but nearly all disordered Si atoms were 5-coordinated. The authors found no noticeable difference between radiation amorphized zircon and quenched zircon. Their quenched zircon was produced by melting the zircon structure at 14,000 K, followed by fast-quenching to 0 K. They found that the zircon structure crystallized on quenching if it was melted at 5,000 K, instead of 14,000 K. Appearance of SiO_2-rich and ZrO_2-rich nanophases was observed. The average bridging number of oxygen between silicon atoms was found to be between 1 and 2.

8.1.3 Trachenko *et al.* [3, 5-9]

Trachenko *et al.* performed classical MD simulations on collision cascades

in zircon [3, 5-9]. The potential used in [5] was the potential 2 in Chapter 3, which resulted in inaccurate elastic constants. Collision cascades caused by 1-keV PKAs in a simulation cell with 8,640 atoms were simulated at both 300 K and 600 K. A substantial decrease of radiation damage was found in cascade simulation with higher ambient temperature. It was found that the damaged structure was less resistant to further radiation damage than undamaged crystalline zircon, although one of the criteria used, the displacement of atoms in already damaged structure, was not a very convincing metric by which to quantify structural damage to an already damaged structure. The ballistic and thermal spike phases of collision cascades were analyzed. Increasing polymerization of SiO_n units was observed with increasing radiation dose. SiO_n units with n = 4, 5, and 6 were found. The authors also reported an increase of density in the core of the damaged region.

The same potential as in [5], the potential 2 in Chapter 3, was used in [6]. Simulation cells with 193,000 atoms and 375,000 atoms were used for simulations of 30 keV and 70 keV collision cascades, respectively. Polymerization of SiO_n units was found, again. However, the authors reported a depleted core, surrounded by densified boundary, even though they had reported a densified core previously [5]. This apparent discrepancy was not discussed by the authors. The same authors used the same potential (potential 2 in Chapter 3) once again in further article [8] to investigate overlap of two displacement cascades. Simulation cells with 81,000 atoms, 192,000 atoms and 375,000 atoms were used for 30 keV and 70 keV PKAs. A variable time step size from 0.01 fs to 1 fs was used to perform the MD simulation to 20 ps. They found again a depleted region in the cascade core, surrounding by a densified shell. They also found that the cascade caused by the 2nd PKA was deflected away from the cascade by the 1st PKA due to the

densified shell. Based on this observation, they used percolation theory to develop a model explaining the large volume swelling of zircon when it amorphizes. The same depleted region in the core of the cascade was also reported by the same authors in [9], where the potential 1 in Chapter 3 was used, and the cascades caused by two overlapping 50 keV U PKA were simulated in a cell with 1,029,000 atoms using constant energy ensemble.

The results of Trachenko *et al.* prompted criticism by Corrales *et al.* [10]. According to Corrales *et al.*, the potential used by Trachenko *et al.* did not adequately describe the atomic scattering physics in zircon, since it produced a bulk modulus and elastic constants significantly higher than experimental values, which resulted in a more rigid structure. The potential used by Trachenko *et al.* also did not use any well-established short-range repulsive term, such as the ZBL potential. The criticism about the potential was confirmed by our own calculations. Although Trachenko *et al.* defended the potential in their response to the comments from Corrales *et al.* [3], it should be noticed that a new potential (potential 1 in Chapter 3), which produced the correct bulk modulus and elastic constants and incorporated the ZBL potential at short range, was used by Trachenko *et al.* in later simulations [9] (the criticism from Corrales *et al.* was published in 2003; the paper using the new potential was published in 2004).

Another criticism by Corrales *et al.* was that the simulation cell size was too small for the energetic cascades simulated, based on calculations using a modified SRIM code. However, based on our own simulations, the requirement on simulation sizes from calculations using SRIM code is generally too conservative.

The third criticism concerned temperature control. The standard temperature

rescaling technique would artificially quench the collision dynamics and result in smaller cascades. Trachenko *et al.* in later simulations [9] used the NVE ensemble. Although there is no problem using the NVE ensemble when the system size is big enough, using boundary energy removal is better since it reduces the required simulation cell size thus results in better usage of computing resources.

Trachenko *et al.* defended their simulations [3]. They stated that even when a ZBL potential was incorporated, there was no noticeable difference. A depleted region in the core of the cascade and a denser boundary were still found, which formed the major cornerstone of a volume-swelling model based on percolation theory. They also proclaimed that there were no problems with their methodology and the way they conducted velocity rescaling, but as described before, they nonetheless refined their potentials and methodologies in later simulations.

8.1.4 Devanathan *et al.* [11, 12]

Devanathan *et al.* simulated melted and melt-quenched amorphous zircon [11] and investigated defect production in collision cascades in zircon [12]. The potential used in both of these studies was the potential 4 described in Chapter 3. A simulation cell with 5,184 atoms was used in [11] to simulate melting-quenching with different imposed volume swelling (8% and 18%). Melt-quenching using constant pressure ensembles was not performed, most probably due to the difficulty of large swelling, since the potential used was not charge-balanced with regard to phase separation products. Bond lengths found in amorphous zircon were 1.55 Å for Si-O and 1.95 Å for Zr-O. Polymerization of Si coordination units was found. At 5000 K, only 23.5% of Si atoms were unconnected.

Defect production was investigated in [12] using PKAs with energies from 0.25 to 5 keV. The simulation cell used had 5,184 atoms and 86,400 atoms for simulations of 0.25 keV and 5 keV cascades, respectively. When selecting simulation cell size, 20 atoms were used for each eV of PKA energy (thus, for example, a 1-keV PKA required a simulation cell with $1000 \times 20 = 20{,}000$ atoms). The NVE ensemble was used for simulations. Initially the structure was kept at a temperature of 30 K. After introducing the PKA into the system, temperature rose about 200 K. Zr on Si anti-site defects and ring-type O replacement were found. The number of interstitials peaked at about 0.5 ps for 5-keV cascades, but their method of counting interstitials based on the Wigner-Seitz cell was not appropriate to heavily damaged structures. In-cascade amorphization was not found for PKAs with energy up to 5 keV, but the authors did not look into the connectivity and did not provide a clear definition of amorphization.

8.2 MD simulations of zircon in this study

The collision cascade simulations of zircon in this study used simulation cells with up to 14,112 atoms. Cascade simulations were performed using variable time step size and with boundary energy removal. Zr and U PKAs with energies up to 10 keV were used.

Threshold displacement energies in zircon were systematically determined. Many special directions, such as toward immediately neighboring atoms or open spaces surrounding the PKA, were considered. The general practice in the literature is to consider threshold displacement energies along well-defined crystallographic directions ([100], [021], *etc.*). However, this choice misses some important special directions, such as the direction toward the

center of the neighboring Si atom for an O PKA. It was found that an energy transfer of at least 391 eV was required to displace the O PKA along this direction.

Cascade detail was extensively examined, including PKA trajectory, cascade extent, time scale, thermal spike, recoil density, distribution of PKA energy among sub-lattices and number of displaced atoms. The crystallographic features of the zircon structure were found to have profound implications for collision cascades. It was found that energetic PKAs were always deflected into the open channel along the *z* direction. Their displacements along the longitudinal *x* direction were never greater than about 4 nm in our simulations. Estimates of cascade extent assuming a homogeneous medium greatly were found to over-predict the PKA displacement along the longitudinal *x* direction.

The effects of PKA mass on collision cascades were studied by comparing the cascades caused by Zr and U PKAs. The U atoms were assumed to be simply "super-mass" Zr atoms in this study: U-Zr, U-Si and U-O interactions were supposed the same as Zr-Zr, Zr-Si and Zr-O interactions, respectively. It was found that heavier PKAs produced longer cascades, more structural damage, and higher temperature in the thermal spike. U traveled further along the longitudinal *x* direction because it was less prone to change of direction. The depleted regions in the core of the cascades surrounded by a densified shell, which were found in simulations by Trachenko *et al.* as described in Section 8.1.3., were not found in our study.

It is also noteworthy that after extensive tests of recently published zircon potentials, it was found that three out of the five tested potentials yielded poor elastic constants and were adjudged unfit for use in convincing

simulations. The published simulation results using these potentials should therefore be viewed cautiously.

Melts and melt-quenched zircon structures were also simulated. Volume expansions of 8% or 18% were imposed for melt-quenching using the originally chosen potential (potential 4 in Chapter 3), since the volume expansion was anomalously large if a constant pressure ensemble was used. Melt-quenching using the new charge-balanced potential was performed using a constant pressure ensemble. The volume expansion of quenched zircon was about 20% compared to crystalline zircon. Radiation-induced amorphization was simulated by overlap of PKAs, and the resulting structure was compared to melt and melt-quenched structures.

8.3 Topological identification of crystalline and amorphous zircon

This study has provided a method to differentiate crystalline and non-crystalline atoms in various zircon structural assemblies, based on local topology. The idea is straightforward: if the local environment surrounding a specific atom is similar to the local environment in the crystalline structure, this atom is considered a crystalline atom. The information about local environment was encoded in the language of primitive-rings, ring statistics and local clusters. Topological signatures were developed separately for atoms in different sub-lattices.

A preliminary application of this methid to a simpler material, SiC, was made earlier by Dr. Xianglong Yuan in the Hobbs group (unpublished). In order to minimize minimize overlap of spheres of influence of defects at high density, subsets of the full local cluster topology were sought by which to characterize crystalline environments. However, the topological

signatures resulting ended up encoded in unnecessarily arcane rules that were specific to the diamond structure. As a result, the topological signatures were procedurally complex, time consuming to implement, and unable to be used on other structures. Rules would have to be developed for every structure encountered. It was therefore decided to develop signatures that employed only the concepts of primitive-ring and local cluster. These signatures are easier to implement, because several algorithms have already been published for systematically identifying primitive-rings and local clusters, and can be spatially restricted at will by truncating signature ring size. They can also easily be generalized to other structures, since in developing the topological signatures for this study, nothing specific about the zircon structure was used. In fact, such topological signatures can be developed for all materials.

The early-stage evolution of non-crystalline disorder and the subsequent recrystallization in zircon collision cascade simulations were successfully modeled by using the topological signatures to identify non-crystalline atoms. Simply using the number of displaced atoms was unable to correctly show the initial peak of structural damage that is followed by the subsequent annealing stage. Using the topological signatures, amorphization within a single collision cascade was observed; thus overlap of cascades is not considered necessary for amorphization of zircon.

A crystal is an orderly periodic array of atoms. An atom by itself cannot be identified as either crystalline or amorphous; it is the relationships with other atoms that matter. From this perspective, topological identification of crystalline atoms adheres to the essential definition of a crystal, since it deals with the connectivity of atoms directly.

The method of topological signatures is better than the Wigner-Seitz cell method, which depends on the original crystalline reference grid. In heavily damaged structures, the original grid does not provide any useful reference. In the radiation-induced amorphous structure simulated in this study, the method of topological signatures was able to differentiate the amorphous region in the center of the simulation box and the crystalline region surrounding it. A few isolated remnant crystalline islands were identified in the amorphous region. About 5% of atoms in zircon melts and melt-quenched structures were identified as crystalline atoms.

The method of topological signatures is also preferable to methods based only on local structures limited to first coordination shell, since often there is little or no difference in the short-range order between crystalline and amorphous structures. One can decide whether or not to include ring contents of larger rings into the topological signature, thus effectively controlling the range of the topological signatures.

8.4 Charge-balance with regard to phase-decomposition products

It is now generally accepted that zircon undergoes phase separation into SiO_2- and ZrO_2-rich local regions upon amorphization. This phase-separation was observed in our simulations. However, it was found in simulations using constant pressure ensembles that the zircon structure underwent abnormally large volume swelling when it amorphized, either thermally or induced by radiation. The huge volume expansion was found to be caused by the ion charges used in the potential model, which gave non-zero charge to SiO_2-like polymerized regions. The ion charges were balanced overall, but not balanced with regard to the phase decomposition products. The strong Coulombic repulsive force within the decomposition

products was the driving force for the large volume expansion. After the ion charges were re-balanced with regard to phase decomposition products, the volume expansion was found to be under control.

The importance of overall charge-balance is obvious, but the importance of charge-balance with regard to phase decomposition products was never appreciated before. This might be one of the reasons why there have been few published simulation results for amorphous zircon using constant pressure ensembles. The charge imbalance of SiO_2 units was also found to produce a large fraction of 3-coordinated Si in amorphous zircon, which was also unrealistic. This problem, too, was solved by using a charge-balanced potential. Compared to melt-quenched zircon using non-charge-balanced potential, the melt-quenched zircon structure obtained using charge-balanced potential had most of Si atoms 4-coordinated and yielded a more realistic Si-O bond length of 1.66 Å. These results with the charge-balanced potential are in good accord with those obtained from *ab initio* simulations [13], though the degree of silica-unit polymerization was found to be larger (up to $Q \sim 2.8$). The issue of charge-balance with regard to phase decomposition products applies to all complex ceramics that decomposes into separate phases upon amorphization (*e.g.* spinels like $MgAl_2O_4$, $ZrSiO_4$, $(Ca,Ln,Ac)_2(Zr,Ti,Ac)_2O_7$ pervoskites, *etc.*).

8.5 Differences between radiation amorphized and quenched zircon

Different amorphous zircon structures were found to be topologically different. Upon amorphization of zircon, the average (primitive) ring size and the number of atoms in the local cluster were found to increase. Larger average ring sizes were found in more pervasively amorphized structures. The radiation-induced amorphous structure was the least pervasively

amorphized one, followed by the melt-quenched structures. The liquid-state amorphous structure was most pervasively amorphized and exhibited the largest average (primitive) ring size.

References of chapter 8

[1] B Park, W.J. Weber and L.R. Corrales. Molecular-Dynamics Simulation Study of Threshold Displacements and Defect Formation in Zircon. Phys. Rev. B 64, 174108 (2001).

[2] B. Park, W.J. Weber and L.R. Corrales. Erratum: Molecular-Dynamics Simulation Study of Threshold Displacements and Defect Formation in Zircon [Phys. Rev. B 64, 174108 (2001)]. Phys. Rev. B 65, 219902(E) (2002).

[3] K. Trachenko, M.T. Dove and E.K.H. Salje. Reply to Comment On "Large Swelling and Percolation in Irradiated Zircon". J. Phys.: Condens. Matter 15, 6457 (2003).

[4] J.P. Crocombette and D. Ghaleb. Molecular Dynamics Modeling of Irradiation Damage in Pure and Uranium-Doped Zircon. J. Nucl. Mater. 295, 167 (2001).

[5] K. Trachenko, M.T. Dove and E.K.H. Salje. Atomistic Modelling of Radiation Damage in Zircon. J. Phys.: Condens. Matter 13, 1947 (2001).

[6] K. Trachenko, M.T. Dove and E.K.H. Salje. Structural Changes in Zircon under Alpha-Decay Irradiation. Phys. Rev. B 65, 180102(R) (2002).

[7] K. Trachenko, M.T. Dove and E.K.H. Salje. Publisher's Note: Structural Changes in Zircon under Alpha-Decay Irradiation [Phys. Rev. B 65, 180102 (2002)] Phys. Rev. B 65, 189902(E) (2002).

[8] K. Trachenko, M.T. Dove and E.K.H. Salje. Large Swelling and Percolation in Irradiated Zircon. J. Phys.: Condens. Matter 15, L1 (2003).

[9] K. Trachenko, M.T. Dove, T. Geisler, I. Todorov and B. Smith. Radiation Damage Effects and Percolation Theory. J. Phys.: Condens. Matter 16, S2623 (2004).

[10] L.R. Corrales, W.J. Weber, A. Chartier, C. Meis and J.-P. Crocombette. Comment on "Large Swelling and Percolation in Irradiated Zircon". J. Phys.: Condens. Matter 15, 6447 (2003).

[11] R. Devanathan, L.R. Corrales, W.J. Weber, A. Chartier and C. Meis. Molecular Dynamics Simulation of Disordered Zircon. Phys. Rev. B 69, 064115 (2004).

[12] R. Devanathan, L.R. Corrales, W.J. Weber, A. Chartier and C. Meis. Molecular Dynamics Simulation of Defect Production in Collision Cascades in Zircon. Nuclear Instruments and Methods in Physics Research B 228, 299 (2005).

[13] E Balan, F Mauri, C Pickard, I Farnan and G Calas. The aperiodic states of zircon: an ab initio molecular dynamics study. Am. Mineral. 88, 1769 (2003).